PERSPEKTIVEN ZUR BEOBACHTUNG DER ELEKTROSCHWACHEN PRODUKTION EINZELNER TOP-QUARKS MIT DEM CMS EXPERIMENT

Julia Bauer

Zur Erlangung des akademischen Grades eines

DOKTORS DER NATURWISSENSCHAFTEN

von der Fakultät für Physik des
Karlsruher Institut für Technologie (KIT)

genehmigte

Dissertation

von

Dipl.-Phys. Julia Bauer
aus Sinsheim

Freude am Schauen und Begreifen
ist die schönste Gabe der Natur.

(A. Einstein)

Zusammenfassung

Schon seit mehreren tausend Jahren beschäftigt sich der Mensch mit den existenziellen Fragen nach seiner Herkunft und dem Sinn seines Daseins. Aus diesem Grundbedürfnis heraus haben sich unterschiedlichste Zugänge entwickelt, die auf ganz eigene Weise versuchen, Antworten zu geben. Die Physik, als eine der ältesten grundlegenden Naturwissenschaften, konzentriert sich hierbei vor allem auf die Erklärung von beobachteten Phänomenen und die theoretische Beschreibung der zu Grunde liegenden Zusammenhänge. Die bereits etwa 400 v. Chr. von Demokrit formulierte Idee, das Universum bestehe aus leerem Raum und einer fast unendlichen Zahl unteilbarer Teilchen, beschäftigt noch heute tausende von Physikern, die sich theoretisch und experimentell mit den fundamentalen Bausteine der Materie und deren Wechselwirkung auseinandersetzen. Spätestens seit Galileo Galilei ist das Experiment fester Bestandteil der wissenschaftlichen Arbeitweise. Das daraus resultierende Wechselspiel von theoretischer Beschreibung beobachteter Phänomene sowie der Induktion theoretischer Modelle in experimenteller Weise hat sich in den letzten Jahrhunderten als sehr effektiv erwiesen. Gepaart mit dem enormen technologischen Fortschritt konnten im vergangenen Jahrhundert grundlegende Erkenntnisse über den Aufbau der Materie gewonnen werden. Nicht minder große Anstrengungen auf dem Gebiet der theoretischen Physik führten zur Entwicklung der relativistischen Quantenfeldtheorie, die Basis der heutigen theoretischen Beschreibung der Elementarteilchen und deren Wechselwirkungen.

Ein experimentelles Grundprinzip spielt bei der Untersuchung der Materie bis heute eine besondere Rolle. In sogenannten Streuexperimenten werden Projektilteilchen auf eine zu untersuchende Probe, das sogenannte Target, geschossen. Aus der gemessenen Winkelverteilung der gestreuten Projektile können dann Rückschlüsse auf bestimmte Eigenschaften der Probe gezogen werden. So war es Rutherford im Jahre 1911 möglich, durch Beschuss von Goldfolien mit Heliumkernen zu belegen, dass Atome aus einem sehr kompakten, geladenen Kern bestehen, der von Elektronen umgeben ist [1]. Durch Erhöhung der Energie in den Kollisionen können immer kleinere Strukturen aufgelöst werden. War man in den 1930er Jahren überzeugt, mit dem Neutron, Proton und Elektron die fundamentalen Bestandteile der Materie identifiziert zu haben, so weiß man heute, dass auch die Kernbausteine eine Substruktur aufweisen. Die Entdeckung neuer Teilchen nahm in den 50er und 60er Jahren eine rasante Entwicklung. Mit der Erfindung der Blasenkammer 1952 konnte erstmals das Target und das Nachweisgerät der Spuren der in der Wechselwirkung erzeugten geladenen Teilchen in einer einzigen Apparatur kombiniert werden.

Dies ebnete den Weg zur Beobachtung unzähliger neuer Teilchen, die mit dem damaligen Verständnis der Elementarteilchen nicht erklärbar waren. Ähnlich zu der Anordnung der chemischen Elemente im Periodensystem durch Erkenntnis der zu Grunde liegenden atomaren Struktur mussten zunächst noch fundamentalere Bausteine eingeführt werden, um die Vielzahl an Teilchen zu ordnen. Mit dem 1964 von Murray Gell-Mann [2] und George Zweig [3] postulierte Konzept der Quarks als eine Klasse von elementaren Teilchen konnte der beobachtete Teilchenzoo erfolgreich strukturiert werden. Erste experimentelle Hinweise auf die Existenz von Quarks als Bausteine der Protonen und Neutronen wurden daraufhin Ende der 60er Jahre in tiefinelastischer Elektron-Nukleon-Streuung gefunden. Aus diesen Anfängen ist in den darauffolgenden Jahrzehnten schrittweise eine Theorie entstanden, die heute als Standardmodell der Elementarteilchenphysik bezeichnet wird.

Das Top-Quark im Standardmodell der Elementarteilchenphysik

Das Standardmodell beschreibt sowohl die fundamentalen Fermionen, als auch die Wechselwirkungen zwischen ihnen. Man unterscheidet drei Kräfte: die elektromagnetische, die starke und die schwache Kraft, die über sogenannte Austauschteilchen, den Bosonen, vermittelt werden. Abbildung 1 gibt einen Überblick über den bis heute beobachteten Teilcheninhalt des Standardmodells und deren Wechselwirkungen. Die Fermionen, zu denen auch die fundamentalen Bausteine der Materie zählen, sind in zwei Klassen unterteilt. Man unterscheidet zwischen den Quarks, die als einzige Fermionen der starken Wechselwirkung unterliegen, und den Leptonen. Zusätzlich lassen sich die Fermionen in drei Familien gliedern, so dass sich die in Abbildung 1 gezeigte Aufteilung ergibt. Bei den Quarks unterscheidet man sechs verschiedene Arten, sogenannte Flavor: Up (u), Down (d), Charm (c), Strange (s), Top (t) und Bottom (b). Bei den Leptonen gibt es drei verschiedene elektrisch geladene Vertreter, das Elektron (e), das Myon (μ) und das Tau (τ), sowie die dazugehörigen elektrisch neutralen Neutrinos. Mit der Beobachtung des Tau-Neutrinos im Jahre 2000 am Fermilab in Chicago/USA wurde auch die Existenz des letzten Fermions des Standardmodells erfolgreich im Experiment bestätigt [4].

Nachdem bis Ende der 70er Jahre bereits fünf von den sechs Quarks nachgewiesen waren, dauerte es noch bis 1995, bis mit der Beobachtung des Top-Quarks durch die beiden Experimente CDF und DØ am Tevatron-Beschleuniger in Proton-Antiproton-Kollisionen bei einer Schwerpunktsenergie von 1.8 TeV auch die Existenz des letzten Mitglieds dieser Gruppe belegt werden konnte [5,6]. Mit einer Masse von $173.1\,\text{GeV}/c^2$ ist das Top-Quark das bei weitem schwerste Fermion. Bedingt durch die große Masse ist seine mittlere Lebensdauer mit etwa $4 \cdot 10^{-25}\,\text{s}$ sogar kürzer als die typische Zeitskala für die starke Wechselwirkung, die etwa $10^{-23}\,\text{s}$ beträgt. Dies führt dazu, dass das Top-Quark zerfällt, bevor es einen Bindungszustand einnehmen kann, während die anderen Quark-Flavor auf Grund ihrer längeren Lebensdauern Hadronen bilden. Damit bietet das Top-Quark als einziges Quark die Möglichkeit, die Eigenschaften eines quasi-freien Quarks zu studieren. Der Zerfall des Top-Quarks ist durch den Flavor-ändernden geladenen Strom der schwachen Wechselwirkung bestimmt. Hierbei wandelt sich das Top-Quark durch Abstrahlung eines W-Bosons in
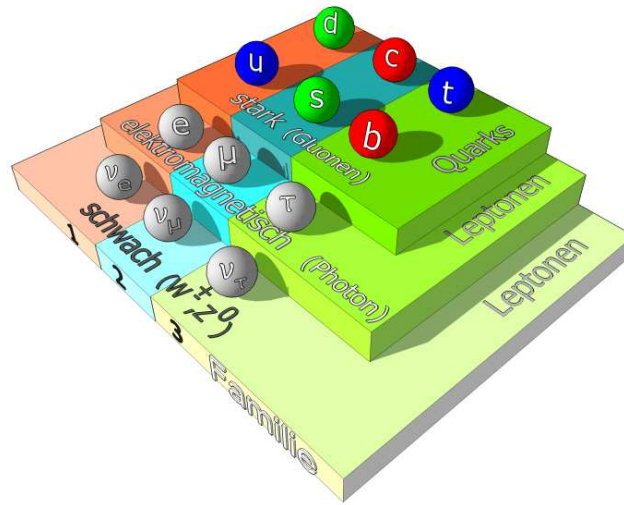
Abbildung 1: Schematischer Überblick über das Standardmodell der Teilchenphysik. Die Fermionen, angedeutet durch Kugeln, sind in zwei Klassen, die Leptonen und Quarks, unterteilt. Jede dieser Klassen besteht aus drei sogenannten Familien, wobei die Masse der jeweiligen Mitglieder von Familie 1 zu Familie 3 größer wird. Je nach Eigenschaft der Teilchen unterliegen sie verschiedenen Wechselwirkungen. Während die Neutrinos, gezeigt auf der untersten Stufe der Teilchenpyramide, nur auf die schwache Kraft sensitiv sind, wechselwirken die restlichen Leptonen auf Grund ihrer elektrischen Ladung auch elektromagnetisch. Die sechs Quarks, die zusätzlich zur elektrischen auch eine sogenannte Farbladung tragen, nehmen zudem auch an der starken Wechselwirkung teil.

fast 100 % der Fälle in ein b-Quark um. Das W-Boson wiederum kann hadronisch in zwei Quarks oder leptonisch in ein geladenes Lepton (e, μ, τ) und das dazugehörige Neutrino $(\nu_e, \nu_\mu, \nu_\tau)$ zerfallen. Seit seiner Entdeckung wird das Top-Quark intensiv studiert, und einige theoretische Vorhersagen konnten erfolgreich bestätigt werden. Dennoch gibt es eine Reihe fundamentaler Eigenschaften, wie den Spin oder die elektrische Ladung des Top-Quarks, die noch immer nicht abschließend untersucht sind. Seine große Masse macht das Top-Quark zu einem besonderen Objekt, dessen Eigenschaften sensitiv sein könnten auf Phänomene jenseits des Standardmodells, wodurch eine möglichst präzise Untersuchung dieses Quarks weiterhin ein spannendes Forschungsfeld bietet. Einen umfassenden Überblick über die Top-Quark-Physik einschließlich aktueller experimenteller Ergebnisse findet man in [7].

Das heutige Wissen über dieses spezielle Quark wurde größtenteils aus der Untersuchung jener Top-Quarks gewonnen, die über die starke Wechselwirkung produziert werden, wobei in Quark-Antiquark-Annihilationen oder Gluon-Fusions-Prozessen auf Grund der Flavor-Erhaltung dieser Wechselwirkung immer Paare von Top- und Antitop-Quarks erzeugt werden. Die Wahrscheinlichkeit dafür, dass eine bestimmte Wechselwirkung zwischen Teilchen stattfindet, wird in der Teilchenphysik durch den Wirkungsquerschnitt ausgedrückt und kann, abhängig von der Topologie des Prozesses, bis zu einer gewissen Genauigkeit theoretisch vorhergesagt werden. Der Wirkungsquerschnitt für die Produktion von Top-Quark-Paaren über die starke Wechselwirkung konnte mittlerweile am Tevatron sehr präzise zu $\sigma_{t\bar{t}} = 7.50 \pm 0.48 \, \mathrm{pb}$ [8]

bestimmt werden. Das Standardmodell sagt jedoch noch einen weiteren Produktionsmodus im elektroschwachen Sektor vorher, bei dem einzelne Top-Quarks in geladenen Strömen über den Austausch von W-Bosonen produziert werden, im Folgenden Einzeltopquark-Produktion genannt. Die Vermessung dieses Produktionsmechanismus' bietet einzigartige Möglichkeiten, gewisse Aspekte der elektroschwachen Theorie des Standardmodells zu testen. Die Stärke der Kopplung des W-Bosons an das b- und Top-Quark wird in der elektroschwachen Theorie über das Matrixelement V_{tb} der CKM-Matrix beschrieben [9, 10]. Bisher konnte der Wert von V_{tb} nur indirekt unter der Annahme einer unitären CKM-Matrix und der Existenz von drei Teilchenfamilien bestimmt werden. Eine Messung des Wirkungsquerschnitts der elektroschwache Produktion bietet jedoch auf Grund der Proportionalität zu $|V_{tb}|^2$ einen direkten Zugang zur Bestimmung dieses Matrixelements. Des Weiteren kann die linkshändige Struktur der elektroschwachen Wechselwirkung durch Analyse der Winkelkorrelationen zwischen den Zerfallsprodukten des Top-Quarks überprüft werden.

Die Vorhersage für den Wirkungsquerschnitt der elektroschwachen Produktion ist im Vergleich zur Top-Quark-Paarerzeugung im starken Sektor etwa um einen Faktor drei kleiner. Des Weiteren ist es wesentlich schwieriger, Untergrundprozesse, die eine ähnliche Topologie im Endzustand besitzen, effektiv zu unterdrücken, da die Wirkungsquerschnitte einiger dieser Prozesse mehrere Größenordnungen über dem des Signals liegen. So dauerte es nach der Entdeckung des Top-Quarks weitere 14 Jahre, bis die beiden Tevatron-Experimente CDF und DØ im Frühjahr 2009 die erste statistisch signifikante Beobachtung der elektroschwachen Produktion einzelner Top-Quarks erlangen konnten [11, 12]. Trotz dieses Erfolges, der ein wichtiges Puzzlestück zum Gesamtbild des Standardmodells beiträgt, wird die präzise Untersuchung dieser elektroschwachen Prozesse auf Grund der geringen Anzahl an produzierten Signalereignissen am Tevatron nicht möglich sein. Diese statistische Limitierung der Messungen am Tevatron wird man mit dem Large Hadron Collider (LHC) überwinden.

Der Large Hadron Collider

Der LHC ist ein gewaltiger Synchrotron-Beschleuniger mit einem Umfang von etwa 27 km. Er befindet sich am Europäischen Kernforschungszentrum CERN in Genf und ist dafür konzipiert, Proton-Kollisionen bei einer Schwerpunktsenergie von bis zu 14 TeV sowie Kollisionen von Blei-Ionen bei einer Schwerpunktsenergie von 5,52 TeV pro Nukleon zu ermöglichen.

Eine der Hauptmotivationen für den Bau eines solch leistungsstarken Beschleunigers ist die noch immer offene Frage nach dem Ursprung der Masse der fundamentalen Teilchen. Ein weit verbreiteter Ansatz zur Implementierung des Phänomens der Teilchenmassen in die Theorie des Standardmodells ist der Higgs-Mechanismus [13]. Durch das Konzept der spontanen Symmetriebrechung können massive Bosonen aber auch Fermionen im mathematischen Rahmen des Standardmodells erzeugt werden, ohne elementare Prinzipien der Theorie zu verletzen. Dabei wird die Existenz eines weiteren Bosons, des sogenannten Higgs-Bosons, vorhergesagt. Die bisher

noch ausstehende Beobachtung dieses Teilchens wäre ein fundamentales Indiz für die Gültigkeit dieses Modells. Doch nicht nur das Higgs-Boson steht im zentralen Interesse des Physikprogramms des LHC. Obwohl die Vorhersagen des Standardmodells in verschiedensten Bereichen bereits eindrucksvoll und teilweilse auch äußerst präzise bestätigt werden konnten, gibt es durchaus theoretische Fragestellungen, aber auch experimentelle Beobachtungen, die Erweiterungen des Standardmodells erfordern. Viele der mit den Erweiterungen verbundenen Effekte oder Existenzen neuer Teilchen werden am LHC voraussichtlich überprüft werden können. Nachdem im September 2008 erstmals Protonstrahlen im LHC zirkulierten, kam es kurz darauf zu einem schweren technischen Zwischenfall, der eine gut einjährige Reparatur- und Testphase nach sich zog. Im November 2009 konnte der Betrieb wieder aufgenommen werden, allerdings bei zunächst vorsichtig gewählten Bedingungen. So sah die Planung für die erste Betriebsphase noch bis vor kurzem eine verringerte Schwerpunktsenergie der Proton-Kollisionen von $\sqrt{s} = 10\,\text{TeV}$ vor.

Da Proton-Kollisionen bei solch hohen Schwerpunktsenergien am LHC zum ersten Mal experimentell zugänglich sein werden, wird man zunächst Prozesse, die in bisherigen Experimenten bereits gut vermessen wurden, dazu verwenden, die von den LHC-Experimenten gewonnenen Daten zu validieren. Abbildung 2 zeigt einen Überblick über die Wirkungsquerschnitte einiger repräsentativer Prozesse des Standardmodells in Abhängigkeit der Schwerpunktsenergie. Auf dem Weg zum Nachweis des Higgs-Bosons liegen eine ganze Reihe Prozesse, deren Wirkungsquerschnitt um einige Größenordnungen höher ist. Diese Prozesse müssen zunächst jeweils intensiv studiert werden, um mit deren Verständnis auf die Suche nach noch kleineren, bisher nicht beobachtbaren, Signalen zu gehen. So wird auch die starke Produktion von Top-Quark-Paaren mit einem Wirkungsquerschnitt, der etwa um einen Faktor 100 höher liegt als am Tevatron, ein Standardprozess sein, der schon in relativ kleinen Datenmengen nachzuweisen sein wird [15]. Auch die Beobachtung der elektroschwachen Produktion einzelner Top-Quarks wird am LHC leichter zugänglich sein als am Tevatron. Wie in der Abbildung 2 zu sehen ist, steigt der Wirkungsquerschnitt für die Produktion von W-Bosonen, einer der Hauptuntergründe, weit weniger stark an als für Top-Quark-Prozesse, so dass ein signifikant besseres Signal-zu-Untergrund Verhältnis im Vergleich zum Tevatron erwartet werden kann.

Die Elektroschwache Einzeltopquark-Produktion am LHC

Das Standardmodell sagt drei verschiedene Moden für die Produktion einzelner Top-Quarks über die elektroschwache Wechselwirkung vorher. Je nach Virtualität des ausgetauschten W-Bosons spricht man vom t-Kanal, s-Kanal oder der assoziierten Produktion. Im sogenannten t-Kanal spaltet sich ein Gluon im Anfangszustand in ein $b\bar{b}$-Quark-Paar auf. Das b-Quark streut daraufhin durch den Austausch eines W-Bosons an einem leichten Quark aus dem zweiten Proton und wandelt sich hierbei in ein Top-Quark um. Die Produktion im s-Kanal beschreibt eine Quark-Antiquark-Annihilation zu einem hochvirtuellen W-Boson, das wiederum in ein b- und ein Top-Quark zerfällt. In der assoziierten Produktion wird ein reelles W-Boson
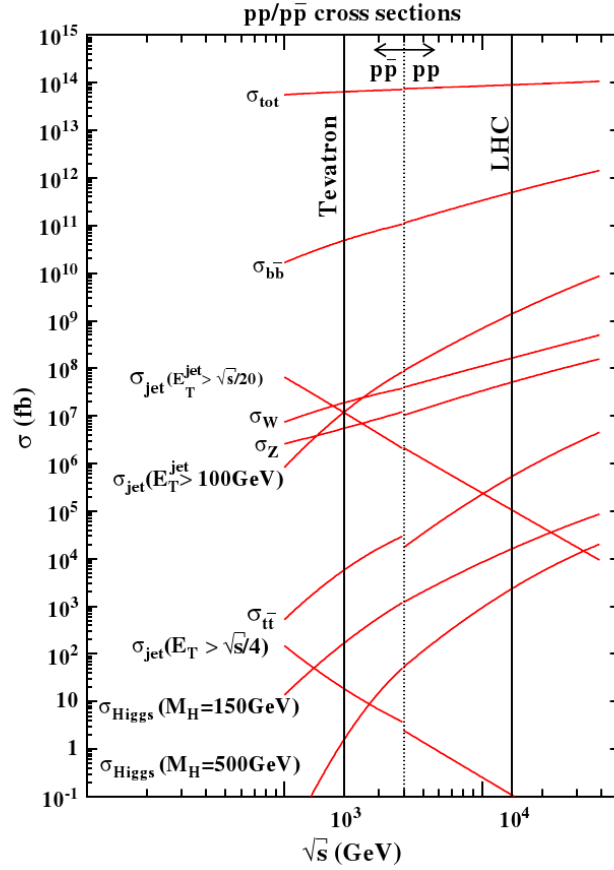
Abbildung 2: Wirkungsquerschnitte für einige repräsentative Prozesse in Abhängigkeit der Schwerpunktsenergie [14]. Beim Übergang vom Tevatron zum LHC bei $\sqrt{s} = 10\,\text{TeV}$, wie von den vertikalen schwarzen Linien angedeutet, steigt der Wirkungsquerschnitt für die Produktion von Top-Quark-Paaren um etwa einen Faktor 100 an. Die Produktion von W-Bosonen hingegen, die den Hauptuntergrund zur Einzeltopquark-Produktion darstellt, steigt, wie in der Abbildung gut zu sehen ist, deutlich flacher mit der Schwerpunktsenergie an, so dass am LHC ein wesentlich besseres Signal-zu-Untergrund-Verhältnis als am Tevatron erwartet werden kann.

zusammen mit einem Top-Quark erzeugt. Die vorhergesagten Wirkungsquerschnitte der drei Prozesse für Proton-Kollisionen bei einer Schwerpunktsenergie von $10\,\text{TeV}$ sind $\sigma^{\text{NLO}}_{t-\text{Kanal}} = 124^{+5.3}_{-6.5}\,\text{pb}$ für den t-Kanal [16], $\sigma^{\text{NLO}}_{s-\text{Kanal}} = 5.0 \pm 0.005\,\text{pb}$ für den s-Kanal [17] und $\sigma^{\text{NLO}}_{tW} = 29 \pm 0.03\,\text{pb}$ für die assoziierte Produktion [18], wobei die beiden letzten Werte ausgehend von einer Schwerpunktsenergie von $14\,\text{TeV}$ entsprechend skaliert wurden. Wegen des vergleichsweise hohen Wirkungsquerschnitts wird eine Wiederentdeckung der Einzeltopquark-Produktion am LHC im t-Kanal erwartet. Der Enzustand dieses Prozesses ist gekennzeichnet durch das gestreute leichte Quark, das meist sehr weit in Vorwärtsrichtung emmitiert wird, ein b-Quark von der anfänglichen Gluonaufspaltung, das sogenannte Spectator-b-Quark, und den Zerfallsteilchen des Top-Quarks. Auf Grund der Struktur der elektroschwachen Wechselwirkung über geladene Ströme zerfällt das Top-Quark in fast $100\,\%$ der Fälle in

ein W-Boson und ein b-Quark. In der hier vorgestellten Analyse wird der Zerfallskanal des Top-Quarks auf den myonischen Endzustand eingegrenzt. Es werden also nur solche Ereignisse als Signal angesehen, bei denen das W-Boson aus dem Top-Quark-Zerfall leptonisch in ein Myon und das zugehörige Neutrino zerfällt: $t \to bW \to b\mu\nu_\mu$. Trotz des vergleichsweise geringen Verzweigungsverhältnisses dieses Kanals von etwa $11\,\%$ ist seine Signatur die vielversprechendste. Durch die Präsenz des Myons im Endzustand können Untergrundereignisse der QCD-Multijet-Produktion sehr effektiv unterdrücken werden, was unabdingbar ist, um den Signalprozess in Daten zu isolieren.

Ein Grundprinzip der starken Wechselwirkung besagt, dass nur farbneutrale Objekte als freie Teilchen beobachtet werden können. Dieses als Confinement bekannte Prinzip führt dazu, dass Quarks immer nur in der Form von zusammengesetzten Hadronen nachgewiesen werden. Bei der Produktion eines Quarks in einer harten Wechselwirkung wie dem Signalprozess bewegt sich dieses Quark mit hoher Energie vom Wechselwirkungspunkt weg. Auf Grund des Confinements bildet sich um dieses primäre Quark herum durch Gluonabstrahlungen und Quark-Antiquark-Paarbildung ein Teilchenjet aus unzähligen Hadronen aus. Dieser Jet entspricht in Energie und Richtung in etwa dem zu Grunde liegenden Parton, und durch die Anwendung geschickter Rekonstruktionsmethoden können Informationen über das primäre Quark aus dem gemessenen Jet extrahiert werden. Die Topologie eines typischen t-Kanal Signalereignisses, die es im Experiment nachzuweisen gilt, zeichnet sich daher durch einen Jet, initiiert von dem gestreuten leichten Quark, und einem sogenannten b-Jet, der von dem b-Quark aus dem Top-Quark-Zerfall stammt, aus. Das Myon, als eines der leptonischen Zerfallsprodukte des Top-Quarks, lässt sich sehr genau vermessen, wohingegen das Neutrino wegen seines sehr kleinen Wirkungsquerschnittes den Detektor ohne Wechselwirkung verlässt und somit nicht direkt nachweisbar ist. Um dennoch Rückschlüsse auf die Kinematik des Neutrinos ziehen zu können, wird die Tatsache ausgenutzt, dass sich auf Grund der Impulserhaltung der Gesamtimpuls der in der Reaktion erzeugten Teilchen in der Ebene transversal zur Strahlrichtung gerade kompensieren muss. Das unbeobachtete Entkommen eines Neutrinos führt somit zu einem Ungleichgewicht, der sogenannten fehlenden Transversalenergie.

Um die Wechselwirkungsprodukte der Proton-Kollisionen am LHC nachzuweisen, wurden insgesamt sechs Experimente entlang des Beschleunigerrings installiert, wobei vier der Detektoren unmittelbar um die Strahlkreuzungspunkte herum aufgebaut wurden. Die vorgestellte Analyse wurde im Rahmen des Compact-Muon-Solenoid (CMS)-Experiments vorbereitet, einer der zwei komplexen Vielzweckdetektoren, die unterschiedlichste Technologien kombinieren, um den Nachweis eines breiten Spektrums an Teilchen über einen großen Energiebereich zu ermöglichen. Besondere Kennzeichen des CMS-Detektors sind der leistungsstarke supraleitende Solenoid-Magnet, der einen Großteil der Detektorkomponenten umgibt, und das komplexe Myon-Nachweissystem, die auch den Namen des Experiments prägten. Die Anordnung der Detektorkomponenten folgt einem annähernd zylindersymmetrisch Prin-

zip, mit der Symmetrieachse entlang der Strahlrichtung und dem Kollisionspunkt der Protonstrahlen im Zentrum des Detektors. Abbildung 3 zeigt schematisch den Aufbau des CMS-Detektors sowie die Signatur einiger repräsentativer Teilchenarten in den entsprechenden Nachweiskomponenten. Direkt um den Wechselwirkungspunkt herum befinden sich Spurrekonstruktionssysteme. Die verwendete Technologie basiert auf Siliziumhalbleitern, wobei im innersten Bereich ein Pixeldetektor, im äußeren Bereich ein Streifendetektor zum Einsatz kommt. Im Anschluss daran sind die Kalorimeter zur Energiemessung der in der Wechselwirkung produzierten Teilchen untergebracht. Es ist unterteilt in ein elektromagnetisches und ein hadronisches Kalorimeter. Das elektromagnetische Kalorimeter besteht aus Blei-Wolframat-Kristallen zum Nachweis von Photonen und Elektronen. Es ist umgeben von dem hadronischen Kalorimeter, in dem sich Messingplatten als Absorber und Szintillatorschichten abwechseln und das dem Nachweis von Hadronen wie Protonen, Pionen oder Kaonen dient. Diese inneren Komponenten sind von dem Solenoid umgeben, dessen homogenes Magnetfeld der Stärke 3.8 T eine präzise Bestimmung
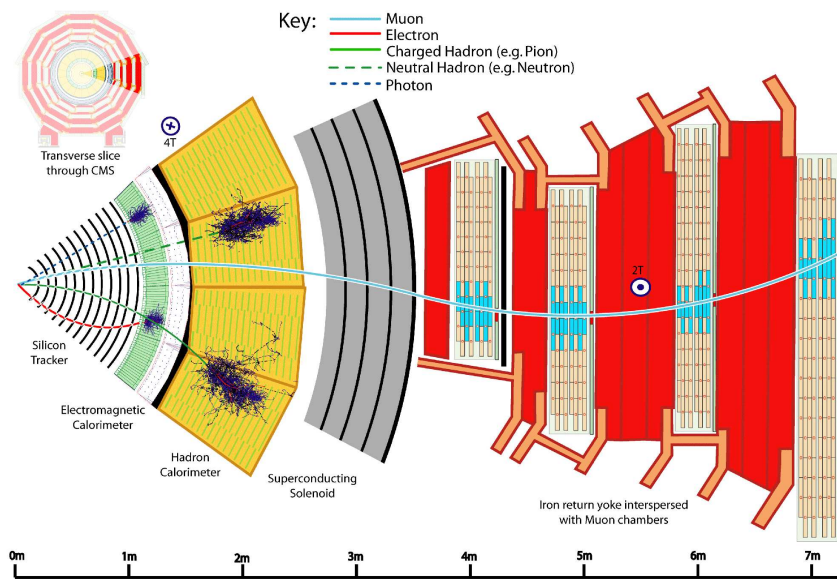

Abbildung 3: Überblick über den Aufbau des CMS-Detektors und die Signatur einiger repräsentativer Teilchenkategorien. Vom Wechselwirkungspunkt nach außen sind - im Innern des supraleitenden Solenoid-Magneten - die Spurnachweis-Detektoren (Tracker), elektromagnetisches und hadronisches Kalorimeter angeordnet. Im Anschluss daran befindet sich das Myonsystem, das aus Spurnachweis-Kammern, eingebettet in das Eisenrückführjoch des Magneten, besteht. Geladene Teilchen hinterlassen Signale in den Tracker-Komponenten, aus denen ihre Spur rekonstruiert werden kann. Die Krümmung dieser Spuren auf Grund der Bewegung der geladenen Teilchen in dem Magnetfeld gibt Aufschluss über den Impuls und das Ladungsvorzeichen des vermessenen Teilchens. Elektronen und Photonen werden im elektromagnetischen Kalorimeter, neutrale und geladene Hadronen im hadronischen Kalorimeter absorbiert, wodurch ihre Energie bestimmt werden kann. Geladene Teilchen, die in dem außen liegenden Myonsystem nachgewiesen werden, sind mit hoher Wahrscheinlichkeit Myonen, da diese den Detektor als minimal ionisierende Teilchen fast ungestört mit nur geringem Energieverlust durchqueren.

von Impuls und Ladungsvorzeichen geladener Teilchen in den Siliziumdetektoren ermöglicht. Myonen, die in den Proton-Kollisionen erzeugt werden, durchqueren die Kalorimeter fast ungestört und deponieren nur eine geringe Menge ihrer Energie in der Größenordnung von etwa 2 GeV. Diese Eigenschaft nutzt man aus, indem man außerhalb der Kalorimetrie ein Myon-System, basierend auf Spurrekonstruktions-Detektoren, anschließt. Geladene Teilchen, die in diesen äußersten Spurkammern detektiert werden, sind mit sehr hoher Wahrscheinlichkeit Myonen. Die Myonkammern sind in ein gewaltiges Rückführjoch aus Eisen integriert, so dass hier ohne Verwendung eines zusätzlichen Magnetsystems ein Magnetfeld der Stärke von etwa 2 T zur Vermessung der Myonen im äußersten Detektorbereich zur Verfügung steht.

Monte-Carlo Simulation des Signalprozesses

Um in der Entwicklungsphase das Design eines Detektors zu optimieren oder Analysestrategien zu entwickeln, verwendet man in der Hochenergiephysik sogenannte Monte-Carlo-Simulationen. Um die vielfältigen physikalische Prozese einer Proton-Kollision so realistisch wie möglich zu modellieren, gibt es unterschiedliche, sehr komplexe Programme. Da einige Aspekte solch hochenergetischer Wechselwirkungen nur phänomenologisch beschrieben werden können, müssen die Parameter der Simulation an Kollisionsdaten angepasst werden, sobald diese verfügbar sind. Um jedoch zuvor die Güte der Simulation abzuschätzen, kann man verschiedene Simulationen eines bestimmten Prozesses miteinander vergleichen. Ein wichtiger Aspekt ergibt sich im Rahmen der Simulation des t-Kanal-Prozesses. Um die Kinematik der Partonen im Endzustand dieser Wechselwirkung möglichst realistisch zu beschreiben, müssen Effekte berücksichtigt werden, die von Beiträgen nächsthöherer Ordnung Störungsrechnung (NLO) kommen. Da der Phasenraum dieser Beiträge sich mit dem des Prozesses führender Ordnung (LO) teilweise überdeckt, muss ein spezielles Matching durchgeführt werden, um sicherzustellen, dass jeder Punkt im Phasenraum nur einfach besetzt ist. Die Lösung dieses Problems wird vereinfacht, indem nur die wichtigste NLO Korrektur zum t-Kanal-Prozess berücksichtigt wird. Für die Simulation der einzelnen Beiträge wurden die LO Simulationsprogramme MadGraph/MadEvent [19] und PYTHIA [20] verwendet. Die Normierung der Rate des t-Kanal-Prozesses wurde mit Hilfe des Programms ZTOP [21] bestimmt, welches differentielle Verteilungen mit NLO-Genauigkeit berechnen kann. Die aus dieser Methode gewonnene t-Kanal-Modellierung wurde im Rahmen der hier vorgestellten Arbeit mit zwei weiteren Simulationen verglichen. Während das CompHep basierte SingleTop-Paket [22] einen vergleichbaren Ansatz wählt, werden in MC@NLO [23] alle NLO Korrekturen in der Simulation des t-Kanal-Prozesses berücksichtigt. Der Vergleich der drei Simulationsmodelle zeigt im Allgemeinen eine gute Übereinstimmung. Die beobachteten Diskrepanzen konnten vollständig verstanden werden und sind auf grundlegende Unterschiede in der Behandlung bestimmter Aspekte des Signalprozesses zurück zu führen. Ein Vergleich der Monte-Carlo-Simulationen mit erst kürzlich veröffentlichten Berechnungen von differentiellen Verteilungen der Endzustandspartonen des t-Kanal-Prozesses [24] zeigt jedoch

signifikante Unterschiede in der Kinematik des Spectator-b-Quarks. Die Ergebnisse implizieren, die angewandte Matching-Methode gegebenenfalls für zukünftige Analysen anzupassen. Eine Möglichkeit, den Einfluss der beobachteten Unterschiede auf die finale Analyse abzuschätzen, bietet sich bei der Behandlung der Effekte als systematische Unsicherheit.

Selektion der Signalereigniss-Kandidaten

Im Rahmen der hier vorgestellten Analyse wurde untersucht, welche Möglichkeiten zur Wiederentdeckung der elektroschwachen Einzeltopquark-Produktion sich bei CMS bieten. Das verwendete Analyseszenario ging dabei von einer Datenmenge von $200\,\mathrm{pb}^{-1}$ aus, die bei einer Schwerpunktsenergie von $10\,\mathrm{TeV}$ aufgezeichnet wurden. Wie in Abbildung 2 zu sehen ist, beträgt der gesamte inelastische Wirkungsquerschnitt für Proton-Kollisionen etwa $100\,\mathrm{mb}$. Dies bedeutet, dass nur etwa jedes 750 millionste Ereignis, das bei der Kollision zweier Protonen stattfindet, wirklich ein Signalereignis ist. Um die Signalereignisse in den Daten isolieren zu können, wird eine Selektion durchgeführt, die bestimmte kinematische Besonderheiten des Signalprozesses ausnutzt, um Untergrundereignisse möglichst effektiv zu unterdrücken. Die beiden Prozesse, die bei der Suche nach der elektroschwachen t-Kanal-Produktion von Top-Quarks am dominantesten beitragen, sind die Produktion von QCD-Multijets und die Produktion von W-Bosonen in Assoziation mit leichten Quarks (u, d, s) und Gluonen. Die Wirkungsquerschnitte dieser Prozesse liegen jeweils etwa sechs und drei Größenordnungen über dem Wert für den Signalprozess im t-Kanal. Wie oben bereits erläutert, wird eine effektive Unterdrückung der QCD-Multijet-Ereignisse hauptsächlich dadurch ermöglicht, dass die Signaldefinition auf den myonischen Endzustand eingeschränkt wird. Die Forderung nach einem isolierten Myon, das im Detektor einen großen Abstand zu Jet-Objekten aufweist, reduziert den Anteil dieser Untergrundkategorie an dem selektierten Datensatz auf einen Wert vergleichbar mit dem des Signals. Myonen in den Ereignisse, die dennoch selektiert werden, sind entweder Objekte, die fälschlicherweise als Myonen identifiziert wurden, oder aber Myonen, die aus dem Zerfall von B-Hadronen oder Pionen und Kaonen in den Jets stammen. Um den Beitrag dieser Ereignisse noch weiter zu reduzieren, kann man die transversale Masse des W-Boson, M_T, betrachten, die aus dem gemessenen Myon und der fehlenden Transversalenergie berechnet wird. Im Gegensatz zu Signalereignissen, bei denen das Myon aus dem Zerfall eines W-Bosons stammt, zeigt die Verteilung von M_T für QCD-Multijet-Ereignisse ein deutlich anderes Verhalten, was wiederum dazu ausgenutzt werden kann, den Beitrag dieses Untergrundes durch einen geeigneten Schnitt auf ein tolerierbares Maß zu reduzieren. Bezüglich der zweiten dominanten Untergrundklasse, der Produktion von W-Bosonen in Assoziation mit leichten Quarks und Gluonen, kann die Präsenz des b-Quark-Jets in Sinalereignissen ausgenutzt werden, um den Untergrundbeitrag zu kontrollieren. Die Identifikation solcher b-Jets, genannt b-Tagging, basiert auf der Tatsache, dass Jets, die B-Hadronen enthalten, andere Eigenschaften aufweisen als Jets von leichten Quarks oder Gluonen. Ein wesentlicher Unterschied resultiert aus der verhältnismäßig langen Lebensdauer der B-Hadronen von etwa $1.5\,\mathrm{ps}$. Somit legt das B-Hadron unter Berücksichtigung relativistischer Effekte vor seinem Zerfall eine nachweisbare

Wegstrecke von bis zu einigen Millimetern im Detektor zurück. Die Rekonstruktion der Spuren seiner Zerfallsteilchen passen somit nicht zum Primärvertex der harten Wechselwirkung. Im einfachsten Falle kann solch eine Diskrepanz zwischen den rekonstruierten Spuren in einem Jet und dem Primärvertex daher verwendet werden, um b-Jets von leichten Quark- oder Gluon-Jets zu separieren. Verlangt man in dem Ereignis genau einen als b-Jet identifizierten Jet, kann man den Beitrag der W-Boson-Ereignisse sehr effektiv um drei Größenordnungen reduzieren.

Nach Anwendung aller Selektionsschnitte wurden die resultierenden Ereigniszahlen auf eine Datenmenge von $200\,\mathrm{pb}^{-1}$ normiert. Daraus ergibt sich ein erwarteter Datensatz mit insgesamt etwa 330 Ereignissen, worin etwa 102 Signalereignisse enthalten sind. Der Untergrundbeitrag wird dominiert von Top-Quark-Paar-Erzeugung, welche mit fast 140 erwarteten Ereignissen in der gleichen Größenordnung wie der Signalanteil liegt. Das Signal-zu-Untergrund-Verhältnis in diesem Datensatz beträgt etwa 0.45, was für ein Zählexperiment eine naive Signifikanz von $S/\sqrt{B} = 6.7$ ergibt. Bei dieser Methode werden allerdings keinerlei Unsicherheiten auf die Rate der Untergundprozesse angenommen, welche aber gerade in der Anfangszeit der LHC-Physik signifikant sein können, solange die vorhergesagten Wirkungsquerschnitte der Prozesse nicht experimentell bestätigt wurden. Berücksichtigt man diese Unsicherheiten, so wird klar, dass die Existenz von Signalereignissen in einem reinen Zählexperiment nur schwer mit ausreichender statistischer Signifikanz zu etablieren sein wird.

Extraktion des Signalanteils und statistische Interpretation

In der vorgestellten Studie wurde ein Ansatz gewählt, der die Verteilungen diskriminierender Observablen in einem Likelihood-Fit ausgenutzt, um in dem selektieren Datensatz zwischen Signal- und Untergrundbeiträgen zu unterscheiden und die Anzahl der Signalereignisse abzuschätzen. Im Rahmen dieser Arbeit wurden zwei unterschiedliche Observablen getestet, die beide kinematische Informationen über das Top-Quark benötigen. Hierzu muss der Vierervektor des Top-Quarks aus seinen gemessenen Zerfallsteilchen rekonstruiert werden. Die hier verwendete Methode kombiniert eine etablierte Rekonstruktion der vollen Neutrino-Kinematik aus der fehlenden Transversalenergie [25] mit einer einfachen, aber sehr guten Jetzuordnung, wobei angenommen wird, dass der Jet mit dem b-Tag aus dem Top-Quark-Zerfall stammt. Diese Zuweisung erweist sich in über 90 % der Fälle als korrekt.

Mit der Kenntnis des Vierervektors des Top-Quarks bietet die invariante Masse dieses rekonstruierten Objekts eine Observable, die sich für Signal und Untergrund unterschiedlich verhält. Die in einer Datenmenge von $200\,\mathrm{pb}^{-1}$ erwartete Verteilung ist in Abbildung 4 (a) gezeigt. Wie man in Abbildung 4 (c) sehen kann, weisen die Verteilung für Top-Quark-Prozesse ein deutliches Maximum um die Top-Quark-Masse auf, während die anderen Untergrundprozesse deutlich unterschiedliche Verteilungen zeigen. Die zweite Observable, die untersucht wurde, nutzt eine besondere Eigenschaft des Signals aus, die in der elektroschwachen Natur des Produktionsmechanismus' begründet liegt. Auf Grund der linkshändigen Struktur dieser Wechselwirkung sind die Spinzustände der produzierten Top-Quarks vollständig polarisiert, was zu starken Winkelkorrelationen zwischen den Teilchen im Endzustand

führt. Die Spinbasis, die diese Polarisation im t-Kanal-Prozess maximiert, ist die Projektion des Top-Quark-Spins auf die Flugrichtung des down-type Quarks. In guter Näherung kann hier die Flugrichtung des gestreuten leichten Quarks genommen werden. Da das Quark als einzelnes Objekt im Experiment nicht direkt messbar ist, muss diese Basis entsprechend umdefiniert werden. Wie in [26] gezeigt wird, bietet die sogenannte Spectator-Basis ein ideales System, um die Polarisation der Top-Quarks zu maximieren. Eine besonders sensitive Winkelverteilung ist $\cos\theta_{lj}^*$, wobei θ_{lj}^* der Winkel zwischen dem Jet, der keinen b-Tag hat, und dem Myon, beide gemessen im Ruhesystem des Top-Quarks, ist. Die erwartete Verteilung, normiert auf eine Datenmenge von $200\,\mathrm{pb}^{-1}$, ist in Abbildung 4 (b) gezeigt, der Vergleich für die unterschiedlichen Prozesskategorien in (c). Während das t-Kanal-Signal eine starke Korrelation in dieser Observablen aufweist, ergeben sich für die Untergründe flache Verteilungen. Dies legt die Idee nahe, eine Abweichung in der beobachteten Verteilung von einem flachen Untergrundmodell als Signal zu interpretieren.

(a)

(b)

(c)

(d)
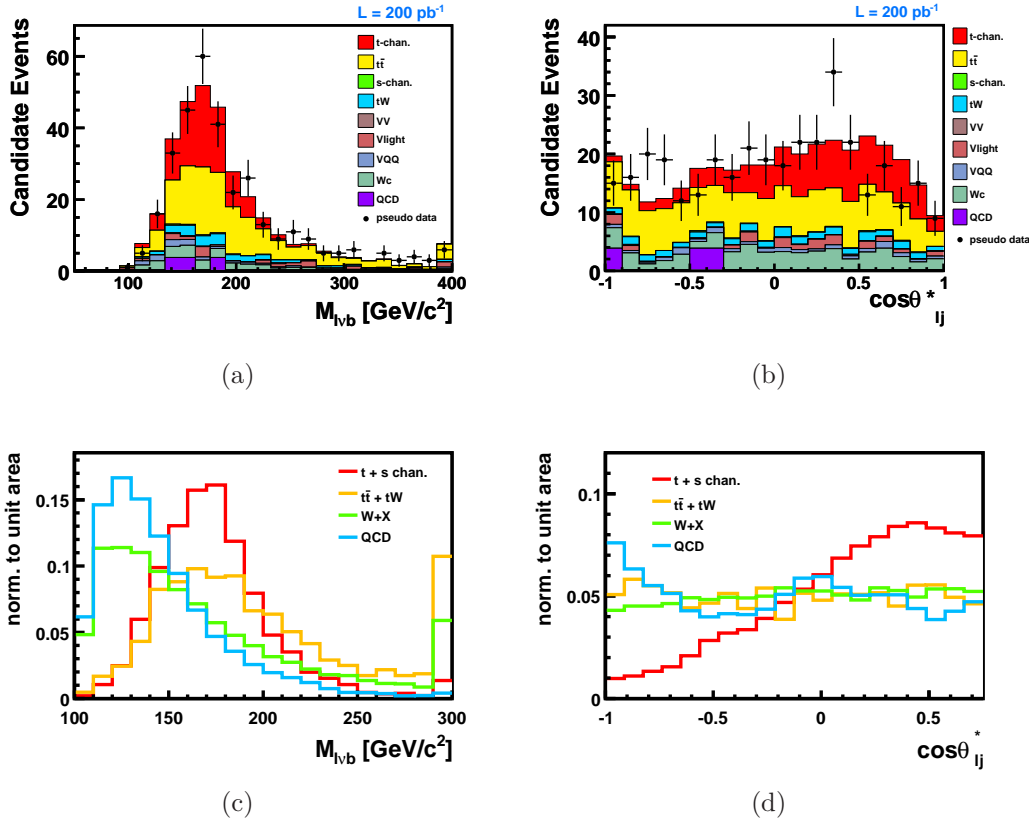
Abbildung 4: Verteilungen der invarianten Top-Quark-Masse $M_{l\nu b}$ (linke Spalte) und der Polarisationvariable $\cos\theta_{lj}^*$ (rechte Spalte). Die oberen beiden Abbildungen zeigen die erwartete Verteilung der beiden diskriminierenden Observablen normiert auf eine Datenmenge von $200\,\mathrm{pb}^{-1}$ für $M_{l\nu b}$ (a) und $\cos\theta_{lj}^*$ (b). Ein Vergleich der auf gleiche Fläche normierten Verteilungen für das Signal und die verschiedenen Untergrundkategorien ist in den unteren Abbildungen gezeigt, für $M_{l\nu b}$ (c) und $\cos\theta_{lj}^*$ (d).

Unter Berücksichtigung systematischer Unsicherheiten, sowohl aus dem Bereich der MC-Modellierung, als auch instrumentellen Ursprungs, wurde die Unsicherheit auf eine Messung des Wirkungsquerschnitts der elektroschwachen Einzeltopquark-Produktion im t-Kanal bestimmt, unter der Annahme, dass der gemessene Signalwirkungsquerschnitt gerade der theoretischen Vorhersage entspricht. Bei Verwendung der invarianten Top-Quark-Masse als diskriminierende Observable ergibt sich eine Messunsicherheit von:

$$M_{l\nu b}: \quad \left.\frac{\Delta\sigma_{\text{t-chan.}}^{\text{est.}}}{\sigma_{\text{t-chan.}}^{\text{est.}}}\right|_{\sigma_{\text{t-chan.}}^{\text{est.}}=\sigma_{\text{t-chan.}}^{\text{SM}}} = \pm 26\%\,(\text{stat.}) \pm 48\%\,(\text{syst.}) \pm 10\%\,(\text{lum.})\,,$$

wohingegen der Fit an die Polarisationsobservable folgende Unsicherheit erwarten lässt:

$$\cos\theta_{lj}^*: \quad \left.\frac{\Delta\sigma_{\text{t-chan.}}^{\text{est.}}}{\sigma_{\text{t-chan.}}^{\text{est.}}}\right|_{\sigma_{\text{t-chan.}}^{\text{est.}}=\sigma_{\text{t-chan.}}^{\text{SM}}} = \pm 35\%\,(\text{stat.}) \pm 15\%\,(\text{syst.}) \pm 10\%\,(\text{lum.})$$

Es stellt sich heraus, dass die rekonstruierte Top-Quark-Masse, obwohl sie eine wesentlich kleinere statistische Unsicherheit aufweist, doch sehr stark durch systematische Effekte limitiert ist. Hier spielt vor allem die Unsicherheit auf die Jet-Energie-Skala eine große Rolle, deren Variation sowohl die Rate der verschiedenen Prozesse als auch die Form der gefitteten Verteilung signifikant verändert. Die Polarisationsobservable $\cos\theta_{lj}^*$ hingegen erweist sich als vergleichsweise stabil, so dass eine Messung des Wirkungsquerschnitts in dem angenommen Szenario von $200\,\text{pb}^{-1}$ bei $10\,\text{TeV}$ zunächst noch statistisch limitiert sein wird. Bis in der Anfangszeit der CMS-Datennahme der t-Kanal-Prozess als Signal etabliert sein wird, werden die Analysen stets die Frage beantworten müssen, welche statistische Signifikanz die beobachteten Signalereignis-Kandidaten aufweisen. Zur Beantwortung dieser Frage wurde untersucht, mit welcher Wahrscheinlichkeit ein beobachtetes Signal durch eine Fluktuation des Untergrundes erklärt werden kann. Unter der Annahme der Existenz des Signalprozesses wie vom SM vorhergesagt erhält man somit aus der hier vorgestellten Analysestrategie für beide diskriminierenden Observablen eine erwartete Signifikanz von je 2.7σ. Als zentrales Ergebnis der hier vorgestellten Arbeit ergibt sich somit, dass es auf Basis der präsentierten Analysemethode möglich ist, eine erste Evidenz für elektroschwache Einzeltopquark-Produktion im t-Kanal in einer Datenmenge von $200\,\text{pb}^{-1}$ bei einer Schwerpunktsenergie von $10\,\text{TeV}$ zu erlangen.

Im Laufe des Jahres nach dem Zwischenfall am LHC im September 2008 wurden umfangreiche Untersuchungen zu den Ursachen durchgeführt. Die Erkenntnisse, die aus diesen eingehenden Studien gewonnen wurden, legten eine Anpassung der Parameter für die erste Betriebsphase der Maschine nahe. Zum erneuten Start des LHC im November 2009 wurden die Protonstrahlen zunächst bei einer Schwerpunktsenergie von $900\,\text{GeV}$ zur Kollision gebracht, bevor sich im Dezember eine nur wenige Tage dauernde Betriebsphase bei $\sqrt{s} = 2.36\,\text{TeV}$ anschloss. Im Februar 2010 wurde, entgegen der vorherigen Planung, entschieden, die Energie, auf die die Proton-Strahlen jeweils beschleunigt werden, auf maximal $3.5\,\text{TeV}$ zu limitieren, um

somit einen von den Untersuchungen vorgegebenen Toleranzbereich der Stromlast in den supraleitenden Magneten einzuhalten. Es ist vorgesehen, den Experimenten solange Proton-Kollisionen bei einer Schwerpunktsenergie von $7\,\mathrm{TeV}$ bereitzustellen, bis eine Datenmenge entsprechend einer integrierten Luminosität von etwa $1\,\mathrm{fb}^{-1}$ aufgezeichnet wurde. Unterbrochen wird dieser Betrieb voraussichtlich im Herbst 2010 für eine kurze Periode, in der der LHC in den Betrieb mit Blei-Ionen wechselt. Nach Abschluss der Datennahme spätestens Ende 2011 ist eine längere Wartungspause geplant, die genutzt werden soll, um umfangreichen Reparaturen und Aufrüstung des Beschleunigers durchzuführen. Diese werden benötigt, um letztendlich die eigentlichen Kenngrößen des LHC, wie die nominelle Schwerpunktsenergie für Proton-Kollisionen von $14\,\mathrm{TeV}$, zu erreichen.

Eine erste Abschätzung des hier vorgestellten Analyseszenarios entsprechend einer Schwerpunktsenergie von $7\,\mathrm{TeV}$ hat gezeigt, dass die Datenmenge, die benötigt wird um vergleichbare Ergebnisse zu erzielen, etwa doppelt so groß sein muss. Dies spiegelt die Tatsache wieder, dass sich der Wirkungsquerschnitt des Signals wie auch der relevanten Untergrundprozesse etwa halbiert, wenn die Schwerpunktsenergie von $10\,\mathrm{TeV}$ auf $7\,\mathrm{TeV}$ reduziert wird. Eine Projektion der Analyse auf die nominelle Datenmenge von $1\,\mathrm{fb}^{-1}$, die bis Ende 2011 zur Verfügung stehen soll, ergibt eine erwartete Signifikanz von etwa 4σ.

Vielversprechend zeigen sich die Ergebnisse, die aus den ersten Kollisionsdaten bei $\sqrt{s} = 7\,\mathrm{TeV}$ gewonnen werden, die seit der Wiederaufnahme des LHC-Betriebs Ende März 2010 aufgezeichnet werden. Auch wenn die Wiederentdeckung des Top-Quarks größere Datenmengen erfordern wird, bieten die bisher aufgezeichneten Ereignisse schon jetzt wertvolle Informationen zur Validierung der in die Analyse eingehenden Messgrößen. Basierend auf der in dieser Arbeit vorgestellten Analyse erscheint es daher realistisch, durch Optimierung der einzelnen Analyseschritte und Berücksichtigung des sich rasch entwickelnden Detektorverständnisses die erforderlichen Signifikanz von 5σ für den Nachweis der elektroschwachen Einzeltopquarkproduktion in dem geplanten Datensatz von $1\,\mathrm{fb}^{-1}$ zu erreichen.

Prospects for the Observation of Electroweak Top-Quark Production with the CMS Experiment

Zur Erlangung des akademischen Grades eines

Doktors der Naturwissenschaften

von der Fakultät für Physik des
Karlsruher Institut für Technologie (KIT)

genehmigte

Dissertation

von

Dipl.-Phys. Julia Bauer

aus Sinsheim

Introduction

Several major efforts in the field of theoretical and experimental particle physics over the last century lead to the establishment of the Standard Model (SM) of elementary particle physics. This framework, based on the concept of quantum field theory, describes the fundamental fermions and their interaction via three different fundamental forces, the strong, the electromagnetic, and the weak interaction. Predictions of the SM on various sectors have been intensively tested and successfully confirmed by high-energy experiments over the last decades. In the framework of the SM the fermions can be divided into two classes, leptons and quarks, each class comprising six different members. While five among six quarks have been observed until the late 1970s, the top quark was the last member of the quark family discovered in 1995 by the Tevatron experiments CDF and DØ [5,6] in proton-antiproton collisions at a center-of-mass energy of $\sqrt{s} = 1.8\,\mathrm{TeV}$. Since then, the top quark has been of huge interest and testing its properties constitutes an exciting exercise for high-energy physicists, as reviewed in [7].

The mass of the top quark constitutes one of its most interesting properties, since this parameter plays a key role for the prediction of the Higgs-boson mass. A recent Tevatron combination of several CDF and DØ measurements yields a top-quark mass of $(173.1 \pm 1.3)\,\mathrm{GeV}/c^2$ [27]. The largest part of our knowledge about this special quark is extracted from top quarks being produced in pairs via the strong interaction in quark-antiquark-annihilation or gluon fusion processes. Being the dominant production mechanism, its cross section has been well measured at the Tevatron with a relative uncertainty of about $6.5\,\%$ [8]. The SM, however, predicts yet an additional production mechanism in the electroweak sector. Therein, the top quarks are produced singly in charged current interactions, which is often referred to as single top-quark production. With a cross-section being about three times smaller compared to the corresponding value for the strong interaction and a much more complex background situation, the confirmation of the electroweak top quark production took much longer. Fourteen years after the discovery of the top quark, the Tevatron experiments finally announced the first observation of singly produced top quarks in 2009 [11,12]. Such a persistent hunt has been motivated by various promising aspects connected to the electroweak production of top quarks. Measuring the cross section provides a direct access to the coupling of the W boson to the top quark, and thus allows a direct measurement of the CKM matrix element V_{tb}. In contrast to an indirect determination, which involves the assumption of a unitary matrix, a precise direct measurement of this diagonal matrix element adds essential information about the possible existence of additional quark generations.

Furthermore, the distinct V–A structure of the electroweak theory can be tested in precise studies of singly produced top quarks. Due to the short lifetime of the top quark of about 10^{-25} s [28] the timescale for its decay is too short for QCD interactions to alter its properties. As a consequence, the spin configuration of the top quark at its production is directly translated into large angular correlations of the decay products. In the case of electroweakly produced top quarks, the study of these angular correlations can be used to test the V–A structure of the electroweak theory, due to which the top quarks are produced 100% polarized. As these tests are sensitive to anomalous couplings of the top quark, they open a window to physics beyond the SM. However, such precise studies require a large amount of signal events and a very good control of background contributions.

With the statistically significant observation of the electroweak top-quark production, the Tevatron experiments have contributed an important piece of evidence to the experimental proof of the SM. Unfortunately, the Tevatron is not able to provide conditions required for a precise testing of the features of the electroweak top-quark production mode. This statistical limitation is expected to be overcome with the Large Hadron Collider, LHC, a proton-proton collider which has been built at the European research laboratory CERN. Operating at its design center-of-mass energy of 14 TeV, top-quark pairs will be produced with a cross section being about a factor 100 higher compared to the value at the Tevatron, whereas the cross sections of the main background processes are much less enhanced. While the observation of the strong production mode has shown to be feasible with an integrated luminosity of a few pb^{-1} [15], the "rediscovery" of single top-quark production is expected to be more demanding. The cross section is by a factor of about 3.5 smaller than for top-quark pair production and, in particular, the background processes are much harder to control.

Three modes are distinguished for the electroweak production of top quarks: the t-channel, the s-channel, and the associated tW production. At the LHC, the rediscovery is expected to happen first in the t-channel mode describing the exchange of a virtual W boson striking a b quark. This channel is by far the most abundant of the three at LHC energies and has the most striking final-state topology. Exploiting the muonic decay channel, where the top quarks decays as $t \rightarrow bW \rightarrow b\mu\nu$, the presence of a muon in the final state provides an efficient suppression of multijet background contributions.

In the first phase of the LHC operation, the analyses will be statistically limited by the amount of recorded data. Therefore, the statement of first single top-quark analyses will focus on the statistical significance of the potentially observed signal events. The studies presented in this thesis have been conducted to evaluate the prospects for an observation of electroweakly produced top quarks in the t-channel. The experimental scenario assumes a center-of-mass energy of 10 TeV and an integrated luminosity of 200 pb^{-1}, which was the standard analysis scenario foreseen for the first LHC physics run after the machine incident of September 2008.

In order to determine the fraction of signal events in an event sample enhanced with signal-candidate events by a dedicated event selection, discriminating signal

properties are exploited in a likelihood fit. The performance of two different discriminating observables is tested, both requiring the full reconstruction of the top-quark four-vector from its decay products. Once the top-quark kinematics are accessible, the invariant mass spectrum provides such a powerful separation observable. A second considered observable takes advantage of angular correlations between the final-state objects of the t-channel process, reflecting the polarization of the electroweakly produced top quarks. With this polarization observable a unique property of the signal process is exploited, providing a very robust discriminator at the same time. In the present thesis, these two discriminating observables are evaluated with a view to the prospects for an observation of electroweak top-quark production with the CMS experiment.

Contents

Chapter 1

Theory

In a huge effort on the field of theoretical physics during the 20th century, the basis for a general description of elementary particles and their interactions was formed. Using the mathematical concept of quantum-field theory [29] it was possible to combine quantum mechanics and relativity, leading to the successful development of the Standard Model of elementary particle physics (SM). Predictions by the SM on various sectors have shown to explain experimental data up to energies $\mathcal{O}(200\,\text{GeV})$ and have been tested to a very high precision over the past decades. The SM, however, cannot be accepted as the final theoretical formulation. The masses of the particles predicted by the model are free parameters and have thus to be determined experimentally. Furthermore, gravitation, the force dominating macroscopic scales, cannot be included in the framework of quantum field theory but is described by General Relativity [30].

The paragraphs below shortly summarize the main aspects of the SM, its particle content up to present knowledge, and interactions among them. Special attention is then paid to the top quark, its different production mechanisms, the decay, and characteristic properties of singly produced top quarks.

1.1 The Standard Model of Elementary Particle Physics

The SM is a particular quantum field theory, based on a set of fields and the gauge symmetries $SU(3)_C \times SU(2)_L \times U(1)_Y$. The building blocks of all matter are fermions, which are point-like and structure-less spin $s = \frac{1}{2}$ particles. Interactions between the fermions are described by quantized fields. Requiring the fields to be locally gauge invariant, the gauge bosons are obtained in form of vector bosons with spin $s = 1$. They are interpreted as force mediators. The Lagrangian of the SM is an expression describing the nature of the particles and forces between them. Its terms describe the kinetic energy of the gauge fields and their self interaction as well as the kinetic energy of the fermions and their interaction with the gauge fields.

Fermions

Table 1.1 summarizes the fermion content of the SM and lists their mass and electrical charge. Two classes appear in the model, quarks and leptons. Leptons come as electrically charged particles (e, μ, and τ) or neutral particles (neutrinos ν), three of them in each category. In the SM, neutrinos are predicted as massless fermions. Observations by experiments studying solar and atmospheric neutrinos, however, strongly indicate a non-vanishing though small mass of the neutrinos [31]. The upper mass limits given in the table are obtained from direct measurements and are still very loose. Tighter constraints on the sum of the neutrino masses can be obtained from cosmology [32, 33].

In the quark sector, six different flavors are described by assigning flavor quantum numbers [34]. The up-type quarks u, c, and t carry an electric charge of $+\frac{2}{3}Q_e$, the down-type quarks d, s, and b have $-\frac{1}{3}Q_e$ charge, where Q_e is the absolute value of the electron charge. The fermion spectrum shown in table 1.1 is extended by the existence of an anti-particle for each lepton and quark, featuring identical quantum numbers except for opposite electric and color charges, where the color charge is a consequence of the strong interaction described below.

The fermions can be grouped into three generations, based on the increasing mass scale of the members. As one can see, the mass scale of the quarks spans five orders of magnitude, beginning at a few MeV for the light quarks u and d, up to about $1.7 \cdot 10^5$ MeV for the heaviest particle, the top quark. Since only the lightest particles are stable, all visible matter surrounding us on earth and in the universe is made up from first generation particles. The two quarks, u and d, are the main constituents of atomic nuclei. In combination with electrons they form electrically neutral atoms. Members of higher generations have a limited lifetime and can only be produced and studied in high-energy experiments by man or in high-energy events in nature, such as interactions of primary cosmic rays with nuclei of the atmosphere.

All fermion masses are free parameters in the SM, thus the values are not predicted and have to be determined experimentally. A better understanding of the origin of the found mass values as well as of the pattern of the observed mass hierarchy are still open questions in particle physics.

Gauge Bosons

The SM contains three independent gauge groups, each modeling a different interaction. The corresponding forces and some properties of the gauge bosons are summarized in table 1.2.

The theory of quantum chromodynamics (QCD) [35] describes the strong interaction by attributing a color charge to the quarks, whereas leptons do not carry color at all. QCD is based on the non-Abelian gauge group of local $SU(3)_C$ transformations of the quark-color fields. Invoking local gauge invariance of the corresponding Lagrangian yields eight massless gauge bosons, the gluons. Since gluons are color-charged as well, each carries one unit of color and one unit of anti-color, they interact also with each other. This intrinsic property leads to a principle that is known as "confinement": quarks cannot exist as free particles [36]. The strong force always

Name	Symbol	Electric Charge $[Q_e]$	Mass $[\text{MeV}/c^2]$
electron	e	-1	0.511
electron neutrino	ν_e	0	$\leq 2 \cdot 10^{-6}$
up quark	u	$+\frac{2}{3}$	1.5 ... 3.3
down quark	d	$-\frac{1}{3}$	3.5 ... 6.0
muon	μ	-1	105.7
muon neutrino	ν_μ	0	≤ 0.19
charm quark	c	$+\frac{2}{3}$	$(1.16 ... 1.34) \cdot 10^3$
strange quark	s	$-\frac{1}{3}$	70 ... 130
tau	τ	-1	1177
tau neutrino	ν_τ	0	≤ 18.2
top quark	t	$+\frac{2}{3}$	$(171.8 ... 174.4) \cdot 10^3$
bottom quark	b	$-\frac{1}{3}$	$(4.13 ... 4.37) \cdot 10^3$

Table 1.1: The elementary fermionic particles (spin s$= \frac{1}{2}$) with their electric charge in units of the electron charge and their mass [28]. Experimental uncertainties are quoted only if affecting the given accuracy.

binds quarks together to form bound states called hadrons, which are color-singlet states. Two groups of hadrons are distinguished. Mesons consist of a quark and an anti-quark, baryons are built of either three quarks or three anti-quarks. The most popular representatives of the baryon group are protons and neutrons, the constituents of atomic nuclei. In high energy experiments, single quarks and gluons are produced in inelastic scattering processes. Since they are confined by the strong interaction, they form hadrons when propagating away from the interaction point. Depending on the energy of the initially produced parton, a whole bunch of hadrons is produced. These objects, called jets, contain information about the initial parton and can be measured experimentally.

Phenomena involving electrically charged particles are described by the field theory of quantum electrodynamics (QED) [37]. It is an Abelian gauge theory with symmetry $U(1)_{em}$ and the charge generator Q. The massless gauge bosons of the electromagnetic field are photons, which are neutral with respect to electrical charge, thus the reach of the electromagnetic force is infinite.

Besides electromagnetic and strong interactions, one observes a further, much slower process, which was identified as weak interaction. Two different modes are observed, so-called charged current reactions mediated by the electrically charged $W^\pm$ bosons, and neutral currents under the exchange of Z^0 bosons. In the following, these bosons are referred to as W and Z bosons. It was found that the charged current coupling is restricted to left-handed particles, thus left- and right-

handed fields are introduced, with the weak isospin T as generator of the underlying symmetry group $SU(2)_L$. The W bosons couple only to the left-handed field component, whereas the Z boson couples to both fields, though with different strength. The left-handed states of a generation of fermions are grouped into weak-isospin doublets, each containing either an up- and down-type quark, or a lepton and the corresponding lepton-neutrino. Since one has observed weak processes in the quark sector between quarks of different generations, it was necessary to introduce the concept of quark mixing. In order to keep the structure of weak-isospin doublets, the weak interaction couples to the rotated quark states. By convention, the mixing is introduced to the down-type quark sector such that the weak eigenstates are given as a linear combination of the original mass eigenstates [10]. More details are given in section 1.1.1. In the 1960s, Glashow [38], Salam [39], and Weinberg [40] proposed a concept for the unification of electromagnetic and weak interactions. The underlying symmetry group of this combined sector was enlarged to $SU(2)_L \times U(1)_Y$. Here, the hypercharge generator Y was introduced ($Q = T^3 + \frac{Y}{2}$), since the original charge generator Q of the electromagnetic group does not satisfy the $SU(2)_L$ group of the weak interaction. In this unification each subgroup of the combined symmetry group keeps its own coupling constant.

Summarizing, leptons participate in weak and, if electrically charged, in electromagnetic processes, whereas quarks as color-charged particles are also sensitive to strong interactions.

Name	Symbol	Mediated Force	Electric Charge $[Q_e]$	Mass $[\mathrm{MeV}/c^2]$
photon	γ	electromagnetic	0	0
gluon	g	strong	0	0
Z boson	Z^0	weak	0	91.188 ± 0.002
W bosons	$W^{\pm}$	weak	± 1	80.398 ± 0.025

Table 1.2: Overview of the gauge bosons of the Standard Model, each mediating a different force; the electric charge and the mass of the bosons is given [28].

1.1.1   Electroweak Symmetry Breaking and the Higgs Mechanism

In contrast to what is observed in the experiments, where massive gauge bosons mediate the weak interaction, our model discussed so far describes only massless gauge bosons and massless fermions. The requirement of local gauge invariance prohibits the introduction of mass terms to the Lagrangian by hand, since the Lagrangian would no longer be invariant under local gauge transformations. In addition, the theory would become non-renormalizable and would loose all its predictive power. There are many models that overcome this problem in various ways. The most famous ansatz within the framework of the SM is the Higgs mechanism which allows to include massive particles in a gauge invariant way, preserving renormalizability.

To achieve that with a minimal choice, four scalar fields are added to the Lagrangian in the form of an isospin doublet. Requiring the Lagrangian to be invariant under local, rather than global, gauge transformations, leads to a certain choice of the vacuum expectation value of the scalar Higgs potential. This yields a Lagrangian which is no longer symmetric with respect to the additional scalar fields when expanding around the non-zero minimum of the potential. By this procedure, known as spontaneous symmetry breaking, the gauge bosons become massive, which fits in the requirement for a gauge theory of electroweak interactions involving massive intermediate particles. However, according to the Goldstone theorem [41], a massless scalar occurs whenever a continuous symmetry of a physical system is broken. Thus, besides the desired massive vector bosons one always obtains massless scalar Goldstone bosons, which are, however, not observed. A solution was proposed by Higgs [13]: he showed that if the Goldstone bosons couple to gauge bosons the gauge fields acquire mass. The Goldstone bosons themselves can be eliminated from the Lagrangian by choosing an appropriate gauge. The degree of freedom of the scalar Goldstone bosons is absorbed as the longitudinal degree of freedom of the gauge fields, which would be absent if their mass were zero.

Considering the unbroken unified electroweak theory, the Lagrangian contains an isotriplet of vector fields, $W^i_\mu, i = 1, 2, 3$, the gauge bosons of the weak isospin group $SU(2)_L$, and a single vector field B_μ, the gauge boson of the weak hypercharge $U(1)_Y$. In order to formulate the Higgs mechanism such that the W and the Z bosons become massive and the photon remains massless, four scalar Higgs fields arranged in a weak isospin doublet with weak hypercharge $Y = 1$ are introduced to the Lagrangian. Breaking the symmetry spontaneously then yields the massive $W^\pm$ bosons as a linear combination of the original $W^{1,2}_\mu$ fields, whereas the photon and the Z^0 boson are manifested as mixed states of the original gauge fields W^3_μ and B_μ. This association is defined by the mixing angle θ_W, known as Weinberg angle, which is fixed by the mass ratio of the W and Z bosons: $\cos \theta_W = \frac{m_W}{m_Z}$. Three of the introduced gauge fields can be gauged away into the longitudinal degree of freedom of the W and Z bosons, the only remnant is the neutral Higgs field. The mass of the corresponding scalar Higgs boson, however, remains unpredicted by the model and has to be determined experimentally. Up to now, none of the experiments was able to find such a Higgs particle, thus huge effort is spent on the restriction of the mass range by exploiting both direct and indirect constraints. A lower mass limit $m_H \geq 114.4 \, \text{GeV}/c^2$ is set by direct searches of the LEP experiments [42] and global fits to electroweak precision data including the direct searches yield an upper bound of $m_H \leq 186 \, \text{GeV}/c^2$ at 95% C.L. [43]. The recent combination of results from direct searches performed by the CDF and DØ collaborations at the Tevatron excludes a mass range of $163 \, \text{GeV}/c^2 \leq m_H \leq 166 \, \text{GeV}/c^2$ at 95% C.L. [44] for a SM Higgs boson.

Fermion masses are generated by so-called Yukawa interactions of the fermion fields with the Higgs fields. Adding the corresponding terms for the leptons and the Higgs field to the Lagrangian generates massive leptons, but only for the lower weak isospin doublet members e, μ, and τ, whereas the neutrinos remain massless. Since for the quark sector both weak isospin doublet entries need to acquire

mass, an additional conjugate Higgs multiplet is introduced. As a result of the spontaneous symmetry breaking of this modified Lagrangian, a non-diagonal mass matrix is obtained. As Cabibbo had shown for the quark sector describing four quark flavors, this mass matrix can be diagonalized by unitarity transformations such that the mass eigenstates are connected to the weak eigenstates by a mixing in the down-type quark sector [10]. Kobayashi and Maskawa extended this concept to the full SM quark-flavor content and included the mechanism of CP violation in their formulation of the 3×3 mixing matrix, called CKM matrix [9]:

$$
\begin{pmatrix} d' \\ s' \\ b' \end{pmatrix} = \begin{pmatrix} V_{ud} & V_{us} & V_{ub} \\ V_{cd} & V_{cs} & V_{cb} \\ V_{td} & V_{ts} & V_{tb} \end{pmatrix} \cdot \begin{pmatrix} d \\ s \\ b \end{pmatrix} \tag{1.1}
$$

Considering charged current interactions, this opens the theoretical window for couplings between quarks of different generations, which has been widely observed by experiments. The coupling strength between two quark flavors i, j is proportional to the matrix element $|V_{ij}|^2$. As the matrix elements are free parameters, their values have to be determined from measurements. The results determined from a global fit that uses all available measurements and imposes the unitarity condition yields the following values [28]:

$$
\begin{pmatrix} 0.97419 \pm 0.00022 & 0.2257 \pm 0.0010 & 0.00359 \pm 0.00016 \\ 0.2256 \pm 0.0010 & 0.97334 \pm 0.00023 & 0.0415^{+0.0010}_{-0.0011} \\ 0.00874^{+0.00026}_{-0.00037} & 0.0407 \pm 0.0010 & 0.999133^{+0.000044}_{-0.000043} \end{pmatrix} \tag{1.2}
$$

Direct measurements of single matrix elements are only available for the u- and c-quark sector. The two top quark related elements V_{td} and V_{ts} are determined from the measurement of $B - \bar{B}$ meson oscillations, where the B_d^0 system provides access to V_{td}, whereas information about V_{ts} can be extracted from the oscillation measurements in the B_s^0 system. The absolute value of the ratio of the two matrix elements, $|V_{td}/V_{ts}|$, provides the most accurate information, since uncertainties due to the theoretical QCD calculation can be eliminated. Concerning the third element, V_{tb}, the direct determination has become possible only recently from measurements of electroweak top-quark production processes, which will be discussed in section 1.3.2.

It is important to note that, although the Higgs sector provides a way to generate mass terms for the gauge bosons and the fermions in the SM Lagrangian by respecting local gauge invariance, the method is not finally satisfying. All the obtained fermion masses as well as the Higgs boson mass are free parameters and the theory provides no prediction for them. In addition, the predicted massive Higgs boson is still a missing piece in the picture of the SM and its observation is needed to clarify whether the SM Higgs mechanism is sufficient to model the nature or if a more complex extension is needed.

1.2 Hard Scattering Processes

In order to study processes between elementary particles, huge accelerators are built where hadrons or leptons are collided at high energies. The rate for a certain process to happen is described by the cross section. In quantum physics, Fermi's Golden Rule [45] allows to calculate the transition rate between an initial and a final state of a quantum system by evaluating the Lorentz-invariant matrix element $\mathcal{M}$ of a certain process and integrating over the phase space of the final state configuration. The mathematical concept for the description of transitions between different quantum states is perturbation theory, considering the coupling strength α_i as perturbation. Although the series should be dominated by the leading-order (LO) term due to the precondition of convergence, the results become more reliable when higher-order contributions are taken into account, and certain phenomena only arise at next-to-leading order (NLO) or at even higher orders. As the evaluation of $\mathcal{M}$ becomes extremely more complex with each additional order, calculations of contributions beyond NLO are rarely available.

The matrix element depends on information about the kinematics of the incoming and outgoing partons, the exchanged gauge bosons and about the interaction between both. Introducing Feynman rules, each mathematical term entering the matrix element calculation can be represented by a certain graphical symbol. This allows to depict a process in so-called Feynman diagrams. An example is shown in figure 1.1, where a quark and an anti-quark annihilate to a gluon, which then splits up to a quark-anti-quark pair again. The lines represent the propagation of partons in space-time, the nodes connecting the particles contain the coupling nature and strength.
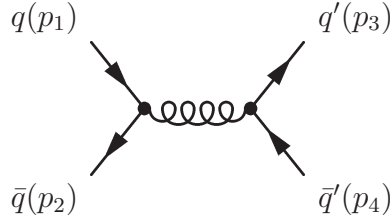

Figure 1.1: Feynman diagram for the annihilation of a quark-anti-quark pair ($q\bar{q}$) into a gluon, which then splits again in a $q'\bar{q}'$ pair.

Considering a process where exactly two partons with four-momenta p_1 and p_2 interact, producing two outgoing partons (p_3, p_4) the Lorentz-invariant Mandelstam variables can be defined as:

$$\begin{aligned}
s &= (p_1 + p_2)^2 = (p_3 + p_4)^2 \\
t &= (p_1 - p_3)^2 = (p_2 - p_4)^2 \\
u &= (p_1 - p_4)^2 = (p_2 - p_3)^2
\end{aligned} \tag{1.3}$$

Introducing these variables allows for a Lorentz-invariant formulation of the matrix element and its representation becomes more convenient.

When colliding hadrons, such as protons, the substructure of the hadron has to be taken into account. This means that the hard scattering process will take place between constituents of the hadron and not the hadrons itself. Thus, the cross section has to be evaluated at parton level. The kinematic behavior of the constituents of a hadron is described by Parton Distribution Functions (PDFs). They are obtained from deep inelastic scattering experiments which test the inner structure of the hadrons. The PDF $f_{i,A}(x_i, \mu^2)$ describes the probability density at a certain scale μ for finding a parton i inside the hadron A carrying the momentum fraction x. Several parametrizations for the PDF are available, figure 1.2 shows the CTEQ6L1 [46] PDF of u and d quarks and gluons in a proton, the scale is set to $\mu^2 = (170 \, \text{GeV}/c^2)^2$. The transition between the partonic system and the actual
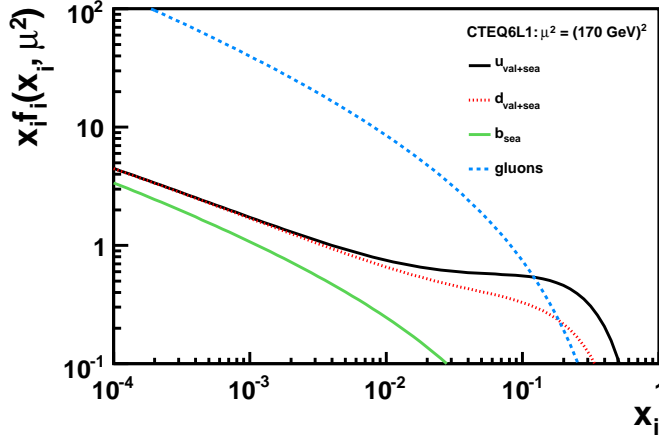

Figure 1.2: The CTEQ6L1 parton distribution function of u, d, and b quarks and gluons in a proton. For the u and d quark both the valence and the sea contribution is shown. The scale is set to a top-quark mass of $170 \, \text{GeV}/c^2$.

hadronic collision is accomplished by the factorization ansatz [47]. It provides a method to calculate the hadronic cross section σ, based on the partonic cross section $\hat{\sigma}$, which is convoluted with the PDFs of the incoming hadrons:

$$\sigma(AB \to cd + X) =$$
$$\sum_{i,j=q,\bar{q},g} \int dx_i dx_j f_{i,A}(x_i, \mu_F^2) f_{j,B}(x_j, \mu_F^2) \cdot \hat{\sigma}_{ij}(ij \to cd; \hat{s}, \mu_R^2, \mu_F^2). \quad (1.4)$$

Here, μ_F is the factorization scale which can be thought of as the scale that separates the long- and short-distance physics, and μ_R is the renormalization scale for the QCD running coupling. Formally, the cross section calculated to all orders in perturbation theory is invariant under changes in these parameters, the μ_R^2 and μ_F^2 dependence of the partonic cross section exactly compensating the explicit scale dependence of the parton distributions and the coupling constant. This compensation becomes more exact as more terms are included in the perturbation series. In the absence of a

complete set of higher-order corrections, it is necessary to make a specific choice for the two scales in order to make cross-section predictions. Different choices will yield different numerical results, a reflection of the uncertainty in the prediction due to unknown higher order corrections. The partonic cross section also depends on the square of the center-of-mass energy of the colliding partons: $\hat{s} = x_i x_j (p_A + p_B)^2$. If the two incoming hadrons have the same energy E, $\hat{s}$ is given by $\hat{s} = 4 x_i x_j E^2$.

1.3 The Top Quark

The first direct observation of top quarks was reported by the Fermilab Tevatron experiments CDF and DØ in 1995 in proton-anti-proton collisions at a center-of-mass energy of $1.8\,\text{TeV}$ [5, 6]. The data amount collected by the two experiments during the Tevatron Run I and the subsequent Run II at a slightly higher center-of-mass energy of $1.96\,\text{TeV}$ allows measurements of various top-quark properties with increasing precision. The most recent combination of top-quark mass measurements by the Tevatron Electroweak Working Group, including preliminary CDF and DØ measurements from Run II, yields $(173.1 \pm 1.3)\,\text{GeV}/c^2$ [27]. Thus, the top quark is by far the heaviest of the quarks. As a consequence, its lifetime of $\tau \sim 10^{-25}\,\text{s}$ [28] is shorter than the typical time scale for QCD interaction $(1/\Lambda_{QCD} \sim 10^{-23}\,\text{s})$, thus the top quark decays before it hadronizes. Properties of the top quark, like the spin polarization, are passed to the decay products without being distorted by the strong interaction. This provides the unique opportunity for studying a quasi-free quark. In the electroweak sector, the top quark plays an important role for the prediction of the Higgs boson mass. Considering virtual corrections to the W-boson propagator, a dependence of the W-boson mass on the masses of the top quark and the Higgs boson is introduced. Precision measurements of these quantities thus allow to confine the parameter space for the Higgs boson mass.

After a short illustration of top-quark decays, this section discusses the various production modes of top quarks. The SM predicts top quarks generated in strong interactions as well as several electroweak production modes. The latter processes are in particular sensitive to new physics phenomena. Finally, the spin polarization of electroweakly produced top quarks, a striking characteristic of these modes, is introduced.

Decay of Top Quarks

Since the large top-quark mass exceeds the W-boson mass by a factor of two, the decay is driven by electroweak processes and the lifetime of the top quark is very short. It decays to almost 100% into a W boson and a b quark, decay modes involving a d or s quark are strongly suppressed by the small CKM off-diagonal matrix elements V_{td} and V_{ts} (see equation 1.2). The different final states are classified according to the subsequent decay of the W boson, which is illustrated in figure 1.3. The hadronic channel (a) is characterized by a W boson going into quarks, $W \rightarrow q\bar{q}'$, whereas in the leptonic channel (b) the W boson decays into a charged lepton and the corresponding neutrino, $W \rightarrow l\nu_l$. The branching ratios are 67.6% and 32.3%,
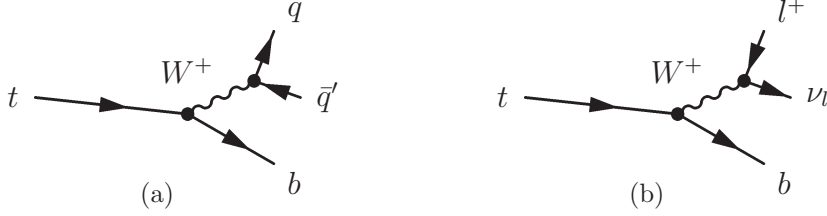
respectively [28].

Figure 1.3: Feynman diagrams of the hadronic (a) and the leptonic (b) top-quark decay. Only decays via a Wtb vertex are shown since other modes are strongly suppressed by the small CKM matrix elements V_{td} and V_{ts}, see eq. 1.2.

1.3.1 Production of Top-Quark Pairs via the Strong Interaction

Due to the flavor conserving nature of the strong interaction, top quarks are always produced pairwise in strong interactions. The leading order Feynman diagrams are shown in figure 1.4. Depending on the initial state parton content, we distinguish between the quark-anti-quark annihilation (1.4 (a)) and gluon fusion processes (1.4 (b), (c), (d)). The contribution of each process to the total cross section is driven by
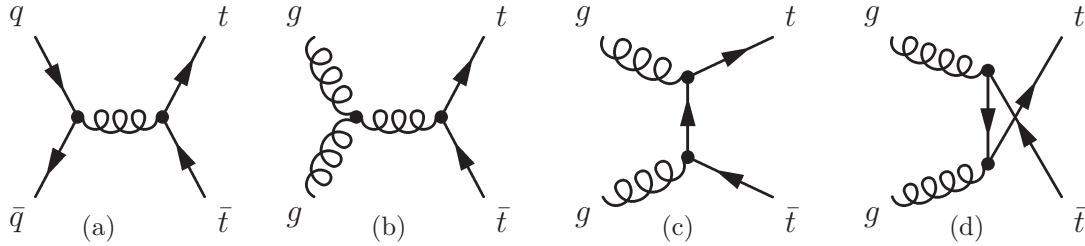

Figure 1.4: Leading order Feynman diagrams of $t\bar{t}$ production: (a) light quark-anti-quark annihilation ($q\bar{q} \rightarrow t\bar{t}$), and gluon fusion ($gg \rightarrow t\bar{t}$) (b), (c), (d).

the PDF of the initial state partons at a given energy scale μ^2, which is typically at the threshold value of the top-quark mass m_t^2. Assuming a collision center-of-mass energy of 10 TeV, the typical momentum fraction necessary to produce a top quark is estimated by $m_t/\sqrt{s} = 0.017$. Thus, already low parton momentum fractions x suffice to generate a top-quark pair. As can be seen from figure 1.2, the low x region is totally dominated by gluons. Consequently, one expects the gluon fusion to be the most important production mode. Calculations yield a contribution of about 90% of gluon induced processes to the total cross section, whereas the quark-anti-quark annihilation accounts to only about 10%. Calculations of the cross section reached

an accuracy of the level of higher order terms, including higher order threshold logarithms. One of the most recently published calculations [48] yields:

$$\sigma_{t\bar{t}}^{\text{NNLO+NLL}} (10\,\text{TeV}) = 414_{-38}^{+36}\,(\text{scale})\,_{-18}^{+20}\,(\text{PDF})\,\text{pb}, \tag{1.5}$$

for a center-of-mass energy of $\sqrt{s} = 10\,\text{TeV}$, assuming a top-quark mass of $171\,\text{GeV}/c^2$ and the PDF parametrization CTEQ6.5. The uncertainties on the central value are dominated by the scale dependence uncertainties, which are derived from a scale variation of 0.5 to 2 times the central value $\mu = m_t$. The uncertainties due to the PDF parametrization are based on the estimation provided by the CTEQ collaboration. Pair production will be the dominant top-quark production channel at the LHC, and recent studies by the CMS collaboration have shown that the cross section is expected to be measured in the muonic decay channel ($t \rightarrow Wb \rightarrow \mu\nu b$) within a statistical and systematic uncertainty of about 20% each in a data amount of $20\,\text{pb}^{-1}$ collected at $\sqrt{s} = 10\,\text{TeV}$ [15].

1.3.2 Production of Single Top-Quarks via the Electroweak Interaction

Besides the production of top-quark pairs via the strong interaction, the weak interaction provides additional mechanisms for top-quark production. In contrast to the strong interaction, the top quarks are singly produced. Three different channels are predicted within the SM. They are classified by the virtuality of the involved W boson, $Q^2 = -q^2$, where q is the four-momentum of the W boson. The corresponding LO Feynman diagrams are depicted in figure 1.5. In the s- and t-channel process, named by the Mandelstam variable characterizing each process, the produced top quark comes with a b-quark or a light quark, respectively, and the involved W boson has a large non-zero virtuality. In the third mode, the associated production, a real W boson is generated in association with the top quark. We will see that the t-channel and the associated production modes are sensitive to the b-quark structure function which has to be introduced in order to avoid singularities in the cross-section calculation.
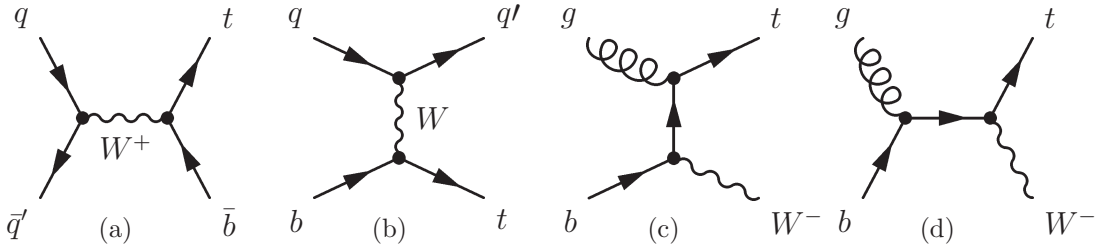

Figure 1.5: LO Feynman diagrams for the different single top-quark production modes: s-channel (a), t-channel (b), and associated production (c), (d)).

After a long search the Tevatron experiments CDF and DØ finally reported the observation of singly produced top quarks in Spring 2009 [11, 12]. Once the signal is established, the different processes provide various interesting measurements.

The electroweak modes are a test of the left-handed structure of the underlying interaction, and, since the top quarks are produced via a Wtb vertex, the cross section is directly proportional to $|V_{tb}|^2$. This provides the unique possibility for a direct experimental access to the CKM matrix element V_{tb}. Evaluating their combined cross-section measurements, the CDF and DØ experiments obtain a value of $V_{tb} = 0.91 \pm 0.08$ at 95% C.L., assuming $\sigma_{t+s}^{\text{theory}} = 3.14 \, \text{pb}$ [49].

Production channels involving a Wts or Wtd vertex are strongly suppressed due to small CKM matrix elements (see equation 1.2). Thus, only single top-quark production via the Wtb vertex is considered in the following. Concerning the initial state of the s-channel process and the light-quark line of the t-channel graph, only the first-generation quark doublet (u, d) contributes significantly [50]. The different production modes are reviewed in more detail in the paragraphs below.

t-channel Production

In the t-channel, a b quark from the proton quark-sea scatters electroweakly a light quark, generating a top quark (figure 1.5 (b)). Since the b quark originates from a gluon splitting into a $b\bar{b}$ pair, this mode is also known as W-gluon fusion mode. In proton-proton collisions, top and anti-top quarks are produced with different rates. Due to the valence quark content of protons (uud), the top quarks contribute roughly twice the rate than anti-top quarks. Some Feynman diagrams representing real
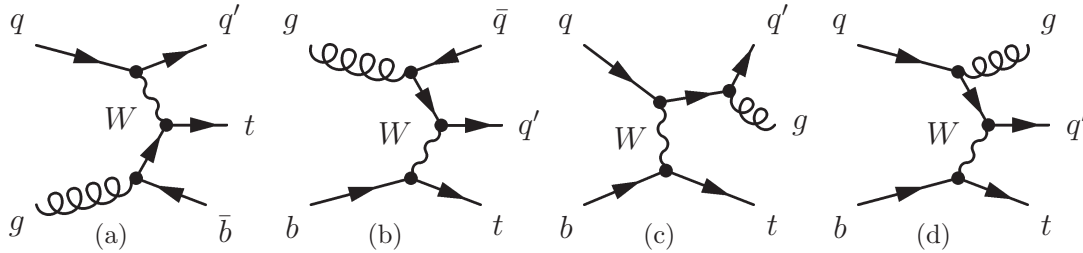

Figure 1.6: Feynman diagrams of t-channel single top-quark production for some real NLO contributions: initial state gluon splitting ((a), (b)) and gluon radiation in the initial (c) and final (d) state.

corrections to the leading-order process are shown in figure 1.6. The most important contribution comes from the $2 \rightarrow 3$ process (figure 1.6 (a)), starting with an initial state gluon splitting up into a $b\bar{b}$ pair, where the final state b quark is called spectator b-quark in order to distinguish it from the b quark from the top-quark decay. In the 5-flavor scheme (5FS), the b quark is taken to be massless. This treatment leads to singularities in the collinear regime of the spectator b-quark, since logarithmic terms of the form of $\ln\left(\frac{Q^2+m_t^2}{m_b^2}\right)$ delay convergence of the perturbation series. Following the factorization ansatz, a b-quark PDF is introduced that absorbs the singularities and provides a resummation of the logarithms to all perturbative orders. The $2 \rightarrow 2$ Born diagram shown in 1.5 (b) then becomes the LO Born process. As the b-quark PDF already contains the gluon splitting up to a certain factorization scale, special care has to be taken when adding the $2 \rightarrow 3$ correction to the Born diagram in order

to avoid phase space double counting. Different methods are used to remove affected terms in the calculation, yielding results compatible within the uncertainties [49].

Recently, a first NLO calculation of the t-channel process based on the 4-flavor scheme (4FS) has been published [16], keeping the b quark massive. In this case, the $2 \to 3$ diagram is considered as leading order process. The NLO calculation is thus accurate to the next higher order in the strong coupling with respect to this diagram. Different scales are chosen for the vertices in the light-quark line (l) and heavy-quark line (h), $\mu_l = (m_t + m_b)/2$ and $\mu_h = (m_t + m_b)/4$. Using the PDF set CTEQ6.6, a top-quark mass of $m_t = 172 \, \text{GeV}/c^2$, and a b-quark mass of $m_b = 4.5 \, \text{GeV}/c^2$, they obtain

$$
\begin{aligned}
\sigma^{\text{NLO}}_{\text{t-chan.}} (10 \, \text{TeV}, \ t) &= 79.8^{+3.2}_{-3.8} \text{ pb (4FS)}, \\
\sigma^{\text{NLO}}_{\text{t-chan.}} (10 \, \text{TeV}, \ \bar{t}) &= 44.2^{+1.6}_{-2.3} \text{ pb (4FS)}.
\end{aligned}
\tag{1.6}
$$

The quoted uncertainty contains contributions from the PDF uncertainty, scale dependence, and uncertainties on the top- and b-quark masses. In addition, the authors compare the result of their calculation to a parallel evaluation of the NLO cross section in the 5FS based on the $2 \to 2$ diagram. They find that the predictions for the total cross section obtained from the two different schemes are consistent within the uncertainties and show differences of the order of about 5%.

s-channel Production

In the s-channel, the top quark is produced via a quark-anti-quark annihilation to a W boson, which splits into a top and a b quark. This mode is strongly suppressed at the LHC, since any anti-quark has to come from the proton quark-sea. As for the t-channel mode, the rate of produced top quarks and anti-top quarks is different reflecting the (uud) valence-quark content of the colliding protons. Some NLO Feynman diagrams for real corrections are shown in figure 1.7.
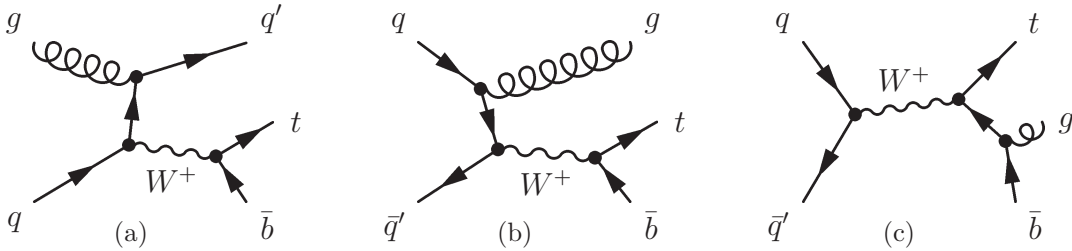

Figure 1.7: Feynman diagrams of s-channel single top-quark production for some real NLO contributions: initial state gluon splitting (a), initial (b) and final (c) state gluon radiation.

A NLO calculation of the cross section considering both real and virtual corrections and including the resummation of soft gluon corrections is provided in [51]. Evaluating the cross section at a top-quark mass of $m_t = 175 \, \text{GeV}/c^2$, with the MRST2004 [52] PDF, and all scales set to m_t one obtains:

$$
\begin{aligned}
\sigma_{\text{s-chan.}}(14 \, \text{TeV}, \ t) &= 7.23^{+0.55}_{-0.47} \text{ pb}, \\
\sigma_{\text{s-chan.}}(14 \, \text{TeV}, \ \bar{t}) &= 4.03^{+0.14}_{-0.16} \text{ pb}.
\end{aligned}
\tag{1.7}
$$

The quoted uncertainty contains uncertainties due to the scale dependence and the PDF parametrization. Since no proper theoretical calculation of the cross section for a center-of-mass energy of 10 TeV is available up to now, CMS applies a scaling to the prediction given in [17]. The scaling is based on the ratio of LO calculations and yields:

$$\sigma_{\text{s}-\text{chan.}}^{\text{scaled}}(10\,\text{TeV},\ t) = 3.1\,\text{pb},$$
$$\sigma_{\text{s}-\text{chan.}}^{\text{scaled}}(10\,\text{TeV},\ \bar{t}) = 1.9\,\text{pb}. \tag{1.8}$$

Comparing figure 1.7 (a) to the t-channel diagram in figure 1.6 (a), an identical initial and final state particle content is found. However, the color of the (b, t) pair produced in the t-channel stems from a gluon splitting, thus represents a color-octet, whereas the (b, t) pair in the s-channel diagram is generated by a Wtb vertex as a color singlet. This difference prohibits an interference of the two contributions.

Associated Production (tW)

The tW mode, where a top quark is produced in association with a real or close to real W boson (see figure 1.5 (c), (d)), is the second most important channel at the LHC. NLO calculations including the resummation of soft gluon corrections using a top-quark mass of $m_t = 175\,\text{GeV}/c^2$, the MRST2004 PDF, and setting all scales to m_t, predict a cross section of [51]:

$$\sigma_{tW}^{\text{NLO}}(14\,\text{TeV}) = 82.2 \pm 5.9\,\text{pb}, \tag{1.9}$$

where the uncertainty contains again uncertainties due to the scale dependence and the PDF parametrization. In order to obtain the cross section for the lower center-of-mass energy, a similar scaling as for the s-channel mode, based on [18] is applied and yields:

$$\sigma_{\text{tW}-\text{chan.}}^{\text{scaled}}(10\,\text{TeV}) = 29\,\text{pb}. \tag{1.10}$$

An implication arises when NLO corrections to the associated production are considered. As one can see from figure 1.8, showing some of the NLO Feynman diagrams, the final states are identical to the top-quark pair production mode at LO, given one top quark already decayed into a b quark and a W boson. This leads to an interference of both processes and it becomes unclear, whether it is meaningful to define tW production as a separate process, or whether one should instead consider given final states comprised of W bosons and b quarks. The interference is in particular relevant for the part of the phase space where the top quarks are produced close to the mass shell. The effect of the interference for the case that the processes are considered separately was studied in [53]. A software is used [54] containing two definitions of the tW mode such that the difference between them provides a measure of the systematic uncertainty due to interference effects. In the first definition, called diagram removal, all diagrams shown in figure 1.8 are removed from the NLO tW cross section. The second approach, called diagram subtraction, implements a subtraction term designed to cancel locally the $t\bar{t}$ contribution. Several scenarios were studied, either tW events should be isolated as signal from $t\bar{t}$ production, or tW and $t\bar{t}$ events were treated as background to a third process. They find that the

results of the two definitions of the process agree very well within scale variation uncertainties, regarding the rate as well as kinematic distributions.
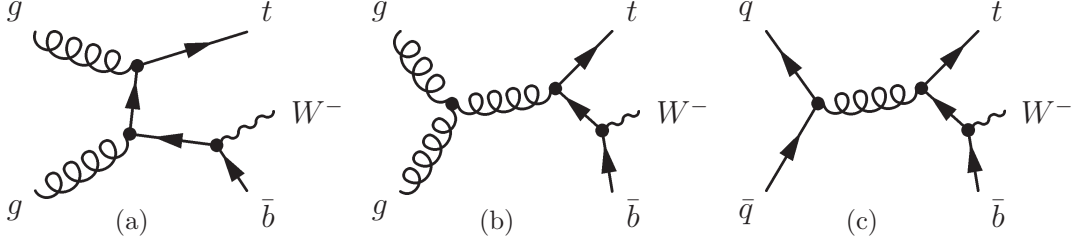

Figure 1.8: A subset of diagrams contributing to tW production at NLO, consisting of top-quark pair production with weak decay of one of the final state top quarks into a W boson and an anti-b quark.

The cross sections for the different electroweak top-quark production modes are summarized in table 1.3 for two center-of-mass energies, specifics are given in the last column. In all the production channels a reduction of the center-of-mass energy from 14 to 10 TeV reduces the cross sections by roughly a factor of two. The s-channel production mode is strongly suppressed compared to the other modes in proton-proton collisions at such center-of-mass energies due to the gluon dominated PDF of the colliding protons, but also due to the fact that the initial anti-quark has to come from the proton quark-sea. The associated production, however, contributes significantly to the total signal, but also to the top-quark pair production channel due to similar final state signatures. The main contribution comes from the t-channel mode with a cross section that is only a factor of about three smaller than the rate for pairwise produced top quarks.

New Physics and Electroweak Top-Quark Production

Extensions to the SM can involve new particles like a heavy W' boson [57] or a charged Higgs boson [58]. Given the existence of such particles, electroweak top-quark production would directly be affected since the exchanged W boson might be replaced by the exotic bosons. Such models are highly suppressed in t-channel production but would enhance the s-channel mode. The t-channel is in particular sensitive to anomalous couplings [59] or flavor changing neutral currents [60] between the top quark and any other quark. Single top-quark production is not only sensitive to many new physics effects, but also contribute a significant background to all signals which signature includes W bosons and b quarks. These backgrounds appear in a number of Higgs search channels [61] and other new physics such as supersymmetry searches [62].

At present, the strongest constraint on the CKM matrix element V_{tb} comes from the 3×3 unitarity of the CKM matrix, which fixes the value to be very close to one. In [50] two minimal extensions of the SM are studied that allow a value for V_{tb} considerably different from one. The authors consider the addition of extra

Cross sections for top-quark production [pb]			
Process		$\sqrt{s} = 10\,\text{TeV}$ $\quad$ $\sqrt{s} = 14\,\text{TeV}$	Comments
tW-channel	$\sigma_{t+\bar{t}}$	29 $\qquad$ 82.2 ± 5.9	$m_t = 175\,\text{GeV}/c^2$, MRST2004, $\sqrt{s} = 10\,\text{TeV}$ from scaling
s-channel	σ_t	3.1 $\qquad$ $7.23^{+0.55}_{-0.47}$	$m_t = 175\,\text{GeV}/c^2$, MRST2004,
	$\sigma_{\bar{t}}$	1.9 $\qquad$ $4.03^{+0.14}_{-0.16}$	$\sqrt{s} = 10\,\text{TeV}$ from scaling
t-channel	σ_t	$79.8^{+3.2}_{-3.8}$ $\qquad$ $147^{+5.7}_{-6.5}$	$m_t = 172\,\text{GeV}/c^2$, CTEQ6.6
	$\sigma_{\bar{t}}$	$44.2^{+1.6}_{-2.3}$ $\qquad$ $86.8^{+3.0}_{-4.2}$	
$t\bar{t}$	$\sigma_{t+\bar{t}}$	414^{+41}_{-42} $\qquad$ 908^{+87}_{-90}	$m_t = 171\,\text{GeV}/c^2$, CTEQ6.5

Table 1.3: Summary of top-quark production cross sections. For each channel, the values are given at two different center-of-mass energies. The uncertainties of the s- and tW-channel cross sections are omitted here as they only represent the statistics of the computation. Since the calculations are obtained from different publications, details on the used top-quark mass and PDF set are given in the last column. Since the theoretical calculations were done over the past years, the current PDF set was used, respectively, with the CTEQ6.6 parametrization being the latest standard set. Details on the different general-purpose sets can be found in [52, 55, 56]. The values for the s- and tW-channel at $\sqrt{s} = 10\,\text{TeV}$ are obtained from a scaling as described in the text.

fermions, either a vector-like up-type quark (t') or a fourth quark generation, i.e. the new quarks t' and b'. The strongest constraint on these models comes from the well measured ratio $R_b = \Gamma(Z \to b\bar{b})/\Gamma(Z \to \text{hadrons})$. Combining it with the direct experimental lower bound on the t'-quark mass by the CDF collaboration, $m_{t'} \geq 311\,\text{GeV}/c^2$ [63], one finds a very strong lower bound on $|V_{tb}|$ of $|V_{tb}| \gtrsim 0.94$ at 95% C.L. This often leads to the statement that such extensions are already ruled out. However, this very strong bound relies on two assumptions. The first one is that the corrections to R_b induced by loop effects are only coming from the t' contribution, and therefore models with an extended particle content may be less constrained. The second assumption, which is at the basis of the lower bound on the t' mass by CDF, is that the branching ratio of $t' \to Wq$ is one. If at least one of these assumptions is not fulfilled, the idea of additional fermions remains possible. Finally, a measurement of the different single top-quark production mechanisms will be important to complete the knowledge of the weak current coupling of top quarks and to reveal possibly new physics.

1.3.3 Spin Polarization in Electroweak Top-Quark Production

One consequence of the top-quark lifetime being shorter than the typical time required for QCD interactions is the conservation of the spin information: top quarks decay in the same spin state as they were produced. The SM V−A coupling of the W boson to the top quark leaves an imprint in the form of strong angular correlations among the decay products of the top quark. The differential distribution of the decay angle θ is given by [26]:

$$\frac{1}{\Gamma}\frac{d\Gamma}{d\cos\theta} = \frac{1}{2}(1 + A_{\uparrow\downarrow}\cos\theta), \tag{1.11}$$

with the spin asymmetry $A_{\uparrow\downarrow} = \frac{N_\uparrow - N_\downarrow}{N_\uparrow + N_\downarrow}$. In the following, θ denotes the angle between the charged lepton from the top-quark decay and the chosen spin axis, as measured in the top-quark rest frame. In order to be able to extract the most significant θ distribution, the spin asymmetry $A_{\uparrow\downarrow}$ has to be maximized, that is, a spin basis has to be constructed in which the top quark is predominantly produced in one of the two possible spin states, spin up or spin down.

Considering the $2 \rightarrow 2$ process (figure 1.5 (b)) in the zero momentum frame (ZMF), where the sum of all particle momenta is zero, the initial spin projection is zero. Since the d-type quark in the final state is massless, it is produced with totally left-handed helicity and, due to angular momentum conservation, the top quark is left-handed as well. As top quarks are massive they are not ultra-relativistic particles, thus boosting to a different frame introduces a right-handed helicity component. Translating this consideration to the $2 \rightarrow 3$ process, the presence of a third particle in the final state frees the top quark from the requirement of being fully left-handed in the ZMF. In addition, the fraction of left-handed top quarks is again reduced when boosting to a different frame, leading to a significantly smaller fraction of left-handed top quarks compared to the $2 \rightarrow 2$ mode.

A problem occurs with the fact that the ZMF is not accessible in real experiments, since all final state partons would need to be measured and reconstructed. Therefore, one should find a way to decompose the top-quark spin in a manner which does not depend on any particular frame. As shown in [26], such a natural spin axis in single top-quark events is the direction of the d-type quark. The top quarks are 100% spin-up polarized in this direction. Since the exact direction of the d-type quark is unknown in the experiment, it is necessary to choose the direction which is most likely to be correct. In the proposed spectator basis, the direction of the spectator jet is used as top-quark spin axis, where the spectator jet is the jet emerging from the outgoing light quark in the final state. The overall fraction of spin-up quarks in such a basis is found to be about 95% in proton-proton collisions at a center-of-mass energy of 14 TeV. Concerning the production of anti-top quarks, the d-type quark is more likely to be in the initial state. As a consequence, the spectator basis represents a wrong direction of the spin axis. However, momentum transfer via the t-channel deflects the incoming quark just slightly. Thus, the spectator jet momentum points in nearly the same direction as the original light-quark momentum. Since the

spectator jet and initial light quark posses nearly parallel momentum vectors, it does not degrade the degree of spin polarization very much. Overall, they find that about 93% of the anti-top quarks are produced with spin down in the spectator basis.

The distribution of the variable $\cos\theta$ as obtained from a Monte Carlo simulation is shown in figure 1.9. Since studies have shown that typical background processes contributing to the single top-quark signal are rather flat in $\cos\theta$, this quantity will later be used in the analysis to discriminate between signal and background in a set of selected event candidates.
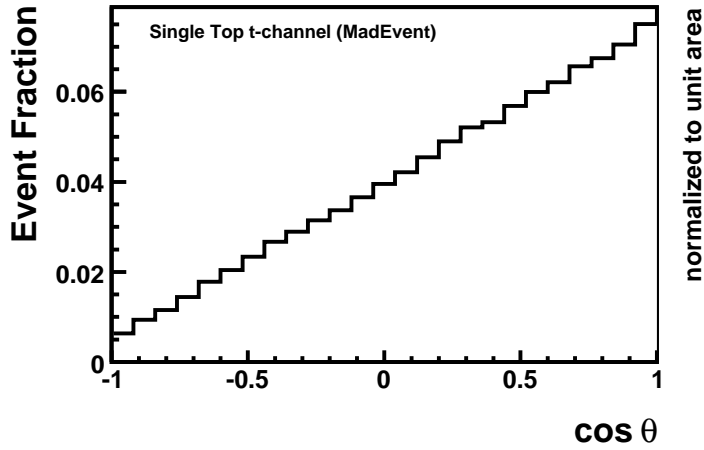
Figure 1.9: The polarization variable $\cos\theta$ for single top-quark events in the t-channel, where θ denotes the angle between the charged lepton from the top-quark decay and the outgoing light quark, as measured in the top-quark rest frame. The events were simulated by the Monte Carlo generator MadEvent (see chapter 3.2).

Chapter 2

Experimental Setup

The Large Hadron Collider (LHC) is a new powerful ring collider providing high energetic hadron beams. It was built at the European Organization for Nuclear Research (CERN) in Geneva, Switzerland, and is designed to provide proton beams with an energy of 7 TeV and lead ions beams with an energy of 2.76 TeV/u (per nucleon), respectively. The LHC is hosted in the former LEP tunnel, built at a mean depth of 100 m below the surface. The first part of this chapter gives an overview of the pre-acceleration chain which is necessary in order to reach such high hadron energies and a description of the LHC. Collisions of the hadrons are observed and
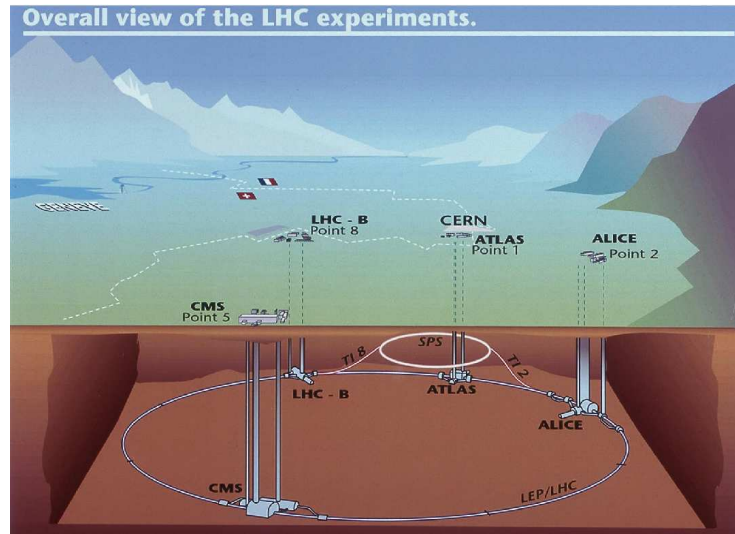

Figure 2.1: Overview [64] of the four main experiments installed at the LHC ring, ALICE, ATLAS, CMS, and LHCb. The LHC is hosted in the former LEP tunnel, built at a mean depth of 100 m below the surface. The LHCf and TOTEM experiments share the interaction point with ATLAS and CMS, respectively.

recorded by several detectors along the ring as shown in figure 2.1. Six different experiments are installed at the LHC. A large ion collider experiment (ALICE [65]) is a detector specialized in analyzing lead-ion collisions. It will study the properties of quark-gluon plasma, a state of matter where quarks and gluons, under conditions of

very high temperatures and densities, are no longer confined inside hadrons. Such a state of matter probably existed just after the Big Bang, before particles like protons and neutrons were formed. The LHC beauty (LHCb [66]) experiment is specialized to the study of the slight asymmetry between matter and antimatter which is present in processes involving b mesons. Instead of surrounding the entire collision point with an enclosed detector, the LHCb experiment uses a series of subdetectors covering the forward region only to detect boosted b-meson events. The LHC forward (LHCf [67]) is a small experiment that will measure neutral pions produced very close to the direction of the beams in proton-proton collisions. The motivation is to test models used to estimate the primary energy of ultra high-energy cosmic rays. The Total Elastic and diffractive cross section Measurement (TOTEM [68]) experiment will measure the total proton-proton cross-section and study elastic scattering and diffractive processes. A Toroidal LHC Apparatus (ATLAS [69]) is a general-purpose detector designed to cover the widest possible range of physics at the LHC, from SM processes and the search for the Higgs boson to new physics phenomena. The Compact Muon Solenoid (CMS) is a general-purpose detector with the same physics goals as ATLAS, but different technical solutions and design. ALICE, ATLAS, CMS, and LHCb are installed in four huge underground caverns built around the four collision points of the LHC beams. TOTEM shares the interaction point with CMS and LHCf is located near ATLAS.

Since the studies presented in this thesis are performed within the framework of the CMS experiment, the components of this detector are discussed in more detail in the second part of this chapter. Subsequently, a brief description is given on how the huge amount of data recorded by the detector is processed and distributed from CERN to physicists all over the world.

2.1   High Energetic Hadrons in the LHC

In order to accelerate the protons or lead ions to their nominal energy of 7 TeV and 2.76 TeV/u, respectively, a complex chain of pre-accelerators is used, each optimized for the particular energy range it covers. A schematic overview of the pre-acceleration chain of the LHC is shown in figure 2.2.

The protons are obtained from the ionization of hydrogen gas by a pulsed duoplasmatron [71], where electron bombarding of the hydrogen plasma is used to produce a current of protons. In a duoplasmatron, the discharge of the hydrogen plasma is constricted near the anode in order to increase the energy of the primary ionizing electrons and to enhance the plasma density. Further compression is achieved by adding a strong magnetic field around the constriction. The extracted protons are then accelerated by a 90 kV supply and sent to a radio frequency quadrupole that both focusses and speeds up the particle beam to 750 keV. A chain of different accelerators follows, each providing a particular energy rise of the beam. First, the beam is accelerated to an energy of 50 MeV in a LINear ACcelerator (LINAC 2). It is then transferred to the Proton Synchrotron Booster (PSB) [72], where the particles are further accelerated to 1.4 GeV. From there, the protons are injected into the Proton-Synchrotron (PS) [73]. In the PS, the pulsed beam obtained from the
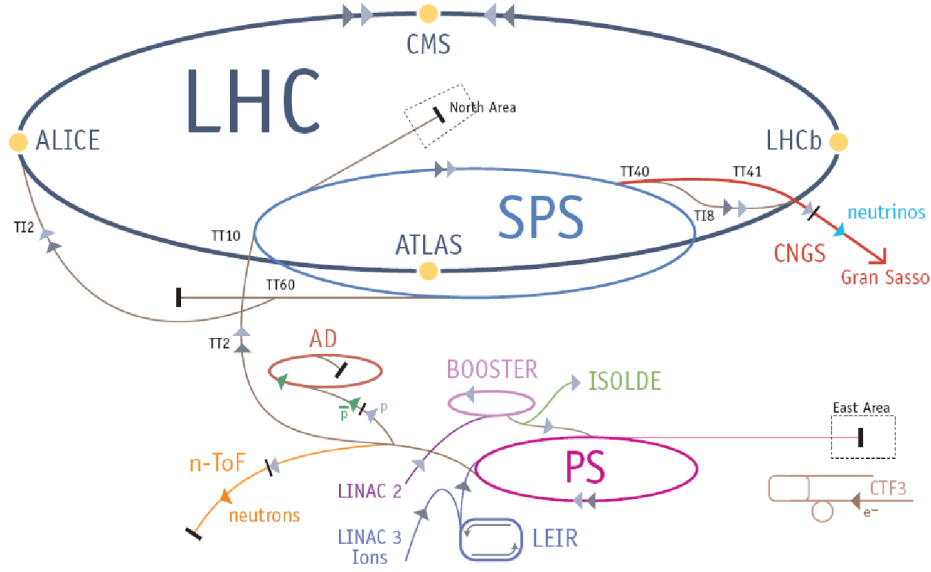
Figure 2.2: Sketch of the accelerator chain [70] used to fill the LHC with pre-accelerated protons or lead ions. On their way to the LHC, protons traverse the chain LINAC 2, Booster (PSB), PS, SPS, whereas lead ions coming from the LINAC 3 are sent through LEIR, PS, and SPS. As one can see in the sketch, many parallel experiments are supplied with beam taken out of different acceleration levels, which is not discussed here.

proton extraction process is transformed into bunches with 25 ns bunch spacing and the beam energy is increased to 25 GeV. Subsequently, the beam enters the last interstation on the way to the LHC, the Super Proton Synchrotron (SPS) [74] which increases the beam energy up to 450 GeV. Finally, the two counter-rotating beam pipes of the LHC are filled by twelve SPS cycles each. The whole procedure of filling the LHC with both beams will take about 10 minutes.

In the case of heavy ion operations, the LHC is filled with two beams of lead ions which pass through a similar acceleration chain as the protons. The lead ions are produced with an electron cyclotron resonance [71]. A very high plasma density can be attained by the use of microwave frequencies, thus adequate for the production of multi-charged ions. Many different charge states are obtained with a maximum around the charge state Pb^{29+}. These are selected and accelerated to 4.2 MeV/u before passing through a carbon foil which strips further electrons off the lead ions yielding mainly Pb^{54+}. The beam is then accumulated and accelerated to 72 MeV/u in the Low Energy Ion Ring (LEIR) and transferred to the PS, where it is further accelerated to 5.9 GeV/nucleon. After passing the beam through a second foil where it is fully stripped to Pb^{84+}, it is sent to the SPS for a last pre-acceleration to 177 GeV/u. This beam is then transferred to the LHC that accomplishes the final acceleration step before the beams are brought to collision.

The LHC [75] is a synchrotron accelerator with a circumference of about 27 km. Eight arcs and eight insertions are installed alternately alongside the ring, thus the LHC is organized in octants as depicted in figure 2.3.

The arcs contain a total of 1,232 dipole magnets bending the charged hadrons to their orbit. Since these dipole magnets do not fill the whole circumference of the ring, the bending radius of the circulating hadrons is reduced to 2,804 m, which is much less than the radius of 4,297 m when approximating the LHC by a ring of 27 km circumference. For a proton beam energy of 7 TeV, this requires a magnetic field strength of 8.33 T in order to guide the particles through the ring. Such a high field strength can only be provided by superconducting dipole magnets. Their operating temperature of 1.9 K is accomplished by helium cooling, where the helium itself is cooled down in a complex three-step process. In addition to the dipole magnets, a large variety of about 8,400 additional multipole magnets is installed for trajectory corrections and an optimal beam focussing.

The insertions consist of a long straight section plus two transition regions. The exact layout of the straight section depends on the specific use of the insertion: in sections 1, 2, 5, and 8 the beams are collided in the center of an experiment. Two sections (2, 8) also contain the beam injection lines connecting the SPS and the LHC. Beam cleaning, which makes sure that stray beam particles are absorbed by a set of collimators, is provided in sections 3 and 7, while the beam dumping system for both beams is located at section 6, where the beams can be redirected onto a cylinder of graphite composite absorbing the beam energy at a controlled place. At section 4, a total of eight radio frequency cavities per beam are used to accelerate the circulating hadron beams while keeping them tightly bunched. Each superconducting cavity, operating at 4.5 K, delivers an accelerating field of 5 MV/m at 400 MHz.

The beam degrades with time due to the collisions within the experiments and interactions with residual gas in the beam pipe. In order to avoid interactions of the beam particles with gas molecules, the beam pipe is evacuated to a pressure of 10^{-13} atm. Thus, a typical beam life-time of about 12 hours can be achieved.

The luminosity $\mathcal{L}$ is one of the most important parameters of an accelerator. It is a measure for the flux density of beam particles created by the accelerator at the collision point. The number of collisions in a given time interval is obtained by $N = \sigma \int \mathcal{L} \cdot \mathrm{d}t$, where σ is the cross-section of the considered process. The luminosity is determined by several beam parameters such as the number of bunches, the revolution frequency, and the number of particles per bunch. The better the beam is focussed, the higher is the luminosity. The design luminosity of the LHC is $\mathcal{L} = 10^{34} \, \mathrm{cm}^{-2} \, \mathrm{s}^{-1}$ for proton and $\mathcal{L} = 10^{27} \, \mathrm{cm}^{-2} \, \mathrm{s}^{-1}$ for lead ion beams. In order to achieve this, the beams have to be filled with the maximal number of bunches each containing the nominal number of hadrons. Table 2.1 summarizes the pre-acceleration steps for both protons and lead ions and gives some of the design parameters of the LHC. The number of bunches and the filling structure of the LHC beams is determined by the transfer scheme of SPS cycles to the LHC. At each transfer enough space has to be reserved to accommodate the rise time of the injection kicker magnets as well as for the beam dump kicker magnet. This leads to a
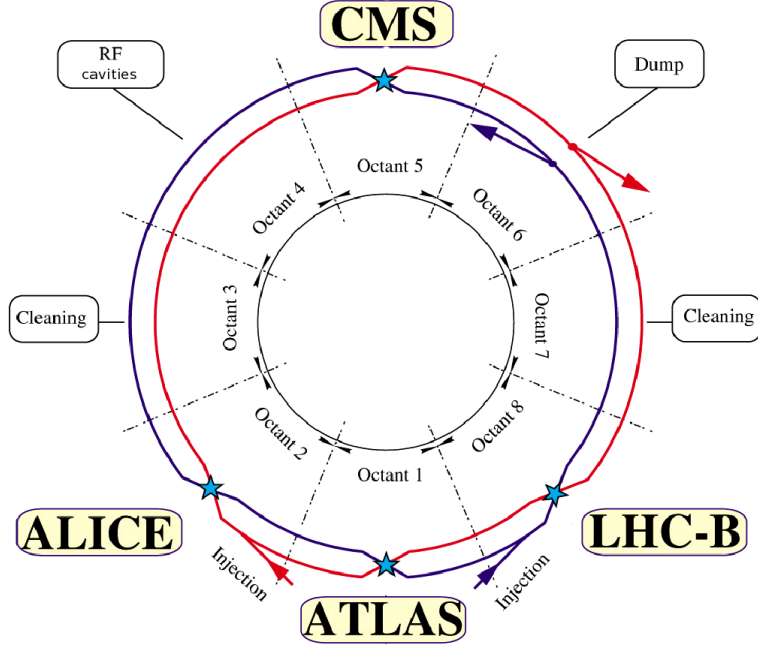
Figure 2.3: Sketch of the LHC [75]: the ring is organized in octants, distinguished by the different tasks which are performed. An octant starts from the middle of an arc and ends in the middle of the following arc and thus spans a full insertion. A section is defined as the part of the machine between two insertion midpoints. The straight sections which are located at the center of an octant are not explicitly shown here.

particular, complex bunch pattern for a total LHC filling.

The official start-up of the LHC took place in September 2008, when first single proton-bunches were circulated in both beam directions. Shortly after that, a serious incident caused a 14 month shutdown necessary for repairs and re-fitting of particular systems. During a magnet power test in sector 34, a faulty electrical connection between a quadrupole and the neighboring dipole caused a resistive zone. An electrical arc developed, which punctured the nearby enclosure of the liquid helium. Large amounts of helium gas were released into the insulating vacuum of the cryostat. Self-actuating relief valves opened, releasing a large amount of helium in the tunnel. However, they could not handle such a huge pressure. Hence, large pressure waves traveled along the accelerator in both directions, causing significant collateral damage on the machine. Consequently, a total of 14 quadrupole and 39 dipole magnets had to be replaced, several electrical interconnections had to be repaired, and the beam tube vacuum had to be cleaned over a distance of 4 km. In addition to the repair work, the machine was guarded against such exposures by the installation of new helium pressure release ports, the extension of the magnet protection system with 6,500 new detectors, and a new longitudinal restraining system was fitted to the quadrupole magnets. Resumption of the LHC beam activity was in November 2009 with the commissioning of the circulating beams. First proton collisions at a center-of-mass energy of 900 GeV were provided in November 2009,

Protons		Lead Ions		
Accelerator	Energy	Accelerator	Energy	^{208}Pb charge state
LINAC2	50 MeV	LINAC3	4.2 MeV/u	Pb^{29+}
PS Booster	1.4 GeV	LEIR	72 MeV/u	Pb^{54+}
PS	25 GeV	PS	5.9 GeV/u	Pb^{54+}
SPS	450 GeV	SPS	177 GeV/u	Pb^{84+}
LHC	7 TeV	LHC	2.76 TeV/u	Pb^{84+}
2,808 bunches		592 bunches		
1.1×10^{11} protons/bunch		7×10^7 lead ions/bunch		
$\mathcal{L} = 10^{34}\,\mathrm{cm^{-2}\,s^{-1}}$		$\mathcal{L} = 10^{27}\,\mathrm{cm^{-2}\,s^{-1}}$		

Table 2.1: Overview of the accelerator complex for protons and lead ions. The different accelerators, their design beam energy, and the ionization degree of the lead ions in each phase are summarized in the upper part of the table. The lower part gives some design parameters of the LHC machine.

followed by a short period at $\sqrt{s} = 2.36$ TeV in December 2009. In the early phase of LHC running, the beam parameters are chosen carefully in order to gain experience with the machine step by step. Once a stable operation of the machine is achieved, the parameters will subsequently be increased. The current scenario for the first physics run, beginning in April 2010, foresees an energy of 3.5 TeV per beam. The run will last until an integrated luminosity of $1\,\mathrm{fb^{-1}}$ has been collected by the main experiments ATLAS and CMS, interrupted by a heavy-ion phase in the end of 2010. Following the 7 TeV proton run, but not later than by the end of 2011, a long-term shutdown is planned to prepare the machine for operations at $\sqrt{s} = 14$ TeV.

2.2   The CMS Experiment

The CMS experiment [76] is a multi-purpose detector designed to explore physics at the TeV energy scale in proton-proton collisions. In the design phase of CMS in the early 1990s the detection of the SM Higgs boson was used as a benchmark to test the performance of the proposed layout. The decay modes of the Higgs boson cover a wide range, depending on the mass of the boson. The deduced detector requirements for CMS to meet the goals of the LHC physics program can be summarized by the following preferences: good muon identification and momentum resolution over a wide range of momenta, a good charged particle momentum resolution and reconstruction efficiency in the inner tracking system, good electromagnetic energy resolution with a wide geometrical coverage, and hadron calorimetry with fine lateral segmentation and a geometrical coverage extended to the forward region.

    The right-handed coordinate system adopted by the CMS experiment has its origin centered at the nominal collision point inside the experiment, the y-axis pointing vertically upward, and the x-axis pointing radially inward toward the center of the LHC. Thus, the z-axis points along the beam direction towards the Jura. The az-
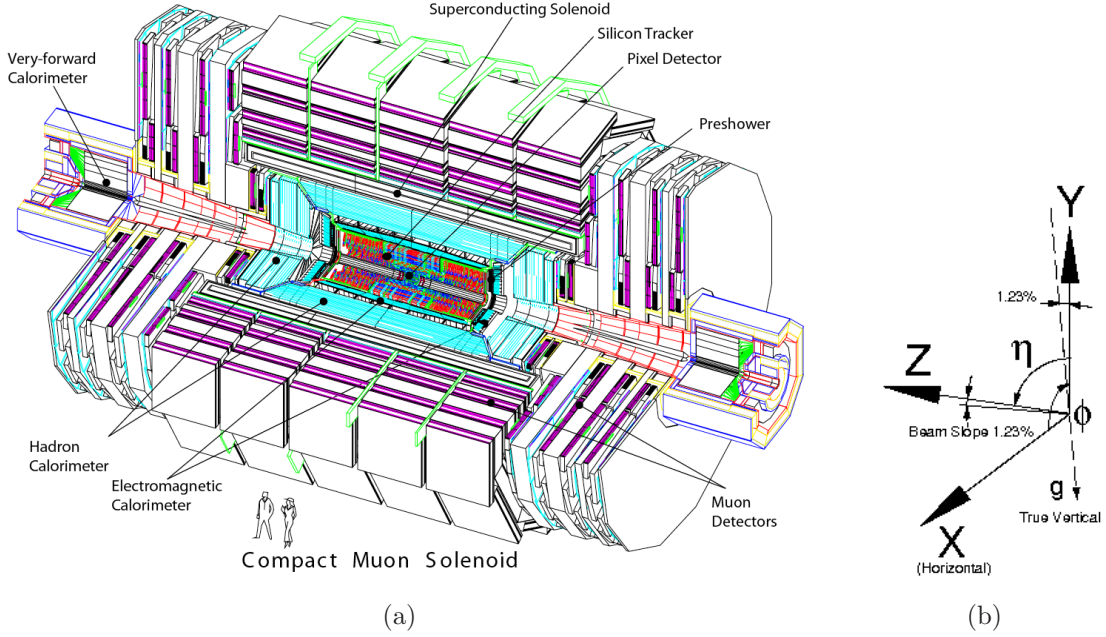
Figure 2.4: (a) Schematic overview of the CMS detector [76] where one quarter of the detector was removed to open the view onto the inner components. The interaction point in the center of the detector is enclosed by the inner tracking system, followed by the electromagnetic and the main hadronic calorimeter, which are all hosted inside the superconducting solenoid. The solenoidal magnet is surrounded by an outer hadron calorimeter and the voluminous muon systems. (b) The right-handed coordinate system of CMS: the x-axis points radially inwards to the center of the LHC ring, the y-axis points upwards, and the z-axis points towards the Jura. Since the plane of the LHC ring has a slight slope of 1.23% with respect to the horizontal by construction, the coordinate system of CMS is tilted accordingly.

imuthal angle ϕ is measured from the x-axis in the $x-y$ plane. With the polar angle θ measured from the z-axis, the pseudorapidity η is defined as $\eta = -\ln\tan(\frac{\theta}{2})$. The momentum and energy measured transverse to the beam direction, denoted by p_{T} and E_{T}, respectively, are computed from the x and y components. The imbalance of energy measured in the transverse plane is denoted by $E_{\mathrm{T}}^{\mathrm{miss}}$ and known as missing transverse energy.

Figure 2.4 shows an overview of the CMS detector structure. The main distinguishing features are the high-field solenoid, a full silicon-based inner tracking system, and the full active scintillating crystal-based electromagnetic calorimeter. The overall dimensions of the CMS detector are a length of 21.6 m, a diameter of 14.6 m, and a total weight of 12,500 tons. The detector is divided into five wheels in the z direction, which were lowered to the underground cavern after being fully assembled on the surface. Due to the requirement of an unambiguous determination of the sign of muons with a momentum up to 1 TeV/c, a powerful superconducting solenoid magnet was chosen. It has a length of 12.9 m, an inner diameter of 5.9 m and operates at a field strength of 3.8 T. The inner tracking system and the main calorimetry are hosted inside the solenoid, whereas an extension of the hadron calorimeter and the complex muon system are installed outside.

A one-month-long data-taking exercise was conducted in the autumn of 2008, called CRAFT, in preparation for the intended LHC startup. During this exercise, CMS recorded about 270 million cosmic-muon events with the solenoid at its nominal axial field strength of 3.8 T. These data provides an excellent starting point for commissioning of most of the subdetectors. The exercise was very important for calibration studies and improved the alignment of the detector components significantly. A summary of the results can be found in [77].

The following subsections describe the different detector components, starting at the nominal interaction point in the center of the detector and following the geometric order radially outwards. A detailed review of the CMS detector can be found in [76, 78].

2.2.1 Inner Tracking System

The CMS tracker [79] is a unique instrument, in both size and complexity, for the measurement of the trajectories of charged particles with excellent momentum, angle, and position resolution. It consists of two systems based on silicon sensor technology: one employing silicon pixels and another using silicon microstrips. The pixel detector surrounds the beam pipe and contains 66 million detector channels. It is, in turn, surrounded by the silicon strip tracker, which comprises four main sub-systems. The central region, called barrel, is divided into the tracker outer barrel (TOB) and the tracker inner barrel (TIB) complemented on each side by the tracker inner disks (TID). The tracker endcaps (TEC) extend the barrel system in the forward region. Overall, the tracker cylinder is 5.5 m long and 2.4 m in diameter, with a total active area of 198 m². It is housed inside a temperature-controlled outer support-tube and will operate at a temperature around $-20°$ C. Figure 2.5 shows schematically the structure of the system.
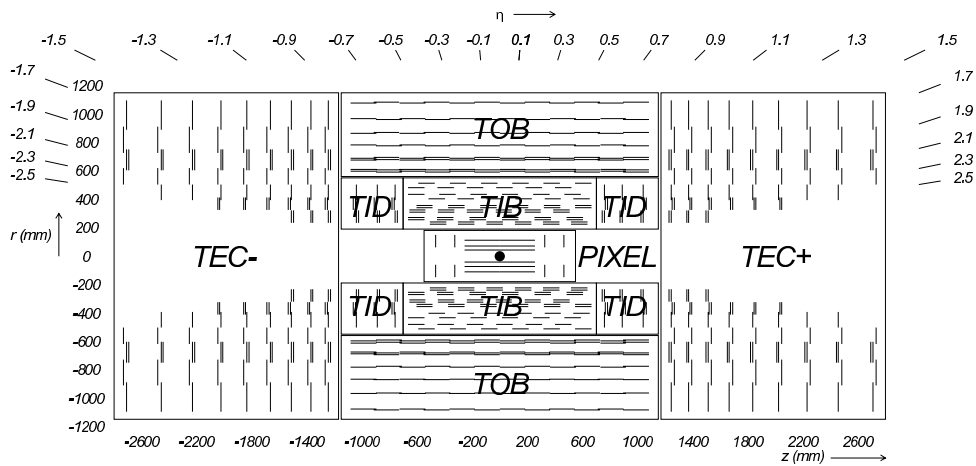

Figure 2.5:   Schematic overview of the CMS tracking system [78]. The silicon pixel detector in the center is surrounded by the silicon strip detector which consists of endcaps and different barrel components.

Silicon Pixel Detector

The pixel detector consists of three barrel layers with two endcap disks on each side on them, as shown in figure 2.6. The three layers are located at mean radii of 4.4 cm, 7.3 cm, and 10.2 cm, and have a length of 53 cm. The two endcap disks, extending from 6 to 15 cm in radius are placed on each side at $|z| = 34.5$ cm and 46.5 cm. A design with a pixel shape of 100×150 µm has been adopted in both the $(r - \phi)$ coordinate for the endcap and the z coordinate for the barrel region. The barrel comprises 768 pixel modules arranged into half-ladders of four identical modules each. The endcap disks are assembled in a turbine-like geometry with blades rotated by 20°. Seven different modules are mounted on each of the 24 blades, leading to a total of 672 pixel modules.

Both the blades and the modules on the blades overlap in order to provide a hermetic coverage. The spacial hit resolution measured in CRAFT data was found to be about 20 µm for the $(r - \phi)$ measurement and about 30 µm for the z measurement [80], which is in line with the expectations [76].
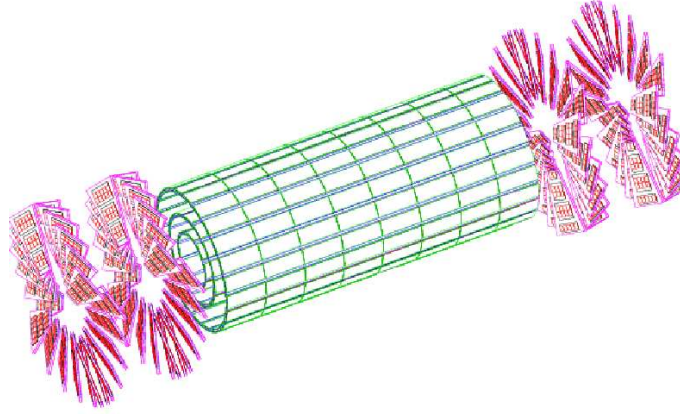

Figure 2.6: Sketch of the silicon pixel detector [76]. It is built of three barrel layers and two endcap disks which are assembled in a turbine-like geometry.

Silicon Strip Detector

The silicon strip detector consists of 15,148 single-sided detector modules and comprises 9.3 million detector channels, divided into several barrel and endcap subsystems as shown in figure 2.5.

The TIB is made of four layers and covers up to $|z| \leq 65$ cm, using silicon sensors with a thickness of 320 µm, and a strip pitch which varies from 80 µm to 120 µm. In order to provide measurements in both $(r - \phi)$ and $(r - z)$ coordinates the first two layers are equipped with stereo modules. These double-sided modules are constructed from two single-sided modules mounted back-to-back with a stereo angle of 100 mrad between the strips.

The TOB comprises six layers with a half-length of $|z| \leq 110$ cm. As the radiation level is smaller in this region, thicker silicon sensors (500 µm) can be used to maintain

a good signal-to-noise ratio for longer strip length and wider pitch. The strip pitch varies from 120 µm to 180 µm. The first two layers of the TOB also provide a stereo measurement in both $(r - \phi)$ and $(r - z)$ coordinates with a stereo angle of again 100 mrad.

The endcaps are divided into the TEC and the TID. Each TEC consists of nine disks that extend into the region $120 \, \text{cm} \le |z| \le 280 \, \text{cm}$, and each TID is made of 3 small disks that fill the gap between the TIB and the TEC. The TEC and TID modules are arranged in rings centered around the beam line and have strips that point towards the beam line, therefore having a variable pitch. Stereo modules are installed on the first two rings of the TID as well as on the innermost two rings and the fifth ring of the TEC. The thickness of the sensors is 320 µm for the TID and the three innermost rings of the TEC and 500 µm for the rest of the TEC.

Simulation studies based on an ideal tracker geometry imply a transverse momentum resolution of about 1.5% for muons with a transverse momentum of the order of 100 GeV/c. The critical task for achieving the design track-parameter resolution is the precise determination of the position of all silicon modules. A hit-position resolution of $(10 - 30)$ µm requires an alignment precision better than 10 µm. Different methods are employed to achieve this alignment precision of the tracker modules. Optical surveys, like photogrammetry, provide initial alignment parameters and are complemented by an independent laser alignment system. Using data from the CRAFT exercise, combined with the information obtained from the optical surveys, the position of the modules was determined with a precision of $(3 - 4)$ µm RMS in the barrel and $(3 - 14)$ µm RMS in the endcaps in the most sensitive coordinate [80]. The results were validated with data from the laser alignment system and are found to agree well with the simulations.

2.2.2   Electromagnetic Calorimeter – ECAL

The ECAL [81], which surrounds the inner tracking system, is a hermetic, homogeneous crystal calorimeter composed of 75,848 lead tungstate ($PbWO_4$) crystals. The choice of lead tungstate is motivated by its properties: it is radiation hard up to an irradiation of the order of Mrd, has a short radiation length of $X_0 = 0.89 \, \text{cm}$ and a small Molière radius of $\rho_M = 2.2 \, \text{cm}$, which allows to build a compact calorimeter. The response of the crystals is very fast, 80% of the light is emitted within 25 ns corresponding to the nominal LHC bunch-crossing rate. The relatively low light yield of about 30 photons/MeV, however, has to be compensated by the use of photodetectors with an intrinsic gain. Since the ECAL is hosted within the detector solenoid, the photodetectors have to be able to operate in a strong magnetic field. Thus, silicon avalanche photodiodes (APDs) are used in the barrel region and vacuum phototriodes in the endcaps. The sensitivity to temperature changes of both the crystals and the APD response require a very strict temperature stability.

Figure 2.7 shows a schematic overview of the ECAL structure. It consists of a barrel region (EB) extending to a pseudorapidity of $|\eta| = 1.48$, and two endcaps (EE) with a coverage up to $|\eta| = 3.0$. In the central part 61,200 lead tungstate crystals are mounted, closed by 7,324 crystals in each of the two endcaps.
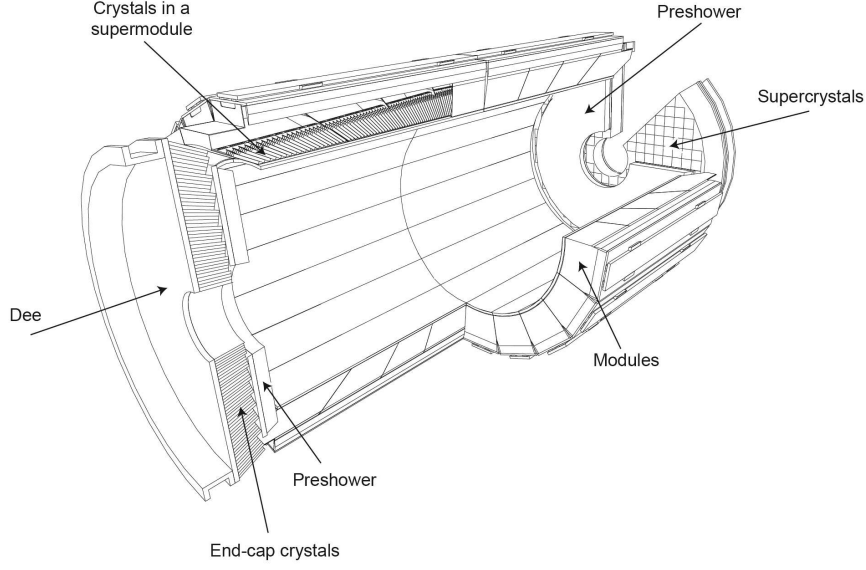
Figure 2.7: A sketch of the electromagnetic calorimeter [82]. The barrel region, where single crystals are combined to supermodules, is extended to $\eta = 3.0$ by the endcaps which consist of two so-called Dees on each side.

The EB has an inner radius of 129 cm and is built of 36 identical supermodules each covering half the barrel length. The crystals have a front-face cross-section of $(22 \times 22)\,\mathrm{mm}^2$ and a length of 230 mm, corresponding to $25.8\,\mathrm{X}_0$.

The EEs are located at a distance of 314 cm from the nominal collision point, covering a pseudorapidity interval of $1.48 \leq |\eta| \leq 3.0$. Each endcap is assembled on semi-circular aluminum plates, called Dees, from which structural units of 5×5 crystals, known as supercrystals, are cantilevered. The endcap crystals have a length of 220 mm, corresponding to $24.7\,\mathrm{X}_0$, and a front-face cross-section of $(28.6 \times 28.6)\,\mathrm{mm}^2$.

A pre-shower device is placed in front of the endcap crystals for the identification of neutral pions. In addition, it supports the identification of electrons against minimal ionizing particles and improves the position determination of electrons and photons. The active elements of the pre-shower detector are two planes of silicon-strip detectors with a pitch of 1.9 mm, lying behind disks of lead absorber at depth of $2\,\mathrm{X}_0$ and $3\,\mathrm{X}_0$.

The energy resolution of the calorimeter $(\frac{\sigma_E}{E})^2$ can be parametrized by

$$\left(\frac{\sigma_E}{E}\right)^2 = \left(\frac{S}{\sqrt{E}}\right)^2 + \left(\frac{N}{E}\right)^2 + C^2. \tag{2.1}$$

Here, S represent the stochastic term, which depends on event-to-event fluctuation in lateral shower containment, photo-statistics and photodetector gain; N represents the noise term, which depends on the level of electronic noise and additional particles causing signals that overlap in time, called event pile-up; C represents the constant term, which depends on non-uniformity of the longitudinal light collection,

leakage of energy from the rear face of the crystal and the accuracy of the detector intercalibration constants. The target value for the constant term which dominates the resolution at high energies is 0.5% for both the barrel and the endcaps. Measurements performed with test beam electrons with energies between 20 GeV and 250 GeV have shown that the electromagnetic energy resolution and noise performance of the ECAL barrel meet the CMS design goals. The mean values of the three terms in equation 2.1 are 2.8% for S, 41.5 MeV for N, and 0.3% for the constant term [76].

The constant term is especially sensitive to the temperature stability of the crystals. Thus, the temperature of the ECAL barrel is required to be stable within 0.05 °C and 0.1 °C for the endcaps. During the CRAFT exercise, where the ECAL was operated with more than 98.5% of channels active, the stability of electronic noise, high voltage, and temperature were found to satisfy the ECAL performance targets and therefore do not significantly contribute to the constant term of the energy resolution [82]. Given a stable temperature, the measurement of changes in the lead-tungstate crystal transparency under irradiation is critical in order to maintain the stability of the constant term. Therefore, a complex laser monitoring system is installed which monitors the transparency changes of each crystal at the 0.2% level, with one measurement every half an hour.

The intercalibration, which corrects for variations in the channel-to-channel response, has been prepared in several steps. Laboratory measurements of each crystal during the assembly phase provided first data, followed by the pre-calibration of some supermodules with electron test beams. The ultimate precision of the intercalibration will be obtained from collision data. Measurements performed in CRAFT data are at a precision level of $1 - 2\%$ for the barrel and better than 10% for the endcaps [82], already confirming the laboratory measurements. Thus, they are suitable as initial values for the crystal calibration using collision data. The calibration of the absolute energy scale can be performed with collision data using $Z \rightarrow e^+e^-$ events [83].

2.2.3   Hadron Calorimeter – HCAL

The barrel and endcap HCAL subdetectors, HB and HE, respectively, completely surround the ECAL and are fully immersed within the high magnetic field of the solenoid. They are joined hermetically with the barrel extending the coverage out to $|\eta| = 1.4$ and the endcap covering the overlapping range $1.3 \leq |\eta| \leq 3.0$. The forward calorimeters (HF) are located at $|z| = 11.2$ m from the interaction point and extend the pseudorapidity coverage overlapping with the endcap from $|\eta| = 2.9$ up to $|\eta| = 5$. The central shower containment in the region $|\eta| \leq 1.26$ is improved with an array of scintillators located outside the magnet in the outer barrel hadronic calorimeter (HO). The configuration of the four main HCAL components is shown in figure 2.8. The design was strongly influenced by the choice of magnetic parameters, since most of the calorimetry is located inside the magnet coil. Thus, brass was chosen as absorber material as it has a reasonably short interaction length and is non-magnetic. As active medium, plastic scintillator tiles are used, which are

read out by embedded wavelength-shifting fibers. The assembly of the overlapping absorber structure enables the HCAL to be built with essentially no uninstrumented cracks or dead areas in ϕ. More details on the design and construction of the HCAL can be found in [84].
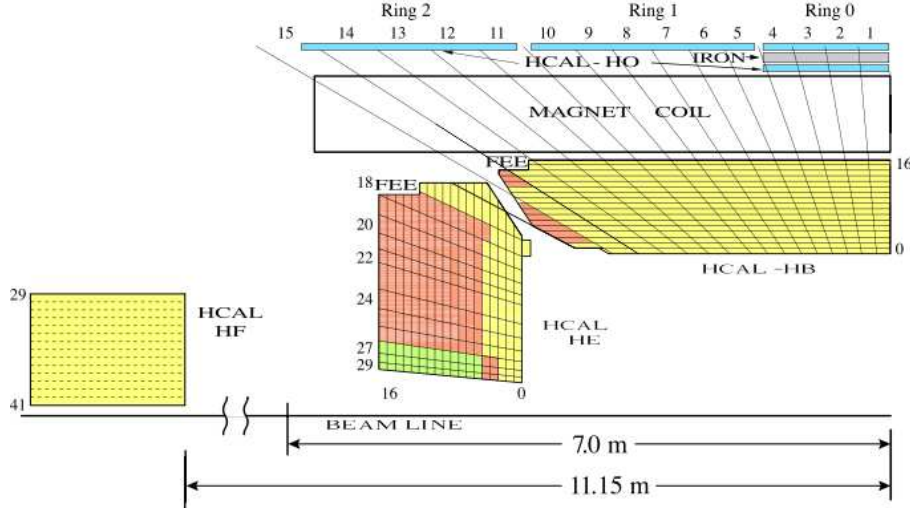

Figure 2.8: Transverse section through a quarter of the HCAL, showing the geometrical configuration [85]. The barrel and the endcap detectors are placed inside the solenoid, followed by the outer calorimeter. The HF modules are located at almost $|z| = 11.2$ m from the interaction point. The color code denotes the longitudinal segmentation of the read-out system, the location of the front-end electronic devices is indicated by the label FEE.

The HB is an assembly of two half barrels, each composed of 18 identical 20° wedges in ϕ, going from an inner radius of 1.78 m to an outer radius of 2.88 m. The wedge is composed of flat brass-alloy absorber-plates parallel to the beam axis. The innermost and outermost absorber layers are made of stainless steel in order to ensure the necessary structural strength. There are 17 active plastic scintillator tiles with a thickness of 3.7 mm interspersed between the absorber plates. The first active layer is placed directly behind the ECAL and has roughly double the thickness (9 mm) to actively sample low energy showering particles from support material between the ECAL and the HCAL. The corresponding projective tiles from each of the 17 active layers are connected in the readout, thus forming 32 barrel HCAL towers in η. This leads to a total of 2,304 towers with a segmentation of $\Delta\eta \times \Delta\phi = 0.087 \times 0.087$.

The HO is primarily constructed to increase the effective thickness of the hadron calorimetry to over 10 interaction length, thus reducing the tails in the energy resolution function. Due to the limited depth of the barrel detector, about 5% of all particles above 100 GeV deposit some energy in the HO. The HO is located inside the barrel muon system and is hence geometrically constrained by that system. Scintillator detectors with a thickness of 10 mm line the outside of the outer vacuum tank of the coil and cover the region $|\eta| \leq 1.26$, which is divided into five sections. These rings are called -2, -1, 0, 1, and 2, each covering 2.5 m in z. The ring 0 has two scintillator layers on either side of an iron absorber with a thickness of about

18 cm, at radial distances of 3.85 m and 4.10 m, respectively. The other rings have single layers at a radial distance of 4.10 m. The scintillator segmentation follows the HB tower geometry.

The HE calorimeter is tapered to interlock with the barrel calorimeter. It is composed entirely of brass absorber plates in an 18-fold ϕ-geometry matching that of the barrel calorimeter. The 14 towers in η cover the range $1.3 \leq |\eta| \leq 3.0$, leading to a total of 2,304 HE towers. For the five outermost towers with respect to $|\eta|$ the ϕ segmentation is 5° and the η segmentation is 0.087. For the eight innermost towers the ϕ segmentation is 10°, whilst the η segmentation varies from 0.09 to 0.35 at the highest $|\eta|$. The thickness of the absorber plates is 78 mm while the thickness of the 19 active plastic scintillator layers is 3.7 mm.

The HF calorimeters extend the coverage of the forward region to $3.0 \leq |\eta| \leq 5.0$ and provide the possibility to tag or veto on forward jets, which is important for certain rare event signatures to be identified. The modules are located at $|z| = 11.2$ m from the interaction point. They are made of steel absorbers and embedded radiation-hard quartz fibers. The signal originates from Cerenkov light emitted in the quartz fibers, which is then channelled by the fibers to the photomultipliers. Each HF module is constructed of 18 wedges in a non-projective geometry with quartz fibers running parallel to the beam axis. Long (1.65 m) and short (1.43 m) quartz fibers are placed alternately with a separation of 5 mm. There are 13 towers in η, all with a size of $\Delta\eta \sim 0.175$, except for the towers with the lowest and highest absolute value of η. These have a size of $\Delta\eta \sim 0.1$ and $\Delta\eta \sim 0.3$, respectively. The ϕ segmentation of all towers is 10°, except for the one with the highest $|\eta|$ value which has $\Delta\phi \sim 20°$. This leads to 900 towers and 1,800 channels in the two HF modules.

The performance of the HB was determined in combination with the EB in a test beam setup. The resolution obtained from these measurements for single particle beams like pions, protons, electrons, and muons is

$$\left(\frac{\sigma_E}{E}\right)^2 = \left(\frac{a}{\sqrt{E}}\right)^2 + b^2, \tag{2.2}$$

where $a = 84.7 \pm 1.6\%/\sqrt{E(\text{GeV})}$ and $b = 7.4 \pm 0.8\%$ [85]. The resolution of the endcaps is similar to the barrel. The corresponding values for the HF are $a = 198\%$ and $b = 118\%$. The initial calibration information was obtained from quality control tests performed with collimated radiation sources and from laser data. The energy scale constants are primarily obtained from combining test beam data with radiation source data taken for a limited number of modules. They were updated with data taken during CRAFT, and will improve with the analysis of early LHC data.

2.2.4 Muon System

The main tasks of the muon system are muon identification, momentum measurements, and triggering of muons (see chapter 2.2.5). The system is hosted in the return yoke of CMS in a magnetic field of about 2 T, with the yoke serving also as

hadron absorber for a good muon identification. Figure 2.9 shows the layout of the muon system. The central barrel part covers a pseudorapidity range of $|\eta| \leq 1.04$ and the forward endcap disks enclosing both ends of the barrel cylinder extend the coverage to $1.04 \leq |\eta| \leq 2.4$. Three types of gaseous detectors are used to identify muons. The choice of detector technologies was driven by the very large surface of $25,000\,\mathrm{m}^2$ to be covered and by the different radiation environments. In the barrel region, the neutron induced background is small and the muon rate as well as the residual magnetic field is low. Thus, drift tube (DT) chambers were chosen. In the endcap region, where the muon and the neutron induced background rate is high and the magnetic field is considerably stronger, the muon system is equipped with cathode strip chambers (CSCs). They have a fast response time, a fine segmentation, and a high radiation resistance. The third component is made of resistive plate chambers (RPCs) which are used in both the barrel and the endcap region. They provide a very fast response with a good time resolution, but with a coarser position resolution than the DT chambers or CSCs. The RPCs can therefore identify unambiguously the correct bunch crossing the measured signal belongs to. A more detailed description of the muon system can be found in [86].
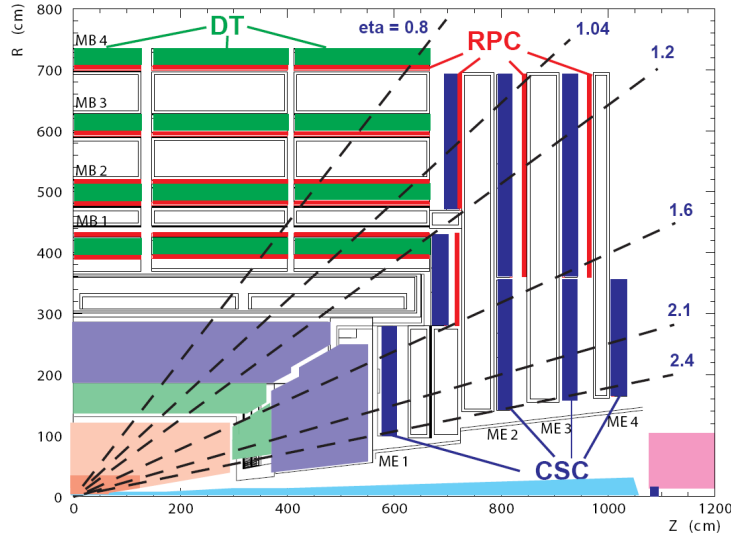

Figure 2.9:   Layout of one quarter of the muon system [76]. In the barrel region DT chambers (green) and RPCs (red) are provided, in the endcaps the muons are detected by CSCs (blue) and RPCs.

The barrel system consists of four concentric stations of detectors arranged in cylinders which are interleaved with the iron yoke at radii of approximately $4.0/4.9/5.9/7.0\,\mathrm{m}$ from the beam axis. Each of the five wheels in z is divided into 12 sectors, where one sector covers a $30°$ azimuthal angle, leading to a total of 250 DT chambers in the barrel region. The two innermost stations, named MB1 and MB2, consist of sandwiches made of a DT chamber placed between two RPCs. The two outermost stations, MB3 and MB4, consist of packages of a DT chamber coupled

to a layer of RPCs which is placed on the innermost side of the station. Depending on the sector and the station, the RPC layer contains one, two, or four chambers. The stations MB1, MB2, and MB3 each contain eight DT chambers which measure the muon coordinate in the $(r - \phi)$ bending plane, and four chambers which provide a measurement in the z direction along the beam axis. The fourth station, MB4, does not contain the z-measuring planes. The number of chambers in each station and their orientation were chosen to provide good efficiency for linking together hits from different muon stations to a single muon track and for rejecting hits originating from background events.

In each endcap there are four stations of CSCs, labelled ME1 to ME4, with chambers positioned perpendicular to the beam axis and interspersed between the flux return plates. In each disk the chambers are divided into two concentric rings around the beam axis, or three rings for ME1. Each CSC is trapezoidal in shape and consists of six gas gaps. All CSCs, except those in ME1 and ME3, are overlapped in ϕ in order to avoid gaps in the muon acceptance. Every CSC allows the measurement of the space coordinates (r, ϕ, z) in each of the 6 layers. In addition, a plane of RPCs is embedded in each of the first three stations as indicated in figure 2.9, covering the pseudorapidity range up to $|\eta| \leq 1.6$.

Track-based alignment techniques using cosmic muons were applied to align the DT chambers in the barrel region. An alignment precision of better than $700\,\mu m$ was achieved for the first three DT layers. Concerning the CSCs, a local alignment precision of $270\,\mu m$ was demonstrated within each ring of CSCs using LHC beam-halo muons recorded during beam operations in 2008 [77].

2.2.5   Processing of Collision Data

At the LHC design luminosity the beam crossing intervals of the proton bunches is $25\,ns$, corresponding to a crossing frequency of $40\,MHz$. Since it is impossible to store and process the large amount of data associated with the resulting high number of events with a rate implied by the collision frequency, a drastic reduction of $\mathcal{O}(10^5)$ is necessary. This task is performed by the trigger system, which decides whether an event is kept or discarded, based on particular detector information. The required rejection power is achieved by splitting the task into two steps. The first step, the so-called Level-1 (L1) trigger, consists of custom-designed, largely programmable electronics and is designed to reduce the rate of events accepted for further processing to less than $100\,kHz$. The second step, the so-called High Level Trigger (HLT), is a software system implemented in a filter farm of about one thousand commercial processors and is designed to reduce the maximum L1 trigger accept rate of $100\,kHz$ to a final output rate of approximately $100\,Hz$ for mass storage. The full CMS trigger and data acquisition (DAQ) system is documented in [87].

The CMS DAQ system is composed of eight vertical slices, each of them capable of operating more or less independently from the others. Figure 2.10 gives an overview of the general architecture of one such slice. Digitized data from the detector front-end electronics is stored in the detector front-end modules upon the recep-
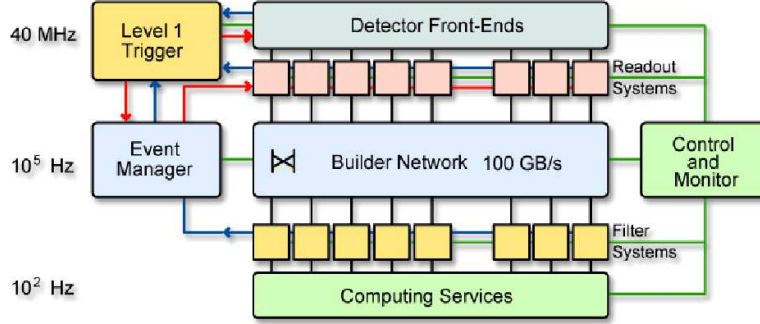
Figure 2.10: Sketch of the general architecture of the CMS DAQ system [76]. After the accept signal from the L1 trigger, the detector information fragments are passed to the readout units (RU, pink boxes). The event manager is responsible for the data flow in the RUs and their memory occupancy. The information is processed further through the builder network by the builder units (yellow boxes), which defragment the information of the events and passes them to the filter system of the HLT. The control and monitoring system is responsible for the configuration control and monitoring of all the elements.

tion of a L1 trigger accept signal. The L1 trigger calculation involves the calorimetry and muon systems, as well as some correlation of information between these systems. The decision is based on the presence of so-called trigger primitives, objects such as photons, electrons, muons, and jets above a certain energy or momentum threshold. Global sums of the transverse energy as well as of the missing transverse energy are also employed. The L1 trigger latency, between a given bunch crossing and the distribution of the trigger decision to the detector front-end electronics, is $3.2\,\mu s$. During the L1 trigger decision-making period, all the high-resolution data is held in pipelined memories in the detector front-ends. Based on the result of the Level-1 trigger, the data from the pipelined memories are transferred to front-end readout units (RU). The event manager coordinates the data flow in the RU builders and keeps track of the memory occupancy of the RUs. A fast access of the data is provided by a builder network, a collection of networks capable of supplying 800 Gb/s sustained throughput to the filter systems. The readout builder network is used to send the event fragments from the RU to the builder units, where the event is defragmented, before being passed to the HLT. All the elements are monitored by the control and monitoring system which is also responsible for the configuration control. The HLT, which is part of the filter system, executes more complex physics selection algorithms on the events read out, in order to accept the ones with the most interesting physics content. The output of the HLT is then at a rate suitable for mass storage.

Although the event rate is significantly reduced by the trigger system, the data flow of all the different LHC experiments is still at around $700\,\mathrm{MB/s}$, resulting in a total amount of data of about $15 \cdot 10^6\,\mathrm{GB}$ per year. This demands immense requirements on analysis software, computing resources, and storage capacity, which cannot easily be accomplished by single institutions. The worldwide LHC computing grid [88] provides a hierarchical tier structure with one Tier-0 center based

at CERN and several Tier-1 and Tier-2 distributed all over the world. The CMS computing model [89] is based on these globally distributed computing and storage resources, whose structure is shown schematically in figure 2.11. The idea is that the collision data, as well as simulated Monte Carlo (MC) data, will be distributed over the grid and physicists can access them from their local institute and run their analysis directly on the hosting site. Each layer of the tier structure serves particular computing tasks. The Tier-0 center collects all raw collision data which pass the CMS trigger system. A first reconstruction of the desired physics objects is performed with a rate of about 150 events/s. A copy of the Tier-0 datasets is then distributed among the Tier-1 sites, where re-reconstructions due to improved or exchanged reconstruction algorithms are run. Calibration and alignment jobs as well as the filtering of smaller datasets matching particular needs of certain physics groups belong to the Tier-1 site duties. The resources of the subsequent layer of Tier-2 sites are divided between local institute members and the CMS community. They provide storage capacities for the smaller group datasets and simulated MC datasets and have to support offline calibration and alignment tasks. The final layer of Tier-3 sites is not explicitly stated in the worldwide LHC computing model. The layer provides additional resources for the local user community and is mainly used for interactive analysis and software development.
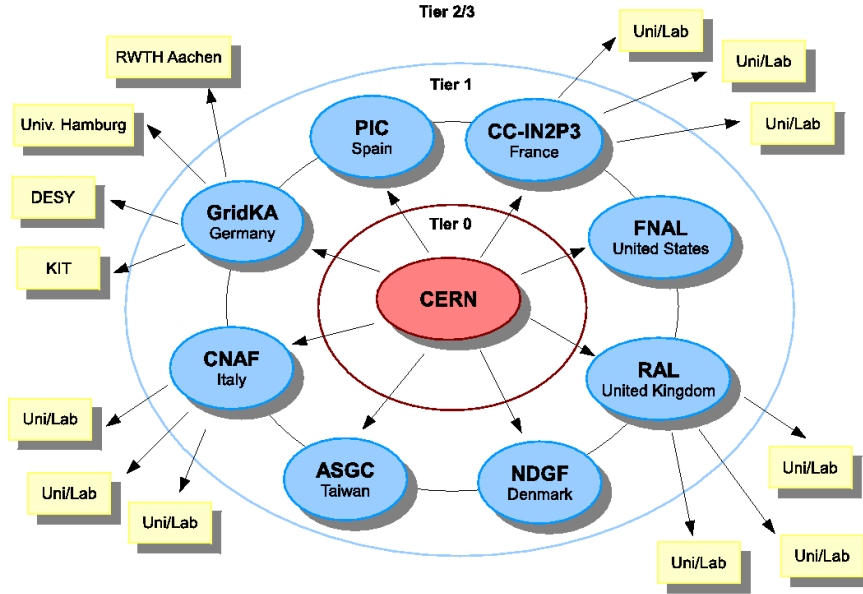

Figure 2.11: Schematic overview of the CMS computing grid. The single Tier-0 site is located at CERN, receiving all data that is collected by the experiment. From here, the data is transferred to Tier-1 centers in the whole world. Customized datasets and MC simulation data are further distributed to the 51 Tier-2 sites, where physicists can access them for their analyses, mainly performed on one of the more than 25 Tier-3 sites.

Chapter 3

MC Simulation of Single
Top-Quark Production

The Monte Carlo (MC) simulation of physics processes provides fundamental information for dedicated aspects of high-energy particle physics. The objective is to simulate events as detailed as could be observed by a perfect detector. These simulations are an instructive tool for the optimization of the detector design, for the study of interesting physics scenarios, and for the development of analysis strategies such that signal-to-background ratios are optimized.

Many different aspects have to be considered in order to simulate interactions taking place in high-energetic proton-proton collisions. The first part of this chapter introduces the main aspects of such simulations and describes briefly the different generator tools used for the present analysis. In the second part, the simulation of t-channel single top-quark production is studied. Here, the simulation of the LO process needs to be expanded by an approximation of NLO corrections in order to obtain a reasonable modeling. The applied matching method is described and the resulting simulation is compared to several other MC t-channel models. Finally, the simulations are compared to the predictions of recent NLO calculation.

3.1   MC Event Simulation

MC event generators accumulate our understanding of the SM into one package. Numeric simulations are used to randomly generate hard parton interactions according to the probability density of the phase space and the matrix element of certain physics processes. The integration of the squared amplitude over the whole phase space is necessarily performed using MC techniques [28].

Events occurring in proton-proton collisions at the LHC are not only described by the hard scattering process. The complexity of a hadron-collision process is sketched in figure 3.1. Several stages have to be implemented in the event simulation in order to obtain results that are comparable to data. This is not done in one step, but by factorizing the full problem into a number of components, each of which can be handled reasonably accurately.

In first approximation all processes have a simple structure at the level of inter-
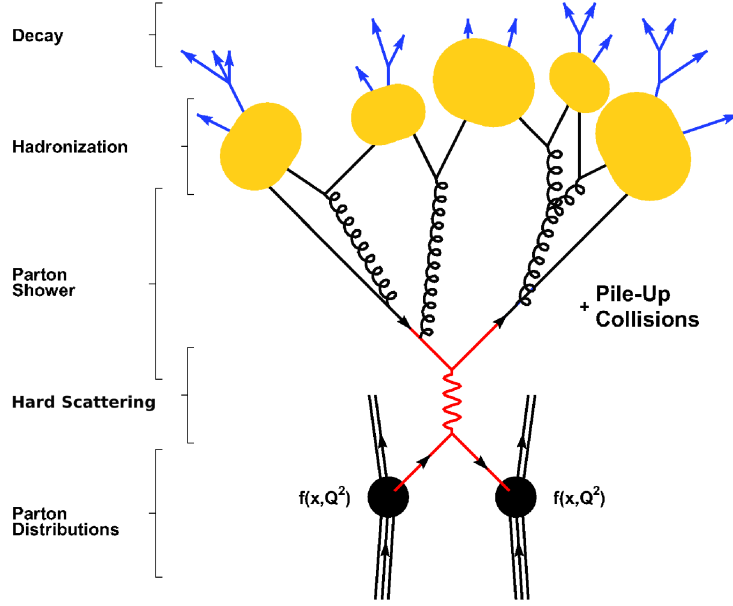
Figure 3.1: Schematic view of a hadron collision event showing the evolution of the pro-
duced particles. The incoming protons are characterized by the parton distribution func-
tions. The hard scattering process, taking place at high energies, i.e. at short distances, is
exactly calculable at LO using perturbative methods. The parton shower phase is dominated
by radiations of quarks and gluons in the initial and the final state, which can be modeled
by the DGLAP evolution equations. During the hadronization, colored partons are bound
into colorless hadrons. Since this takes place in the confinement region, where the strong
coupling constant α_s becomes larger than one and thus perturbation theory is no longer
applicable, the mechanism has to be described by phenomenological models.

actions between the fundamental objects of nature. However, several extensions of
this picture complicate the simulation. The bulk of corrections is universal and does
not depend on the details of the studied process, but only on a few key numbers
such as the momentum transfer scale of the process. For a full simulation of hadron
interactions, like proton-proton collisions, the following subprocesses are required to
be included.

Hard Scattering

The incoming protons are characterized by a set of PDFs $f(x, Q^2)$ which define
the partonic substructure in terms of flavor composition and momentum sharing.
From each of the two initial hadrons one parton enters the hard QCD process.
Since this scattering process takes place at large momentum-transfer scales Q^2 for
which the strong coupling constant α_s is small, the cross section of the hard process
can be computed at least to lowest order perturbation theory. In the hard process
a number of primary outgoing fundamental objects are produced. The nature of
this process, i.e. the color flow and the momentum-transfer scale, determines the
main characteristics of the whole event. In the case of the production of short-lived
particles like top-quarks, the hard-scattering in figure 3.1 also contains the calculable
decay of these partons.

Parton Shower

One shower initiating parton from each beam may start off a sequence of branchings, such as $q \to qg$ building up an initial-state parton-shower (PS). Final state gluons may be radiated off the top and b quarks, they again branch into further colored partons to build up final-state showers. The structure of these gluon radiations is given in terms of branchings. They can be described mathematically by the DGLAP QCD evolution equations [90–92], where the probability of radiating a gluon ($g \to gg/q\bar{q}, q \to qg/gq$) is considered according to the Altarelli-Parisi splitting functions. Each parton is characterized by the virtuality scale Q^2. The choice of the hard scattering scale is based on the used PDFs, which means that the inclusive effects of initial-state radiation are already included, thus it remains to construct the exclusive showers. This is done by starting from the two incoming partons at the hard interaction tracing the shower backwards in time to the shower initiators. This evolution is modeled in terms of a sequence of decreasing Q^2 and increasing momentum fractions x. Final-state showers are modeled by a decreasing Q^2 scale along the positive time direction. Since the branching of quarks and gluons is due to soft and collinear gluon emissions, the mathematical description of parton showers contains singularities. Thus, PS generators have to model these effects by using a generator dependent cut-off scale for the respective ordering parameter. The shower evolution is cut off at some lower scale Q_0, typically around $1\,\text{GeV}$ for QCD branchings. A maximum scale Q_{max} is introduced where the showers are matched to the hard interaction itself. This cut-off is chosen to stay away from non-perturbative physics, but still allows a sufficient showering to describe the process as realistic as possible. Coherence effects due to corrections to the leading-log calculation lead to an ordering of subsequent emissions in terms of decreasing angles. This behavior is implemented in the PS by using a certain angular ordering parameter, like the mass or the transverse momentum of the radiating parton or the angle of the radiation itself.

In the PS approach, not the full matrix-element expressions are used, but only approximations derived by simplifying the kinematics and the interference structure. PS simulations are therefore expected to give a good description of the substructure of jets in the low transverse-momentum region, but in principle the shower approach has limited predictive power for the rate of well-separated jets.

Hadronization

Perturbative QCD, formulated in terms of quarks and gluons, is valid at short distances. At long distances, the coupling constant of QCD becomes large and perturbation theory breaks down. In this confinement region, the colored partons are transformed into colorless hadrons, a process called hadronization or fragmentation. The hadronization process has yet to be understood from first principle, starting from the QCD Lagrangian. As a result of the perturbative shower-evolution, the partons are grouped into color-singlet clusters that end up close in phase space. These preconfined clusters serve as starting point for the hadronization of the shower partons into color-neutral hadrons. In the absence of a firm theoretical understanding, different phenomenological models to describe the hadronization process have

been developed and are used by the MC event generators. In general, hadronization is of a probabilistic and iterative nature. The process as a whole is described in terms of simple underlying branchings. At each branching, probabilistic rules are given for the production of new flavors and for the sharing of energy between the products. After tuning of the model parameters, the existing hadronization models are in good agreement with a wide range of data.

Underlying Event and Pile Up

The initial parton only takes some fraction of the total proton energy, leaving behind a proton remnant which takes the rest. This remnant is color-charged and therefore color-connected to the hard interaction. This underlying event forms part of the same fragmentation system and has to be taken into account when simulating the main interaction.

Depending on the luminosity of the colliding beams, several interactions can occur during the same bunch crossing. Such events are called pile-up or minimum bias events. For the LHC operating at the design luminosity a total of about 25 pile-up events per bunch crossing are expected. These effects have to be considered in order to obtain a realistic event simulation.

3.2   MC Event Generator

Depending on the included processes, we distinguish between PS generators providing full event simulations as described above, and matrix-element generators simulating only the partons of the hard scattering process and calculating the corresponding cross section. In the following, the different MC generators used for the analysis presented in this thesis are shortly described.

Pythia

PYTHIA [20] is a program for the generation of high-energy physics events including PS, with emphasis on those events where strong interactions play a role and therefore multi-hadronic final states are produced. The angular ordering demanded by the color coherence of the radiated gluons during the PS is organized using $Q^2 = m^2$ as ordering variable. The hadronization process is described by the Lund string model. A string represents the color-flux tube, stretched between a q and a $\bar{q}$ due to the confinement of color-charged particles. The string energy can be converted to further $q\bar{q}$ pairs if the invariant mass of the string is large enough. The chance for producing different flavors depends on the mass of the corresponding $q\bar{q}$ pair. Charmed and heavier quarks are hence not expected to be produced in the soft fragmentation, but only in perturbative parton-shower branchings $g \rightarrow q\bar{q}$. Due to local flavor conservation, quarks are quantum-mechanically created at one point. Thus, the tunneling probability of the $q\bar{q}$ pair to get out to classically allowed regions as well as the chance that a given $q\bar{q}$ pair combination forms a specific meson has to be considered. The hadron production is treated as an iterative process which continues until the string energy is consumed.

MC@NLO

MC@NLO [23] matches next-to-leading order calculations for a given QCD process with a MC parton-showering simulation as implemented in HERWIG [93]. Hard emissions are treated as in NLO computations so that the NLO results for distributions are recovered upon an expansion in α_s, while soft and collinear emissions are handled by the PS simulation of HERWIG. The matching between the hard and the soft/collinear region is smooth. When MC generators simulate events with real parton emission, kinematical configurations are obtained that are also taken into account by the NLO computation. The possibility of having the same kinematical configuration from the MC and from the NLO may lead to double counting. The problem is to merge the PS and the NLO description under avoidance of double-counting. MC@NLO uses the subtraction method [94] for NLO calculations to match the two elements, leading to a small amount of generated events with negative weights. One has to note that these negative weights are of a nature completely different from the separately divergent contributions of real emission and virtual loops appearing in NLO calculations. The distributions of the positively- and the negatively-weighted events are separately finite, which implies the possibility of un-weighted event generation. While spin correlations are taken into account, NLO corrections to the decay of the produced particles are not included. MC@NLO provides a fully exclusive event generation with hadronization according to the MC model, whereby the total exclusive rates are accurate to NLO computations. However, this simulation will not improve the logarithmic accuracy of the original MC generator in those regions of the phase space where resummation is needed.

The PS approach used by HERWIG includes color-coherence effects in all hard subprocesses and azimuthal correlations within and between jets due to gluon interference and polarization. The branching angle between the branching shower-parton and the emitted parton is used as ordering parameter. HERWIG uses the cluster model to describe the hadronization, following up the preconfined clusters resulting from the PS period. The clusters are differentiated by their mass which has to be within a defined range. Since the mass spectrum of the color-singlet pairs is asymptotically independent of the energy and the production mechanism of the event, the light clusters dominate. Due to a finite width of the mass distribution three possible cases have to be considered: if the cluster is too light to decay into two hadrons, it is taken to represent the lightest single hadron of its flavor and its mass is shifted to the appropriate value by an exchange of four momentum with a neighboring cluster in the jet. Massive clusters will be fragmented using an iterative fission model until the masses of the fission products fall below a defined threshold. Clusters with an adequate mass decay isotropically into pairs of hadrons. The probability for a certain hadron to be formed by a cluster is determined by different parameters like the cluster mass or spin and masses of the hadrons.

Matrix-element Generators

Compared to the generators presented above, matrix-element generators do not contain PS methods. Given specific initial and final states, they identify all relevant subprocesses and generate the corresponding amplitudes. The information about the contributing Feynman diagrams is then used to calculate cross sections and to obtain unweighted events at parton level before PS and hadronization. A standard file format, the so-called Les-Houches-event (LHE) file format [95], has been worked out some years ago in order to store process and event information in a common way. This LHE format has been adopted as primary output of matrix-element generators. Thus, the parton-level LHE file can flexibly be passed on to a PS generator like PYTHIA or HERWIG to continue the evolution of partons into fully hadronized final states.

Most of the processes relevant for this thesis were simulated by the matrix-element generator MadGraph/MadEvent [19]. The MadGraph (MG) package automatically generates the amplitudes for all the relevant subprocesses and produces mappings for the integration over the phase space. MG is able to handle tree-level processes with up to eight particles in the final state. This process-dependent information is packaged into MadEvent (ME) and a stand-alone code is produced to calculate the cross sections and to obtain unweighted events. An efficient phase-space integration is achieved by using the technique of single-diagram-enhanced multichannel integration. At this, the integration of the amplitude is decomposed into n independent integrations, where n is the number of channels of the process. In this approach, the complexity of the computation does not increase with the number of channels and it is parallel in nature so that the integration in each channel can be performed by using different resources. The resulting simulated events are passed to the PYTHIA program for further processing.

As already discussed in the general PS description, the matrix-element calculation is used to model well separated and hard jets, whereas the PS formalism is more appropriate for collinear and soft jets. In order to combine processes with different jet-multiplicities from the ME generator without double-counting PS emissions, a phase-space cutoff has to be introduced to separate these two regions. The two matching algorithms widely used are the CKKM [96] and the MLM [97] method. In this thesis, the simulation of multi-jet processes, for example top-quark pair production plus additional jets or the production of W bosons in association with additional jets, uses the MLM matching algorithm. The choice of events is based on a matching of parton-level events to hadronized jet-level events. A parton-level event is defined by applying a minimal E_{T} threshold to the partons from the hard process and by requiring a minimal separation between them of $\Delta R_{jj} > R_{\min}$. In order to obtain the jet-level event, a jet algorithm is applied to the particles after the hadronization process with cluster parameters corresponding to the definition of the parton-level event. Finally, the event is kept only if each jet can be matched to a parton of the hard process. Otherwise, the event is discarded. To model the process inclusively, extra jets with a transverse momentum below the minimal threshold are allowed for the highest jet-multiplicity sample.

The fact that the simulated event samples contain full event information at parton level, so that each particle at hadron level can be traced back, offers several important opportunities. MC samples are used to improve the understanding of the influence of event selection and reconstruction effects on the data samples. In addition, they allow for an estimate of the size and the shape of background contributions. Finally, we use several MC samples to study the systematic effects arising from the choice of one simulation model.

3.3 *t*-channel Modeling

The modeling of the *t*-channel process is special in the sense that NLO corrections have to be combined with the tree-level Born diagram in order to obtain a reasonable MC prediction. The calculation of the $2 \to 3$ process in the tree approximation, depicted in figure 3.2 (a), does not include the large logarithmic QCD corrections that are associated with the $g \to b\bar{b}$ graph and appear for collinear gluon splittings yielding spectator *b*-quarks with low transverse momenta. In a widely used approach, these corrections are summed into the PDF of the *b* quarks. This LO approximation is referred to as the $2 \to 2$ reaction with the *b* quark in the initial state, see figure 3.2 (b). The corrected *b*-quark configuration as well as the initial gluon splitting and the resulting spectator *b*-quark are simulated using the initial-state-radiation mechanism of the PS generator. Figure 3.3 shows a comparison
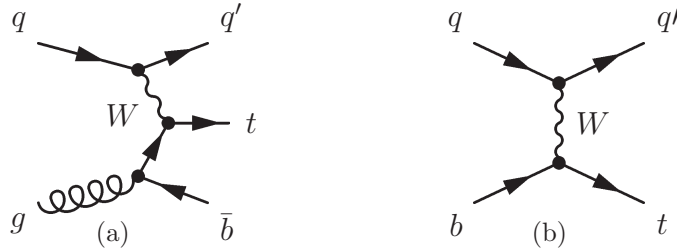
Figure 3.2: Feynman diagrams of *t*-channel single top-quark production. Two different tree-level approximations are considered in the event simulation: the $2 \to 3$ process, where the gluon splitting into $b\bar{b}$ in the initial state is contained in the matrix element (a), and the $2 \to 2$ process, starting with a *b* quark in the initial state (b).

of the transverse-momentum spectra of the spectator *b*-quark, stemming from the initial gluon splitting, for the tree level $2 \to 3$ and the $2 \to 2$ approximation. The different treatment of the initial state in the two approximations has direct impact on the modeling of the spectator *b*-quark. In the $2 \to 2$ process, the soft p_T-region is correctly simulated, while the contribution from the hard region is significantly underestimated. In turn, the spectrum of the $2 \to 3$ process models well the hard-p_T region, but yields a significantly lower rate in the soft-p_T region due to the disregard of the collinear gluon splitting regime. However, the insufficiency of one single picture can be overcome by combining the different approximations used in particular p_T regions.
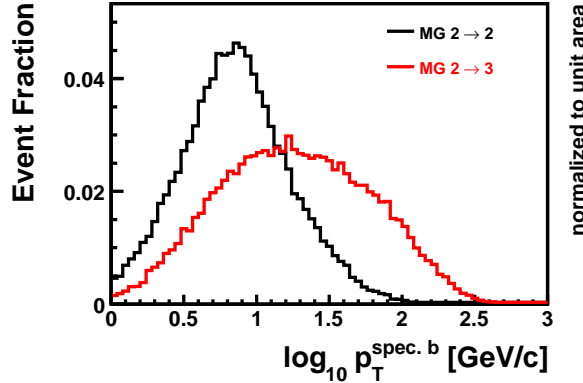
Figure 3.3: The transverse momentum distribution of the spectator b-quark. The x axis is plotted logarithmically in order to emphasize the difference due to the modeling of this parton in the two approaches. In the $2 \rightarrow 2$ process, the spectator b-quark is modeled by the DGLAP evolution during the PS step, whereas in the $2 \rightarrow 3$ simulation this parton is part of in the matrix-element calculation.

3.3.1   Matching Method based on ZTOP

When combining the $2 \rightarrow 2$ and the $2 \rightarrow 3$ contributions, one has to be careful in order to avoid double-counting of the overlapping phase space. The matching method applied in this thesis is based on the idea of matching the p_T distributions of the spectator b-quark as suggested in [22]. It is assumed that the soft-p_T region of the spectator b-quark is better modeled by the $2 \rightarrow 2$ matrix-element computation, whereas the hard-p_T regime is better described by the $2 \rightarrow 3$ contribution. Hence, a matching point has to be defined which separates the soft and the hard region and determines the ratio of the two event categories. In order to obtain a prediction for the normalization of the hard-p_T region, the software package ZTOP [21] is used. ZTOP provides calculations of the fully differential cross section of s- and t-channel single top-quark production at NLO. The integration is based on the phase-space slicing method using the spin-averaging technique. The decay of the top quark is not included. An inherent property of the NLO calculation of differential cross sections is that it has to deal with final-state infrared singularities. This issue is overcome by applying a jet definition and thus providing jet objects instead of partons in the final state. In contrast to jet objects defined in the experimental field which contain multiple particles (see section 4.2.5) these partonic jet objects typically consist only of a few partons. The choice of jet cuts is driven by the detector acceptance, and thus set to a minimal transverse momentum of $p_T^{\min} = 20\,\mathrm{GeV}/c$ and a pseudorapidity range of $|\eta| \leq 5$.

Based on the calculated NLO normalization of the high-p_T tail of the spectator b-quark spectrum, the two contributions, $\sigma_{2\rightarrow 2}$ and $\sigma_{2\rightarrow 3}$, are scaled such that the transition between the two spectra at the matching is smooth and that the predicted total cross section is respected. The total cross section, σ_{NLO}, is also obtained from ZTOP by evaluating fully differential distributions calculated for the top quark. The

boundary condition of this method is defined by:

$$\sigma_{2\to3}\big|_{p_{\mathrm{T}}^{\mathrm{spec.b}} > p_{\mathrm{T}}^{\mathrm{min}}} = \sigma_{\mathrm{ZTOP}}\big|_{p_{\mathrm{T}}^{\mathrm{spec.b}} > p_{\mathrm{T}}^{\mathrm{min}}}, \tag{3.1}$$

and the total cross section is assumed to be composed of:

$$\sigma_{\mathrm{NLO}} = K \cdot \int_0^{K_{\mathrm{T}}} \frac{d\sigma_{2\to2}^{\mathrm{LO}}}{dp_{\mathrm{T}}^{\mathrm{spec.b}}} \, d(p_{\mathrm{T}}^{\mathrm{spec.b}})' + \int_{K_{\mathrm{T}}}^{\infty} \frac{d\sigma_{2\to3}}{dp_{\mathrm{T}}^{\mathrm{spec.b}}} \, d(p_{\mathrm{T}}^{\mathrm{spec.b}})'. \tag{3.2}$$

For each arbitrarily chosen matching point K_{T} one obtains a certain scale factor K for the remaining $2 \to 2$ spectrum, while the result respects the requirement of equation 3.1. From this set of possible matching thresholds K_{T}, the one is chosen that minimizes the difference Δ:

$$\Delta(K_{\mathrm{T}}) = \frac{d\sigma_{2\to2}}{dp_{\mathrm{T}}^{\mathrm{spec.b}}}\bigg|_{p_{\mathrm{T}}^{\mathrm{spec.b}} = K_{\mathrm{T}}} - \frac{d\sigma_{2\to3}}{dp_{\mathrm{T}}^{\mathrm{spec.b}}}\bigg|_{p_{\mathrm{T}}^{\mathrm{spec.b}} = K_{\mathrm{T}}}. \tag{3.3}$$

Figure 3.4 illustrates this process. Performing a scan of potential matching points, the difference Δ between the value of the two properly scaled p_{T} spectra at each particular point is shown in (a). Choosing the point that yields a minimal difference ensures a smooth intersection between the two spectra at the matching point. The resulting matched distribution for $K_{\mathrm{T}} = 13.5 \, \mathrm{GeV}/c$ can be found in (b), yielding a ratio $R = \sigma_{2\to2}/\sigma_{2\to3}$ of 1.84 and a K factor for the $2 \to 2$ process of 2.3.

The modeling of the transverse-momentum spectrum of the spectator b-quark depends on the kinematics of the whole process, and, concerning the $2 \to 2$ process, in particular on the choice of parton shower parameters. Thus, the matching threshold K_{T} has to be determined whenever the configuration of the simulation changes. More details on the matching procedure adopted for CMS as well as the validation of the method is documented in [98].

Implementation into the CMS Software

The MadEvent matrix-element generator is one of the main tools used for the MC production within the CMS collaboration. In order to provide an efficient work flow for the generation of t-channel single top-quark samples, the matching of the two sub-samples was partially implemented into the official CMS software (CMSSW) in the frame of the software package `MadGraphInterface`. Having determined the matching threshold and the efficiencies of both contributions with respect to this threshold, the two independently generated parton-level LHE files for $2 \to 2$ and $2 \to 3$ are first passed to a private software tool. It performs a filtering of the $2 \to 3$ events, where only events with a transverse momentum of the spectator b-quark above the matching threshold are kept. This step is performed directly on the LHE file, where only hard matrix element partons are stored, and produces an output LHE file containing randomly mixed both contributions. The output is then stored in the CERN Monte Carlo data base, from which the official CMS production job can access the pre-filtered file for further processing. After the subsequent PS and hadronization step for which PYTHIA is used, the events are passed through
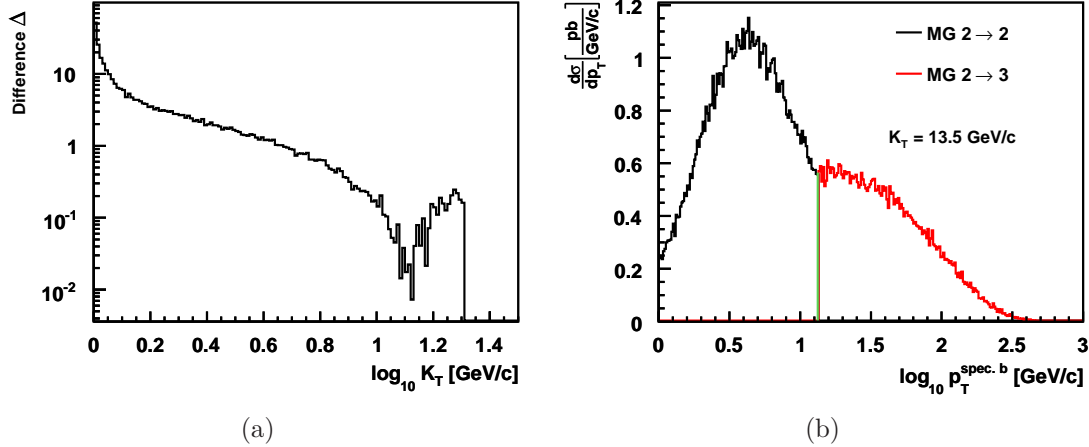
(a)   (b)

Figure 3.4: Determination of the matching point K_T. The difference Δ between the two scaled histograms, as explained in the text, for a scan of different matching points K_T is shown in (a). The eventual matching point is chosen as the point with a minimal difference, yielding $K_T = 13.5\,\text{GeV}/c$. The resulting combined spectrum is shown in (b).

the `STFilter`, a filter sequence that discards events of the $2 \rightarrow 2$ process with a transverse momentum of the spectator b-quark above the matching threshold. Only about one half of the originally generated events contribute to the finally matched phase space. Therefore, it is important to obtain the matched sample as early as possible in the production chain. A modular procedure as described here provides a properly matched and randomly mixed t-channel sample at an early stage, such that only those events are passed to the very time-consuming event simulation which contribute to the eventually matched phase space.

3.3.2   Comparison of Different MC Models

Different MC generators are used by the CMS collaborators in order to simulate single top-quark production, which are in the following compared to each other. The comparison is based on a set of t-channel single top-quark event samples generated for a center-of-mass energy of 14 TeV, using the three MC tools MadGraph, SingleTop [22], and MC@NLO. Two of them, MadGraph and SingleTop, are based on a matrix-element generator where a matching of the two main t-channel contributions is applied in order to obtain a reasonable description. The third generator, MC@NLO, uses exact NLO calculations to simulate the events, and performs a matching of those with the PS simulations based on HERWIG. The applied matching method yields a fraction of about 24% negatively weighted events for the t-channel single top-quark process. Unlike the matrix-element computations of MadGraph and SingleTop, the b quark is treated as massless in MC@NLO, which gives rise to important consequences in some kinematical regions.

The matching procedure which is applied to calculations obtained from the MadGraph generator was described in the previous subsection. The SingleTop package

is based on the matrix-element generator CompHEP [99]. The matching of the two processes, $2 \rightarrow 2$ and $2 \rightarrow 3$, is performed after the simulation of initial- and final-state radiation and is also based on the modeling of the transverse-momentum spectrum of the spectator *b*-quark. The matrix-element calculation is done by means of CompHEP, including the decay of the top quark and the *W* boson. The events are also passed to Pythia for the parton shower and hadronization modeling.

For the SingleTop and the MC@NLO event simulation, a top-quark mass of $m_t = 175\,\mathrm{GeV}/c^2$ was chosen, whereas the MadGraph event sample was generated with $m_t = 170\,\mathrm{GeV}/c^2$. For the sake of clearness, the statistical uncertainties are only drawn for the event sample with the smallest statistics, which is the one simulated with SingleTop.

The transverse momentum and the pseudorapidity spectra for all the final state partons of the *t*-channel process are compared to each other. In addition, the correct spin treatment in the different samples is verified by looking at the polarization of the top quark. As introduced in section 1.3.3, the cosine of the angle between the outgoing light quark and the charged lepton from the top-quark decay, both boosted to the top-quark rest-frame, is expected to yield a characteristic triangular shape with an increasing slope towards $\cos\theta = 1$. As can be seen in figure 3.5 (a), the polarization is well described by all MC models, while MC@NLO shows a slightly steeper slope indicating a stronger polarization. Figure 3.5 (b) shows the transverse momentum and the pseudorapidity distributions of the outgoing light quark, (c) contains the corresponding figures for the top-quark. All three generators are in reasonable agreement, taking into account the different top-quark masses. The comparison for the decay products of the top quark is shown in figure 3.6. Subfigure (a) shows the distributions of the *b*-quark, (b) shows the distributions of the charged lepton and (c) of the neutrino. All the pseudorapidity distributions are found to be in good agreement. Concerning the p_T spectra, small differences are observed for the *b* quark from the top-quark decay as well as for the neutrino distribution. Such small discrepancies are expected, since, as mentioned above, the used top-quark mass is different for the different event samples. In addition, the decay of the *W* boson is restricted to certain lepton categories depending on the used generator. While the SingleTop sample contains only muonically decaying *W* bosons, the MC@NLO simulation allows also for electrons and the MadGraph simulation considers all the three lepton categories (e, μ, τ).

The transverse momentum and the pseudorapidity spectra of the spectator *b*-quark can be found in figure 3.7 (a). Here, an important difference between the matched matrix-element simulation and the MC@NLO model becomes apparent. As the spectator *b*-quark is treated as massless by MC@NLO, the soft p_T region is not modeled correctly. This artifact can also be observed in the pseudorapidity spectrum, where the rate is artificially increased at high $|\eta|$ values. Since the matched matrix-element models contain a description of the collinear gluon splitting regime, the soft region is expected to be described reasonably in the MadGraph and the SingleTop model. Rejecting the soft region of the p_T distribution by an additional cut of $p_\mathrm{T} > 20\,\mathrm{GeV}/c$, the spectra become comparable, as shown in figure 3.7 (b). Nevertheless, small differences remain: the spectrum obtained from SingleTop
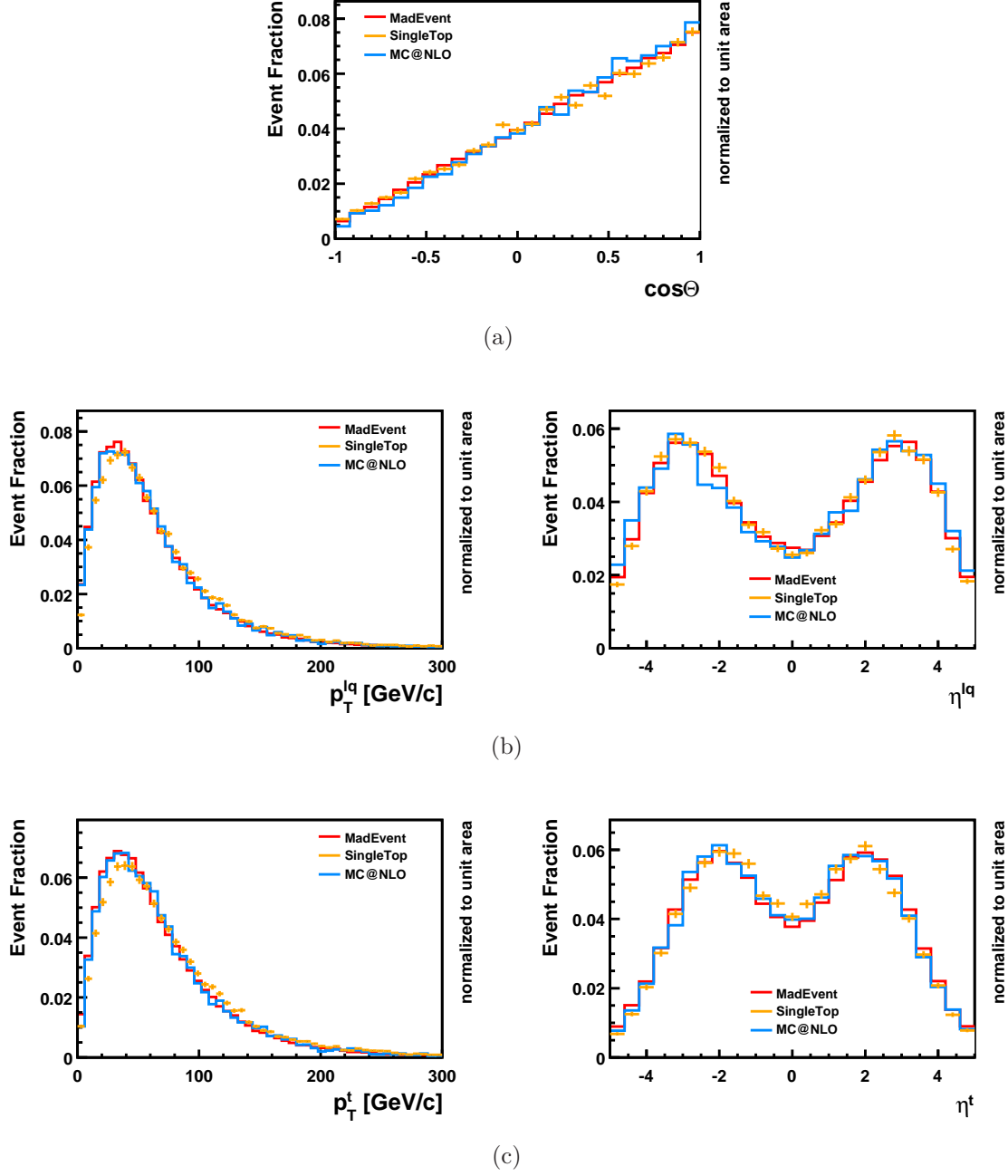
(a)

(b)

(c)

Figure 3.5: Comparison of several kinematic variables at parton level for the three different MC models at $\sqrt{s} = 14\,\text{TeV}$. The polarization variable of the top-quark, $\cos\theta$ (a), the transverse momentum p_T and the pseudorapidity η of the light quark (lq) in the final state (b) and of the produced t-quark (c).
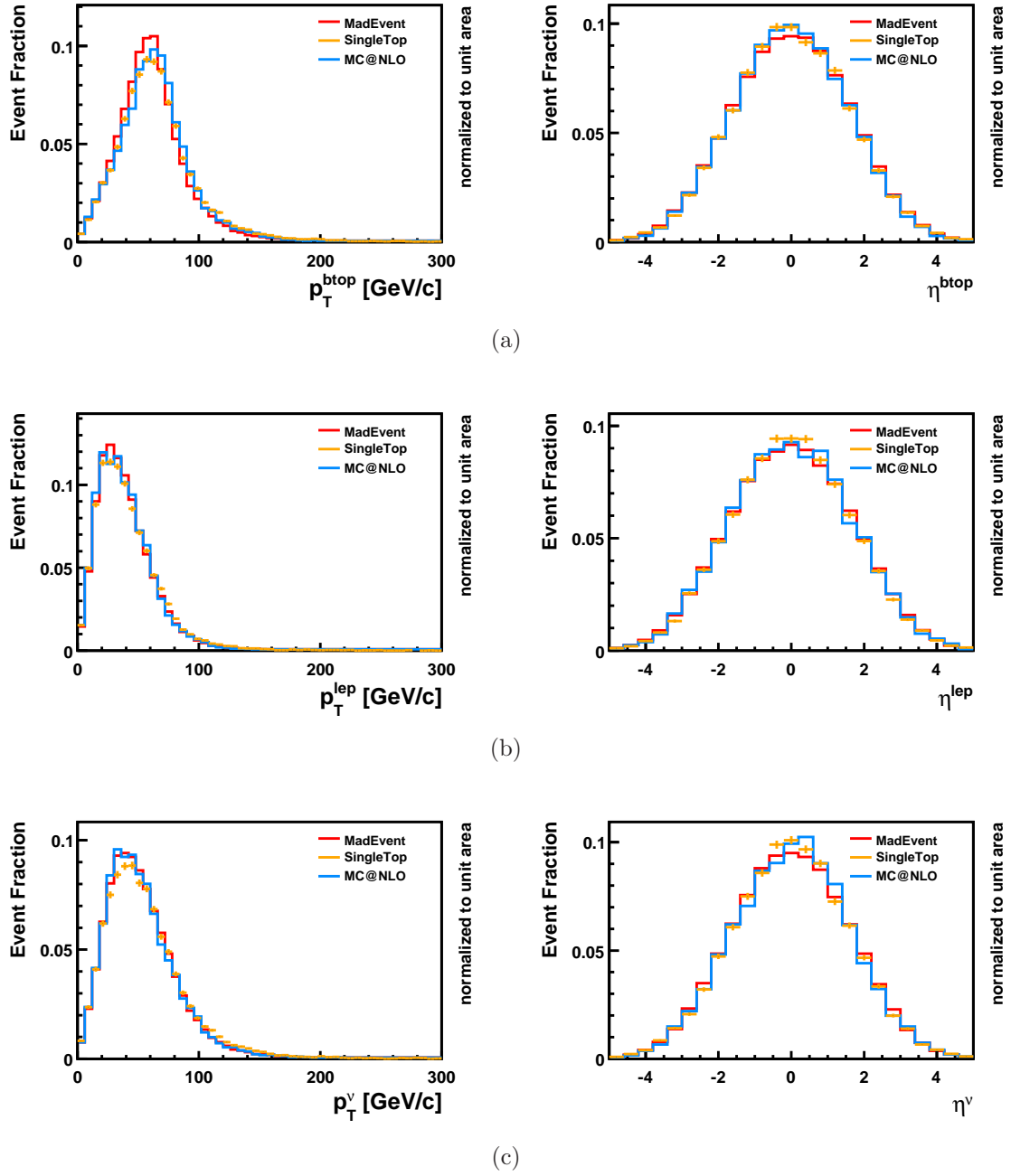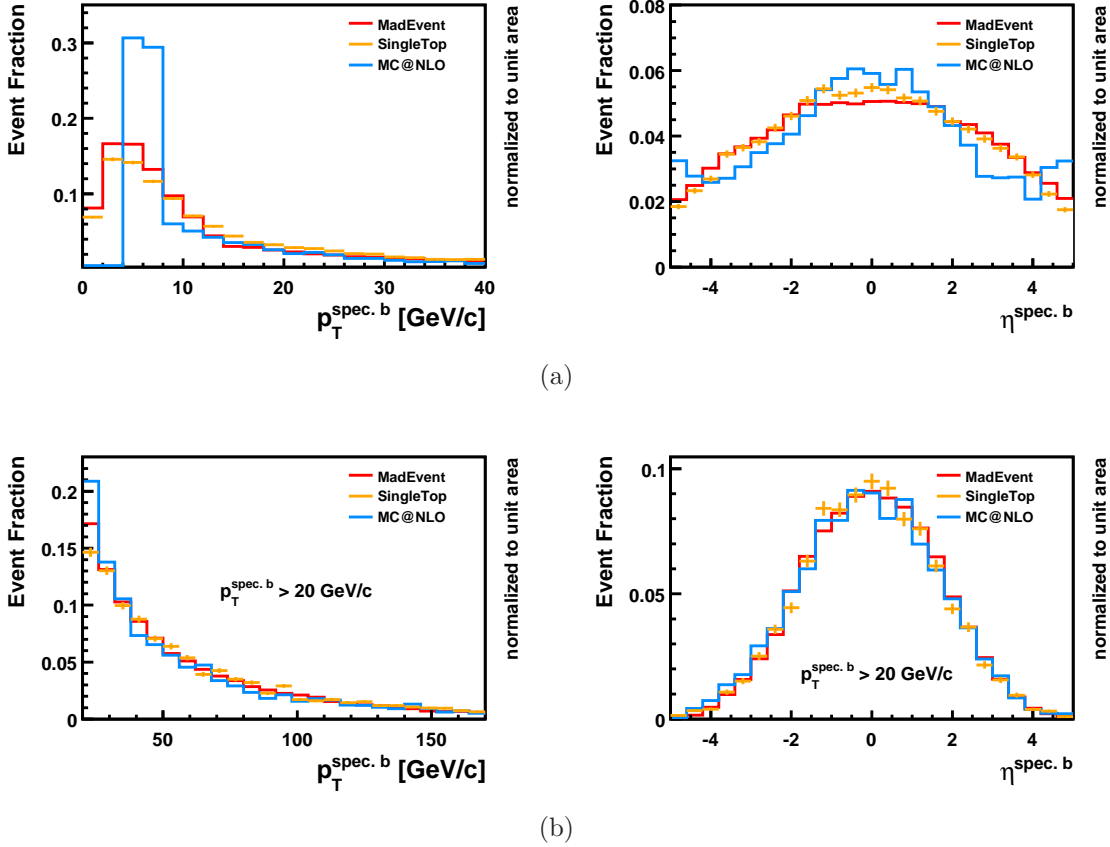
Figure 3.6: Comparison of several kinematic variables at parton level for the three different MC models at $\sqrt{s} = 14\,\text{TeV}$. The transverse momentum p_T and the pseudorapidity η of the decay products of the top quark: (a) the b quark (btop), (b) the charged lepton (lep), (c) and the neutrino (ν).

is slightly harder compared to the MadGraph distribution, while the spectrum of MC@NLO is significantly softer.

Based on this comparison study at parton level, we can conclude that all the relevant physics objects in the t-channel single top-quark process are described comparably well by the three MC models. The matched MadGraph and the SingleTop model, which employ similar approaches, show a reasonable agreement in all the considered distributions, except for small differences in the p_T distributions of the top quark and the light quark. MC@NLO fits in the picture concerning the light quark, the top quark and its decay products, but it shows a major difference in the description of the spectator b-quark. The observed behavior can be interpreted as a consequence of the fact that the b quark is treated as massless in the computation, which might lead to singularities in the soft region. In order to avoid this, the extreme soft region is omitted.

(a)

(b)

Figure 3.7: Comparison of several kinematic variables at parton level for the three different MC models at $\sqrt{s} = 14$ TeV. The transverse momentum p_T and the pseudorapidity η of the spectator b-quark (a). The distribution of MC@NLO is significantly different compared to the ME and the SingleTop simulation, due to the fact that the b quark is treated as a massless particle in MC@NLO. Applying a cut on the transverse momentum of $p_T^{\text{spec.b}} > 20 \, \text{GeV}/c$, the spectra become comparable (b).

3.4 Comparison of the t-channel Simulation to NLO Calculations

In the following the t-channel simulation as obtained from MG is compared to fully differential NLO distributions calculated with MCFM [100] in the four and five flavor scheme as described in [24], for a center-of-mass energy of 10 TeV. At the moment there are two complementary ways to calculate next-to-leading contributions to the t-channel single top-quark production. Traditional NLO calculations [101, 102] are based on the $2 \to 2$ Born process with a b-quark in the initial state, see figure 3.2 (b). The convenience of such an approach is founded in the usage of kinematic approximations and the resummation of logarithmic terms. Such possibly large logarithms of the form $\log \frac{Q^2}{m_b^2}$, which occur due to initial state collinear configurations with $g \to b\bar{b}$ splitting, are consistently resummed into the b-quark PDF leading to an improved stability of the perturbation expansion. The presence of the spectator b-quark and its mass, however, are NLO effects in this approach, thus the description of this parton is at LO accuracy only. An alternative approach is the 4FS calculation [16] based on the $2 \to 3$ Born amplitude, shown in figure 3.2 (a). It describes the process $gq \to t\bar{b}q'$, with the b-quark mass kept finite. In this scheme, the b quarks do not enter in the QCD evolution of the PDFs and of the strong coupling. Due to the inclusion of an additional parton in the final state and the presence of a further mass scale the NLO corrections are much more involved here. However, this approach allows the investigation of features associated with the kinematic description of the spectator b-quark at NLO accuracy. The resulting differential distributions of the top quark and the spectator b-quark, which are presented in [24], turn out to be very well-behaved and are in substantial agreement with predictions based on the $2 \to 2$ process.

When the 4FS calculation became available in 2009, the distributions obtained from this calculation have been compared to the outcome of the MadGraph MC modeling for t-channel single top-quark production. This comparison, which is presented in the following, concentrates on the transverse momentum and pseudorapidity distributions of the top quark and of the spectator b-quark, since these are the most relevant final state partons. The top-quark mass used for the MCFM calculations is set to $172.5 \, \text{GeV}/c^2$, corresponding to the value used for the MC simulation of the MadGraph samples, while the b-quark mass has a slightly different value of $4.5 \, \text{GeV}/c^2$ compared to the MG setting of $4.7 \, \text{GeV}/c^2$. For the NLO calculations the CTEQ6.6 PDF is used, which is the most recent NLO set corresponding to the leading-order CTEQ6l1 set, being used for the MG simulation. In MCFM, the renormalization and factorization scales have a fix value and are chosen as $(m_t + m_b)/2$ for the heavy quark line, and $(m_t + m_b)/4$ for the massless quark line. Since the MG simulation allows for an event dependent scale choice, the factorization and renormalization scales are determined here by $m_t^2 + Q^2$ for both quark lines. Neither in the MCFM calculations nor in the MG simulation cuts are applied to the kinematic properties of the partons.

In a first step, the distributions obtained from the 4FS and 5FS calculations are compared to each other, see figure 3.8. As already stated in [24], a slight difference

is visible between the two approaches. Comparing the shapes, the 4FS yields a slightly harder and more centrally produced top quark than the 5FS approach, whereas the modeling of the spectator b-quarks shows a contrary behavior. Here, the distributions obtained from the 5FS calculation describe a slightly harder and thus more centrally produced spectator b-quark than in the 4FS. This is expected since the NLO 4FS calculation effectively describes NLO corrections to the spectator b-quark kinematics, thus containing additional radiations.
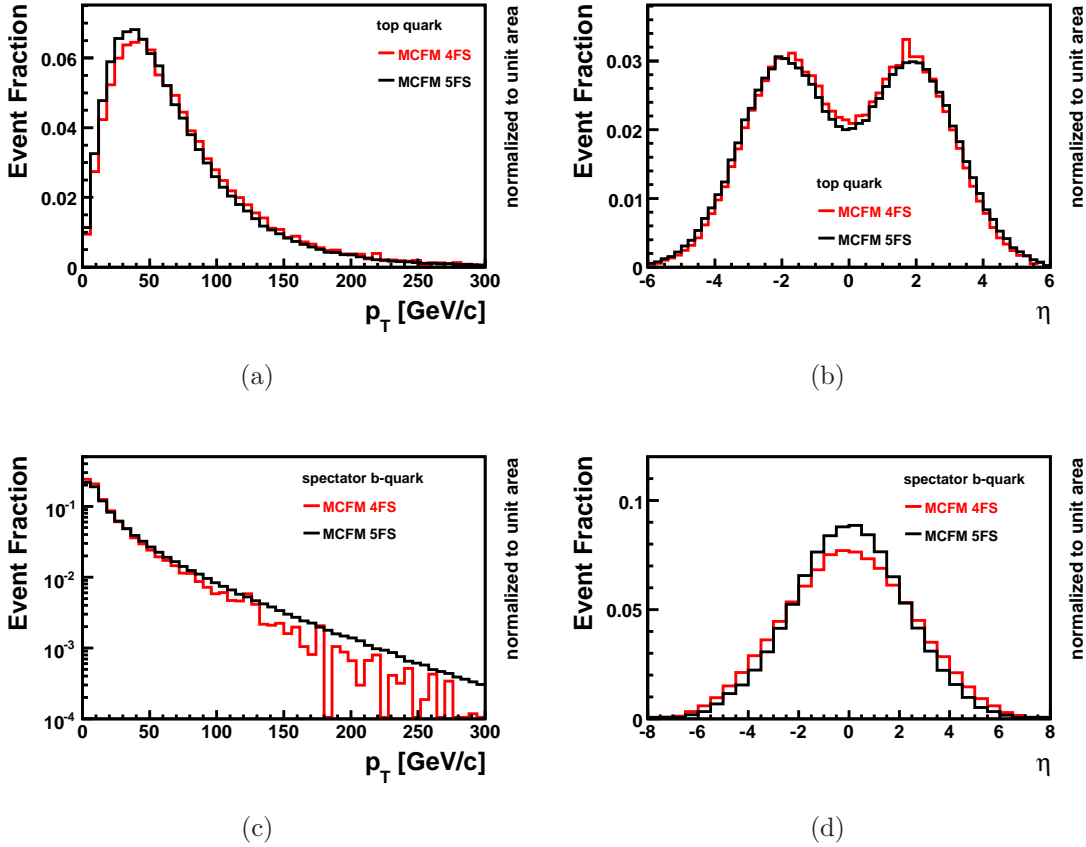
Figure 3.8: Shape comparisons of differential distributions obtained from the 4FS and the 5FS calculations of MCFM for $\sqrt{s} = 10\,\text{TeV}$. The transverse momentum and the pseudorapidity distributions of the top quark are shown in (a) and (b), while the corresponding distributions for the spectator b-quark are shown in (c) and (d).

As introduced above, the description of the spectator b-quark in the 5FS approach is at LO accuracy. Therefore, the predictions of this approach should in general correspond to the modeling obtained from the MG $2 \rightarrow 3$ process. The shape comparison for the top quark and the spectator b-quark are shown in figure 3.9. Since the used MG sample has already undergone the parton showering with PYTHIA, the p_T and η distributions for the top quark are closer to the 4FS prediction than to the 5FS one. However, the modeling of the spectator b-quark in the MG $2 \rightarrow 3$ process shows a very good agreement with the 5FS calculation in

both the transverse momentum and the pseudorapidity distribution.
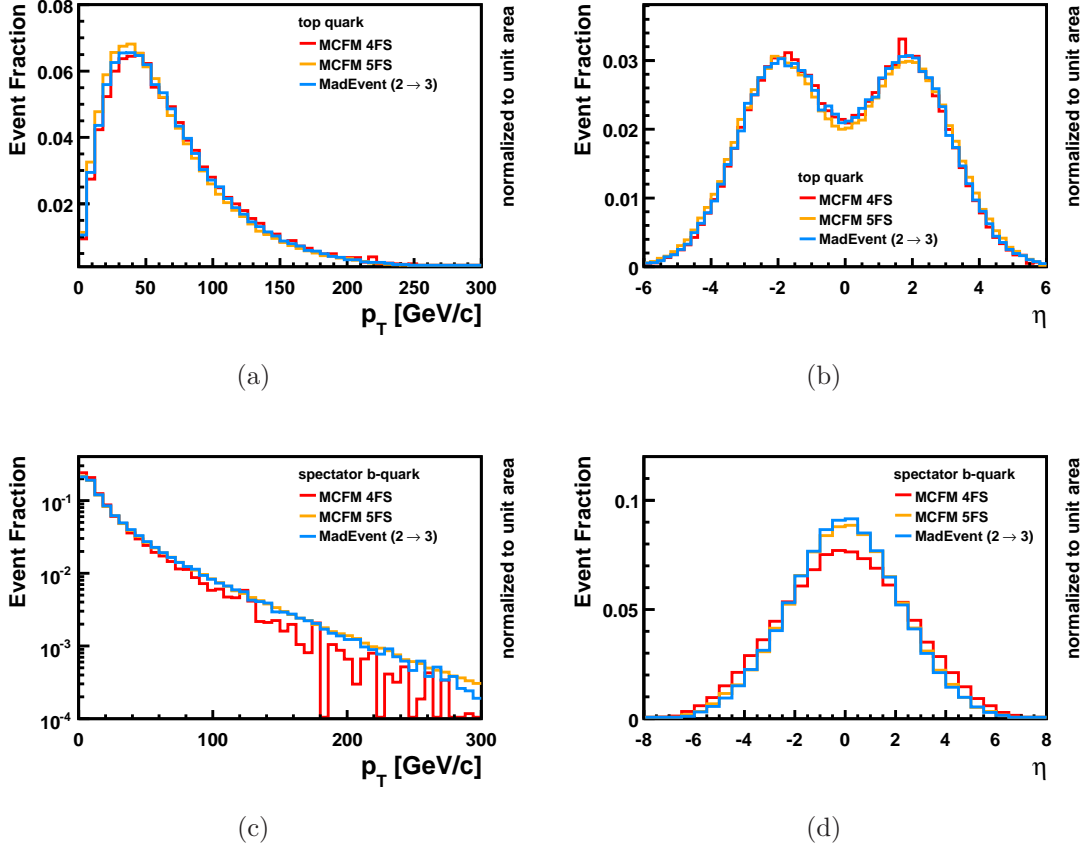
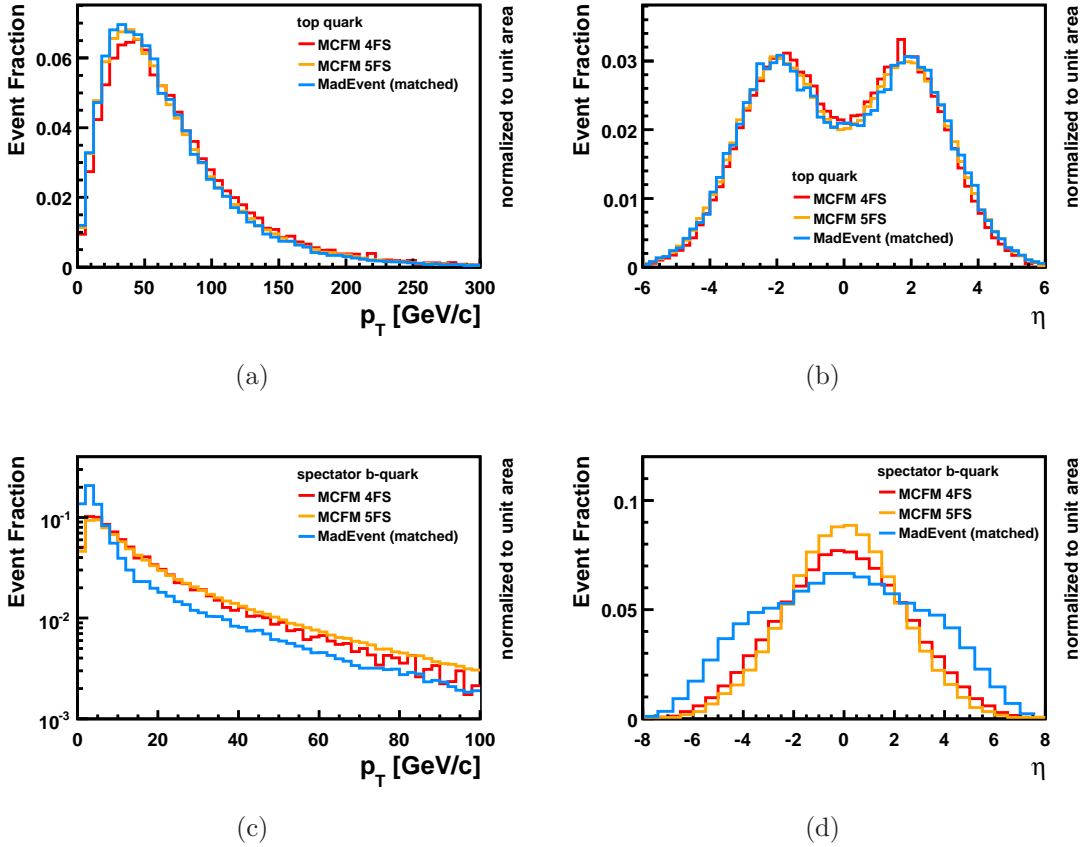**Figure 3.9:** Shape comparison of differential distributions obtained from the 4FS and the 5FS calculations of MCFM to the MG simulation of the *t*-channel $2 \to 3$ process for $\sqrt{s} = 10\,\mathrm{TeV}$. The transverse momentum and the pseudorapidity distributions of the top quark are shown in (a) and (b), while the corresponding distributions for the spectator *b*-quark are shown in (c) and (d).

In a next step, the shapes of the differential distributions obtained from the matched MG sample are compared to the two MCFM calculations. Figure 3.10 contains again the transverse momentum and pseudorapidity spectra for the top quark ((a) and (b)) and the spectator *b*-quark ((c) and (d)). The modeling of the top quark in the matched MG sample is very similar to the MCFM calculation, being more consistent with the 5FS than with the 4FS prediction. Concerning the spectator *b*-quark, the matched MG sample exhibits a significantly different behavior compared to the MCFM distributions. As described in the previous section, the matching takes into account a sizable amount of the $2 \to 2$ phase space, determined by the transverse momentum of the spectator *b*-quark being below the matching threshold K_T. In this approach, the spectator *b*-quark is modeled by the parton shower, meaning that this parton is obtained from a backward evolution of the initial state *b*-quark (see figure 3.2 (b)) by exploiting the DGLAP evolution scheme. Although this approach is not an exact perturbative calculation to a certain order

but a phenomenological modeling of the soft-p_T regime of the initial gluon splitting, the contribution is considered to be crucial for a preferably complete description of the spectator b-quark kinematics. The comparison shows that the transverse momentum spectrum of the spectator b-quark in the matched sample is significantly softer over the whole range, leading to a much stronger populated soft-p_T region. This fact is also reflected in the pseudorapidity spectrum being much broader for the matched MG distribution compared to the 4FS and 5FS calculations.

(a) (b)

(c) (d)

Figure 3.10: Shape comparison of differential distributions obtained from the 4FS and the 5FS calculations of MCFM to the matched MG simulations for $\sqrt{s} = 10\,\mathrm{TeV}$. The transverse momentum and the pseudorapidity distributions of the top quark are shown in (a) and (b), while the corresponding distributions for the spectator b-quark are shown in (c) and (d).

Since the matching of the two leading-order Born processes, $2 \to 2$ and $2 \to 3$, is based on the ZTOP calculation, the ZTOP predictions are also considered in the comparison. Although being conceptually similar, it is important to note that the treatment of the spectator b-quark mass is different in ZTOP than in the 5FS MCFM calculation. While the b quark is assumed to be massless in ZTOP, MCFM uses a finite mass for all final-state particles including the spectator b-quark. Therefore, ZTOP can only provide differential distributions for a spectator b-jet object above a certain momentum threshold, while the spectra obtained from MCFM describe

the particular parton in the full momentum range. The top quark, however, is expected to be modeled similarly, which is confirmed in figure 3.11 (a) and (b), showing a comparison of the transverse momentum and the pseudorapidity spectrum for the 5FS and the ZTOP calculation, as well as for the matched MG sample. Concerning the spectator *b*-quark, only the p_{T} spectrum is studied, since a cut on the pseudorapidity of $|\eta| < 5$ is imposed on the *b*-quark jets in the ZTOP calculation, whereas no such cut is applied in the MCFM calculations. However, comparing the p_{T} spectrum above a value of $20\,\mathrm{GeV}/c$, the differences due to the η cut are expected to be small. Figure 3.11 (c) shows a shape comparison in the p_{T} region above $20\,\mathrm{GeV}/c$ for the spectator *b*-quark modeled by ZTOP and MCFM 4FS and 5FS. As has already been observed above, the spectrum obtained from the 4FS calculation is slightly softer, due to the consideration of NLO effects on the spectator *b*-quark. However, comparing the rate of spectator *b*-quarks in this transverse momentum region, as shown in figure 3.11 (d), it turns out that the prediction from the 4FS is significantly higher, while the prediction obtained from the 5FS is consistent with the result of ZTOP. The corresponding rates are:

$$\sigma_{\mathrm{ZTOP}}^{\mathrm{spec.b}}|_{p_{\mathrm{T}}>20\,\mathrm{GeV}/c,|\eta|<5} = 24.1\,\mathrm{pb},$$

$$\sigma_{\mathrm{5FS}}^{\mathrm{spec.b}}|_{p_{\mathrm{T}}>20\,\mathrm{GeV}/c} = 24.9\,\mathrm{pb},$$

$$\sigma_{\mathrm{4FS}}^{\mathrm{spec.b}}|_{p_{\mathrm{T}}>20\,\mathrm{GeV}/c} = 34.0\,\mathrm{pb}\,.$$

These results suggest to reconsider the basis of the matching procedure described in the previous section. Instead of normalizing the transverse momentum spectrum of the spectator *b*-quark in the hard region to the rate obtained from ZTOP, the prediction obtained from the 4FS calculation might be used, accounting for NLO rate corrections of the spectator *b*-quark.

This comparison has shown that the 5FS calculations, ZTOP and MCFM, are consistent with each other and also with the matched signal modeling regarding the top quark. However, significant differences are observed for the spectator *b*-quark. Concerning the shape modeling, it could be shown that the MG $2 \rightarrow 3$ simulation is very close to the predictions of the 5FS calculation, both yielding transverse momentum spectra being slightly harder compared to the one obtained from the 4FS calculation. In addition, the predicted rate of the spectator *b*-quark is about more than 35% higher in the 4FS calculation than in the 5FS approaches. These differences might be considered as a systematic uncertainty in future analysis iterations by comparing the analysis result obtained from the matched signal sample to the result when the signal is simulated only by the MG $2 \rightarrow 3$ process.
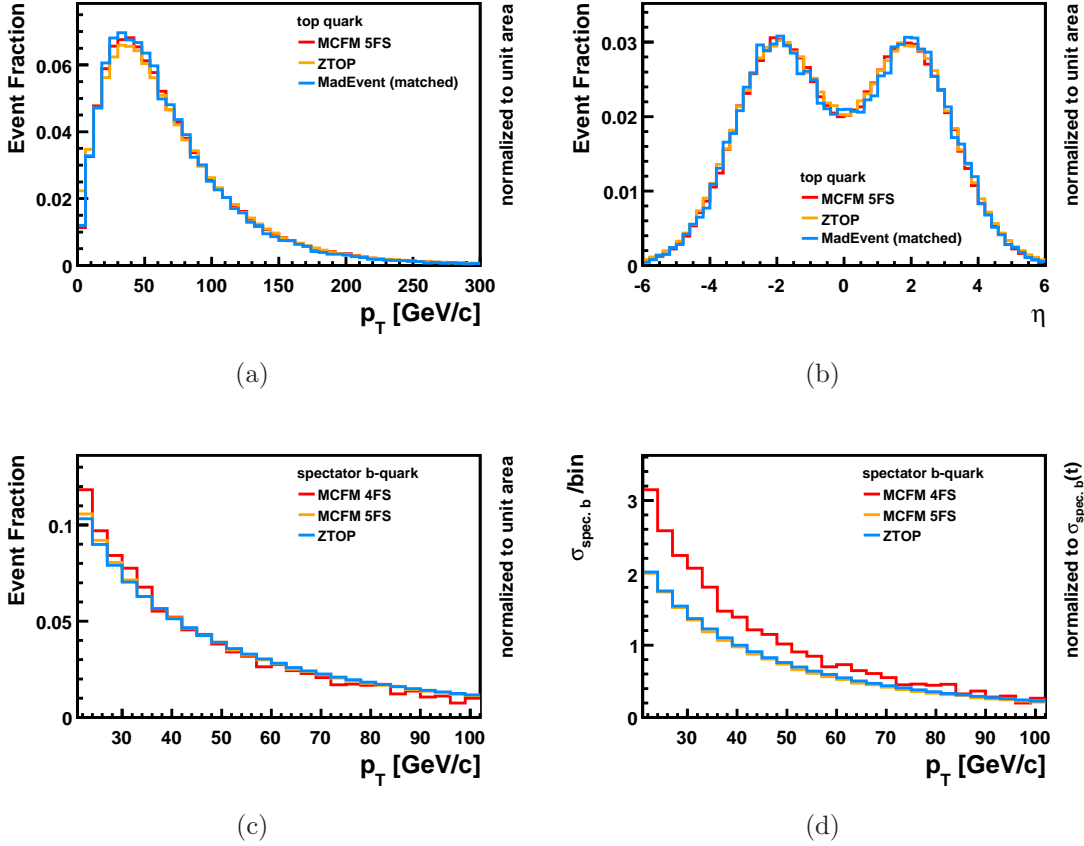
Figure 3.11: Shape comparison of differential distributions obtained from the 4FS and the 5FS calculations of MCFM to the matched MG simulations for $\sqrt{s} = 10 \, \text{TeV}$. The transverse momentum and the pseudorapidity distributions of the top quark are shown in (a) and (b). The shape of the transverse momentum distribution of the spectator b-quark is compared in (c), while the comparison of the same distributions normalized to the corresponding prediction is shown in (d).

Chapter 4

Object Reconstruction and Background Modeling

In order to obtain simulated event data which is comparable to the measured data of the experiment, the result of a MC simulation has to undergo a detector simulation, which models the interaction of the generated particles with the CMS detector. The outcome of the detector simulation is in the same format as data samples obtained from real collisions. In the next step, both the simulated events and events from collisions are evaluated in order to reconstruct physics objects like charged leptons or jets. The CMS offline software (CMSSW) provides all necessary modules for event simulation, reconstruction, detector calibration, and alignment related to the CMS experiment. The infrastructure is based on an event data model, which is capable to hold different types of data from MC simulations, raw detector readout, or reconstructed high-level objects needed for the physics analysis.

The reconstruction of the different objects which are relevant for the present analysis is reviewed in the first part of this chapter. The second part of the chapter briefly describes the modeling of the considered background processes.

4.1   Detector Simulation

To simulate the detector response of a list of particles, two different approaches are available within CMS, a full and a fast detector simulation. The full simulation is based on GEANT4 [103], a general toolkit for the simulation of the passage of particles through matter. It provides a rich set of physics processes describing electromagnetic and hadronic interactions in detail as well as tools for modeling the full CMS detector geometry and the interfaces required for retrieving information from particle tracking through the detectors and through the magnetic field.

Since the full simulation requires a large computing time in the order of minutes for a top-quark event, the approach becomes inconvenient if a large amount of MC events needs to be simulated. Thus, the CMS collaboration developed a fast simulation (FastSim) of the detector with event production rates 100–1,000 times faster than the GEANT4-based simulation, with comparable accuracy [104]. Being much faster than the full simulation, the FastSim provides a practical alternative

for use cases requiring the production of high-statistics or many different MC samples, for example to compare several MC data samples with systematically modified parameters. To achieve the good computing time performance, the FastSim uses a simplified detector geometry and a number of dedicated parametrizations, but contains all relevant material effects needed to describe the passage of particles through the detector. The validation of the FastSim output and the tuning of the parameters are both based on detailed GEANT-based simulations and on test-beam data.

As soon as real collision data arrive, the modeling performance of both detector simulations will be validated with these data, where the adaption of the FastSim will be more flexible and faster due to the parametrized ansatz of the model.

4.2   Object Reconstruction

In order to extract information about the underlying hard interaction of the measured event, the raw detector data obtained from real collisions or the detector simulation needs to be further processed. In a first step detector objects like the tracks of charged particles, calorimeter deposits, or muon track segments are reconstructed. Based on these input objects, physical objects like jets, electrons, or muons can be defined which are eventually used in the analysis to extract information about the original physics process.

4.2.1   Charged Particle Tracking

Charged particles traversing the tracker volume leave hits in the different tracker layers, which then have to be combined in order to reconstruct the trajectories of those particles. The combinatorial track finder (CTF) constitutes the default track finding algorithm in CMS. This algorithm is a Kalman filter (KF) based track finder [105], which uses the KF technique for both the trajectory building and for the estimation of the track parameters. The reconstruction of such a track contains several steps: track seeding, trajectory building, smoothing, and the final fit. For the track seeding, one needs to first identify the hits in the silicon pixel and strip detectors. Seeds are made out of a hit pair in the innermost layers plus a beam spot constraint or out of a hit triplet in the innermost layers, which are supposed to come from one charged particle track. A seed provides the initial trajectory parameters as starting point for the full track reconstruction.

Pattern recognition methods based on KFs are then applied to the seeds in order to build trajectory candidates. The filter proceeds iteratively from the innermost seed layer, starting from a coarse estimate of the track parameters provided by the seed and including the information of the successive detection layers one by one. The trajectory is extrapolated according to the equation of motion of a charged particle in a magnetic field, accounting for multiple scattering and energy loss in the traversed material. Hits are looked for in a window whose width is related to the precision of the track parameters. If a hit is found in the expected position it is added to the candidate trajectory and the track parameters are updated. As hits are added, the knowledge of the track parameters improves and the size of the

search window decreases when propagating to the next surface. Several hits on the new layer may be compatible with the predicted trajectory, yielding a variety of new trajectory candidates. In addition, trajectory candidates are created, in which no measured hit is used, to account for the possibility that the track did not leave any hit on that particular layer. If more than one consecutive hit is not found in the predicted position the trajectory is rejected as a fake and is not further propagated. All resulting trajectory candidates are then grown in parallel to the next compatible layers, until either the outermost layer of the tracker volume is reached or a stopping condition is satisfied. Ambiguities of track candidates arise because one particle track may be reconstructed starting from different seeds or because a given seed may result in more than one trajectory candidate. Such ambiguities are resolved during and after the track finding stage. For any two tracks sharing more than 50% of their hits the one with the lower number of hits, or, in case of equal number of hits, the one with the higher χ^2 value is discarded.

In order to avoid a potential bias of the track parameter estimation by constraints applied during the seeding, the last stage consists of a least-squares fit in the form of a KF for the final estimation of the track parameters. A forward fit proceeding outwards from the interaction region removes the approximations used in the track finding stage and provides an optimal estimate of the track parameters at the outside of the tracker. A final smoothing of the track candidate is achieved by a backward fit in the opposite direction, which yields the estimate of the track parameters in the interaction region and, in combination with the forward fit, at each of the intermediate layers.

An important characteristic of a track is the impact parameter (IP), which is defined as the distance between the track and a reference. Usually, this reference is given by a vertex or a jet axis. The IP can be computed either in the plane transverse to the beam axis or in three dimensions. For both the transverse and the three-dimensional IP, the computation is performed starting from the particle trajectory parameters at the innermost measurement point. In case of the transverse IP, the estimate can be done analytically since the trajectory is circular in the transverse plane. In the three-dimensional case, the extrapolation is performed iteratively.

Considering a vertex as reference, the IP is simply calculated as the distance between the track and the reference vertex at the point of closest approach. The distance of a track to a reference axis like a jet axis, however, is determined as follows. First, the point of closest approach (S) of the track to the reference axis is extracted, then the track is linearized at that point and the minimum distance of the linearized track to the origin of the reference axis (V) is computed. This procedure of the IP computation for a single track with respect to a reference axis is depicted in figure 4.1.

Given that the uncertainty of the IP can be of the same order of magnitude as the IP, a better observable is the IP significance defined as the IP divided by its uncertainty σ_{IP}.
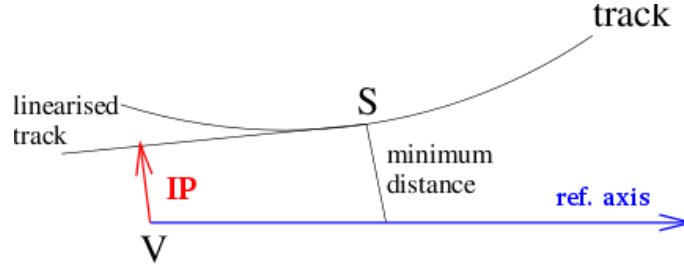
Figure 4.1: Schematic representation of the three-dimensional impact parameter (IP) calculation of a single track with respect to the vertex (V) in three dimensions [106].

4.2.2   Vertex Reconstruction

Reconstructing the primary vertex (PV) in order to identify the position of the underlying hard proton-proton interaction in the event is of particular interest for the evaluation of the reconstructed physics objects. Given a set of tracks, algorithms are used to determine the best estimate of the vertex parameters, as well as indicators for the vertex fit quality. The reconstruction of the PV involves two steps, the vertex finding and the vertex fitting. For the vertex finding, tracks are grouped into vertex candidates.

The algorithms used are different, depending on the physics case. In certain cases where speed is an important requirement and the highest possible efficiencies are not a key issue, as for the HLT, a fast track reconstruction can be performed. It is based on pixel hits and provides the HLT with a fast PV position measurement. In order to achieve the required speed the process is reduced to a one-dimensional search along the z axis. Hits found in three different layers of the pixel detector are clustered into triplets, which can be converted into tracks without further propagation into the tracker.

The PV finding using fully reconstructed tracks provides a precise estimation of the vertex position. Input for the PV reconstruction are tracks that pass a set of dedicated quality cuts. The tracks have to be reconstructed with at least seven hits in the silicon tracker and at least two hits in the pixel tracker. The χ^2 of the track fit, normalized to the number of degrees of freedom, has to be smaller than 5.0. A cut of 5.0 on the maximum IP significance with respect to the beam spot is applied in order to reject tracks which are not compatible with the primary interaction point of the event. Based on this collection, clusters of tracks are formed by considering the z coordinate of their point of closest approach with respect to the beam line.

A fit of all the PV candidates for each of these clusters is performed, respecting a separation in z of at least $1\,\mathrm{mm}$ between single clusters. Several algorithms are available, differing mainly in their sensitivity to outlying tracks, that is, either mismeasured tracks or tracks from another vertex. They can be divided into linear algorithms like the KF and non-linear algorithms like the adaptive vertex fitter (AVF) [107], the latter being more robust with respect to outlying tracks. Finally, poor fits and vertex candidates incompatible with the beam line are excluded. The distance between the resulting vertices and the beam spot must not exceed $0.2\,\mathrm{mm}$

and the fit probability has to be at least 1%. For each vertex candidate, the scalar p_T^2 sum of the associated tracks is calculated. In the present analysis the vertex with the highest value is selected as PV of the hard proton-proton interaction. The resolution of the PV reconstruction, as well as the whole track reconstruction methods, depends crucially on the alignment of the tracking detector components. Several resolution studies are performed in [76]. Assuming a perfectly aligned detector, the resolution of the decay length $c\tau$ in three dimensions was found to be 40.6 μm for the KF approach, whereas the AVF yields 37.4 μm. Studying different standardized misalignment scenarios, the resolution is degraded by about 10 μm.

4.2.3 Muon Reconstruction

The physical muon objects are reconstructed in a multi-faceted way, with the final collection being comprised of three different muon types, stand-alone, global, and tracker muons. Since each sub-detector is able to measure a part of a muon's property, the concept of a global muon is to combine the information from multiple sub-detectors in order to obtain a more accurate description of the muon. For this purpose, stand-alone muons reconstructed from muon system information and the interaction point are combined with tracks reconstructed in the silicon tracker featuring the full tracking resolution. The resulting combined muon object is called global muon. A complementary approach is the reconstruction of so-called tracker muons, where all silicon tracker tracks are considered and muon objects are identified by looking for compatible signatures in the calorimeters and in the muon system. This class of muon objects is basically used in cases where the muons do not leave enough hits in the muon spectrometer to be reconstructed as a stand-alone muon, which happens typically for muons below a transverse momentum of 6–7 GeV/c. Since muons considered in the present analysis are produced at much higher transverse momenta, the explanation of tracker muons is omitted in here. A detailed review of muon reconstruction in CMS for all three categories can be found in [108].

Stand-alone muons are obtained by evaluating the information of the muon systems (RPC, CSC, DT). Chambers compatible with a given seed are identified and a local reconstruction is performed only in these chambers. Hits within the individual chambers are matched to form track segments. Starting from the innermost muon station, KF techniques are used to combine the different track segments and hits from all muon detectors to form stand-alone muon tracks. For this purpose, the state of the track is propagated from one muon station to the next taking into account the muon energy loss in the material, effects of multiple scattering, and the non-uniformity of the magnetic field in the muon system. A suitable χ^2 cut is applied in order to reject bad hits, mostly due to showering and pair production. The procedure is repeated until the outermost measurement surface of the muon system is reached. A backward KF is applied working from the outside in to define the track parameters at the innermost muon station. Finally, the track is extrapolated to the nominal interaction point and a final vertex-constrained fit to the track hits is performed.

In a next step stand-alone muons are extended to include the silicon tracker

information from both pixel and strip detectors, yielding global muons. First, the silicon tracker tracks to combine with the stand-alone muon track have to be identified. The large multiplicity of tracks in the central tracker necessitates the selection of a subset of tracker tracks that roughly correspond in momentum and position to the stand-alone muon track. The method of track matching proceeds in two steps. First, a region of interest is identified and a subset of tracker tracks that are in this region are selected. In a second step, the subset of tracker tracks is iterated applying more stringent spatial and momentum matching criteria to choose the best tracker tracks to combine with the stand-alone muon.

Finally, a global fit is performed on the combined hits from the silicon tracker with those in the muon system originally forming the stand-alone tracks. The global fit algorithm attempts to perform a track fit for each pair of tracker track and stand-alone muon track. If there is more than one possible global muon track resulting from the fit of track pairs, the global muon track with the best χ^2 is chosen. Thus, for each stand-alone muon there is a maximum of one global muon that will be reconstructed.

The resolution for the reconstruction of low- and high-p_{T} muons is summarized in table 4.1. For soft muons the resolution measured in the muon system is limited by multiple scattering in the iron yoke, whereas the resolution for high-p_{T} muons is limited by the resolution of the muon chambers, even if the tracker is taken into account. Analyzing cosmic muon data recorded during the CRAFT run, the momentum resolution of global muons has been found to be better than 2% at low p_{T} values below $200\,\text{GeV}/c$ and of about 8% at values around $500\,\text{GeV}/c$ [109]. Since these resolution values have been obtained with the initial CRAFT-based alignment of the tracker and the muon chambers, they are expected to improve further as collision data are considered.

Muon p_{T} [GeV/c]	Stand-Alone Muons $\Delta p_{\text{T}}/p_{\text{T}}$ [%]	Global Muons $\Delta p_{\text{T}}/p_{\text{T}}$ [%]
10	$8-15$	$0.8-1.5$
1,000	$16-53$	$5-13$

Table 4.1: Resolution of the transverse momentum of the muons using the stand-alone and the global muon reconstruction [110].

Muon Identification

In this analysis, we are interested in muons stemming from the final state of the hard interaction. Global muons reconstructed as described above, however, might also originate from decays of secondarily produced particles like kaons or pions, so-called decay-in-flight muons, or from the decay of B mesons. In addition, high-energetic hadrons which were not stopped in the HCAL might penetrate the muon chambers and lead to the mismeasurement of so-called punch-through hadrons as muons.

In order to suppress such fake muons, an identification (ID) is defined for global muon candidates. It was found that the normalized χ^2 of the global muon fit is a powerful observable to reject both decay-in-flight and punch-through muons. The *global tight prompt muon* ID, used for the selection of muons in the present thesis, contains a cut on the global normalized $\chi^2 < 10$.

Additional track quality cuts like on the IP of the silicon- or the global-track fit, on the normalized χ^2 of the silicon-track fit only, or on the number of hits of the silicon-track fit can further improve the rejection of fake muons. Another general difference between the muon classes is the penetration of the detector. High-p_{T} muons are expected to penetrate deeper into the muon detector. Thus, only very few reconstructed tracks of primary muons end in the first layer of the barrel detector, while this happens quite often for decay-in-flight and punch-through muons. More details of the muon identification are documented in [111].

4.2.4 Electron Reconstruction

Electrons produced at the interaction point leave mainly two distinct footprints when traveling through the detector. As they are charged particles, their track can be reconstructed in the tracker and they deposit energy in the ECAL in the form of electromagnetic showers. However, the reconstruction of electrons is hampered by the amount of tracker material which is discretely distributed in front of the ECAL. Due to the presence of material on the way from the primary interaction point to the calorimeter, the electrons radiate bremsstrahlung photons which induce photon conversions in the tracker material. The average amount of bremsstrahlung depends on the amount of penetrated tracker material, which varies strongly with η. Rising from $\sim 0.3\,\mathrm{X}_0$ at central pseudorapidities to $\sim 1.5\,\mathrm{X}_0$ towards the edge of the barrel ($|\eta| \sim 1.5$) and falling back to $\sim 0.7\,\mathrm{X}_0$ in the endcaps at $|\eta| \sim 2.5$.

In the presence of the magnetic field, the radiated energy is deposited in the ECAL with spread in ϕ. This spread is considered by building a cluster of ECAL clusters, a so-called supercluster (SC), which is extended in ϕ. A primary-electron candidate is thus composed of a single track emerging from the interaction vertex, matched to an electromagnetic supercluster, measured in the angular range $|\eta| < 2.5$ and for $p_{\mathrm{T}}^e \geq 5\,\mathrm{GeV}/c$.

The building of electron objects is initiated by the presence of electromagnetic SCs above the seeding threshold $E_{\mathrm{T}}^{\mathrm{seed}} = 1\,\mathrm{GeV}$. These SCs are used to drive the finding of pixel seeds for the primary electron tracks. Two identified pixel hits serve as seeding for the building and fitting of electron tracks in the silicon tracker. Bremsstrahlung emissions introduce largely non-Gaussian event-by-event fluctuations which affect the energy measurement in the ECAL and the momentum measured in the tracker, as well as electron identification observables. Therefore, dedicated track reconstruction and clustering strategies are required to better cope with these effects. The applied fitting method is based on a non-linear filter approach, a Gaussian Sum Filter (GSF) [112], that can better describe the propagation of electrons than the linear KF methods. A great benefit of using GSF tracks is that meaningful track-parameter uncertainties are available at both ends of the track.

This allows for a good estimation of the electron-track parameters at the ECAL entrance. Most importantly, the fractional amount of momentum carried away by bremsstrahlung photons can be evaluated from the outer- and innermost track parameters.

Electron Identification

A good identification of electron candidates is important in order to suppress fake electrons as efficiently as possible. The fact that electron identification variables exhibit different characteristics for different electron classes leads to the development of a category-based electron ID. The electrons are categorized according to the estimate of energy fraction emitted by bremsstrahlung in the tracker material, f_{Brem}, and the ratio of the energy E collected in the ECAL to the momentum p_{in} of the electron track at the vertex, E/p_{in}.

The physics motivation behind this kind of classification is based on the different behavior of real electrons and fake electrons, mainly induced by charged pions. For electrons the fraction E/p_{in} is most likely measured with a value close to one, whereas charged pions most likely imply $E/p_{\mathrm{in}} < 1$, partly because of the low response of the ECAL to charged pions. Concerning f_{Brem}, electrons usually radiate a significant fraction of energy in the tracker, whereas fake electrons caused by jets have f_{Brem} around zero. Based on the parameter space described by these two variables, three different categories are defined: category 0 describes an electron-like region with little contamination from fakes, category 1 contains a region with a high population from both real and fake electrons, and category 2 covers a region strongly dominated by fake electrons.

The selection of electron candidates in the different categories is performed with cuts on the following five quantities:

- H/E: ratio of the energy deposit in the HCAL (H) and the ECAL (E)

- $\sigma_{\eta\eta}$: a shape variable measuring the η extend of the electron supercluster

- $\Delta\eta_{\mathrm{in}}$ / $\Delta\phi_{\mathrm{in}}$: the difference in η / ϕ between the electron track as parametrized at the vertex, extrapolated in the magnetic field to the ECAL surface under the assumption of no bremsstrahlung, and the actual SC position

- $E_{\mathrm{seed}}/p_{\mathrm{in}}$ the ratio between the energy of the supercluster seed and the electron track momentum measured at the vertex

Different sets of cuts can be used for each category, tuned to the expected signal-over-background ratio. Depending on the selection efficiency and the corresponding fake rejection a loose and a tight selection are distinguished. In addition, two distinct sets of thresholds are used in each selection for barrel and endcap objects.

Only electrons which fulfill the tight criteria are considered in the analysis presented here, the corresponding thresholds are listed in table 4.2. In addition to the above discussed electron categories, the cut threshold on the variable $\Delta\phi_{\mathrm{in}}$ is explicitly loosened for electrons with a value of E/p_{in}. More details on the different electron identification methods can be found in [113].

Variable		Category 0	Category 1	Category 2	$E/p_{\mathrm{in}} > 1.5$
H/E	(barrel)	0.05	0.042	0.045	-
	(endcap)	0.055	0.037	0.05	-
$\sigma_{\eta\eta}$	(barrel)	0.0125	0.011	0.01	-
	(endcap)	0.0265	0.0252	0.026	-
$\Delta\eta_{\mathrm{in}}$	(barrel)	0.005	0.003	0.0065	-
	(endcap)	0.006	0.0055	0.0075	-
$\Delta\phi_{\mathrm{in}}$	(barrel)	0.032	0.016	0.0525	0.09
	(endcap)	0.025	0.035	0.065	0.092
$E_{\mathrm{seed}}/p_{\mathrm{in}}$	(barrel)	0.24	0.94	0.11	-
	(endcap)	0.32	0.83	0.0	-

Table 4.2: Upper thresholds for the discriminating variables used in the tight electron identification. For each electron category, two different sets of cuts are used, for the barrel and endcap region, respectively. For electrons with $E/p_{\mathrm{in}} > 1.5$ the cuts for the variable $\Delta\phi_{\mathrm{in}}$ are loosened.

4.2.5   Jet Reconstruction

Since color-charged partons are confined, only collimated streams of color-neutral objects can be observed by the detector. In order to link these streams to the energetic partons created in the hard process, the concept of jets is introduced. A jet is defined as the cluster of all particles which are supposed to originate from the same initiator. The structure of jet evolution with the different levels of modeling is illustrated by a sketch shown in figure 4.2. The goal of the jet reconstruction is to give an estimate of the four-vectors of the final-state quarks and gluons of the hard interaction. Thus, it tries to reverse the hadronization process to extract information about the underlying hard process. The input for a jet algorithm can be any set of four-momentum-vector like objects. If the reconstruction is done based on calorimeter towers, the resulting jets are called CaloJets, whereas so-called GenJets are obtained from the input of stable particles of the hadronization simulation of an event.

Besides a good correspondence to the parton level and hadron level, a well-behaved jet-cluster algorithm should fulfill two important requirements. It should be collinear-safe, such that the outcome remains unchanged if the energy carried by a single particle is instead distributed among two collinear particles. Collinear safety is typically endangered if the jet finding is based on energetic seeds and a threshold is applied to these seeds. Secondly, the algorithm should be infrared-safe, which means that the result of the jet finding should be stable against the addition of soft radiations. This is motivated by the large probability of additional soft gluon emissions in a hadron shower, the possibility of additional soft contributions from the underlying event, and instrumental contributions such as calorimeter noise. Different algorithms have been developed for the clustering of particles. The two main
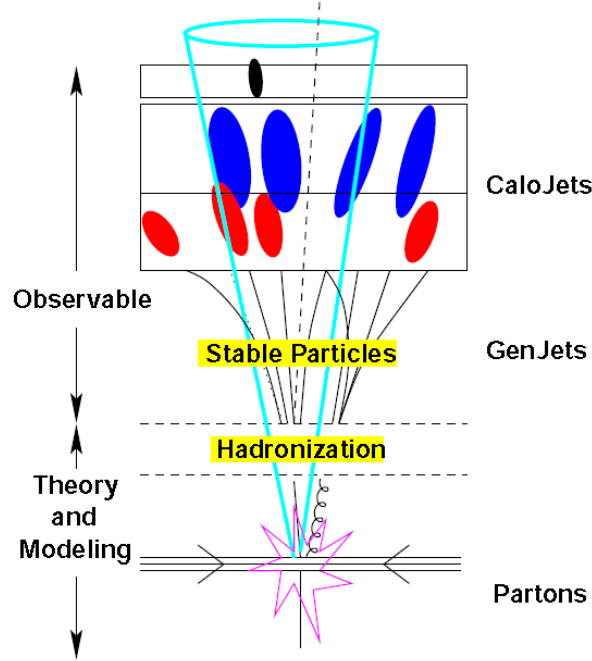
Figure 4.2: Sketch of the structure of jet evolution. The hard process and the subsequent hadronization of the produced colored partons are described by theory and dedicated models, respectively. Stable particles penetrating the detector outwards deposit their energy in the calorimeters. Jet reconstruction algorithms are applied to the calorimeter objects in order to obtain an estimate for the jet inducing parton from the hard process [114].

concepts are briefly described below.

Cone Algorithms: The iterative cone algorithm [115] starts with a list of particles ordered by their transverse momentum. The largest transverse momentum object is taken as seed and all objects within a cone with fixed radius R in the $\eta - \phi$-plane are merged to a so-called proto-jet. The energy and direction of this proto-jet can be calculated as:

$$
\begin{aligned}
E_\mathrm{T} &= \sum_i E_\mathrm{T}^i \,, \\
\eta &= \frac{1}{E_\mathrm{T}} \sum_i E_\mathrm{T}^i \eta_i \,, \\
\phi &= \frac{1}{E_\mathrm{T}} \sum_i E_\mathrm{T}^i \phi_i \,,
\end{aligned}
\tag{4.1}
$$

which is called E_T recombination scheme. The direction of this jet is taken as seed for the next proto-jet and this procedure is iterated until a defined ending criterion is reached. This may be that the change of the proto-jet axis or of the energy is below a certain threshold or that the maximum number of iterations has been performed. The result is a stable proto-jet which is added to the list of reconstructed jets. After having removed all constituents of this jet from the list of objects to cluster, the next

proto-jet is build on the remaining objects. This is repeated until the input list does not contain any object above a certain threshold. The energy and the momentum of the resulting jet object is defined as the sum of energies and momenta of its constituents, which is known as the E recombination scheme. However, as this cone-based algorithm uses seeds above a certain threshold it is not collinear safe.

Improvements for cone algorithms can be achieved by looking for all stable cones in an event. The main problem is that a straight-forward algorithm would test all subsets of N input objects for stability, which requires computing time exponentially growing in N. The SisCone algorithm provably finds all stable cones in the event with a reasonable runtime behavior and ambiguities in the object assignment to a jet are solved by a split-and-merge procedure described in [116]. As a result of this procedure, the algorithm becomes infrared- and collinear safe to all orders of perturbative QCD.

K_{T} **Like Algorithm:** The second class of algorithms, pairwise recombination algorithms, are not based on a fixed geometrical shape of the jet and thus both infrared and collinear safe. Starting with a set of input objects, for each object i the distance to each object j is calculated, as well as the distance to the beam. The size of the jets is controlled by the resolution parameter D, which depends on the geometrical distance ΔR and on the energy of the input object. The distance between the different input objects is then defined as $d_{i,j} = \min(p_{\mathrm{T}i}^{2n}, p_{\mathrm{T},j}^{2n}) \cdot \Delta R_{i,j}^2$ and the distance of an input object to the beam as $d_{i,\mathrm{B}} = p_{\mathrm{T},i}^{2n} \cdot D^2$. The different algorithms vary in the choice of the parameter n. The standard K_{T} algorithm [117] uses $n = 1$, whereas the anti-K_{T} algorithm [118] is defined with $n = -1$ and the Cambridge-Aachen algorithm [119] with $n = 0$. If the smallest distance found is between two objects, these are removed from the list and the merged object is added and the procedure is repeated. If the smallest found distance is the one to the beam, the object is removed from the input list and added to the list of jets. This procedure is repeated until all objects are included in reconstructed jets.

Although the cone algorithms are known not to fulfill the infrared and collinear safety requirements, they constitute the basic class of algorithms having been applied to real collision data so far, because of its comparably moderate computing time consumption. For the studies presented here, CaloJets are considered which are reconstructed by the iterative cone (ICone) algorithm using a cone size of $R = 0.5$, which has been the standard setting used by the collaboration at the time. A comparison between jets reconstructed by the ICone and SisCone algorithm has not shown an observable impact on the analysis result.

Jet Energy Corrections

As mentioned above, the jet reconstruction tries to link properties like momentum and energy of the jet to the underlying parton. Clustering the deposited energy in jet objects is the first step towards such an estimate. However, several corrections need to be applied to the obtained jet objects in order to improve the description. The CMS collaboration developed a factorized multi-level jet energy

correction scheme [120], in which the corrections are applied in the following fixed sequence:

- **Offset corrections:** Pile-up of multiple proton-proton collisions per bunch crossing and electronic noise in the detector produce an energy offset. The goal of the offset correction is to subtract, on average, this unwanted energy from the measured jet energy.

- **Relative (η) and absolute (p_T) corrections:** Since the calorimeter system of CMS is not a homogeneous entity, the calorimeter response, defined as the average calorimeter signal divided by the energy of the particle that caused it, is not uniform over the whole calorimeter space. The jet response varies as a function of jet η for a fixed p_T as well as a function of the jet p_T. The relative corrections are applied in order to remove these variations and make the jet response flat as a function of η. In addition, the p_T dependent corrections make the energy response equal to unity at all transverse momentum values in the control region $|\eta| < 1.3$.

This set of basic jet energy corrections (JEC) covers different instrumental sources of mismeasurements. Thus, they provide the complete correction of a measured Calo-Jet back to the GenJet level. As an example, the impact of the relative correction of the η response, evaluated on MC simulation data, is shown in figure 4.3, for both low-momentum (a) and high-momentum (b) jets. Only the relative and absolute JEC are applied to the objects of the jet collection used in the present thesis.

All these corrections can be directly determined with measured collider data. For the offset energy corrections, calorimeter noise measurements and the estimation of pile-up from zero bias events can be exploited. The most common technique for the relative and absolute corrections is to use the conservation of transverse momentum, known as p_T balance, in $2 \rightarrow 2$ processes. Here, at least one of the two final state objects is a jet whose response is measured relative to the other final state object which serves as reference. There are plans to employ the p_T balance in dijet events, photon+jet events, and Z+jet events [120].

Additional corrections can be applied in order to extract a better estimate for the momentum and energy of the underlying parton from the GenJet level. The JEC concept of CMS foresees the following optional corrections, which were not considered in the present studies. EMF corrections account for variations in the jet response with the electromagnetic energy fraction. Flavor corrections are intended to correct a jet to the particle level assuming that the jet originated from a specific parton flavor. This is motivated by the fact that, for example, light quarks (u, d, s) have higher energy responses than gluons because the former radiate less and thus fragment into higher momentum particles. UE corrections consider additional energy deposits due to the underlying event activity. Parton corrections eventually provide the correction from the GenJet to the parton level. Again, this correction depends on the parton flavor. Gluons, typically radiating more than light quarks, have a lower GenJet response because more final state radiation falls outside the jet area. The correction can be determined from MC simulations for dijet events, but it is model and process dependent.

(a)   (b)
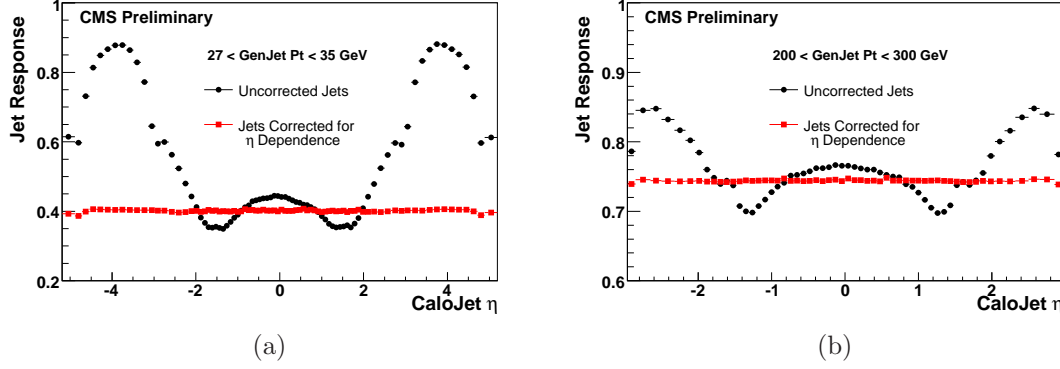
Figure 4.3: The jet response, defined as $p_T^{\text{CaloJet}}/p_T^{\text{GenJet}}$, versus the pseudorapidity of the CaloJet both before and after the η dependent jet corrections [120] have been applied: for GenJets with $27 < p_T < 35\,\text{GeV}$ (a) and for GenJets with $200 < p_T < 300\,\text{GeV}$ (b). The circular marks indicate the jet response for uncorrected jets, where a strong dependence of the response on η is observed. This dependence can be compensated by applying the relative JEC, which yields the flat response function indicated by the rectangles. The position of the flat curve represents the mean response of the central calorimeter covering $|\eta| < 1.3$. Applying in addition the p_T dependent absolute corrections, a jet response can be obtained which is flat in p_T and equal to unity.

4.2.6 Missing Transverse Energy

Considering a collision event where the two incoming objects have only longitudinal momentum, the 2D-momentum in the transverse plane perpendicular to the direction of the incoming beams compensates due to momentum conservation. The presence of weakly interacting particles like neutrinos or the lightest supersymmetric particle, which leave the detector without interacting with the material, leads to an imbalance in the transverse energy measured in the calorimeter. A measure for this imbalance is the missing transverse energy determined from the transverse sum over uncorrected energy deposits in projective calorimeter towers:

$$\mathbf{E}_T^{\text{miss}} = -\sum_{n=1}^{N} \left(E_n \sin\theta_n \cos\phi_n \hat{\mathbf{x}} + E_n \sin\theta_n \sin\phi_n \hat{\mathbf{y}} \right), \tag{4.2}$$

where the index n runs over all calorimeter input objects and $\hat{\mathbf{x}}, \hat{\mathbf{y}}$ denote the unit vectors in the direction of the x and y axis.

Besides the missing transverse energy caused by weakly interacting particles several other effects can contribute to the measured E_T^{miss}. Muons traverse the calorimeter system as minimal ionizing particles, depositing on average only a few GeV of their energy, and thus disturbing the transverse balance of the event. Since the active regions of the CMS detector do not cover the full 4π solid angle, interaction products which move in the very forward direction close to the beam line might escape undetected. In addition, detector malfunctions, dead areas, or particles hitting poorly instrumented regions of the detector contribute to the imbalance.

E_T^{miss} Corrections

Corrections to the missing transverse energy [121] as calculated in equation 4.2 aim to bring the measured value closer to the true one which is assumed to be due to the occurrence of weakly interacting particles in the event. They are applied on an event-by-event basis and help to improve the resolution. Two sets of corrections are required:

- **Type-I correction:** The measured raw energy values are adjusted for the difference between the raw jet energy and the true jet energy. Thus, the correction is also known as jet-energy-scale correction. The corrected missing-transverse-energy vector is given by:

$$(\mathbf{E}_T^{miss})_{corr} = \mathbf{E}_T^{miss} - \sum_{i=1}^{N_{jets}} (\mathbf{p}_{T,i}^{corr} - \mathbf{p}_{T,i}^{raw}) \,. \tag{4.3}$$

  The CMS calorimetry system is non-compensating, which means that its response to neutral and charged pions is very different. This can be taken into account by considering the fraction of jet energy deposited in the ECAL (EMF) when deriving the type-I corrections. As a consequence, only jets below a certain EMF threshold and with a transverse momentum larger than $10\,\mathrm{GeV}/c$ are taken into account for the type-1 corrections, as the JEC for low-momentum jets are known to have large uncertainties.

- **Muon corrections:** As a muon is a minimal ionizing particle over a wide range of particle momenta, it deposits only a small amount of energy in the calorimeter and can thus erroneously contribute to $\mathbf{E}_T^{miss}$. The correction for the muon response is based on the muon momentum measurement from the central tracker and the muon system. In order to correct for the muons, the transverse momenta of all muons in the event are subtracted vectorially from the $\mathbf{E}_T^{miss}$ vector after the deduction of the energy deposition of the muons in the calorimeter towers, labeled as "MuDepTow":

$$(\mathbf{E}_T^{miss})_{corr} = \mathbf{E}_T^{miss} - \sum_{j=1}^{N_{muons}} \mathbf{p}_T^j + \sum_{k=1}^{N_{MuDepTow}} \mathbf{E}_T^k \,. \tag{4.4}$$

Missing-transverse-energy objects used in the present analysis are corrected as type-I and for muons. Additional corrections are intended in order to account for effects due to the soft underlying event and pile-up contributions, but not applied here. Understanding the structure of the observed missing transverse energy and the contributions of different instrumental sources is an important task for the analysis of first collision data.

4.2.7 b-Tagging

For many physics processes it is crucial to identify b-hadron jets, a process known as b-tagging, in order to suppress large background contributions involving light-quark or gluon jets. Many different properties, like the long lifetimes τ, the high masses of the B hadrons, or a relatively high fraction of semileptonic decays distinguish these jets from those originating from gluons and light quarks. A number of b-tagging algorithms have been developed, ranging from comparatively simple and robust approaches to complex multi-variate techniques extracting lifetime and kinematic information. An overview of the different algorithms and their performance on simulated events is studied in [106]. Each algorithm is based on at least one b-tagging observable which discriminates between b, c, and light-quark jets, where light includes jets originating from u, d, s quarks, or gluons.

Tracks are the most powerful ingredient to b-tagging. The most discriminating single-track observable is the IP, which is the distance between the track and the PV at the point of closest approach (see figure 4.1). For B hadrons with a finite lifetime, the typical scale of the IP is set by $c\tau \sim 480\,\mu\text{m}$. The IP is a lifetime-signed quantity, where the sign is obtained from the sign of the scalar product of the IP segment with the jet direction. A sign flip can happen due to differences between the reconstructed jet axis and the true flight direction of the b hadron, caused by the mismeasurement of tracks. For decays without a sizable lifetime, the signed IP significance is expected to be symmetric around zero. For B hadrons decaying weakly, it is mostly positive.

The b-tagging algorithm used in the present analysis is based on the signed IP significance. Tracks associated to a jet are ordered by decreasing $\text{IP}/\sigma_{\text{IP}}$ and the value of the Nth track is used as a discriminating variable. If one is interested in a high efficiency for b-jets, the second track can be used, thus called track counting high efficiency (TCHE) algorithm. In order to obtain a high-purity selection, the third track is a better choice, and the method is called track counting high purity (TCHP). The discriminator values obtained in this way are shown in the upper part of figure 4.4 for different parton-flavor jets. The typical asymmetric behavior of the IP for long-lived hadrons is clearly visible in these distributions.

In order to quantify the quality of a certain b-tagging algorithm, two different kinds of efficiencies are considered: the efficiency of identifying real b-hadron jets and the efficiency of misidentifying light-quark jets as b-hadron jets, which is known as the mistag rate. In the lower part of figure 4.4 the correlation between the two efficiencies for both the TCHP (a) and TCHE (b) algorithm are shown. By nature, these two parameters compete and one has to find an adequate compromise suiting best the analysis purposes.

As a useful reference, the b-tagging physics object group (POG) of CMS determines dedicated working points (WP) for all the available algorithms and for each new setup of event simulation. Three WP are distinguished: loose, medium, and tight. The discriminator value of each WP corresponds to a fixed value of the mistag rate. Considering a mistag rate of 10% yields the loose WP, a mistag rate of 1% corresponds to the medium WP, and the tight WP is obtained by requiring a mistag rate of 0.1%. Table 4.3 summarizes the WP recommendations of the b-tagging POG

(a)

(b)

(c)

(d)
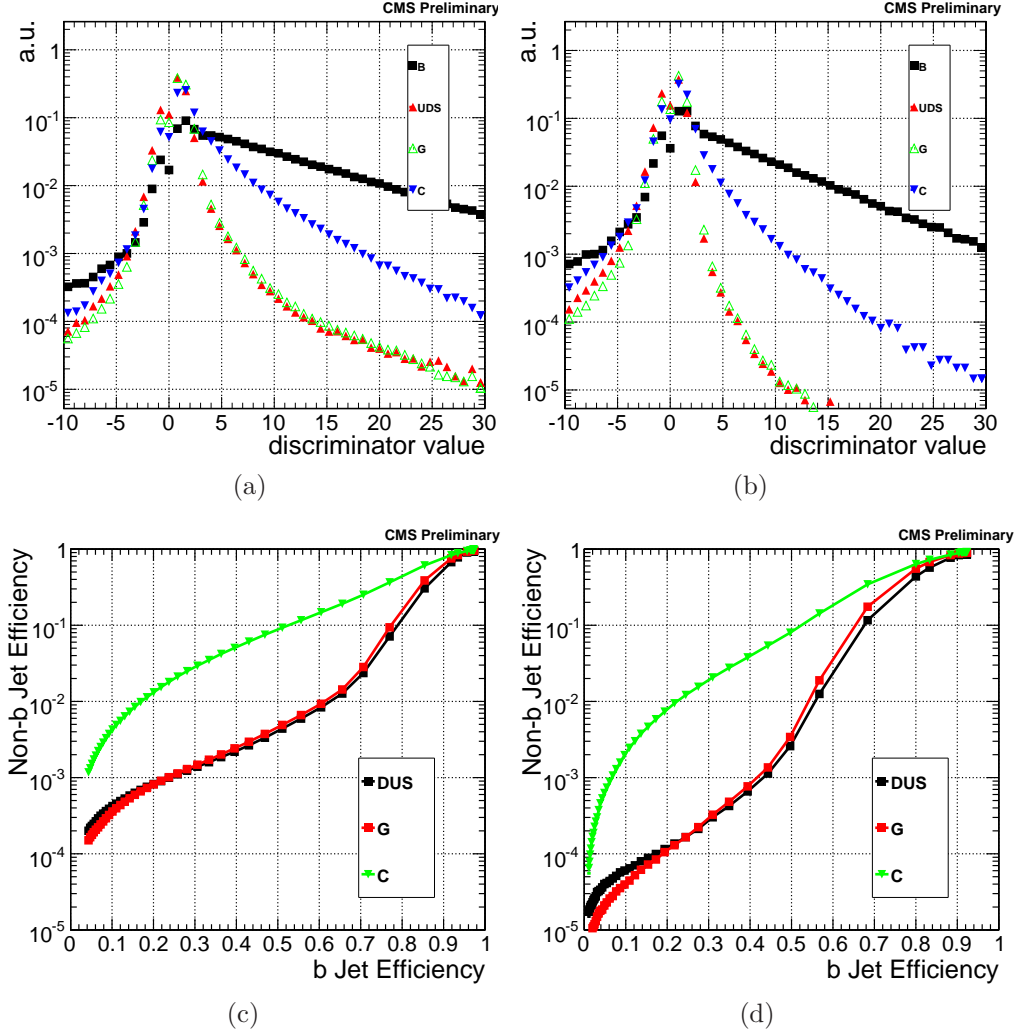
Figure 4.4: The upper row contains the normalized distribution of the discriminator for the track counting high efficiency algorithm (a) and for the track counting high purity algorithm (b), for different jet flavors. The values are extracted from a QCD sample requiring $\hat{p}_T > 80\,\text{GeV}/c$, at least one corrected jet with $p_T > 20\,\text{GeV}/c$, and all reconstructed jets to be within $|\eta| < 2.4$. [106]

In the lower row are shown the mistag rate versus the efficiency for the track counting high purity (c) and track counting high efficiency (d) algorithms for different jet flavors. The values are extracted from a QCD sample requiring $\hat{p}_T > 80\,\text{GeV}/c$, at least one corrected jet with $p_T > 20\,\text{GeV}/c$, and all reconstructed jets to be within $|\eta| < 2.4$. [106]

corresponding to the set of simulated event samples used in this thesis.

In [122] the impact of tracker misalignment on the b-tagging efficiency is studied. Among others, a $100\,\text{pb}^{-1}$ scenario is considered, assuming that the position of the tracker modules is known with a precision of $\mathcal{O}(20\,\text{µm})$ in the pixel and $\mathcal{O}(30\text{–}50\,\text{µm})$ in the strip tracker. They find that the b-tagging performance is only slightly degraded by a few percent in this scenario. Taking into account the fact that the position of the modules has already been determined using CRAFT data to a precision of $3-4\,\text{µm}$ ($3-14\,\text{µm}$) in the barrel (endcap) region, see section 2.2.1,

Tagger	WP	Discriminator	Mistag Rate	b-tagging Efficiency
	loose	2.03	0.1	0.82
TCHE	medium	4.38	0.01	0.65
	tight	14.2	0.001	0.24
	loose	1.47	0.1	0.69
TCHP	medium	2.36	0.01	0.6
	tight	5.36	0.001	0.38

Table 4.3: b-tagging working points for the TCHE and TCHP algorithms as recommended by the b-tagging physics object group for analyses performed in the CMSSW_2_2_X cycle. The values for the mistag rate and the tagging efficiency were derived from simulated QCD dijet events and a top-pair production sample, respectively. Jets are reconstructed by the iterative cone algorithm with a cone size of $R = 0.5$, and the following cuts on the transverse momentum and the pseudorapidity were applied: $p_{\mathrm{T}} > 30\,\mathrm{GeV}/c$ and $|\eta| < 2.4$.

b-tagging will most likely be available very soon after start-up with a considerably high performance.

4.3   Modeling of Background Processes

In order to achieve a good background suppression the analysis concentrates on the leptonic top-quark decay channel, since it is practically impossible to separate the hadronic mode from the overwhelming QCD multijet production background. In this channel, the W boson from the top-quark decays into a charged lepton and a neutrino. Furthermore, the lepton flavor is restricted to the muonic one, since the presence of a well measured muon constitutes a powerful characteristic of the signal, while the rate of this mode with a branching ration of about 11% is still acceptable. Including the electron channel is in principle possible and foreseen in order to increase the number of signal events. However, since electrons are jet objects, the background situation is different compared to the muonic channel and will require further studies. Several processes with a considerable cross section have a similar final state or can imitate the same topology. Different Standard Model background processes are considered in the present thesis in order to obtain a realistic analysis scenario. Despite the fact that the analysis concentrates in the muonic channel, all the MC simulations contain also the electron and τ-lepton final states. While the τ-lepton mode can potentially contribute to the signal by decaying muonically, also the electron mode is important to be considered in order to control dilepton background contributions, as will be discussed in 5.1. In addition, the inclusion of all lepton categories provides the flexibility for the samples being used by different analysis groups.

Two general classes of background contributions can be distinguished. In W-like processes a real W boson is produced, which then decays leptonically. In contrast, non-W processes, mainly QCD multijet production, can mimic the signal signature if a jet fakes the charged lepton, or charged leptons stemming from the decay of secondary jet constituents like B hadrons appear in the reconstructed final state. The first parts of this section summarize the modeling of the W-like processes containing top-quark and vector-boson production, followed by a brief description of the non-W background. In the absence of real collision data, MC simulations are used in order to estimate the background contributions. Unless otherwise stated, the simulation of the matrix element is done by MG/ME, while the showering and hadronization is performed by PYTHIA.

4.3.1   Top-Quark Processes

In the present analysis, only the t-channel single top-quark production is considered as signal, whereas the s-channel and the associated production are valued as background contributions. According to reference [21], kinematical distributions at NLO accuracy for s-channel single top-quark production are the same as the LO ones, only the rate has to be adjusted to the NLO cross section. Thus, only the LO process is considered in the simulation. The decay of the W boson from the top quark is restricted at matrix-element level to leptonic modes, including e, μ, and τ. A Feynman graph of the process including the decay of the top quark is shown in figure 4.5 (a).

Concerning the associated production only the $2 \rightarrow 2$ process is simulated. In

order to obtain a more realistic description of the NLO contributions, a matching would be needed, similar to the procedure applied in the t-channel. In the absence of a proper matching tool, the simulation is currently based on the Born diagram only. The decay of the top quark and the W boson in the final state is simulated inclusively. The signature of the associated production contributes mainly as a background when one W boson decays leptonically into a muon, as shown in figure 4.5 (b).
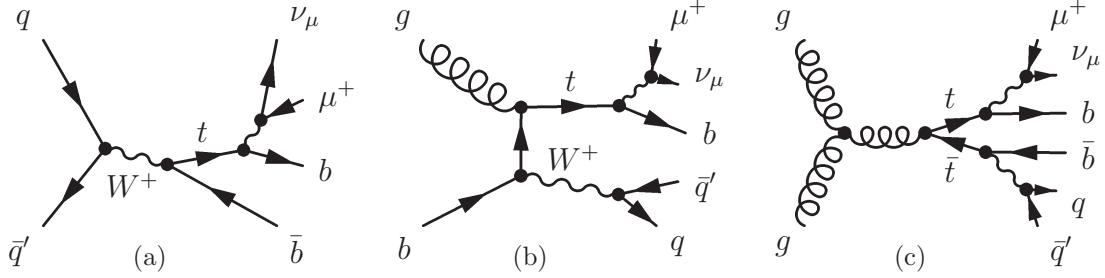
Figure 4.5: Feynman diagrams of s-channel (a) and associated (b) single top-quark production including the decay of the W bosons. Only decay channels with a muon in the final state contribute significantly as background. Subfigure (c) shows a Feynman diagram for a top-quark pair event, where one top quark decay is characterized by a leptonically decaying W boson, whereas the second top-quark decays fully hadronically.

The production of top-quark pairs via the strong interaction is one of the most dominant background processes. Figure 4.5 (c) shows a Feynman diagram for a typical final-state configuration which might potentially be misidentified as a signal event.

Events with different jet multiplicities at matrix-element level were simulated separately, corresponding to the exclusive jet bins 0, 1, 2 and the inclusive jet bin 3 containing events with three additional partons in the matrix-element final-state. After the PS simulation the samples are matched according to the MLM method briefly described in section 3.2.

4.3.2 Vector-Boson Production

Another class of processes contributing a sizable amount of background events to the signal-candidate sample is the production of the W and Z vector bosons, summarized as V. These bosons can be produced in association with either light quarks (u, d, s) and gluons or heavy quarks (c, b), often referred to as Q.

Vector-Boson Production in Association with Light Quarks

Typical Feynman diagrams of vector-boson production in association with light quarks with a leptonic final state are shown in figure 4.6. The fact that there is no heavy quark present in the final state can be exploited to suppress this background significantly by applying b-tagging. Nevertheless, the large rate of the processes (see table 4.4) in combination with a non-vanishing b-tagging mistag rate leads to a significant contribution of the process to the signal-candidate sample.

Concerning the light quark modes, two separate samples are simulated, one including Z+jets events and another one for W+jets events. For the W-boson processes, different parton multiplicities at matrix-element level are generated. The jet bins 0, 1, 2, 3, and the inclusive 4 jet bin (4+) were simulated separately and, after the showering with PYTHIA, matched according to the MLM scheme to one inclusive sample. In order to model Z+jets production, the Drell-Yan process is simulated. It describes the creation of a virtual photon (γ^*) or a Z boson, which then decays into a lepton pair. Since the invariant-mass spectrum of the lepton pair is strongly dominated by the γ^* contribution at low values, a cut at generator level of $m_{ll} > 50\,\mathrm{GeV}/c^2$ is applied. Though the rejected phase space is large, its contribution to the phase space relevant for top-quark analyses is negligible. Analogously to the W+jets modeling, the different jet multiplicities (0, 1, 2, 3, and 4+) are generated separately and then undergo the showering, hadronization, and matching to result in one inclusive sample. The decay of the W and Z bosons is always restricted to the leptonic mode in the simulation, meaning $W \to l\nu_l$ and $Z \to l^+l^-$, where in both cases $l = e, \mu, \tau$. The hadronic mode can be neglected for the muonic decay channel focused on here. Despite the fact that the matrix element of the process contains only light quark partons in the final state, heavy quark hadrons might be present in the hadronized final state, which stem from the parton shower modeling of the simulation. Thus, in order to obtain a MC simulation that is appropriate for the description of the vector-boson production in association with light quarks, the heavy flavor content has to be removed, which will be specifically addressed below.
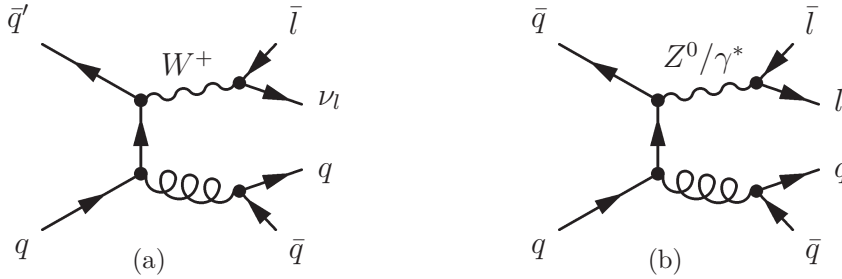
Figure 4.6: Typical Feynman diagrams for the production of W (a) and Z bosons (b) in association with light quarks.

W-Boson Production in Association with a Single Charm Quark

The production of W bosons in association with a single c quark has a very large production rate compared to the signal (see table 4.4). Furthermore, the presence of the c quark in the final state, which can due to its lifetime easily be misidentified as a b-jet, makes these events resembling the signal signature and thus contributing significantly as a background. A Feynman diagram contributing to this background process at LO is shown in figure 4.7. As the simulation of the process includes only this LO graph, the bulk of events contain one reconstructed jet initiated by the c quark. Nevertheless, gluon radiations modeled by the parton shower can lead to the

observation of additional jets, such that the signature resembles the t-channel single top-quark signal.
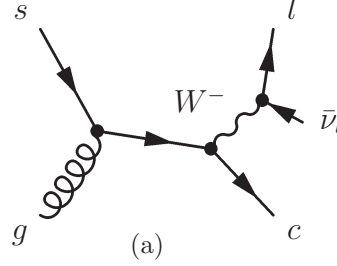
Figure 4.7: Typical Feynman diagram for the production of a W bosons in association with a c quark.

Vector-Boson Production in Association with Heavy-Quarks Pairs

The production of W as well as of Z bosons in association with heavy quarks is simulated in one sample which is called VQQ, where Q indicates the heavy quark flavors b and c. Only the leptonic decay of the bosons to $l\nu$ or ll ($l = e, \mu, \tau$) is simulated. Some typical Feynman diagrams for the set of events contributing to this background are shown in figure 4.8.
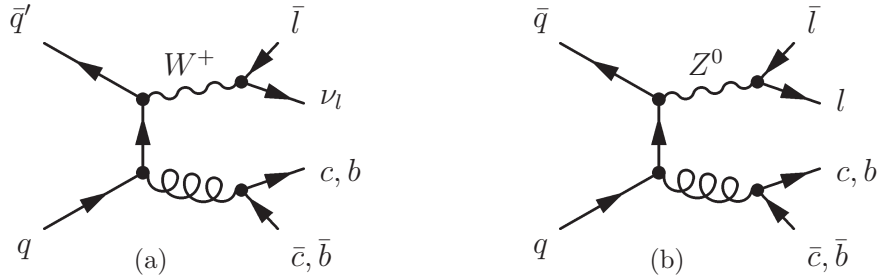
Figure 4.8: Typical Feynman diagrams for the production of W (a) and Z bosons (b) in association with heavy quarks (b, c).

Heavy Flavor Overlap Removal

Heavy-flavor quarks can appear in the matrix-element plus parton-shower scheme in two different ways. Either they are explicitly calculated in the matrix element or they are modeled by the parton showering. In addition to a phase space that is overlapped in extra jet production and resolved by the MLM matching, there is a phase space that is overlapped in heavy-flavor jet production as well. The removal of the additional heavy flavor contribution is necessary and described briefly in the following.

A tool for this so-called heavy flavor overlap removal is available within the CMS offline software and was applied to the vector-boson simulations presented above. Similar to the MLM matching, the method follows the approach of using the distance ΔR between the partons. It attempts to identify, for each event, the flavor content and the development of that event after the hard process simulation. First, all heavy flavor partons p_i of a specific flavor (b, c) are selected. The source of each of these partons is determined, using a classification following the MC simulation scheme, where the parton can either come from the matrix element or the parton shower, and the sister of each heavy flavor parton is found, if one exist. Each heavy-flavor parton is then matched to a GenJet, clustered with the SisCone algorithm using a distance parameter $R_0 = 0.5$. Finally, the separation ΔR between each jet and its sister jet is examined. If $\Delta R < R_0$, meaning that the two partons both match the same jet, the event is classified as a parton shower event, and hence kept in the V+jets sample and discarded in the VQQ sample. Contrary, if $\Delta R > R_0$, meaning that the two partons match different jets, the event is classified as a matrix-element event, and hence taken from the VQQ sample. If only one single heavy-flavor parton is found, it is checked to stem from the matrix element and kept for the VQQ sample. A detailed description of the underlying decision tree can be found in [123]. This procedure results in a set of sub-samples, which can be associated to the physical event categories $Vb\bar{b}$, $Vc\bar{c}$, $V +$ light, and Wc. An overview of the final samples can be found in table 4.4.

Diboson Production

Three different diboson production modes are taken into account, WW, WZ, and ZZ. The corresponding Feynman diagrams can be found in figure 4.9. The WW and WZ production can directly contribute to the signal-candidates, since they can have a final state configuration with a charged lepton, a neutrino, and heavy quarks. In case of ZZ production, one lepton has to get lost in the detector, which coincidentally fakes a neutrino through the resulting missing transverse energy. All the three modes are fully simulated by PYTHIA containing all decay channels of the bosons.
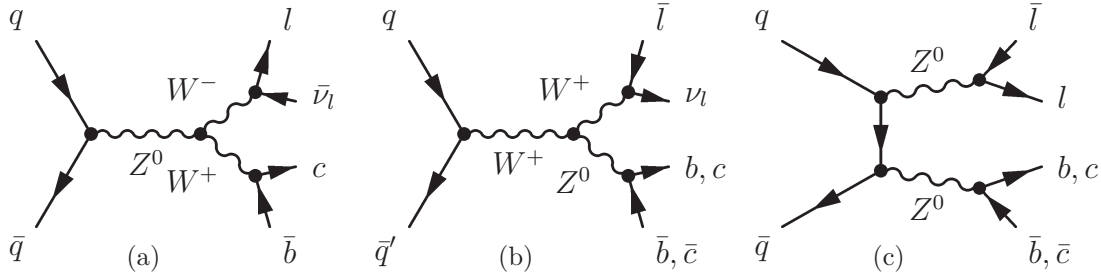
Figure 4.9: Typical Feynman diagrams for diboson production: WW (a), WZ (b), and ZZ (c).

4.3.3 QCD-Multijet Production

A substantial background contribution arises from QCD-induced multijet events. Those events mimic the signal signature by containing muon objects which are erroneously identified as isolated muons, which are well separated in η and ϕ from the next jet. Such muon objects mostly represent muons from a semileptonic b-quark decay occurring either in direct $b\bar{b}$ production (figure 4.10 (a)) or in jets stemming from strong gluon production (figure 4.10 (b)). Simultaneous energy mismeasurements can lead to large artificial missing transverse energy, which additionally features the characteristics of signal events. Since no on-shell W boson is produced, those events are also sometimes referred to as non-W events. While the probability of both the fake of a well-measured charged lepton and the production of large artificial missing transverse energy at once is small, the huge cross section of QCD multijet events makes this background non-trivial.

The modeling of the non-W background is complicated by the fact that fake missing transverse energy due to detector dead regions is hard to consider in the MC simulation. Furthermore, QCD events contributing to the finally selected signal-candidates populate the phase space corresponding to the tails of kinematic distributions. Since only a finite number of events can be simulated the population of such extreme regions is difficult. Thus, the uncertainty of the simulation is quite large. To overcome the insufficient modeling this background contribution has to be determined from collision data. Various methods have been developed for such data-driven estimations. The method investigated for single top-quark measurements is reviewed in section 5.2.

For the present study, PYTHIA is used to simulate QCD multijet events with a muon in the final state, originating from semileptonic decays of hadrons containing a b or c quark. In addition, fake muons due to decay-in-flight are taken into account. A muon-enriched sample was produced by applying cuts on generator level. In particular, there is a requirement on at least one generated muon with $p_T^{\mu} > 15\,\text{GeV}/c$ and only events with $\hat{p}_T > 20\,\text{GeV}/c$ are kept for further simulation.
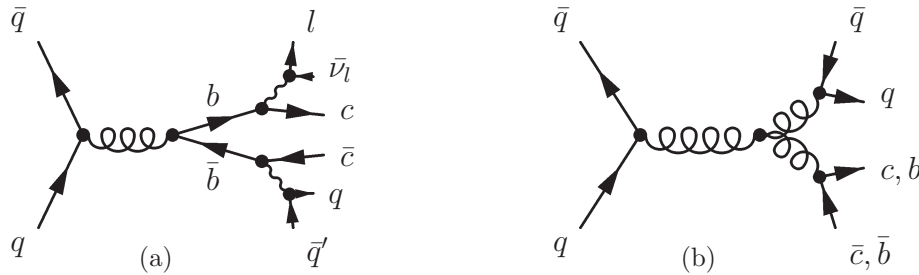
Figure 4.10: Typical Feynman diagrams of two QCD-multijet production modes: direct $b\bar{b}$ production (a) and strong gluon production (b). Since leptonic decays can also occur for c quarks, this picture is obviously simplified with respect to a complete description of the QCD background contributing to the signal region.

A summary of all the considered simulations as well as the cross sections and available simulated sample size can be found in table 4.4. In order to estimate the impact of misalignment or miscalibration of detector components on early data analyses, different scenarios were developed, each corresponding to an assumed detector knowledge after having taken a certain amount of collider data. As the present analysis is not planned to be performed in the early stage of LHC operations, ideal conditions were used for the detector simulation of all the samples. No pile-up contributions were considered in the simulation, since the instantaneous luminosity of the proton beams will be increased carefully. The data amount assumed for the present study is expected to be collected at rather low luminosities of about $(10^{29} - 10^{31})\,\mathrm{cm}^{-2}\,\mathrm{s}^{-1}$ where pile-up effects are still negligible.

Process	Comments	Cross Section [pb]	MC Sample Size
Top-quark production			
t-channel	$W \to l\nu$	42.9 (NLO)	281,756
s-channel	$W \to l\nu$	1.6 (NLO)	11,999
tW-channel	inclusive	29 (NLO)	169,048
$t\bar{t}$	inclusive	414 (NNLO)	905,369
Vector-boson production			
W+light	$W \to l\nu$	40,000 (LO/G)	9,549,245
$Wb\bar{b}$	$W \to l\nu$	54.2 (LO/G)	156,945
$Wc\bar{c}$	$W \to l\nu$	118.8 (LO/G)	529,001
Wc	inclusive	1,490 (LO/G)	3,011,523
Z+light	$Z \to l\nu$	3,700 (LO/G)	1,205,599
$Zb\bar{b}$	$Z \to l\nu$	44.4 (LO/G)	155,411
$Zc\bar{c}$	$Z \to l\nu$	71.7 (LO/G)	359,235
WW	inclusive, Pythia	74 (NLO)	204,722
WZ	inclusive, Pythia	32 (NLO)	238,332
ZZ	inclusive, Pythia	10.5 (NLO)	199,810
QCD-multijet production			
μ-en. QCD	$\hat{p}_\mathrm{T} > 20\,\mathrm{GeV}/c$, $p_\mathrm{T}^\mu > 15\,\mathrm{GeV}/c$	121,675 (LO/G)	6,300,505

Table 4.4: Overview of all MC samples used in the present study, including the signal sample for the t-channel single top-quark production. Unless stated otherwise, the processes were simulated at parton level by MG/ME and the showering and hadronization is done by Pythia. If leptonic decay modes are indicated, they contain $l = e, \mu, \tau$. The cross sections already include the branching ratio if the sample is simulated exclusively or if cuts are applied. The values for top-quark processes are as introduced in chapter 1.3, whereas the cross sections of the single vector-boson production modes as well as the one for the μ-enriched QCD sample are directly obtained from the MC matrix-element calculation of the generator (LO/G). Concerning diboson production, the cross section is calculated at NLO by the MCFM package. The subprocesses of single vector-boson production are extracted from the Z+jets, W+jets, and VQQ samples by using the flavor history tool described in the text.

Chapter 5

Event Selection and Characteristic Signal Properties

As reviewed in the previous chapter, several Standard-Model processes can have a detector signature similar to the t-channel signal process. Thus, an event selection is applied, exploiting differences in kinematic variables and properties between the signal and background in order to reject as many background events as possible while keeping most of the signal events. Based on the MC simulations, the expected event yield in a specific data sample can be estimated, where the simulated events are re-weighted to a particular integrated luminosity $L = \int \mathcal{L} \mathrm{d}t$. This is done by applying the weight

$$ w = \frac{L \cdot \sigma_{\mathrm{eff}} \cdot \epsilon_{\mathrm{sel}}^{\mathrm{tot}}}{N} \,, \tag{5.1} $$

where L is the assumed amount of integrated luminosity, $\epsilon_{\mathrm{sel}}^{\mathrm{tot}}$ is the total event selection efficiency, and N is the total number of considered MC events. Since the simulation of some MC samples only includes certain final states, the branching ratio BR has to be taken into account. In addition, cuts might be applied already at generator level, represented by the filter efficiency $\epsilon_{\mathrm{filter}}$. Considering these facts, the total cross-section σ is reduced to the effective cross-section $\sigma_{\mathrm{eff}} = \epsilon_{\mathrm{filter}} \cdot \mathrm{BR} \cdot \sigma$. The scenario used in the present study assumes a data sample corresponding to $L = 200\,\mathrm{pb}^{-1}$.

Due to the implications discussed in section 4.3.3, the simulation of the QCD multijet background, in the following simply referred to as QCD, has to be considered unreliable. Therefore, dedicated control regions are defined providing signal- or QCD-enriched events samples, which are assumed to behave similar to collision data. Methods for the determination of the QCD fraction in the signal region which are based on such control samples are thus mostly independent of MC simulations and are often called "data-driven". A procedure based on the distribution of the transverse W-boson mass is presented to estimate the QCD contribution in the fully selected candidate-event sample.

The presence of t-channel events in the fully selected sample of signal candidates can be tested by looking at characteristic signal properties like the invariant top-quark mass distribution or the polarization of the top quark. Each of these

observables require the knowledge of the top-quark four-vector, which cannot be directly measured in the experiment but rather has to be reconstructed from the observable final state objects. After the discussion of the applied top-quark reconstruction technique, some characteristic signal properties are presented.

5.1 Event Selection

Since the muonic decay channel of the top quark is defined as signal, the final state topology of the considered t-channel signal is characterized by a reconstructed muon candidate, a certain amount of $E_{\mathrm{T}}^{\mathrm{miss}}$, and most likely two jets, whereof one jet is produced in the forward direction. The presence of a muon candidate in the final state can be exploited by the trigger requirement to provide a filtered data stream enriched by events containing a muon object. In order to obtain a scenario close to the analysis of collision data, the trigger simulation is included in the production of the MC samples. Events considered in the present analysis have to be accepted by the HLT path `HLT_Mu15`, which is contained in the start-up trigger menu proposed for runs at an instantaneous luminosity in the order of $10^{31}\,\mathrm{cm}^{-2}\,\mathrm{s}^{-1}$. This path is seeded by a L1 muon object measured in the muon system with a transverse momentum larger than $10\,\mathrm{GeV}/c$. After the combination of information from the muon system with the tracker measurement by the HLT reconstruction, the muon object is required to have $p_{\mathrm{T}}^{\mu} > 15\,\mathrm{GeV}/c$, within $|\eta^{\mu}| < 2.1$, and the distance in the $x - y$-plane between the muon track and the beam spot has to be below $2\,\mathrm{cm}$.

Considering the events selected by this trigger, a stricter definition is applied to physics objects like muon candidates or jets in order to increase their purity. Finally, the event sample has to undergo a dedicated set of selection criteria which aim for an enrichment in signal and a most efficient rejection of backgrounds. The resulting selected event sample is then re-weighted to the expectation corresponding to an analyzed data equivalent of $200\,\mathrm{pb}^{-1}$.

5.1.1 Object Definition

In a first step, dedicated criteria are imposed on the reconstructed physics objects. Charged leptons are only considered if their transverse momentum exceeds $20\,\mathrm{GeV}/c$. The pseudorapidity range for muons is limited by the trigger acceptance to $|\eta^{\mu}| < 2.1$, whereas electrons are accepted in a range of $|\eta^{e}| < 2.4$. As described in section 4.2.3, the quality of the muon candidates has to fulfill the definition of the *global tight prompt muon* ID. Electron candidates are selected by requiring the tight ID category. Jets are considered if they are reconstructed in a pseudorapidity range $|\eta^{\mathrm{jet}}| < 5$ with a calibrated transverse momentum larger than $30\,\mathrm{GeV}/c$.

5.1.2 Selection Criteria

Only events with at least one muon fulfilling the criteria mentioned above are kept. In order to reduce the contribution of dilepton events, which can arise from $t\bar{t}$ production, events with more than one charged lepton are rejected, where electrons

as well as muons are considered in the count. Subsequently, the remaining charged lepton has to be a muon candidate. Since the muon might not necessarily stem from a leptonic W-boson decay, but from decay activities within a jet, a so-called near-jet veto is applied. The event is rejected if the reconstructed muon is closer than $\Delta R = 0.3$ to one of the accepted jets.

(a)   (b)
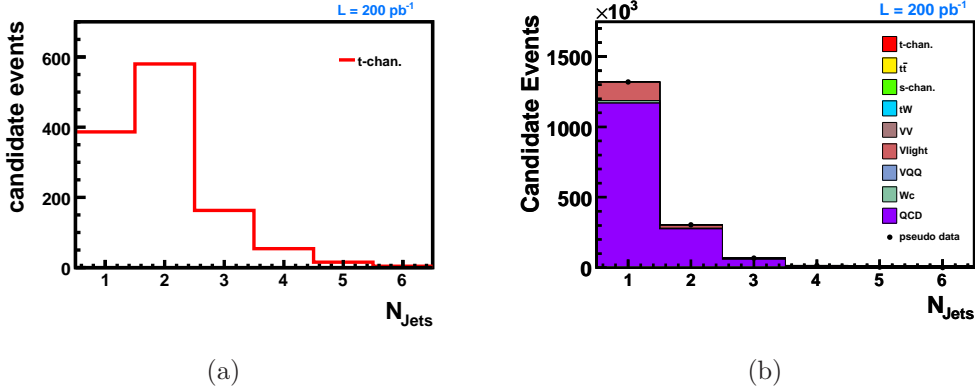
Figure 5.1: Jet multiplicity after the lepton counting and the near-jet veto. Only events with at least one jet are shown for the signal only (a) and for all processes (b), normalized to $L = 200\,\mathrm{pb}^{-1}$. The pseudo data distribution is obtained from a bin-by-bin smearing of the total event yield following Poisson statistics.

As can be seen in figure 5.1(a) most of the signal events exhibit two well-defined jets in the view of transverse momentum and pseudorapidity. These two jets most likely stem from the b quark of the top-quark decay and the scattered light quark. Since the transverse momentum spectrum of the spectator b-quark is much softer compared to the final-state light quark, the jet emerging from this b quark is very likely to fail the required p_T threshold, yielding event topologies with only two selected jets. Therefore, only the subset of events with exactly two jets is considered in the following. The resulting jet multiplicity spectrum, including all background processes, is shown in figure 5.1 (b).

Muon Isolation

Although the definition of the muon object contains quality requirements, and despite the near-jet veto, a considerable amount of QCD events remains in the selected 2-jet subsample due to the presence of muons from B-hadron decays or of decay-in-flight muons. Their contribution can be significantly suppressed by exploiting the isolation of the reconstructed muon object. We define the combined relative isolation as

$$\mathrm{relIso} = \frac{p_\mathrm{T}^\mu}{p_\mathrm{T}^\mu + \mathrm{tkIso} + \mathrm{caloIso}}\,, \qquad (5.2)$$

where tkIso is the scalar sum of the transverse momenta of the tracks in a cone of size $\Delta R < 0.3$ around the muon direction, excluding the track of the muon itself. The calorimeter isolation, caloIso, is defined analogously as the scalar sum

of the transverse energies of the calorimeter deposits in a cone of size $\Delta R < 0.3$ around the muon track, excluding the calorimetric footprint of the muon itself. The
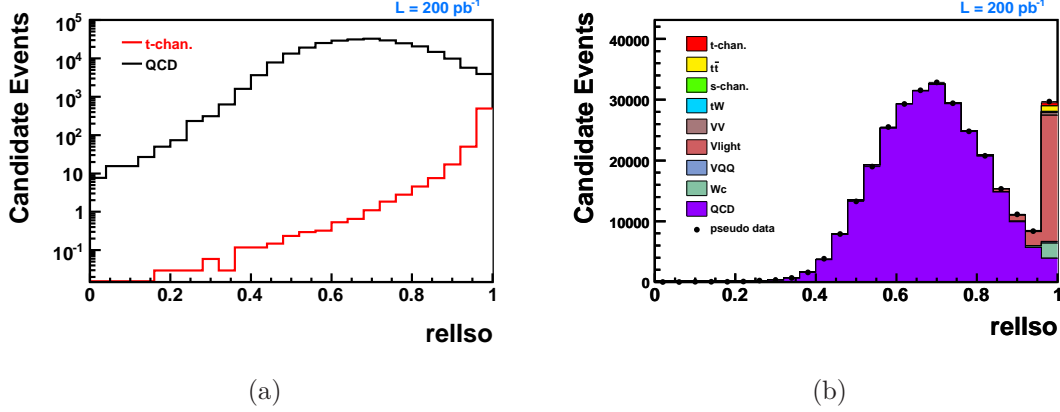
Figure 5.2: Relative isolation (relIso) of the selected muon for events in the 2-jet subsample, for signal and QCD (a) and for all processes (b), normalized to $L = 200\,\mathrm{pb}^{-1}$. The pseudo data distribution is obtained from a bin-by-bin smearing of the total event yield following Poisson statistics.

distribution of the relative isolation is shown in figure 5.2 for events in the 2-jet subsample. In contrast to muons stemming from the decay of a W boson, muons reconstructed in QCD events are in general less isolated as they are most likely produced in the active environment of jets. Therefore, the QCD rejection can be significantly improved by requiring the relative isolation of the reconstructed muon to be above 0.95. The composition of the remaining event sample corresponds to the content of the rightmost bin in figure 5.2 (b) and is at this stage dominated by vector-boson production in association with light quarks and gluons, labeled with "Vlight".

b-Tagging

The signature of the t-channel single top-quark production contains three partons in the final state, one light quark recoiling against the virtual W boson, one b quark from the top-quark decay, and the spectator b-quark from the initial gluon splitting. The spectator b-quark is most likely produced at very high absolute pseudorapidity values and thus outside the tracker acceptance of $|\eta| < 2.5$. One therefore expects that the spectator b-quark is in most cases not identified as a b-quark jet. The b-tagging which is applied to the selected jet candidates follows partially the recommendations of the b-tagging POG summarized in table 4.3. For the track-counting-high-purity (TCHP) algorithm, the tight working point corresponding to a minimal discriminator value of 5.36 is used, while a loose cut value of 1.47 was chosen for the track-counting-high-efficiency (TCHE) category. Considering events with one good muon and two jets, the application of the tight TCHP cut yields an efficiency of 34% for jets matched to b quarks within $\Delta R < 0.3$. Here, only jets
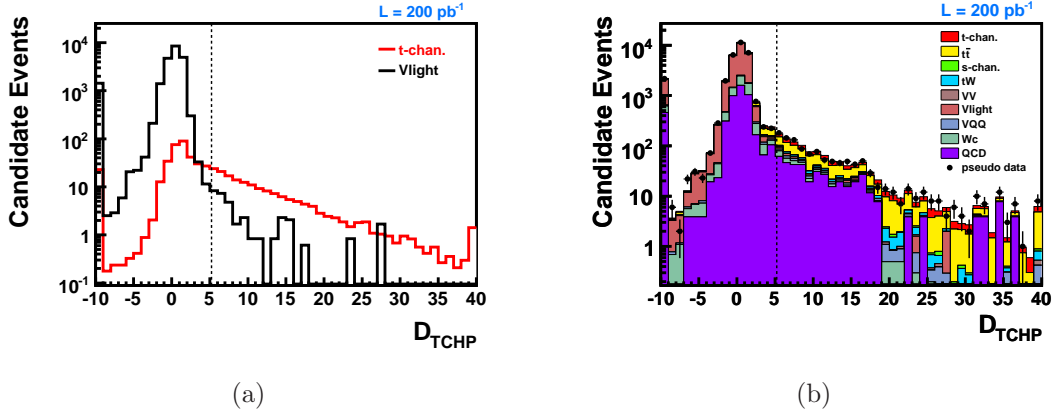
Figure 5.3: The highest discriminator value of the TCHP algorithm (D_{TCHP}) for jets in signal and Vlight events (a) and for jets of all processes (b), normalized to $L = 200\,\mathrm{pb}^{-1}$. The dashed line indicates the lower discriminator threshold applied for the tight b-tagging requirement. The underflow bin contains jets with not enough good tracks to calculate the discriminator, including jets outside the tracker acceptance. The pseudo data distribution is obtained from a bin-by-bin smearing of the total event yield following Poisson statistics.

with $p_{\mathrm{T}} > 30\,\mathrm{GeV}/c$, and within the tracker acceptance of $|\eta| < 2.5$ are taken into account. By analogy with this, the requirement of the TCHE discriminator to be above the loose threshold yields an efficiency of 82.6%. The highest discriminator value of the TCHP b-tagger of the two jets in the event is shown in figure 5.3. As expected, the distribution is asymmetric for the signal process containing B hadrons with a finite lifetime in the final state, whereas the Vlight sample shows a symmetric discriminator spectrum since the jets are mostly initiated by light quarks. The b-tag multiplicity in the 2-jet subsample obtained from the tight TCHP demand is shown in figure 5.4 (a) for the signal, as well as for the dominant background contribution Vlight, and for all considered processes in figure 5.4 (b). Requiring exactly one jet with a TCHP b-tag discriminator value above the tight WP threshold, yielding the so-called 1-tag subsample, reduces the amount of Vlight events by about three orders of magnitude.

Restricting the set of events to the 1-tag subsample, top-quark pair production becomes the dominant background fraction. The fact that the signature of $t\bar{t}$ events contains two b quarks most likely produced within the tracker acceptance can be exploited to further reduce its contribution. Figure 5.5 shows the TCHE discriminator value for the jet that fails the tight cut on the TCHP one. Above the threshold of 1.47 the sample is dominated by $t\bar{t}$. Thus, a second b-jet veto is applied, where events are rejected if this second jet has a TCHE discriminator above the threshold.

(a)   (b)
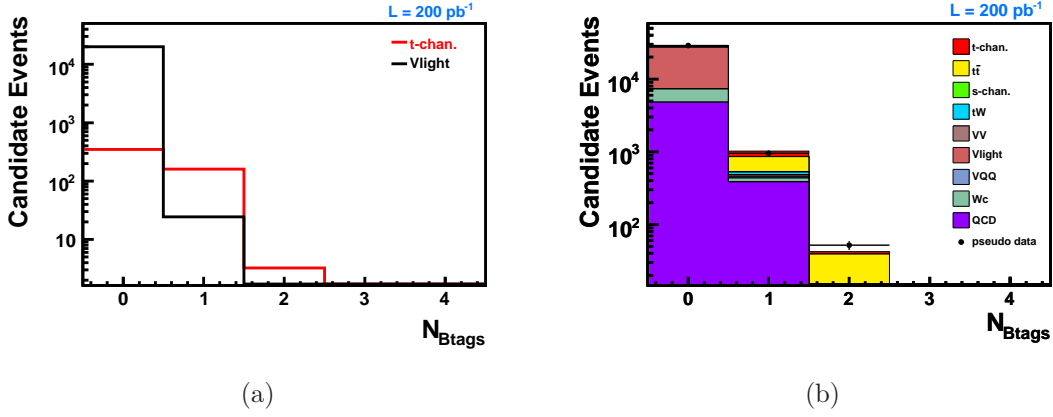
Figure 5.4: Number of b-tagged jets per event when requiring $D_{\mathrm{TCHP}} > 5.36$, for signal and Vlight events (a) and all processes (b), normalized to $L = 200\,\mathrm{pb}^{-1}$.
The pseudo data distribution is obtained from a bin-by-bin smearing of the total event yield following Poisson statistics.

(a)   (b)
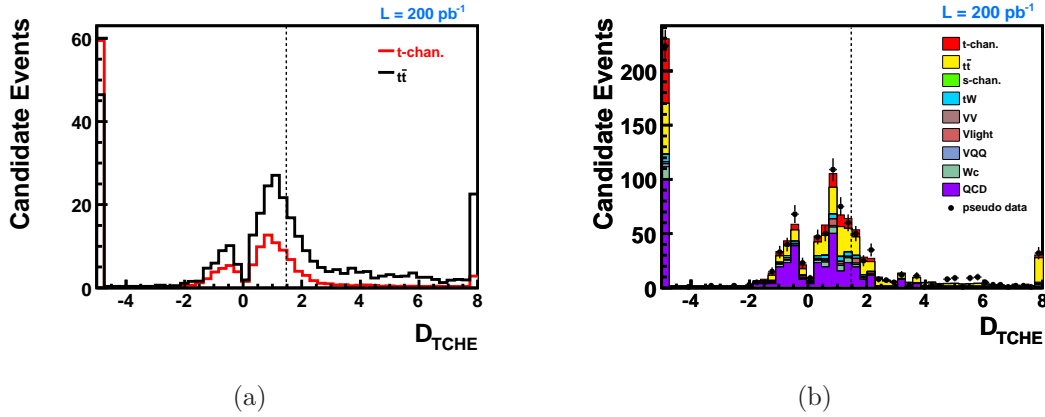
Figure 5.5: The discriminator value of the TCHE algorithm, D_{TCHE}, for the jet that fails the tight cut on the TCHP one for signal and $t\bar{t}$ (a) and for all processes (b), normalized to $L = 200\,\mathrm{pb}^{-1}$. The dashed line indicates the lower discriminator threshold applied for the loose b-tagging requirement. The underflow bin contains jets with not enough good tracks to calculate the discriminator, including jets outside the tracker acceptance. The pseudo data distribution is obtained from a bin-by-bin smearing of the total event yield following Poisson statistics.

Transverse W-Boson Mass

To further suppress contributions from QCD processes where the lepton does not originate from a leptonically decaying W boson the reconstructed transverse W-boson mass is considered. This quantity is defined as:

$$M_{\mathrm{T}} = \sqrt{(p_{\mathrm{T},\mu} + p_{\mathrm{T},\nu})^2 - (p_{x,\mu} + p_{x,\nu})^2 - (p_{y,\mu} + p_{y,\nu})^2} \,, \qquad (5.3)$$
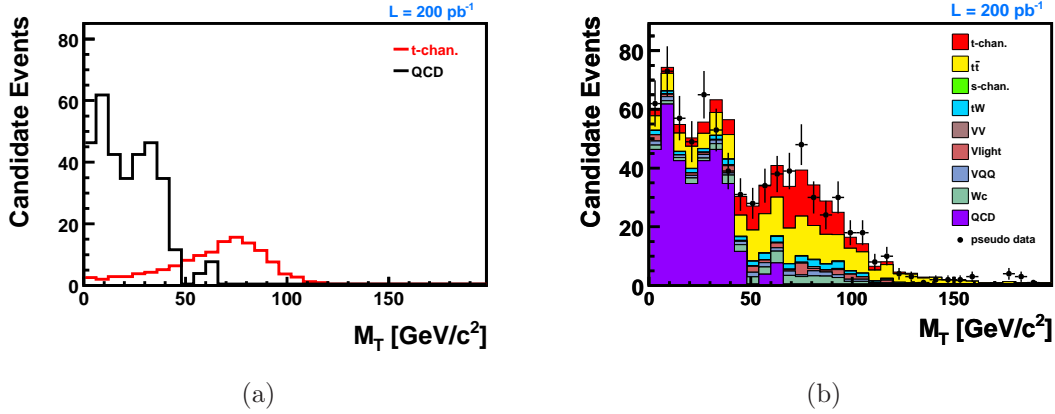
Figure 5.6: The transverse W-boson mass after the full selection except for the M_T cut, for signal and QCD (a) and for all processes (b), normalized to $L = 200\,\mathrm{pb}^{-1}$. The pseudo data distribution is obtained from a bin-by-bin smearing of the total event yield following Poisson statistics.

where the momentum components of the neutrino, $p_{i,\nu}$, $i = x, y, \mathrm{T}$, are approximated by the components of the corrected missing transverse energy, $(E_\mathrm{T}^\mathrm{miss})_i$.

Figure 5.6 shows the shape of the M_T distribution after the preceding selection. The QCD background can be distinguished from W-like processes, since the transverse mass of the alleged W bosons accumulates at low values while all processes with real W bosons tend to cluster around the W-boson mass, with a distribution known as "Jacobian peak". The reconstructed transverse W-boson mass is required to be above $50\,\mathrm{GeV}/c^2$ for events to be kept.

This cut on the transverse W-boson mass is preferred over a cut on the missing transverse energy because of its better separation power between signal and QCD events. In addition, the missing transverse energy turned out to be quite correlated with the muon momentum and muon isolation in the used QCD simulation, since most of the selected QCD events have a true muon stemming from a b- or c-quark decay and therefore $E_\mathrm{T}^\mathrm{miss}$ is due to the presence of true neutrinos.

5.1.3   Expected Event Yield for $L = 200 \, \mathrm{pb}^{-1}$

The relative impact of the presented event selection on the signal and the considered background contributions is shown in table 5.1. After the requirement of exactly one good muon the sample is still dominated by QCD. This motivates the use of the combined isolation variable relIso and an additional selection on the transverse W-boson mass to achieve a good QCD reduction. Nevertheless, QCD remains one of the most difficult backgrounds to predict, and the next section is devoted to a data-driven method to estimate its contribution. The second-most dominating background after the leptonic selection, the production of W bosons in association with light quark jets, is reduced significantly by the use of b-tagging. Figure 5.7 (a)

Process	presel.	relIso	tight b-tag	loose b-veto	M_{T}	$\epsilon_{\mathrm{sel}}^{\mathrm{tot}}$
t-channel	7.4%	87.7%	31.5%	82.1%	72.9%	1.22%
s-channel	6.1%	85.3%	39.4%	39.1%	68.0%	0.55%
tW	3.0%	86.6%	28.4%	76.9%	67.6%	0.38%
$t\bar{t}$	1.3%	86.4%	33.4%	59.5%	70.8%	0.16%
Wc	1.0%	89.5%	1.9%	87.4%	67.2%	0.0099%
$Wb\bar{b}$	0.9%	86.7%	28.9%	49.6%	69.5%	0.0739%
$Wc\bar{c}$	0.6%	87.2%	2.1%	74.1%	67.5%	0.0051%
$W+$light	0.3%	86.2%	0.12%	72.4%	66.7%	0.0001%
$Zb\bar{b}$	0.5%	86.0%	24.8%	71.8%	36.2%	0.0302%
$Zc\bar{c}$	0.5%	85.8%	2.0%	86.2%	24.0%	0.0017%
$Z+$light	0.3%	85.3%	0.36%	80.0%	50.0%	0.0003%
WW	2.8%	87.6%	0.6%	80.7%	52.0%	0.0064%
WZ	1.6%	87.9%	4.3%	48.3%	61.1%	0.0185%
ZZ	0.5%	80.2%	5.9%	56.0%	60.7%	0.0085%
μ-en. QCD	1.1%	1.9%	7.4%	86.0%	3.5%	0.00005%

Table 5.1: Relative selection efficiencies calculated for each selection step with respect to the preceding one. For the efficiencies given in the first column, a preselection is applied containing the trigger request, the object definition, the dilepton veto, and the requirement of exactly two well-defined jets. The last column shows the total event selection efficiency ($\epsilon_{\mathrm{sel}}^{\mathrm{tot}}$) for each process, which is calculated with respect to the content of the corresponding simulated MC data sets as listed in table 4.4
.

shows the jet multiplicity spectrum obtained from the event sample having passed the selection apart from the veto on the second b-tagged jet. As can be seen, the subset of events containing two jets is dominated by top-quark pair production. Those events typically contain two b quarks in the final state, while for signal events in the 2-jet subsample most likely one taggable b quark is present. Thus, the signal-over-background ratio is further enhanced by a veto on a second b-tagged jet, using a loose threshold. The resulting jet multiplicity spectrum is shown in figure 5.7 (b). Despite the cuts explicitly devised against it, $t\bar{t}$ remains the dominant background process. Therefore, the relative contribution of the different final states of this process is

investigated. The subset of $t\bar{t}$ events passing the event selection is dominated by μ + jets events, which contribute with 59.1%, followed by $l + \tau$ events ($l = e, \mu$) with a fraction of 26.1%. Minor contributions come from dilepton channels, where both W bosons decay into electrons or muons, and the hadronic channel, where both W bosons decay hadronically, with a fraction of 12.1% and 2.8%, respectively.
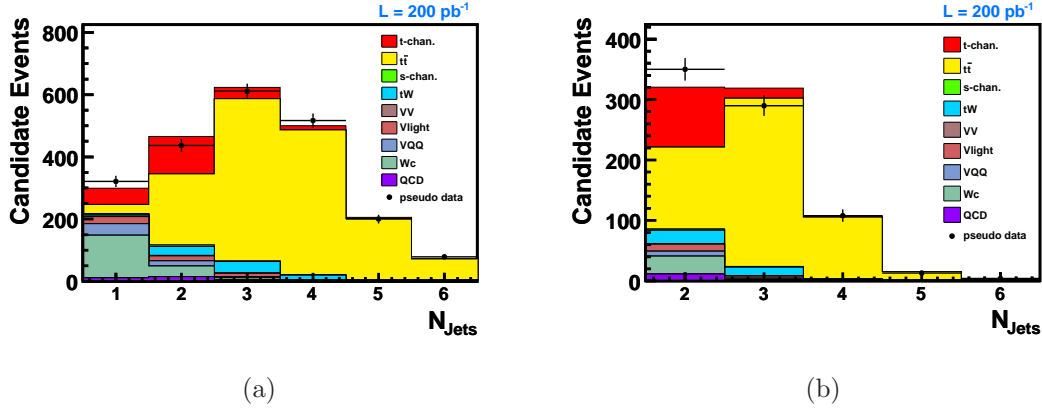
Figure 5.7: The expected jet multiplicity spectrum if requiring at least one jet per event, normalized to $L = 200\,\text{pb}^{-1}$. Events contained in (a) are fully selected except for the second b-jet veto, thus the 2-jet subsample is dominated by $t\bar{t}$ events. Applying the second b-veto (b) leads to a significant suppression of the $t\bar{t}$ contribution in the 2-jet subsample of about 65%. The pseudo data distribution is obtained from a bin-by-bin smearing of the total event yield following Poisson statistics.

The expected event yield after the full event selection, normalized to an integrated luminosity of 200 pb^{-1}, for all considered processes is shown in table 5.2. Among the selected signal events, 98% originate from muonically decaying W bosons. Based on the estimations for 200 pb^{-1}, the presented selection yields a naive significance of $S/\sqrt{B} = 6.7$. This is the expected significance of a counting experiment assuming no uncertainties on the mean background expectation B. Given the moderate signal-to-background ratio of about 0.5, relative uncertainties on B of about 20% would reduce seriously the significance of the signal. Thus, a very precise control of the backgrounds is needed in order to find an evidence of signal through a simple event counting in this scenario. Such precise measurements of the background normalization will not necessarily be available at the time when the present analysis would be performed. Therefore, the needed separation power is achieved by exploiting observables which are able to discriminate between the signal and background processes. As described in chapter 6, the estimation of the signal fraction in the selected event sample is then based on a likelihood fit to a discriminating observable.

Process	$N_{\text{evt}}^{\text{MC}}$	$\epsilon_{\text{sel}}^{\text{tot}}$	$N_{\text{evt}}^{\text{exp}}$
t-channel	3,441	1.22%	102±1.8
s-channel	66	0.55%	1.8±0.2
tW	647	0.38%	22.3± 0.9
$t\bar{t}$	1,485	0.16%	136.0±3.5
Wc	297	0.0099%	29±1.7
$Wb\bar{b}$	116	0.0739%	8.0±0.7
$Wc\bar{c}$	27	0.0051%	1.2±0.2
W+light	14	0.0001%	12±2.6
$Zb\bar{b}$	47	0.0302%	2.7±0.4
$Zc\bar{c}$	6	0.0017%	0.2±0.1
Z+light	4	0.0003%	2±1.2
WW	13	0.0064%	0.9±0.3
WZ	44	0.0185%	1.2±0.2
ZZ	17	0.0085%	0.17±0.04
μ-en. QCD	3	0.000048%	12±6.7
Total background			229±8.4
$S/\sqrt{B}$			6.7

Table 5.2: Expected event yield for an integrated luminosity of $L = 200\,\text{pb}^{-1}$. The table shows the number of selected MC events ($N_{\text{evt}}^{\text{MC}}$), the total event selection efficiency ($\epsilon_{\text{sel}}^{\text{tot}}$), and the number of events expected in a data sample corresponding to an integrated luminosity of $200\,\text{pb}^{-1}$ ($N_{\text{evt}}^{\text{exp}}$). The quoted uncertainties reflect the limited MC statistics.

5.2   Estimation of the QCD-multijet Background

The method studied in connection with the present analysis exploits the transverse W-boson mass M_{T} as discriminating variable to separate signal-like processes, defined as containing a real W or Z boson in the hard process, from the QCD contribution which is the only process considered as background in the following. The overall distribution as measured in data is assumed to be composed of these two contributions and can thus be parametrized by:

$$F(M_{\text{T}}) = a \cdot S(M_{\text{T}}) + b \cdot B(M_{\text{T}}) \,, \tag{5.4}$$

where $S(M_{\text{T}})$ and $B(M_{\text{T}})$ are the expected distributions for signal-like and QCD events, respectively. In order to estimate the two functions, $S(M_{\text{T}})$ and $B(M_{\text{T}})$ independently from the MC simulation, they have to be extracted directly from collision data. Therefore, dedicated control regions are defined by modifying the event selection. A suitable control region provides a sample containing large statistics and being strongly dominated by the respective event category, while resembling kinematically the selected sample. The normalizations a and b of the two event categories will be obtained by a fit of $F(M_{\text{T}})$ to the observed data distribution. The QCD contribution in the signal region, defined by $M_{\text{T}} > 50\,\text{GeV}/c^2$, can then be extracted from the relevant integral of the properly normalized background function.

5.2.1 Extraction of Signal and Background-Enriched Control Samples

The signal- and background-enriched control samples are obtained by exploiting phase space regions being disjoint to the signal-candidate selection. Concerning the QCD background rejection, there is one cut dominating in the event selection, namely the isolation requirement of the muon candidate. Figure 5.8 (a) shows a shape comparison for QCD events having passed several selection chains. Concerning the absence of b-tagging ("pretag"), the shape seems to be largely unaffected compared to the distribution obtained from the standard selection. Requiring the muon to be non-isolated (relIso < 0.8), the resulting distribution describes reasonably well the region above $M_\mathrm{T} \sim 40\,\mathrm{GeV}/c^2$. Differences are observed in the low M_T region, which, however, can be tolerated in this study, since the uncertainty of the method will be dominated by other aspects, as discussed further below. Thus, the requirements for the b-tagging and the isolation are modified in order to obtain a control sample containing a large amount of events. In particular, the QCD-
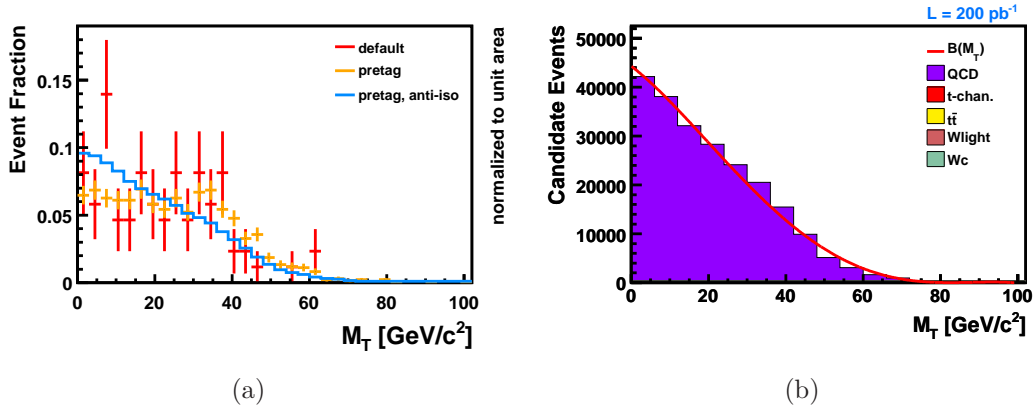
Figure 5.8: Comparison of the M_T distribution of QCD events in different control regions obtained from modified selection cuts (a). In order to increase the statistics, the b-tagging is omitted, yielding the so-called pretag sample, and in addition the isolation cut is modified to relIso < 0.8, which is labeled as "anti-iso". Subfigure (b) shows the expected M_T distribution in the QCD-enriched control region, normalized to $200\,\mathrm{pb}^{-1}$. The shape of the QCD background, which dominates the phase space of the anti-isolated muon, is extracted by fitting a polynomial of rank four as indicated by the red line.

enriched sample is extracted by applying a dedicated selection which differs from the standard one by the absence of b-tagging requirements and by an anti-isolation cut (relIso < 0.8) intended to get rid of most of the signal-like events. Since the amount of MC events is limited, the assumption of kinematic insensibility of the observable M_T with respect to the b-tagging has to be verified with collision data by comparing the anti-isolated pretag sample with the tagged one.

As can be seen in table 5.3 the dedicated selection yields a very clean high-statistics QCD sample with a purity of almost 100%. The expected M_T distribution for $L = 200\,\mathrm{pb}^{-1}$ is shown in figure 5.8 (b). A polynomial of rank four is fitted to

Process	$N_{\text{evt}}^{\text{MC}}$	$N_{\text{evt}}^{\text{exp}}$
QCD	56,920	222,036
t-channel	352	10
$t\bar{t}$	384	30
tW	118	4
$W+$ light	417	340
Wc	282	28
$Wb\bar{b}$	21	1

Table 5.3: Event yield for the main processes obtained from the QCD-enriched selection, where no b-tagging is applied and the relative isolation is required to be below 0.8. The raw number of selected MC events ($N_{\text{MC}}^{\text{evt}}$) as well as the expectation normalized to $L = 200\,\text{pb}^{-1}$ ($N_{\text{evt}}^{\text{exp}}$) are given.

this distribution in order to extract the $B(M_{\text{T}})$ shape:

$$B(M_{\text{T}}) = p_0 + p_1 M_{\text{T}} + p_2 M_{\text{T}}^2 + p_3 M_{\text{T}}^3 + p_4 M_{\text{T}}^4 \,. \tag{5.5}$$

The resulting values of the fit parameters $p_0, p_1, p_2,$ and p_3 are listed in table 5.5.

Concerning the definition of a signal-enriched region, figure 5.9 (a) demonstrates that the M_{T} shape after the full event selection apart from b-tagging and the cut on M_{T} is almost the same for signal and Wlight events, and still quite similar for $t\bar{t}$ events. In addition, it has been checked that the impact of the b-tagging on the M_{T} shape is negligible. Since this QCD estimation can afford a certain degree of approximation, and the modeling of the signal-like components turns out to be uncritical for this study, the different signal-like processes are approximated by one single shape. For the present study a Z-enriched phase space, dominated by Z-boson production processes, is exploited to extract the signal shape $S(M_{\text{T}})$. Events in the Z-enriched control sample are required to have at least two leptons, where the leading two are muons whose invariant mass is in the range $(76 < M_{\mu\mu} < 106)\,\text{GeV}/c^2$, and exactly two jets selected as in the standard selection apart from the absence of b-tagging. In order to model a spectrum similar to the transverse W-boson mass the momenta of the two leading muons are rescaled by the ratio of the W and Z boson mass, M_W/M_Z. One of the muons, randomly chosen, is treated as a neutrino and its transverse momentum is vectorially added to $\mathbf{E}_{\text{T}}^{\text{miss}}$. As can be seen in figure 5.9 (a) the distribution obtained in this way from the Zlight sample has a maximum in the same position as the signal-like events with the standard M_{T} definition. The low-M_{T} region, however, is significant different, while the high-M_{T} region is in general well reproduced. Concerning the purity of the selected event sample, the expectation for the mainly contributing processes, normalized to $L = 200\,\text{pb}^{-1}$, is listed in table 5.4, showing that the sample is clearly dominated by Zlight events with a fraction of about 92%.

The functional form chosen for the parametrization of $S(M_{\text{T}})$ is a Crystal Ball function [124]. It is composed of a central Gaussian with mean m, and standard

Process	$N_{\text{evt}}^{\text{MC}}$	$N_{\text{evt}}^{\text{exp}}$
$Z+$ light	2,732	1,677
$Zc\bar{c}$	1,198	48
$Zb\bar{b}$	791	45
QCD	1	4
t-channel	76	2
$t\bar{t}$	530	48
$W+$ light	4	3

Table 5.4: Event yield for the main processes for the Z-enriched selection described in the text. The raw number of selected MC events ($N_{\text{MC}}^{\text{evt}}$) as well as the expectation normalized to $L = 200\,\text{pb}^{-1}$ ($N_{\text{evt}}^{\text{exp}}$) are given.

deviation σ and a power law tail with power n to low energies joint to the Gaussian at α:

$$S(M_{\text{T}}) = N \cdot G(M_{\text{T}}|m, \sigma) \,, \quad \text{for } \tfrac{M_{\text{T}}-m}{\sigma} > -\alpha \,, \tag{5.6}$$

$$S(M_{\text{T}}) = N \cdot A \cdot \left(B - \frac{M_{\text{T}}-m}{\sigma} \right)^{-n} \,, \quad \text{for } \tfrac{M_{\text{T}}-m}{\sigma} \leq -\alpha \,, \tag{5.7}$$

where α, n, m, σ, and the normalization N are the free parameters of the fit, and

$$A = \left(\frac{n}{|\alpha|} \right)^{n} \cdot \exp\left(-\frac{|\alpha|^2}{2} \right) \,, \tag{5.8}$$

$$B = \frac{n}{|\alpha|} - |\alpha| \,. \tag{5.9}$$

All the parameters are constrained to positive values in order to avoid unphysical fit results and the peak m of the Gaussian, intended to model the high-M_{T} region, is constrained to the range $[60, 150]\,\text{GeV}/c^2$ in order to make sure that it remains in a region close to the value of the W-boson mass. The resulting values of the fit parameters are given in the right-hand section of table 5.5.

(a)   (b)
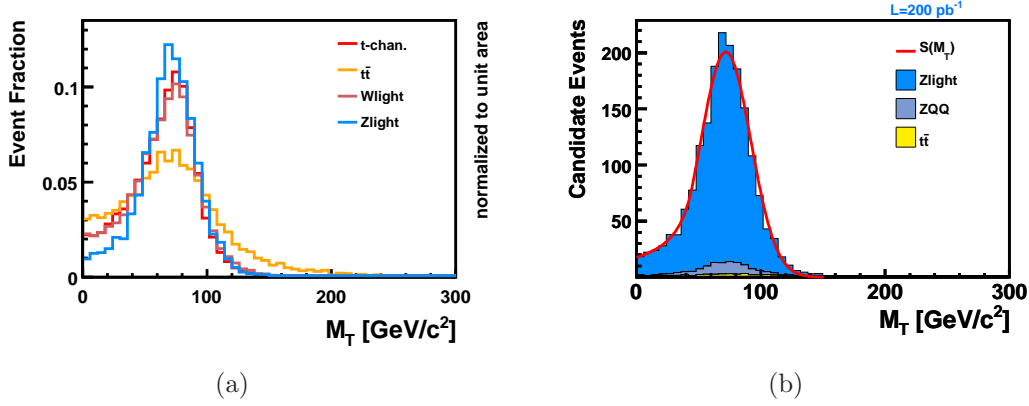
Figure 5.9: (a) Comparison of the M_T distribution of signal-like processes containing a real W boson: signal (red), $t\bar{t}$ (yellow), Wlight (violet), and Zlight (blue). The events from the first three categories have passed the standard selection apart from b-tagging, while the Z + light partons events have passed a dedicated di-leptonic selection and have a different definition of M_T, as explained in the text. (b) Expected M_T distribution in the Z-enriched control region, normalized to $L = 200\,\mathrm{pb}^{-1}$. The selected sample is clearly dominated by the Zlight fraction of about 92%. Fitting this distribution yields the signal shape $S(M_T)$ indicated by the red line.

QCD Shape $B(M_T)$		Signal Shape $S(M_T)$	
Fit Parameter	Parameter Value	Fit Parameter	Parameter Value
p_0	4 ± 27	N	201 ± 7
p_1	-613.8 ± 0.4	α	1.3 ± 0.21
p_2	-13.934 ± 0.005	n	1.2 ± 0.83
p_3	$(291.47 \pm 0.05)10^{-3}$	m	$(72.0 \pm 0.6)\,\mathrm{GeV}/c^2$
p_4	$(-135.43 \pm 0.04)10^{-5}$	σ	$(20.1 \pm 0.6)\,\mathrm{GeV}/c^2$

Table 5.5: Resulting values of the fit parameters for the QCD shape $B(M_T)$ (left column) and for the signal shape $S(M_T)$ (right column).

5.2.2   Fit to the M_T Distribution

The predicted number of QCD events contributing to the signal region is given by:

$$N_{\mathrm{QCD}}^{\mathrm{pred}} = b \cdot \int_{50\ \mathrm{GeV}/c^2}^{\infty} B(M_T) dM_T \,. \tag{5.10}$$

The normalization b of the background shape $B(M_T)$ is obtained from a fit of $F(M_T)$ (see equation 5.4) to the transverse W-boson mass distribution as expected to be measured in a fully selected event sample, shown in figure 5.10. This fit is based on the $B(M_T)$ shape extracted from the QCD-enriched sample, and the $S(M_T)$ shape extracted from the Z-enriched control sample. The fit range is restricted to $[0,100]\,\mathrm{GeV}/c^2$, since the region above this limit does not provide additional

discrimination power versus QCD but introduces possible detector effects and makes the approximation of the $t\bar{t}$ shape less justified. Both normalization parameters, a and b, are fitted simultaneously, yielding $a = 0.19 \pm 0.01$ and $b = (1.70 \pm 0.10)10^{-3}$. Exploiting equation 5.10, the number of QCD events expected in the signal region results as $N_{\text{QCD}}^{\text{pred.}} = 22$.
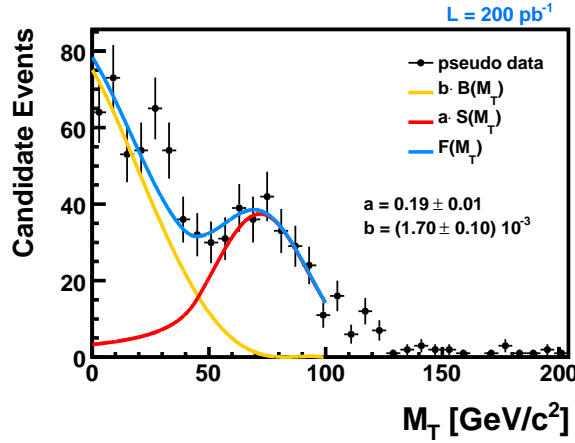
Figure 5.10: In order to extract the normalizations a and b the parametrizations of the signal ($S(M_\text{T})$) and background ($B(M_\text{T})$) shapes are fitted to the M_T spectrum expected in the selected event sample for $L = 200\,\text{pb}^{-1}$. The pseudo data distribution is obtained from a bin-by-bin smearing of the total event yield following Poisson statistics.

In [125] two complementary approaches to extract the signal shape are studied. One method is to use the pure Wlight MC sample selected without b-tagging, yielding a QCD prediction in the signal region of 19.7 events. This value is close to the one obtained from the Z-enriched control sample, since the Wlight and the Z-enriched shape are very similar. However, the modeling of the signal shape is fully based on MC simulations in this procedure. In a third approach, a W-enriched control sample is defined by selecting events as in the standard selection but without applying b-tagging. It turns out, that the selected phase space is, though dominated by Wlight events, significantly contaminated by a QCD contribution of about 27% with respect to the Wlight fraction. Due to the presence of these QCD events, the description of the lower tail of the signal shape differs from the case where clean signal samples are used. Thus, the method yields a lower number of predicted QCD events in the signal region of about 15 events.

For the present analysis, the prediction of 22 events in the signal region obtained from the exploitation of the Z-enriched region is used. A conservative uncertainty of 40% is assigned to this estimation, roughly corresponding to the maximum distance of the results of the different methods divided by their average.

5.3   Characteristic Signal Properties

Once a signal-enriched sample has been selected from real collision data, it is important to check that it exhibits the features expected for single top-quark production. The most obvious is the presence of a top quark, leading to a mass peak when properly combining the final state objects. Another useful feature, exploitable after the reconstruction of the top quark, is the angular distribution of the lepton. The shape is related to the top-quark polarization, which is a specific feature of the electroweak mode of top-quark production. Both will have a central role in the signal extraction technique described in chapter 6 and both require the reconstruction of a top-quark.

5.3.1   Reconstruction of the Top-Quark

Due to its short lifetime, the top quark has to be reconstructed from the decay products by combining them properly. During the reconstruction chain, several ambiguities occur, which lead to the presence of more than one possible top-quark candidate. The applied reconstruction method as well as the associated ambiguity resolution are described in the following.

The first step in the reconstruction of top-quark candidates from the decay products is the reconstruction of the W boson. Since this analysis considers only muonic decays of this boson, we assume that the x and y components of the corrected missing transverse energy are entirely due to the escaping neutrino, and apply the W-mass constraint in order to extract the z component $P_{z,\nu}$:

$$M_W^2 = (E_\mu + \sqrt{\mathbf{E}_\mathrm{T}^{\mathrm{miss}\,2} + P_{z,\nu}^2})^2 - (\mathbf{P}_{\mathrm{T},\mu} + \mathbf{E}_\mathrm{T}^{\mathrm{miss}})^2 - (P_{z,\mu} + P_{z,\nu})^2 \ . \qquad (5.11)$$

This equation has in general two solutions:

$$P_{z,\nu}^{A,B} = \frac{\mu \cdot P_{z,\mu}}{P_{\mathrm{T},\mu}^2} \pm \sqrt{\frac{\mu^2 \cdot P_{z,\mu}^2}{P_{\mathrm{T},\mu}^4} - \frac{E_\mu^2 \cdot \mathbf{E}_\mathrm{T}^{\mathrm{miss}\,2} - \mu^2}{P_{\mathrm{T},\mu}^2}} \ , \qquad (5.12)$$

with

$$\mu = \frac{M_W^2}{2} + \mathbf{P}_{\mathrm{T},\mu} \cdot \mathbf{E}_\mathrm{T}^{\mathrm{miss}} \ . \qquad (5.13)$$

If the discriminant in equation 5.12 becomes negative, or equivalently M_T is larger than the W-boson pole mass of $80.4\,\mathrm{GeV}/c^2$ used in the constraint, the solutions have an imaginary part. This happens in 36.0% of the cases, mostly due to the finite resolution of $\mathbf{E}_\mathrm{T}^{\mathrm{miss}}$.

Several schemes exist to deal with this situation. Taking the real part of equation 5.12 or increase the W-boson mass such that the square root becomes zero are technically simple methods, but lead to a wrong W-boson mass. The method used in the present study eliminates the imaginary component by modifying the components of the missing transverse energy such to give $M_\mathrm{T} = M_W$, still respecting equation 5.11 [25].

Requiring the square root of equation 5.12 to become zero leads to a quadratic relation between $P_{x,\nu}$ and $P_{y,\nu}$ with two solutions $P_{y_{1,2},\nu}(P_{x,\nu})$. The missing transverse energy is modified by restricting the transverse W-boson mass to the pole mass

of $80.4\,\mathrm{GeV}/c^2$. It is assumed that the missing transverse energy measurement is roughly correct. For this reason, the distance δ between the transverse momentum of the neutrino and the missing transverse energy is minimized with respect to both solutions $P_{y_{1,2},\nu}$:

$$\delta_{1,2}(P_{x,\nu}) = \sqrt{(P_{x,\nu} - (\mathbf{E}_\mathrm{T}^\mathrm{miss})_x)^2 + (P_{y_{1,2},\nu}(P_{x,\nu}) - (\mathbf{E}_\mathrm{T}^\mathrm{miss})_y)^2} \qquad (5.14)$$

The smaller solution of $\delta_{1,2}$ is chosen in order to keep the transverse energy of the neutrino close to the measured $E_\mathrm{T}^\mathrm{miss}$. After the minimization, new values $P'_{x,\nu}$ and $P'_{y,\nu}$ and $E_\mathrm{T}^{\mathrm{miss}\prime}$ are obtained, which are used to calculate a new real value for $P_{z,\nu}$. More details and a qualitative study of the missing transverse energy modification as well as of the resulting resolution can be found in [98].

If the discriminant of equation 5.12 is positive, two real solutions are obtained. In this case, the solution with the smallest value of $|P_{z,\nu}|$ is chosen, which describes better the original neutrino in 60% of the events in the sense that the ΔR distance is smaller.

Assignment	Fraction
b-tagged jet is b quark from top quark	92.2%
b-tagged jet is spectator b-quark	4.0%
b-tagged jet is the recoiling light quark	0.1%
b-tagged jet is none of the above	3.7%
untagged jet is b quark from top quark	1.2%
untagged jet is spectator b-quark	1.6%
untagged jet is the recoiling light quark	87.2%
untagged jet is none of the above	10.0%

Table 5.6: Matching of the reconstructed b-tagged and untagged jets to the underlying final-state partons in selected signal events. The matching criterion is fulfilled if the distance in the $\eta - \phi$-plane ΔR between the two objects is smaller than 0.3. Only the b quark from the top-quark decay, the spectator b-quark, and the recoiling light quark are tested as partonic matching partner. Reconstructed jets matching neither parton are thus most likely due to additional gluon radiations.

An additional two-fold ambiguity is present when reconstructing a top-quark hypothesis, since two jets are selected and it is not a priori clear which jet stems from the top-quark decay. This ambiguity is resolved by exploiting the fact that the event topology of a selected signal candidate contains one b-tagged jet, which is assigned to the b-quark from the top-quark decay. In order to verify the quality of this assignment method for signal events, the reconstructed jets are matched in the $\eta - \phi$-plane to the underlying final-state partons. The results of the matching, when applying a matching criterion of $\Delta R < 0.3$ between jet and parton, are shown in table 5.6. It turns out that the b-tagged jet describes in more than 90% of the selected signal events best the b quark from the top-quark decay, whereas the untagged jet can be matched to the recoiling light quark of the t-channel process

in about 87% of all cases. Using this simple assignment method, it is possible to achieve very high matching rates, such that the interpretation of the two selected jets is close to their partonic origin.

5.3.2   The Invariant Top-Quark Mass

The spectrum of the invariant mass of the reconstructed top-quark is certainly an observable to be tested at the very beginning. The observation of a peak at around $173\,\mathrm{GeV}/c^2$ in the selected data sample will be a definite indication of the presence of top quarks. Figure 5.11 shows the invariant mass of the reconstructed top-quark candidate, $M_{l\nu b}$, for events passing the full selection. For QCD and V+X events,

(a)   (b)
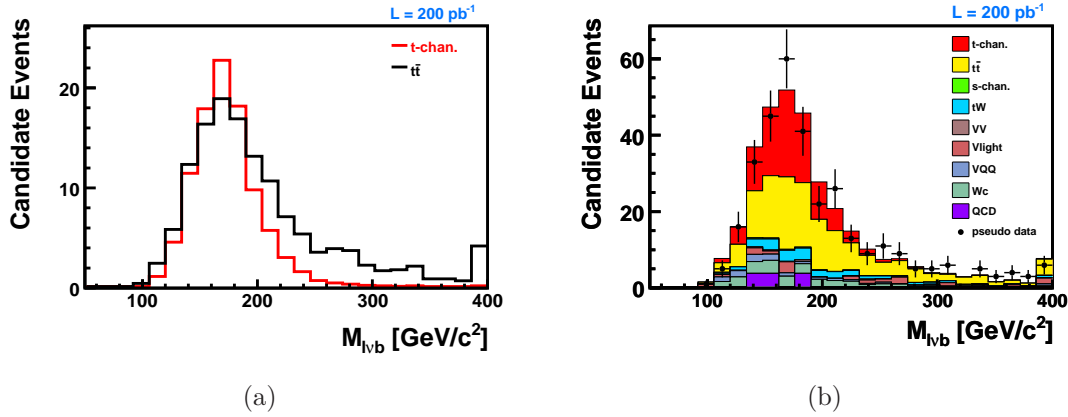
Figure 5.11: Reconstructed top-quark mass after full selection. Subfigure (a) compares the expected signal distribution to the $M_{l\nu b}$ spectrum obtained from $t\bar{t}$ events, whereas the full spectrum considering all background processes is shown in (b). The pseudo data distribution is obtained from a bin-by-bin smearing of the total event yield following Poisson statistics.

$M_{l\nu b}$ tends to be broad and softer. In $t\bar{t}$ events, a peak is present but it is broadened with respect to the signal by several effects. Since two b quarks are present in the final state, we expect to pick up the one not coming from the same top quark as the selected muon in about 50% of the cases. In addition, more than one neutrino contributes to the missing transverse energy if both W bosons from the top-quarks decay leptonically. As will be discussed in the next chapter, the shape information of the invariant top-quark mass spectrum can be exploited to determine the fraction of signal events in the finally selected event sample.

5.3.3   The Polarization of the Top Quark

A specific feature of the signal, stemming from the $V - A$ structure of the weak interaction, is the almost 100% left-handed polarization of the top quark with respect to the spin axis. As introduced in section 1.3.3, the direction of the top-quark spin is reflected in angular correlations of its decay products. In order to maximize the effect the direction of the d-type quark is chosen as spin basis, since about 95% of the

produced top-quark spins are polarized along this direction. The exact direction of the d-type quark is not directly observable in the experiment, and therefore has to be approximated. In the spectator basis, the direction of the spectator jet is used as top-quark spin axis, where the spectator jet is the jet emerging from the outgoing light quark in the final state. As shown in table 5.6, the untagged jet matches the recoiling light quark in almost 90% of the cases. Therefore, the spin axis can be reasonably approximated by the direction of the untagged jet. Since the spin axis is chosen
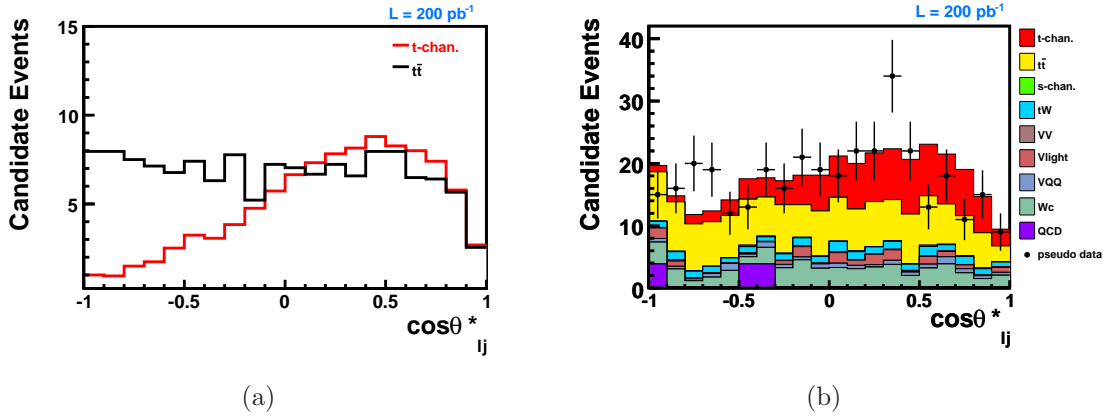
Figure 5.12: Cosine of the angle between the charged muon and the untagged jet, as measured in the reconstructed top-quark rest-frame after the full event selection. Subfigure (a) compares this distribution for the signal to the main background process $t\bar{t}$. The expected distribution in the selected event sample normalized to $L = 200\,\mathrm{pb}^{-1}$ is shown in (b). The pseudo data distribution is obtained from a bin-by-bin smearing of the total event yield following Poisson statistics.

differently when reconstructed objects are considered, the decay angle θ_{lj}^* is now defined as the angle between the direction of the charged lepton and the untagged jet, as measured in the top-quark rest-frame. Figure 5.12 (a) compares the expected distribution of $\cos\theta_{lj}^*$ in the selected event sample for the signal and the dominant background process $t\bar{t}$. Comparing the reconstructed observable to the generated $\cos\theta$ shape (see figure 1.9), one can see that the event rate is strongly suppressed in the region $\cos\theta_{lj}^* \sim 1$ as a consequence of the muon selection. A value of $\cos\theta_{lj}^*$ close to one implies that, in the top-quark rest-frame, the muon has the same direction as the light-quark jet, thus being reconstructed in rather forward regions and nearby a jet object. However, muon candidates produced in the forward region are rejected by the trigger acceptance of $|\eta| < 2.1$. At the same time, the required transverse momentum threshold of $20\,\mathrm{GeV}/c$ tends to select muon candidates reconstructed rather centrally. In addition, the isolation requirement avoids the muon direction to be close to the jet direction. Nevertheless, the characteristic angular correlation between the muon and the untagged jet is preserved to a high level despite selection and reconstruction effects. The expected distribution of the cosine of θ_{lj}^* for all processes after the event selection is shown in figure 5.12 (b). Since the specific angular correlation as a unique property of the signal is preserved, the distribution

can again be used to determine the fraction of signal events in the selected event sample, as will be discussed in the following chapter. In order reduce the sensitivity of the distribution to the above discussed selection effects the considered range of $\cos\theta^*_{lj}$ is in the following restricted to $[-1, 0.75]$. This additional event selection cut yields 89 signal events and a total of about 210 background events. The single event yields for each considered process are listed in table 5.7.

Process	$N^{\mathrm{MC}}_{\mathrm{evt}}$	$\epsilon^{\mathrm{tot}}_{\mathrm{sel}}$	$N^{\mathrm{exp}}_{\mathrm{evt}}$
t-channel	2,951	1.05%	89.0±1.7
s-channel	58	0.48%	1.6±0.2
tW	573	0.34%	19.7± 0.8
$t\bar{t}$	1,361	0.15%	124.5±3.4
Wc	271	0.0090%	26.8±1.6
$Wb\bar{b}$	107	0.0682%	7.4±0.7
$Wc\bar{c}$	21	0.0040%	0.9±0.2
W+light	13	0.0001%	10.9±2.5
$Zb\bar{b}$	42	0.0270%	2.4±0.4
$Zc\bar{c}$	5	0.0014%	0.2±0.1
Z+light	3	0.0003%	1.8±1.1
WW	11	0.0054%	0.8±0.2
WZ	41	0.0172%	1.1±0.2
ZZ	16	0.0080%	0.17±0.04
μ-en. QCD	3	0.00005%	12±6.7
Total background			210±8.1
$S/\sqrt{B}$			6.0

Table 5.7: Expected event yield for an integrated luminosity of $L = 200\,\mathrm{pb}^{-1}$ in the restricted $\cos\theta^*_{lj}$ range [-1, 0.75]. The table shows the number of selected MC events ($N^{\mathrm{MC}}_{\mathrm{evt}}$), the total event selection efficiency ($\epsilon^{\mathrm{tot}}_{\mathrm{sel}}$), and the number of events expected in a data sample corresponding to an integrated luminosity of $200\,\mathrm{pb}^{-1}$ ($N^{\mathrm{exp}}_{\mathrm{evt}}$). The quoted uncertainties reflect the limited MC statistics.

5.3.4   The Pseudorapidity of the 2nd Jet

A distinct kinematic feature of the t-channel single top-quark production mode is the direction of the untagged jet. This jet, most likely stemming from the recoiling light quark, is often reconstructed in the forward region ($|\eta| \geq 3$). Figure 5.13 (a) shows a comparison of the pseudorapidity distribution of the untagged jet (lj) for top-quark pair events and signal events after having passed the full event selection. Requiring the untagged jet to have $|\eta| > 2.5$ would yield a very clean signal sample containing only a minor background contribution. To illustrate the purity of this subset, the resulting invariant top-quark mass spectrum is shown in figure 5.14. The sample is dominated by about 44 signal events, while only two background processes

remain which contribute perceptibly, namely $t\bar{t}$ with about 12 and Wc with about 5 expected events, normalized to $L = 200\,\text{pb}^{-1}$.

(a)   (b)
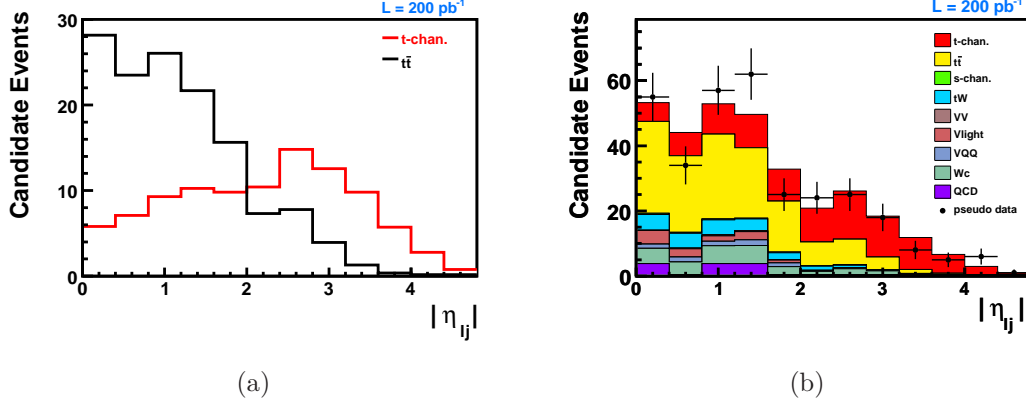
Figure 5.13: Pseudorapidity distribution of the untagged jet after having passed the full event selection. Subfigure (a) shows a comparison between top-quark pair and signal events, (b) shows the pseudorapidity distribution as expected in a selected data sample normalized to $L = 200\,\text{pb}^{-1}$. The pseudo data distribution is obtained from a bin-by-bin smearing of the total event yield following Poisson statistics.

The jet reconstruction in the forward region for absolute pseudorapidity values above 3.0 relies on the hadron forward calorimeter. While the energy and position resolution of this calorimeter is expected to perform very well [126], this subdetector combines electromagnetic and hadronic measurements which makes it a special calorimeter. Furthermore, the uncertainties on the theoretical description of jet production in high pseudorapidity regions are not well understood and a precise modeling of the forward-jet information becomes difficult. A validation of the forward region with collision data will thus be essential prior to an extensive use of its information. Therefore, the pseuodrapidity of the untagged jet has been discarded for the present studies, but nevertheless might prove to be useful for future analysis strategies.

.

(a)
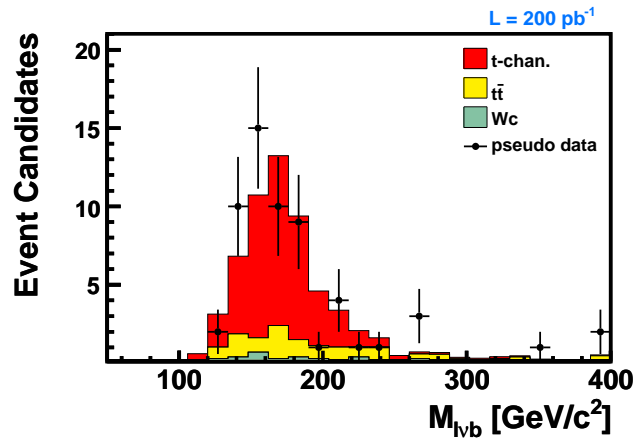
Figure 5.14: $M_{l\nu b}$ spectrum for events with a jet passing the forward jet requirement of $|\eta| > 2.5$, normalized to $L = 200\,\mathrm{pb}^{-1}$. Only the main background processes, $t\bar{t}$ and Wc, are shown.

Chapter 6

Prospects for an Observation of Single Top-Quarks

The goal of the present study is to evaluate the prospects for a cross-section measurement of electroweakly produced top-quarks in the t-channel in an analyzed data amount of $200\,\mathrm{pb}^{-1}$ collected at a center-of-mass energy of $10\,\mathrm{TeV}$. As shown in section 5.1.3, the presented event selection strategy yields a naive signal significance of $S/\sqrt{B} = 6.7$. However, this estimate omits any uncertainties on the background rates, which are always present and not well controlled as long as the rates are not explicitly measured in LHC collision data. These uncertainties will directly affect the significance of a simple counting experiment. In order to minimize model-dependent assumptions on the main background contributions, the signal fraction in the candidate-event sample is determined by a template fit, exploiting the full shape information of a discriminating observable.

The first part of this chapter describes the signal extraction method, covering the statistical concept of the binned likelihood fit, hypothesis testing, and pseudo-experiments, as well as the extraction of suitable templates for different processes. After having presented the estimated fit uncertainty and the expected sensitivity of the method, several sources of systematic uncertainties are studied. Their impact on the signal extraction and on the sensitivity of the method is examined in the second part of this chapter.

6.1 Signal Extraction

The cross section for single top-quark production is extracted by fitting the templates of the signal and various background processes to a discriminating observable distribution obtained from pseudo data using a binned likelihood fit. Two separate discriminating observables are studied here, the invariant top-quark mass $M_{l\nu b}$ and the polarization variable $\cos\theta^*_{lj}$. After introducing the statistical framework, the templates for the different classes of processes which are used for the fit are defined. In order to study the effect of background fluctuations several scenarios are tested with different assumptions on the background rate uncertainty. Finally, the statistical uncertainty of the signal extraction and the expected sensitivity of the method

obtained from the different scenarios are discussed.

6.1.1   Statistical Method

In order to determine the signal fraction in the final sample of candidate events, a binned maximum likelihood fit to a discriminating observable distribution is performed. The likelihood function L, consisting of two terms, is given by

$$L(\beta_1, \ldots, \beta_C) = \prod_{k=1}^{B} P(n_k|\mu_k) \cdot \prod_{j=2}^{C} G(\beta_j|1, \Delta_j) \,, \qquad (6.1)$$

where B is the number of bins, k is the bin index, C is the number of processes including the signal, and j is the process index. The signal process is labeled with $j = 1$, the background processes have indices $j = 2, ..., C$. The likelihood function depends on the parameters $\beta_j = \nu_j/\hat{\nu}_j$, representing the ratio of the measured number of events ν_j to the predicted number of events $\hat{\nu}_j$ for process j. Therefore, β_j can be interpreted as the ratio of the measured to the predicted cross section for process j. The parameter of interest is β_1 which represents the ratio of the measured and the predicted number of single top-quark events. The Δ_j are the relative uncertainties on the predicted number of background processes.

The first term, $P(n_k|\mu_k)$, of equation 6.1 represents the Poisson distribution of the observed number n_k of selected events per bin k:

$$P(n_k|\mu_k) = \frac{\mu_k^{n_k}}{n_k!} \cdot e^{-\mu_k} \,, \qquad (6.2)$$

where μ_k is the expected number of events in bin k of the fitted observable distribution, taken as the sum of the expectations for signal and background processes for this specific bin,

$$\mu_k = \sum_{j=1}^{C} \mu_{jk} = \sum_{j=1}^{C} \beta_j \cdot \hat{\nu}_j \cdot \alpha_{jk} \,, \qquad (6.3)$$

where α_{jk} is the fractional content of the normalized histogram of the chosen sensitive observable in bin k for process j. This quantity fulfills $\sum_{k=1}^{B} \alpha_{jk} = 1$, $\forall j$.

Considering only the Poisson term of the likelihood, the normalization β_j of each background process is treated as a free parameter in the fit. However, it is reasonable to include existing a priori knowledge of the uncertainties of the rates of the processes into the likelihood function and thus to increase the robustness of the application of the maximum likelihood technique. The restriction of process rates is provided by the second term of equation 6.1, a Gaussian centered at one and with a standard deviation Δ_j given by the assumed relative rate uncertainty:

$$G(\beta_j|1, \Delta_j) = \frac{1}{\sqrt{2\pi}\Delta_j} \cdot \exp\left(\frac{-(\beta_j - 1)^2}{2\Delta_j^2}\right) \,. \qquad (6.4)$$

The negative logarithm of the likelihood function is simultaneously minimized for all the fit parameters β_j. The minimization is performed using the MINUIT [127]

package. This yields the maximum value of the likelihood function which is determined by the signal parameter $\hat{\beta}_1$ and a set of background parameters $\hat{\beta}_j$.

Hypothesis Testing

To compute the sensitivity of the method to a potentially observed signal, a hypothesis test is carried out to determine whether the candidate events are preferring the signal-plus-background hypothesis or the background-only hypothesis. The first hypothesis, H_1, assumes that the signal cross-section is the one predicted by the SM, fixing $\beta_1 = 1$. The second one, H_0, assumes that the signal cross-section is zero, setting $\beta_1 = 0$. The objective of the analysis is to observe single top-quark events, thus rejecting the null hypothesis H_0. For each of the two considered hypotheses, an ensemble test of pseudo-experiments is conducted, where a pseudo-experiment represents the simulation of one potential measurement in data. A set of pseudo-experiments based on the same requirements is called ensemble test. For each of these pseudo-experiments the number of events N_j of a process j is drawn from a Poisson distribution of mean $\hat{\nu}_j$, while the number of events of a constrained process are drawn according to a Gaussian with mean $\hat{\nu}_j$ and width $\hat{\nu}_j \cdot \Delta_j$. In addition, the uncertainty due to the limited amount of simulated events is incorporated by fluctuating for each template the number of entries in each bin k. The fluctuated bin content is drawn from a Gaussian with mean k and width d_k representing the uncertainty in the bin.

The hypothesis test is based on a test statistic Q defined as:

$$Q = -2 \cdot \ln \frac{L(\hat{\beta}_1 = 1, \hat{\beta}_j)}{L(\hat{\beta}_1 = 0, \hat{\beta}_j)} \,. \tag{6.5}$$

This choice of the test statistic is motivated by the Neyman-Pearson lemma [128], which indicates that the likelihood ratio is an optimal test for separating the two hypotheses. To evaluate the expected false discovery rate of the analysis assuming the SM a comparison to the null hypothesis H_0 has to be performed using the Q-value distributions. The Q-value distribution obtained from the separate ensemble tests are q_0 for the H_0 hypothesis and q_1 for H_1. With these distributions, the expected significance level can be determined at which H_0 can be rejected assuming H_1 to be true. For this purpose the so-called p-value is defined via:

$$\hat{p}(Q_m) = \frac{1}{A_q} \cdot \int_{-\infty}^{Q_m} q_0(Q) \, dQ \,, \tag{6.6}$$

where $A_q = \int_{-\infty}^{\infty} q_0(Q) \, dQ$ and Q_m is the median of q_1. The meaning of this expected p-value is the following: under the assumption that H_1 is true, one expects to observe $p < \hat{p}$ with a probability of 50%. The p-value can be converted into a number of standard Gaussian deviations σ using the integral of one side of a standardized Gaussian distribution:

$$\sigma = \sqrt{2} \cdot \mathrm{Erf}^{-1}(1 - 2(1 - p)) \,, \quad \text{with} \quad \mathrm{Erf}(z) = \frac{2}{\pi} \int_0^z e^{-t^2} \, dt. \tag{6.7}$$

The criteria used to claim evidence and observation are $p < 1.35 \cdot 10^{-3}$ and $p < 2.87 \cdot 10^{-7}$, which means to see a deviation over the background expectation only which corresponds to a background fluctuation of 3σ or 5σ, respectively.

6.1.2   Template Extraction

For the two considered discriminating observables, $M_{l\nu b}$ and the restricted $\cos\theta_{lj}^*$ in the range [-1, 0.75], templates have to be built, which provide the shape information of a certain process for the likelihood fit. It turns out that background processes belonging to the same physical category often show a very similar behavior in the studied observables. Due to the presence of such similarities, the likelihood fit can hardly separate the different contributions, leading to redundant degrees of freedom in the minimization process. In order to avoid such instabilities and to reduce complexity, processes with similar shapes are combined to one template representing a certain event category. Some templates can be built in situ from control samples containing an enlarged amount of events. The different event categories and the definition of the respective control regions, if exploited, are the following:

Top-Quark Processes:

Single top-quark production in the s-channel yields a shape similar to the t-channel in both $M_{l\nu b}$ and $\cos\theta_{lj}^*$, see figure 6.1 (a) and figure 6.1 (c). Thus, the s-channel is considered as a signal component in the fit, to be later subtracted according to the cross-section ratio predicted by the SM. The template for the combined t- and s- channel process is taken from the MC simulation, at which the properly weighted template for the s-channel is added to the corresponding weighted t-channel one.

As shown in figure 6.1 (b) and figure 6.1 (d) the $M_{l\nu b}$ and $\cos\theta_{lj}^*$ shapes are similar for $t\bar{t}$ and tW, motivating again the use of one common template, which is either taken from MC simulations, where the processes are again added with the proper weight, or assumed to be flat. A method to check the flatness of $\cos\theta_{lj}^*$ for $t\bar{t}$ events in an enriched control region is suggested below.

QCD:

The QCD template is obtained from the anti-isolated sample where no b-tag requirement is applied, as discussed in section 5.2, with the addition of the $M_{\mathrm{T}} > 50\,\mathrm{GeV}/c^2$ cut. This particular selection sequence is referred to as "pretagMTW" in the following. The shape comparisons between this control sample and the final candidate-event sample are shown in figure 6.1 for $M_{l\nu b}$ (e) and $\cos\theta_{lj}^*$ (f). There is a good agreement for the invariant top-quark mass spectrum within the statistical uncertainties, whereas the shape of the polarization variable seems to exhibit a non-flat structure. The impact of this deviation is specifically addressed in section 6.2.2.
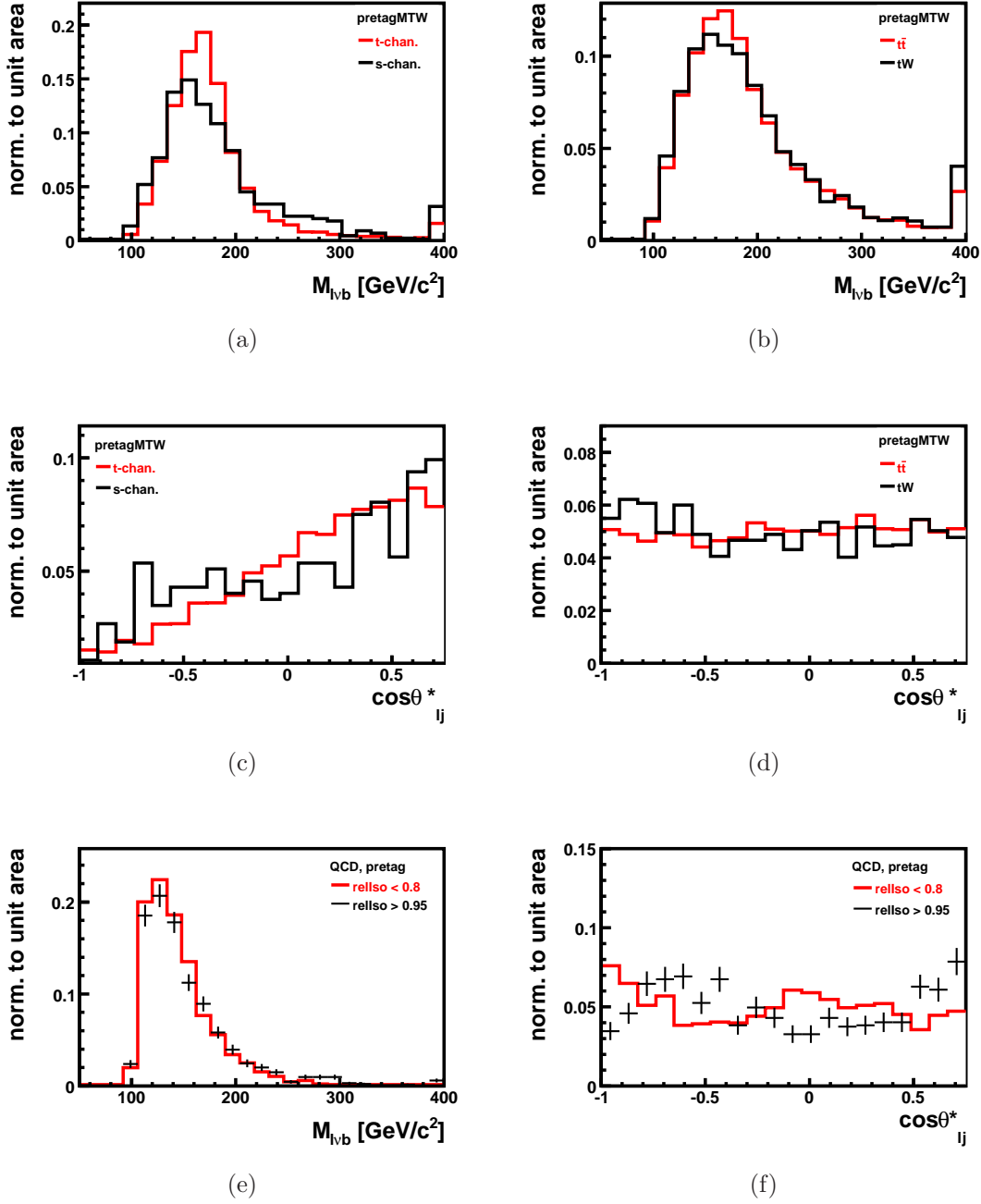
Figure 6.1: Comparison of $M_{l\nu b}$ shapes for t- and s-channel single top-quark production (a), and $t\bar{t}$ and tW production (b), and of the restricted $\cos\theta^*_{lj}$ for t- and s-channel single top-quark production (c), and $t\bar{t}$ and tW production (d). The comparison is performed for a selection without the b-tagging requirement in order to enhance the number of events while applying the cut on the transverse W-boson mass. This particular candidate-event sample is referred to as "pretagMTW". The lower row shows the shape for QCD events with anti-isolation (relIso < 0.8) compared to the distribution obtained with the standard isolation (relIso > 0.95) for $M_{l\nu b}$ (e) and the restricted $\cos\theta^*_{lj}$ distribution (f).

W+X:

Events of the W+X as well as of the Z+X family tend to be similar to each other, see figures 6.2 (a) and (c), and figures 6.2 (b) and (d), respectively for $M_{l\nu b}$ and $\cos\theta^*_{lj}$. Since the two categories are also similar to each other and the Z+X contribution is expected to be almost negligible, a combined W/Z+X template is used, in the following referred to as "W+X" only. It is obtained from a W-boson enriched MC sample where no b-tagging is applied. The comparison of the resulting distributions to the ones obtained from the standard event selection is shown in figure 6.2 (e) and (f) for both discriminating observables. Due to the small number of remaining MC events after the standard event selection, the meaning of this comparison is weak. However, in figure 6.2 (a) and figure 6.2 (c) it has been demonstrated that the shapes of the different W-boson processes are similar to each other in the pretag sample. Requiring a b-tagged jet modifies in first approximation simply the composition of the W+X sample by suppressing significantly the W + light fraction. Therefore, it is assumed that using the pretag sample to extract the W+X template has a negligible effect. For future analysis iterations, when the number of available simulated events of the W+X process are significantly larger, this approximation might become redundant, since a statistically stable template can be extracted from the sample having passed the standard selection.

No specific template has been considered for diboson events due to the smallness of their contribution and their resemblance with the W+X process family. Since both considered observables, $M_{l\nu b}$ and $\cos\theta^*_{lj}$, require the top-quark momentum information, the choice of the reconstructed top-quark candidate in the control samples with no b-tagging applied has to be modified. Here, the most central jet in the event is assigned to the b quark from the top-quark decay.

The ultimate fit templates representing the four different process categories are shown in figure 6.3 for both discriminating observables $M_{l\nu b}$ (a) and $\cos\theta^*_{lj}$ (b). It can be seen that for $\cos\theta^*_{lj}$ the background templates deviate very little from flatness, which suggests the usage of only one flat distribution approximating all the background processes. A significant deviation is observed for the QCD processes. However, this is a relatively minor contamination and the impact of the deviation of its shape from flatness for this process as well as for the other background categories is evaluated in a dedicated robustness test in section 6.2.2.

The flatness of $t\bar{t}$ events in $\cos\theta^*_{lj}$, which is a crucial assumption for the fit to this variable since $t\bar{t}$ events constitute the main background contribution, can be tested in a $t\bar{t}$ control region. Such an enriched sample can be obtained by selecting events where the second jet fulfills the loose b-tag as well, thus fails the b-veto. The event yield of this orthogonal selection is shown in table 6.1, and the expected $\cos\theta^*_{lj}$ shape for this sample is provided in figure 6.4. Due to the relatively low purity of this control region of about 64%, one needs to correct for the residual presence of signal events in order to test the flatness. This can be done in an iterative procedure. The result of the full signal extraction can be used to estimate the signal contamination in this sample, and its contribution can be subtracted. A more natural strategy, however, would be to enhance the purity of the control region such that an iterative
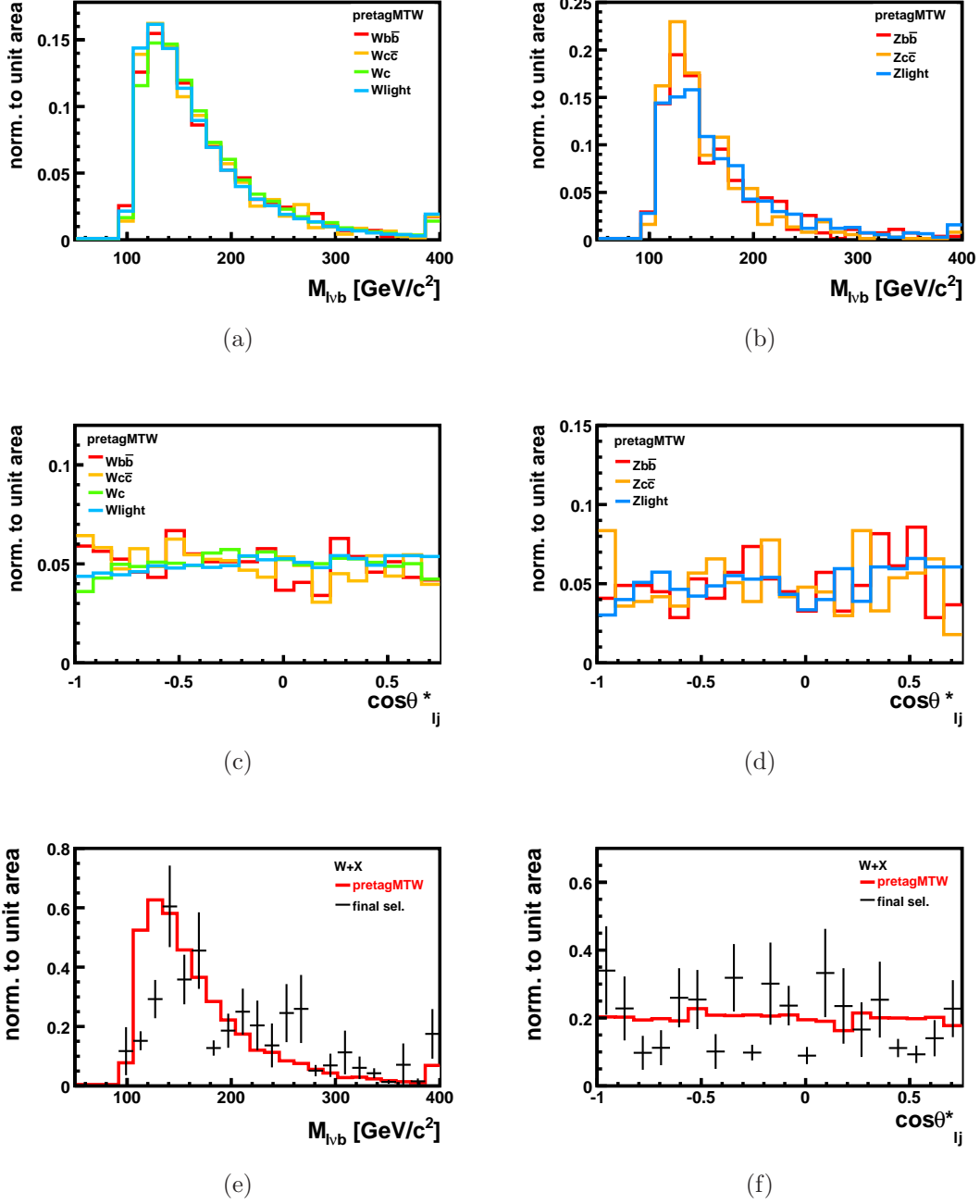
Figure 6.2: Comparison of $M_{l\nu b}$ shapes for W+X (a) and Z+X (b), and of restricted $\cos\theta^*_{lj}$ shapes for W+X (c) and Z+X (d). The comparison is performed for a selection without the b-tagging requirement in order to enhance the number of events while applying the cut on the transverse W-boson mass. This particular candidate-event sample is referred to as "pretagMTW". The combined W+X shapes obtained from this "pretagMTW" sample are compared to the result of the standard selection for $M_{l\nu b}$ (e) and the restricted $\cos\theta^*_{lj}$ (f).

(a)

(b)
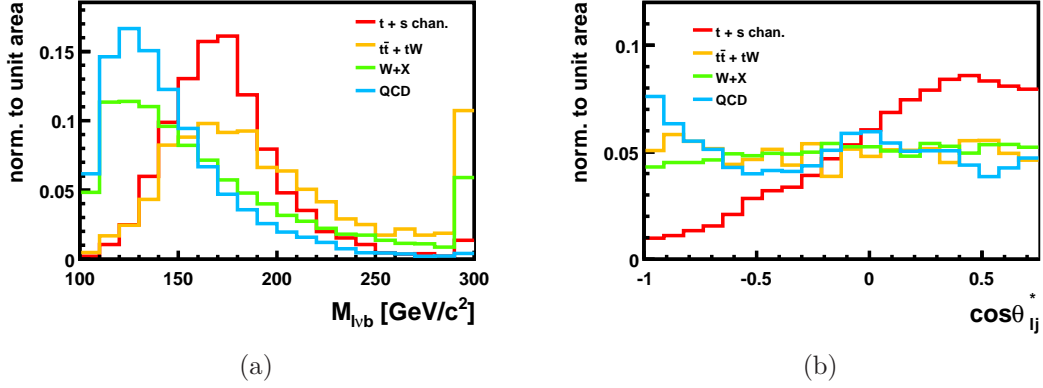
Figure 6.3: Final fit templates for $M_{l\nu b}$ (a) and the restricted $\cos\theta^*_{lj}$ (b). For both discriminating observables, four process categories are distinguished: $t + s$ chan., $t\bar{t} + tW$, W+X, and QCD.

procedure can be avoided. Looking at the discriminator value of the jet that does not pass the tight b-tagging criteria, shown in figure 5.5 (a), one can see that the region of large discriminator values is dominated by jets from $t\bar{t}$ events, whereas the signal contribution is already negligible at values above 2.5. Thus, using a tighter working point for the second b-jet veto would yield a $t\bar{t}$ sample with a much higher purity, suitable for a prompt check of the flatness of this background contribution in the observable $\cos\theta^*_{lj}$.

Process	$N^{\mathrm{MC}}_{\mathrm{evt}}$	$N^{\mathrm{exp}}_{\mathrm{evt}}$	$f[\%]$
t-channel	705	20.8	14.3
s-channel	107	2.9	2.0
tW	191	6.6	4.5
$t\bar{t}$	1,016	92.9	64.0
QCD	1	3.9	2.7
$Wb\bar{b}$	134	9.3	6.4
$Wc\bar{c}$	13	0.6	0.4
Wc	40	4.0	2.8
$W+$ light	5	4.2	2.9

Table 6.1: Event yields for the main processes in the $t\bar{t}$-enriched selection accepting events which failed the second-b veto. The table shows the number of selected MC events ($N^{\mathrm{MC}}_{\mathrm{evt}}$), the number of expected events normalized to $L = 200\,\mathrm{pb}^{-1}$ ($N^{\mathrm{exp}}_{\mathrm{evt}}$), and the fraction f of events of each process in percent.
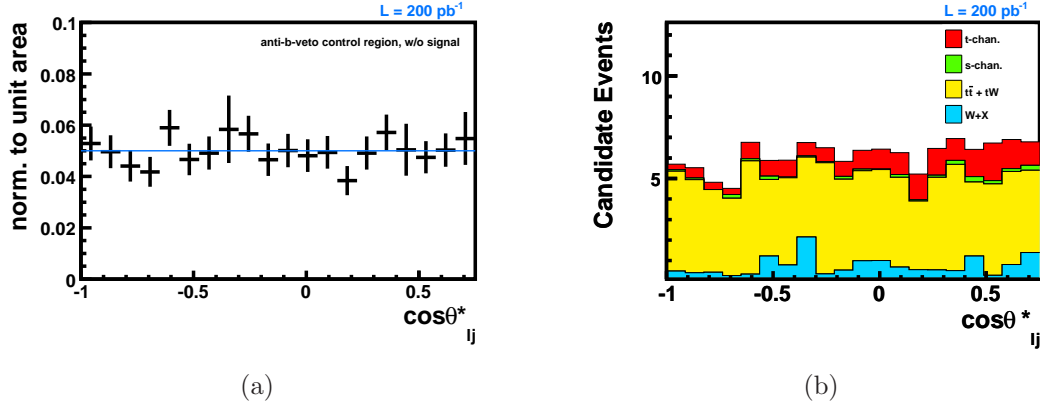
Figure 6.4: Distribution of the restricted $\cos\theta^*_{lj}$ for events in the $t\bar{t}$-enriched control region, that is for events failing the second b-veto. The shape for these events except for the signal contribution is shown in (a), indicating a flat behavior. The expected distribution including the t-channel signal fraction and normalized to $L = 200\,\mathrm{pb}^{-1}$ is shown in (b).

6.1.3 Fit to the Discriminating Observables

The signal parameter β_1 and the background parameters β_j of the likelihood function given in equation 6.1 are estimated by minimizing the negative logarithm of the likelihood function. This is done separately for the two studied observables, $M_{l\nu b}$ and the restricted $\cos\theta^*_{lj}$. Table 6.2 summarizes the used event yield estimates for the different process categories. For both variables, different scenarios are considered with varied assumptions on the background uncertainties. These scenarios as well as the results of the fit are presented in the following.

	$M_{l\nu b}$	$\cos\theta^*_{lj}$ [-1,-0.75]
Process	$N_{\mathrm{evt}}^{\mathrm{exp}}$	$N_{\mathrm{evt}}^{\mathrm{exp}}$
t/s-channel	103	91
$t\bar{t}/tW$	158	144
QCD	22	22
$W + X$	50	46

Table 6.2: Expected number of events for the different process categories used for the fit to $M_{l\nu b}$ and the restricted $\cos\theta^*_{lj}$ distribution, normalized to $L = 200\,\mathrm{pb}^{-1}$.

Fit to the Invariant Top-Quark Mass $M_{l\nu b}$

Concerning the fit to $M_{l\nu b}$ four different scenarios are tested, each applying a different restriction of background processes driven by the assumption of an a priori knowledge of the expected process rate. Thereof, one scenario (S_1) is treated as

the standard scenario, where the applied constraints are motivated by the following considerations. The rate of $t\bar{t} + tW$ events is constrained within $\pm 20\%$, which is motivated by studies for the prospect of early top-quark pair production cross-section measurements [15]. The most important issues with the simulation of W+X processes will be the radiation modeling, affecting the number of jets with a chance to pass the transverse-momentum threshold of the event selection, and the fraction of W/Z-boson production in association with heavy flavor quarks. Since both of them will require much work to be extracted from data, their combined rate is unconstrained in the standard scenario S_1. For the QCD background, an uncertainty of 40% is applied, following the estimation of the data-driven method described in section 5.2. Variations to these baseline assumptions provide additional scenarios, which are defined as follows:

- S_2: as S_1, but the rate of W+X processes is constrained within $\pm 50\%$ compared to the nominal value

- S_3: as S_1, but the rate of $t\bar{t} + tW$ processes is constrained within $\pm 50\%$ compared to the nominal value

- S_4: as S_1, but the rate of $t\bar{t} + tW$ processes is unconstrained

The different scenarios with the corresponding parameter constraints are listed in table 6.3.

Fit to the Polarization Variable $\cos\theta_{lj}^*$

In the case of the polarization variable $\cos\theta_{lj}^*$ the fit is restricted to the $[-1, 0.75]$ interval corresponding to the region of linear rise. This choice is motivated by the fact that this restriction reduces the sensitivity to all the modeling details affecting isolation and other aspects of the muon selection, thus permits the template extraction from anti-isolated control samples. As already implied above, the standard fitting scenario, S_{flat}, assumes a flat background model, thus the likelihood function to be minimized depends only on two parameters, the signal parameter β_1 and an overall background parameter β_2, representing the sum of all background contributions, which is unconstrained. Two scenarios are considered in addition to this approximation, based on the four different process categories shown in figure 6.3 (b) separately. The choice of background constraints corresponds to the S_1 and S_2 scenarios used for $M_{l\nu b}$, as described in the previous passage.

Results

Prior to the evaluation of physical results for the signal estimation and of the expected uncertainties for all the different scenarios, the method is tested for consistency. In order to check the linear behavior of the fitting mechanism, the signal input parameter $\beta_{1,\text{in}}$ is subsequently increased in steps of 0.2 in the interval $I = [0, 2]$ and compared to the corresponding fit response $\beta_{1,\text{fit}}$. The result exhibits a linear correlation over the whole tested range as shown in figure 6.5 (a) and (b) for the two

considered discriminating observables. To control the deviation of the fitted signal parameter $\beta_{1,\text{fit}}$ from the input parameter $\beta_{1,\text{in}}$, the so-called pull is defined as:

$$\text{pull}(\beta_{1,\text{fit}}) = \frac{\beta_{1,\text{fit}} - \beta_{1,\text{in}}}{\sigma(\beta_{1,\text{fit}})} \,, \tag{6.8}$$

with $\sigma(\beta_{1,\text{fit}})$ being the uncertainty on the parameter $\beta_{1,\text{fit}}$ as obtained from the minimization procedure. Assuming an unbiased fit method, the pull distribution evaluated from a set of pseudo-experiments should be centered at zero. The width of this distribution reflects the quality of the uncertainty estimation of the fit method. If the deviation of the fit input value β_{in} from the result β_{fit} is on average of the same size as the uncertainty estimated by the fit, the width of the pull distribution is close to one. The obtained well-behaved pull distributions for the fits to the two discriminating observables are shown in figure 6.5 (c) and (d), respectively.
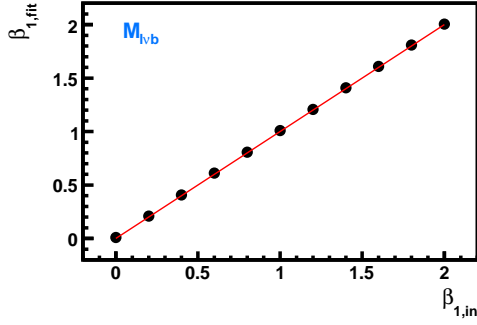
(a)
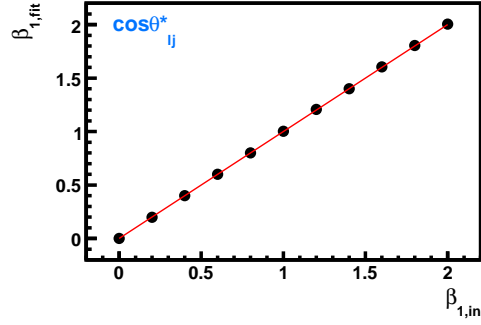
(b)
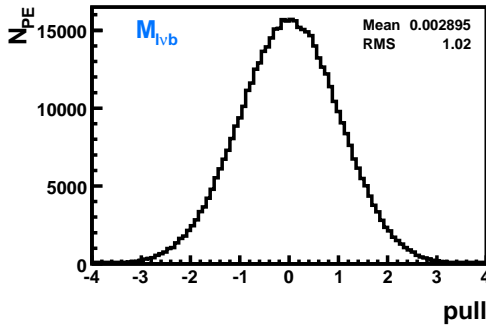
(c)
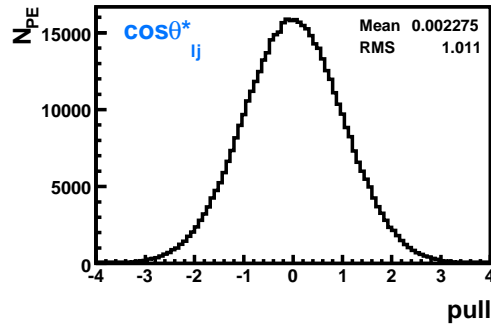
(d)

Figure 6.5: Linearity check for $M_{l\nu b}$ in the standard scenario S_1 (a) and $\cos\theta^*_{lj}$ in the standard scenario S_{flat} (b). The pull distributions are shown in the lower row for $M_{l\nu b}$ (c) and $\cos\theta^*_{lj}$ (d). Both distributions are centered at zero and have a width close to one.

In order to estimate the statistical uncertainty of the method, pseudo-experiments are conducted, each yielding an estimate for the signal parameter β_1. In the asymptotic case of large event numbers, β_1 follows a Gaussian distribution and the width

(a)   (b)
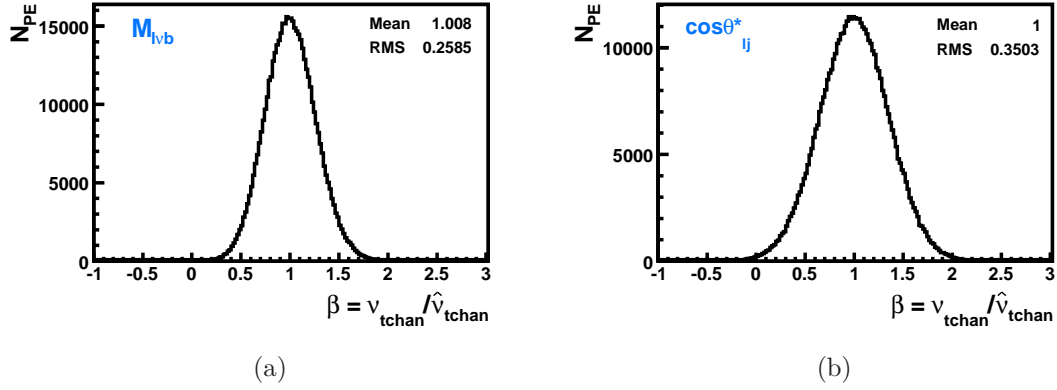
Figure 6.6: Distribution of the signal parameter β_1 as obtained from 500,000 pseudo-experiments for $M_{l\nu b}$ in the S_1 scenario (a) and $\cos\theta^*_{lj}$ in the S_{flat} scenario (b).

of the obtained β_1 spectrum can be interpreted as the statistical uncertainty of the fitting method. Figure 6.6 shows the β_1 distributions for $M_{l\nu b}$ and $\cos\theta^*_{lj}$ in the S_1 and S_{flat} scenarios, respectively. Evaluating these distributions yields statistical uncertainties of 26% for $M_{l\nu b}$ as discriminating observable, whereas the fit to $\cos\theta^*_{lj}$ yields an uncertainty of 35%. The expected sensitivities obtained from a hypothesis test based on the corresponding Q-value distributions (equation 6.5) are 3.5σ for $M_{l\nu b}$ and 2.8σ for $\cos\theta^*_{lj}$. A summary of the resulting statistical uncertainties as well as the expected sensitivities for all considered fitting scenarios can be found in table 6.3.

As can be seen from this summary, the more a priori knowledge is provided, which means background rates are constrained, the smaller becomes the statistical uncertainty. A comparison of the different scenarios also shows that, in the case of $M_{l\nu b}$, the accuracy of the $t\bar{t} + tW$ rate constraint has a significant impact on the fit result. This is due to the fact that the shape of this process category is very similar to the signal shape, see figure 6.3 (a), except for a harder tail towards large $M_{l\nu b}$ values. Thus, the fit to $M_{l\nu b}$ profits from a precise control of the top-quark pair production cross-section. In comparison, the method seems to be rather stable when leaving the rate of W+X events free, since the shape of W+X processes is better separated from the signal shape than the $t\bar{t} + tW$ template is.

Looking at the results obtained from the different $\cos\theta^*_{lj}$ fit scenarios, the W+X rate has a more significant impact. Here, the shape is similar to the distribution of all the other background processes and thus introducing uncertainties to the minimization procedure. Reducing the degrees of freedom of the fit to one signal and only one background parameter, as in the flat scenario, provides a performance similar to the constrained scenario S_2, while leaving the background rate completely free.

Figure 6.7 shows the evolution of the expected sensitivity of the $\cos\theta^*_{lj}$ fits with increasing integrated luminosity. For the expected sensitivity to exceed 5σ the method presented here would require an integrated luminosity of about $500\,\text{pb}^{-1}$

Scenario		Constraints to BG Rates			RMS(β_1)	$S_{\exp}$
		$t\bar{t} + tW$	$W + X$	QCD		
$M_{l\nu b}$	S_1	$\pm 20\%$	-	$\pm 40\%$	0.26	3.5σ
	S_2	$\pm 20\%$	$\pm 50\%$	$\pm 40\%$	0.25	3.9σ
	S_3	$\pm 50\%$	-	$\pm 40\%$	0.30	3.2σ
	S_4	-	-	$\pm 40\%$	0.31	2.9σ
$\cos\theta^*_{lj}$	S_{flat}	-	-	-	0.35	2.8σ
	S_1	$\pm 20\%$	-	$\pm 40\%$	0.39	2.4σ
	S_2	$\pm 20\%$	$\pm 50\%$	$\pm 40\%$	0.31	3.1σ

Table 6.3: Summary of the studied fit scenarios for both discriminating observables $M_{l\nu b}$ (upper rows) and $\cos\theta^*_{lj}$ (lower rows). The constraints on the different background categories as well as the resulting widths of the signal parameter (RMS$_{\beta_1}$) and the obtained expected sensitivities $S_{\exp}$ are listed. A detailed description of the different fit scenarios is given in the text.

for the fit to $M_{l\nu b}$ and about $800\,\text{pb}^{-1}$ for the fit to $\cos\theta^*_{lj}$, considering statistical uncertainties as well as uncertainties on the expected background normalization. However, several systematic effects influence the shape of the templates and the expected rates of events. Their impact on the present analysis method is studied in the following section.
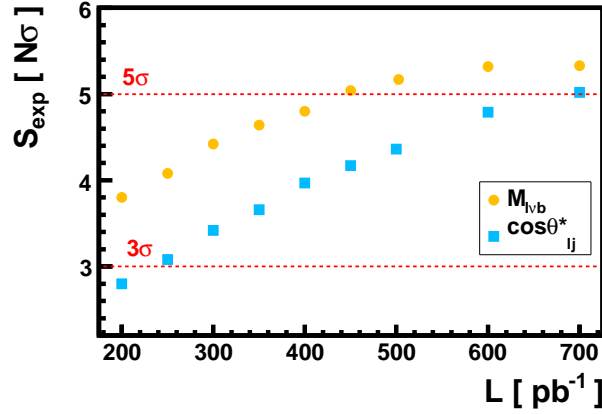
Figure 6.7: Evolution of the expected sensitivity with the integrated luminosity for $M_{l\nu b}$ (yellow dots) and for $\cos\theta^*_{lj}$ (blue rectangles) as obtained in the standard scenarios S_1 and S_{flat}, respectively. Statistical fluctuations of the method as well as uncertainties on the expected background rates are taken into account.

6.2   Systematic Uncertainties

In this section, the impact of systematic uncertainties on the expected sensitivity of the single top-quark extraction and therewith on the accuracy of a cross-section measurement is addressed. In the first part, the different considered sources of systematic effects and their influence to the expected event rates and the shapes of the two discriminating observables are discussed. In the second part, the systematic uncertainties are included in the statistical method and the analysis results are re-evaluated under consideration of these uncertainties.

6.2.1   Sources of Systematic Uncertainties

Several sources of systematic uncertainties have been studied in the context of the present analysis. They are involved due to assumptions made for the MC modeling, like the parametrization of the PDF or the parton shower configuration, or can have an instrumental origin, like the uncertainty on the jet energy scale or on the b-tagging. The different sources and the evaluation of their strength are discussed in the following.

PDF Parametrization

Since a particular parametrization of the PDF is used for the event simulation, this constitutes a potential source of systematic uncertainties. The CTEQ61 PDF [129] provides a set of 20 orthogonal pairs of eigenvalues corresponding to the uncertainties of its determination. Those are treated as independent systematic sources and their impact on the measurement is estimated by re-weighting the selected events and observing the variations in the event yields and on the $M_{l\nu b}$ and $\cos\theta_{lj}^*$ shapes. Figure 6.8 shows the relative variation of the selection efficiencies for the three re-weighted processes, signal, $t\bar{t}$, and tW, versus the PDF-set index. The deviations from the default value are dominated by one eigenvector in the positive and one in the
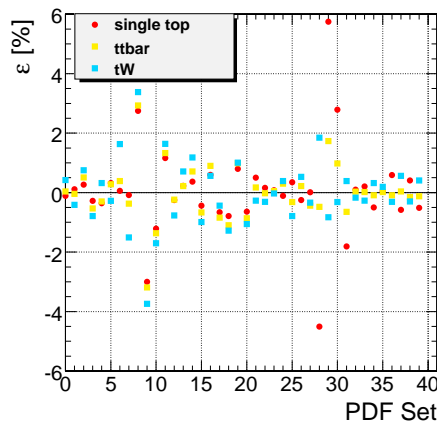
Figure 6.8: Relative variation (in %) of the selection efficiencies for signal, $t\bar{t}$, and tW, versus the PDF-set index in the CTEQ61 collection. [125]

negative direction. Sets number 28 and number 29 in the CTEQ61 collection are the PDF eigenvalues yielding the maximum upward variation of $+5.8\%$ and a maximum downward variation of -4.5% for the selection efficiency of signal events, while for both $t\bar{t}$ and tW sets number 8 and number 9 yield the most extreme deviations. The effect on the shapes of the two considered discriminating observables when comparing the default sample to the ones obtained from the samples re-weighted by the extreme sets is negligible, as can be seen in figure 6.9. The method suggested in [129] to estimate the overall effect of the PDF parametrization on an observable is approximated here by considering only the eigenvectors yielding the maximum rate variation for signal, $t\bar{t}$, and tW, respectively.

Process Modeling

The modeling of initial-state and final-state radiation, in the following referred to as ISR and FSR, has a direct impact on the event selection efficiency of a certain process, due to the modification of the jet topology of the event. Since top-quark pair production constitutes the dominant background fraction, the study of the modeling of ISR and FSR is concentrated on this particular process. However, since this effect is present for all processes, it is planned to extend the study to the full range of processes in future analysis iterations. In order to evaluate the impact of the uncertainty due to the ISR and FSR modeling, three different samples, processed with the fast detector simulation, have been compared to each other: a reference sample, a sample with higher radiation probability and one with lower radiation probability. The relevant settings varied in PYTHIA between the three samples are listed below, with the reference values put in parentheses:

- **Less Radiation:** In order to simulate a sample with a lower radiation probability, the so-called power shower was switched off in PYTHIA by setting `MSTP(68)`$= 1$. The concept of the power shower [130] is to enlarge the phase space being populated by the initial-state shower process by setting the shower starting scale to the center-of-mass energy of the hadron interaction. Disabling this mechanism, the maximal shower parameter is typically limited by the factorization scale μ_f.

- **More Radiation:** For the simulation of a higher radiation probability, the parameter `PARP(64)`, related to the maximal momentum transfer scale of the hard interaction $Q^2_{\max}$, was set to 1 (0.2), and the following parameters related to the QCD scale Λ_{QCD} were modified: `PARP(61)` $= 0.35$ (0.25), `PARP(72)` $= 0.35$ (0.25), and `PARJ(81)` $= 0.35$ (0.25).

The obtained jet multiplicity spectra for the three samples are compared to each other in figure 6.10 (a). As expected, the spectrum is slightly shifted to lower jet multiplicities for a reduced radiation probability, whereas a higher radiation probability leads to a slightly higher average jet multiplicity. A shape comparison of the different systematic samples for the two observables $M_{l\nu b}$ and $\cos\theta^*_{lj}$, as shown in figure 6.10 (b) and (c), confirms that the distributions agree with each other within the statistical uncertainties. However, the selection efficiency is affected due
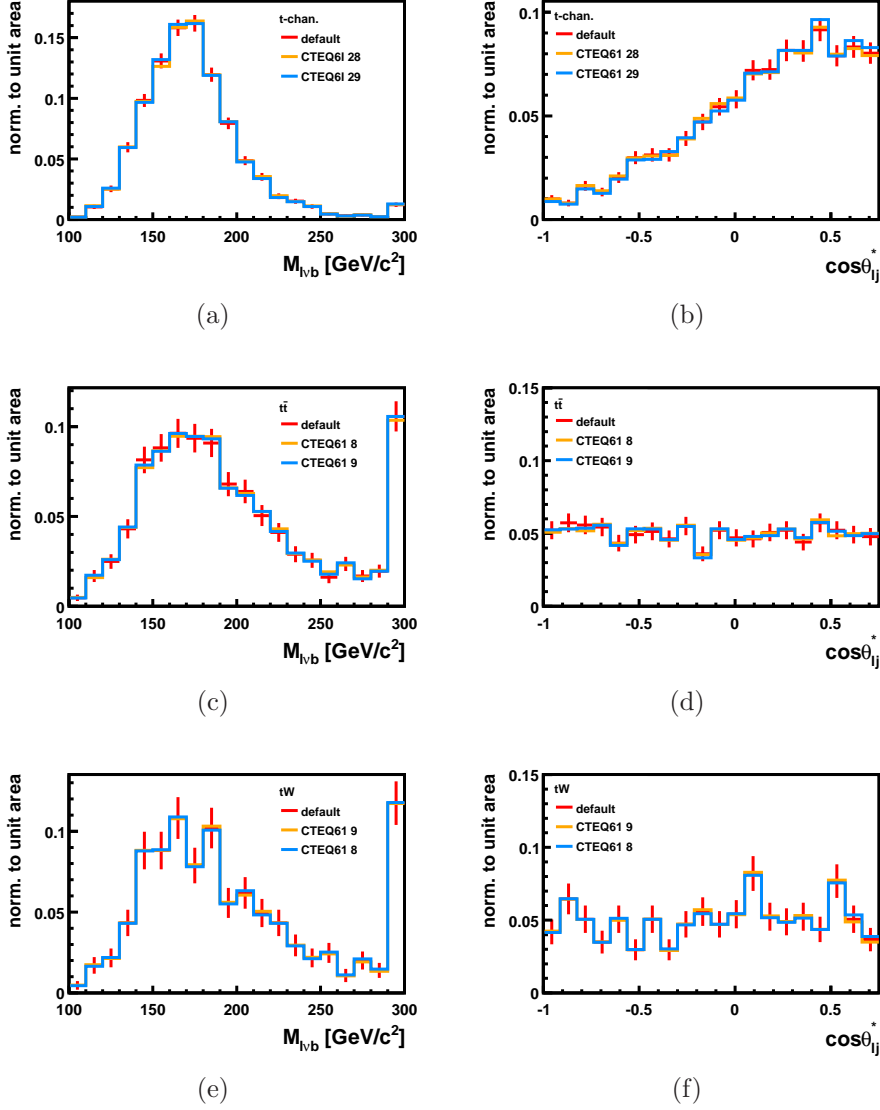
Figure 6.9: Shape comparison between the default sample and samples re-weighted by the PDF set yielding a maximal rate deviation, for $M_{l\nu b}$ (left column) and $\cos\theta^*_{lj}$ (right column). Only the main top-quark processes are considered: t-channel ((a), (b)), $t\bar{t}$ ((c), (d)), and tW ((e), (f)).

to the altered population of the 2-jet subsample. The impact of the variation on the yield of $t\bar{t}$ events after the standard selection is -6.3% for enhanced ISR/FSR and $+14.5\%$ for a lower ISR/FSR, respectively.

As a further test of the $t\bar{t}$ modeling, two samples simulated with different matrix-element calculations are compared to each other. While the standard sample is produced using MadGraph as matrix-element generator and PYTHIA for the parton shower and hadronization simulation, a second sample is simulated fully based on PYTHIA and interfaced with the Tauola package [131] for a proper decay handling of the τ leptons. Figure 6.11 shows the shape comparison for $M_{l\nu b}$ and $\cos\theta^*_{lj}$. No

(a)

(b)

(c)
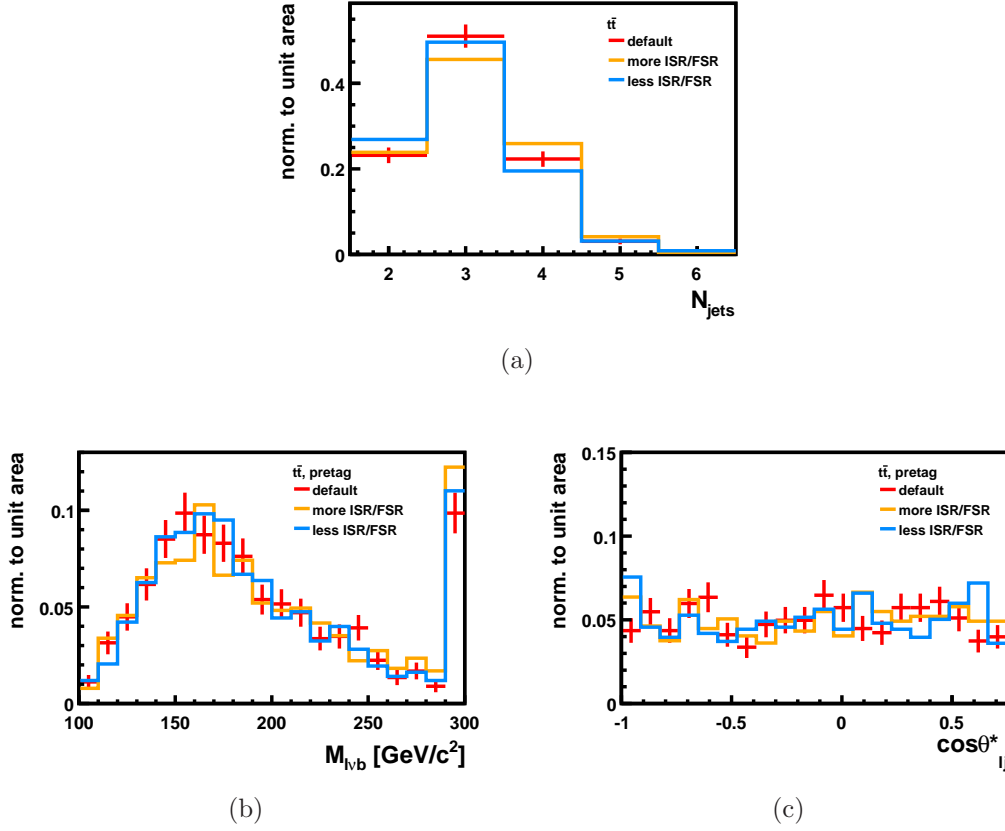
Figure 6.10: Comparison of jet multiplicity spectra for the different $t\bar{t}$ systematic samples with varied ISR/FSR settings (a). The corresponding shapes of the two discriminating variables are shown in (b) for $M_{l\nu b}$ and in (c) for the restricted $\cos\theta_{lj}^*$. The two observable distributions are extracted from the pretag sample where no b-tagging is applied in order to increase the number of simulated events.

significant difference is noticed within the statistical uncertainties. The event yield, however, is lower with respect to the MadGraph sample by about 10%.

Jet Energy Scale and $E_{\mathrm{T}}^{\mathrm{miss}}$

According to a study by CMS collaborators [120], the uncertainty on the JES from data-driven methods to extract jet calibrations is expected to be about $\pm 10\%$ in a scenario with more than $100\,\mathrm{pb}^{-1}$ of analyzed data. Therefore, a simultaneous variation of $1 + \alpha$ on all jet four-momenta is applied, where α can take the values $+10\%$ or -10%.

Concerning the missing transverse energy, two independent sources of uncertainties are considered. Since $E_{\mathrm{T}}^{\mathrm{miss}}$ has "Type-I" corrections implied due to the calibration of the calorimetric clusters associated to jets, its uncertainty is correlated to the JES uncertainty. In order to estimate this source of uncertainty, all jets with a transverse momentum above $20\,\mathrm{GeV}/c$ are corrected by the factors discussed above and $E_{\mathrm{T}}^{\mathrm{miss}}$ is recalculated accordingly. In a second step, an uncertainty for

(a)   (b)
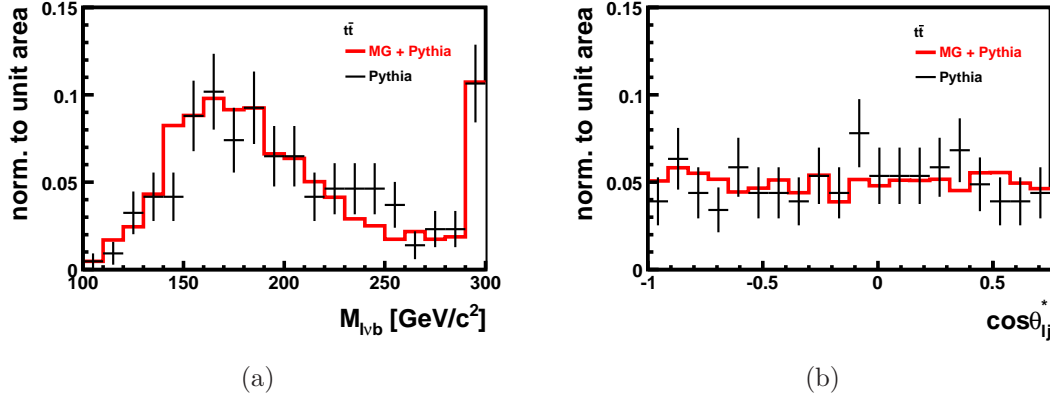
Figure 6.11: Shape comparisons of the invariant top-quark mass (a) and the restricted $\cos\theta_{lj}^*$ (b), for $t\bar{t}$ events where the hard process is generated using MadGraph ("MG + Pythia") or using PYTHIA ("Pythia") only.

the raw $E_{\mathrm{T}}^{\mathrm{miss}}$, obtained from a subtraction of the jet corrections, is considered. The fluctuation of the raw $E_{\mathrm{T}}^{\mathrm{miss}}$ is assumed to be uncorrelated to the JES uncertainty and thus additionally varied by $\pm 10\%$.

The impact of the JES and $E_{\mathrm{T}}^{\mathrm{miss}}$ rescalings on the shapes of $M_{l\nu b}$ and $\cos\theta_{lj}^*$ are shown in figure 6.12 and 6.13, respectively. The distributions for the top-quark processes are extracted from standard selection samples, while the W+X shapes are compared here in the pretag sample due to the limited number of events surviving the standard selection. As expected, the distribution of the invariant mass of the top quark is directly affected by a modification of the jet energy, while the polarization variable $\cos\theta_{lj}^*$ remains unchanged. Concerning the variation of $E_{\mathrm{T}}^{\mathrm{miss}}$, both discriminating observables exhibit a stable behavior within the statistical uncertainties.

b-Tagging

Several collision-data-based methods were studied to estimate the *b*-tagging efficiency as well as the mistag rate in [132] and [133], respectively. Three different scenarios were used, distinguished by the assumed amount of available collision data, thus driving the assumed precision of input parameters. The uncertainty values adopted for the present analysis correspond to a scenario assuming $L = 100\,\mathrm{pb}^{-1}$, since this is the one approximating best the analysis scenario. Considering the tight working point of the track counting algorithm, the studies cited beforehand obtain an uncertainty of 8.2% on the *b*-tagging efficiency and 18.1% on the mistag rate. For the loose working point, the uncertainties result as 8.0% for the efficiency and 3.4% for the mistag rate. These uncertainties have been translated into variations of the *b*-tagging discriminator by studying selected jets from signal events, being reconstructed within the tracker acceptance of $|\eta| < 2.5$ and in the following referred to as taggable. In order to extract a basis for the variation of the *b*-tagging efficiency and the mistag rate, the jets are separated into two categories based on the association
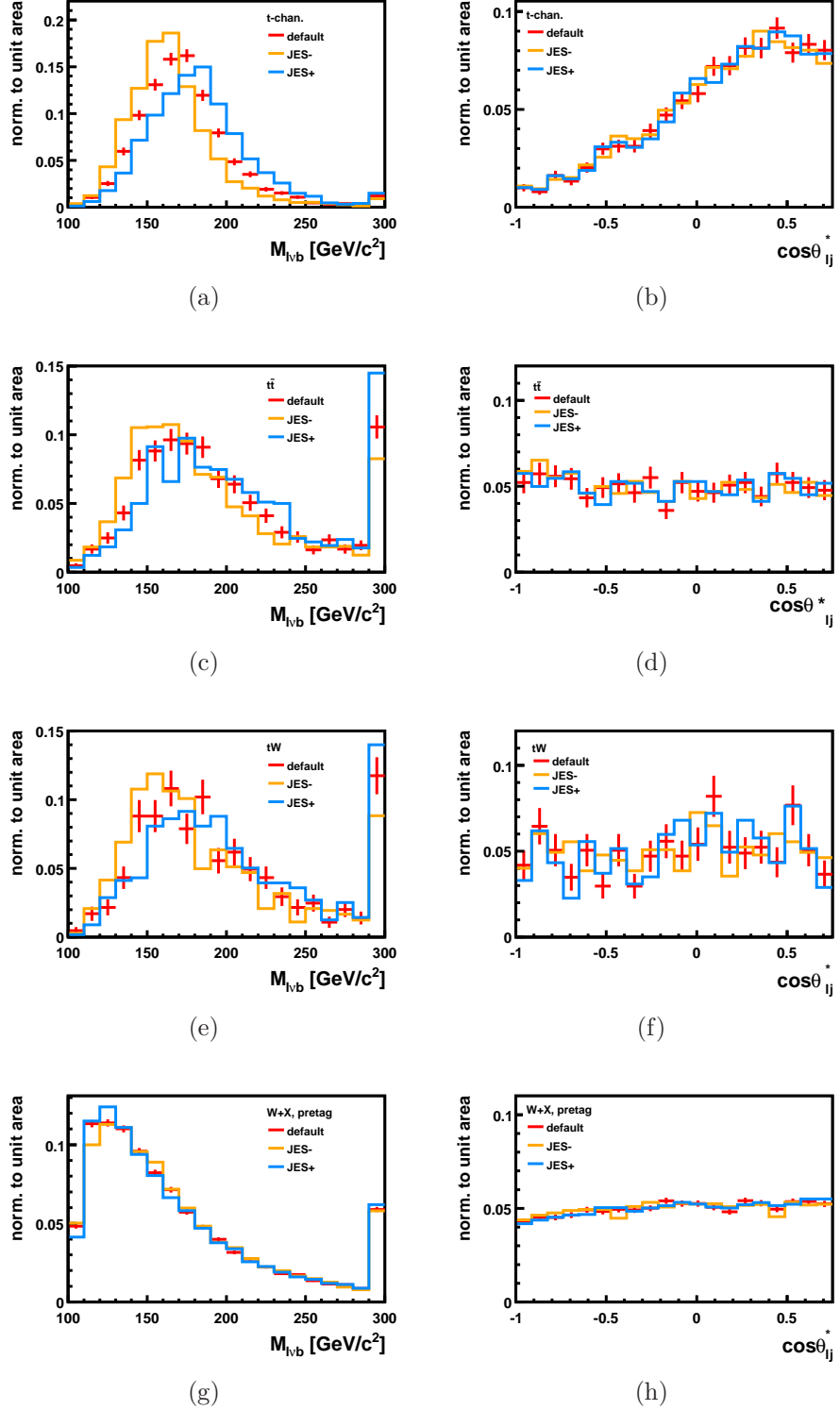
Figure 6.12: Shape comparisons for the invariant top-quark mass $M_{l\nu b}$ (left column) and the restricted $\cos\theta^*_{lj}$ (right column) for a variation of the **jet energy scale**, for signal ((a), (b)), $t\bar{t}$ ((c), (d)), tW ((e), (f)), and W+X ((g), (h)). The shapes of the top-quark processes are extracted from the sample having passed the standard selection, while the W+X shapes are obtained from pretag samples, where no b-tagging was applied in order to increase the number of events.
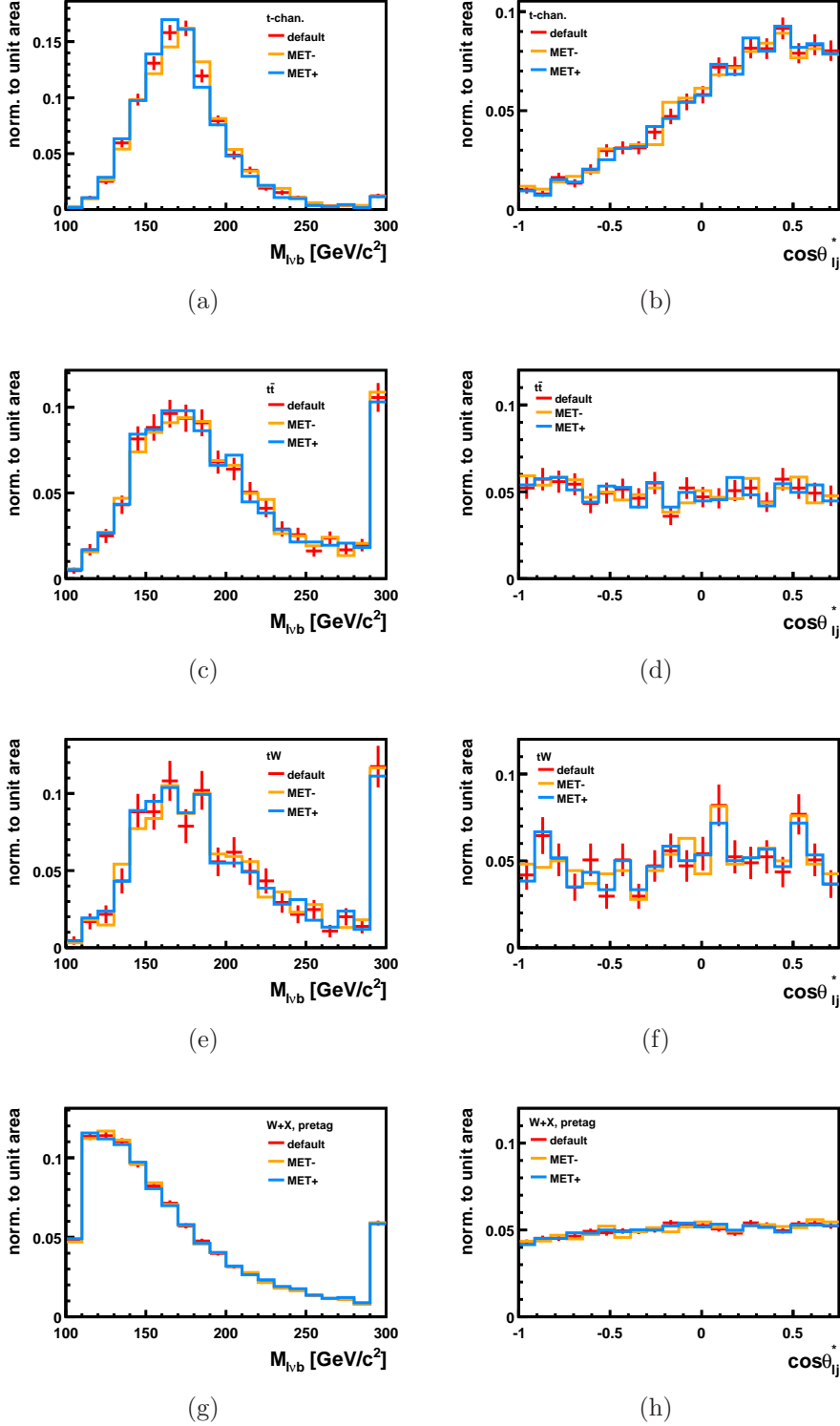
Figure 6.13: Shape comparisons for the invariant top-quark mass $M_{l\nu b}$ (left column) and the restricted $\cos\theta^*_{lj}$ (right column), where the **uncorrected $E^{\mathrm{miss}}_{\mathrm{T}}$ fraction** is rescaled with respect to the non-scaled default sample, for signal ((a), (b)), $t\bar{t}$ ((c), (d)), tW ((e), (f)), and W+X ((g), (h)). The shapes of the top-quark processes are extracted from the sample having passed the standard selection, while the W+X shapes are obtained from pretag samples, where no b-tagging was applied in order to increase the number of events.

to a b-quark parton. This yields a subsample containing taggable jets which most likely originate from a b-quark, and a different subsample where the taggable jets could not be matched to a b-quark parton, thus representing a mistag sample. The b-tagging discriminator value at which the tag is defined is then varied iteratively on these two test-samples until the threshold reflecting the required uncertainty for the b-tagging efficiency and the mistag rate, respectively, is reached. This procedure yields a $[4.87 - 5.91]$ range around the tight TCHP working point of 5.36, and a range of $[0.87 - 2.12]$ around the loose TCHE working point of 1.47, when considering b-quark partons. The translation of the mistag uncertainties yields a range of $[5.01 - 5.91]$ and $[1.45 - 1.48]$ around the tight TCHP and the loose TCHE working point, respectively. The thresholds for the tight and loose selections are taken 100% correlated, while tagging and mistagging uncertainties are considered uncorrelated, as they come from independent data-driven measurements. The impact of both modifications on the $M_{l\nu b}$ and $\cos\theta_{lj}^*$ shapes is negligible, as shown in figure 6.14 for the varied b-tagging efficiencies and in figure 6.15 for the varied mistag rates.
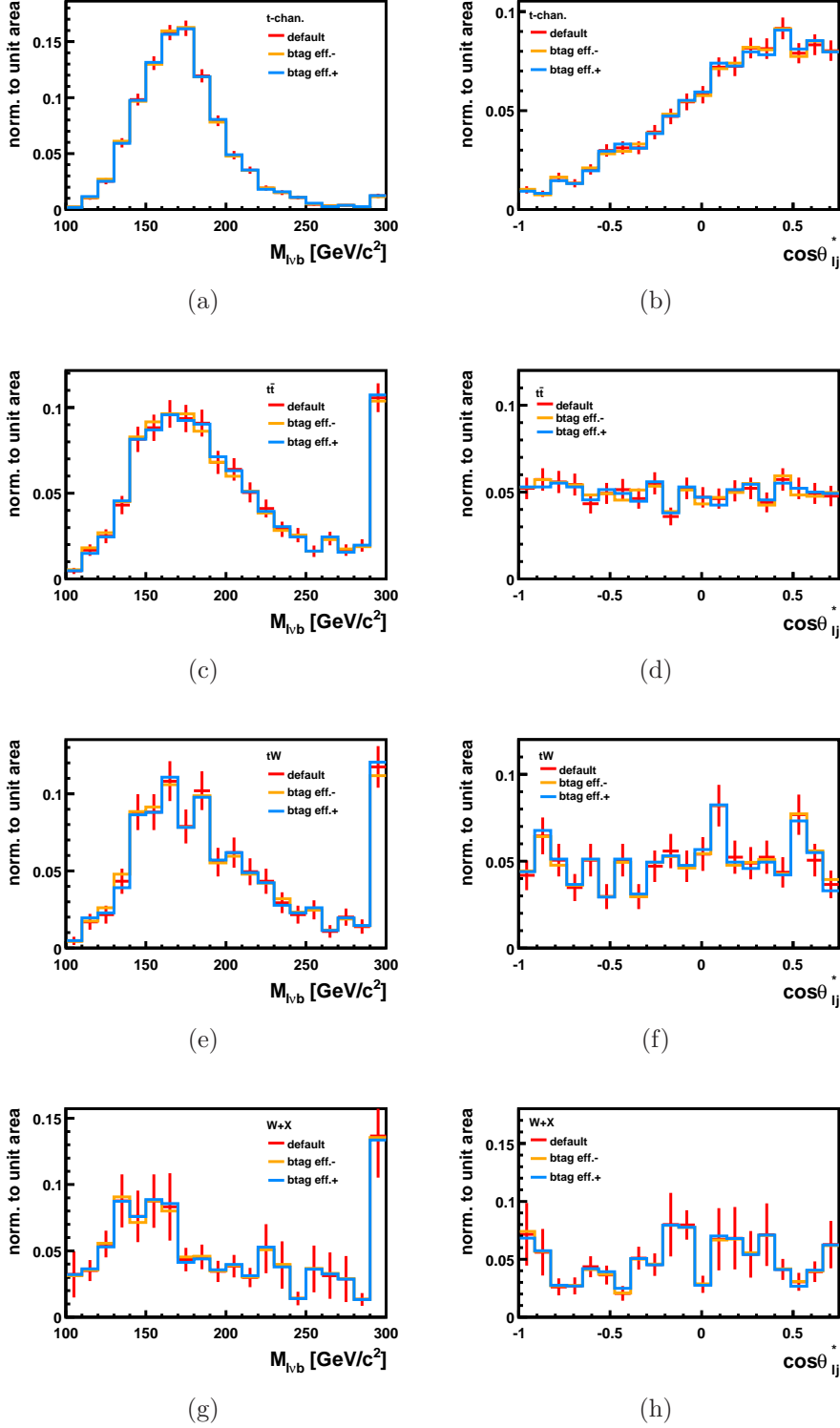
Figure 6.14: Shape comparisons for the invariant top-quark mass $M_{l\nu b}$ (left column) and the restricted $\cos\theta^*_{lj}$ (right column), where the applied discriminator working points are modified with respect to the expected uncertainty on the corresponding b-**tagging efficiency**; for signal ((a), (b)), $t\bar{t}$ ((c), (d)), tW ((e), (f)), and W+X ((g), (h)).
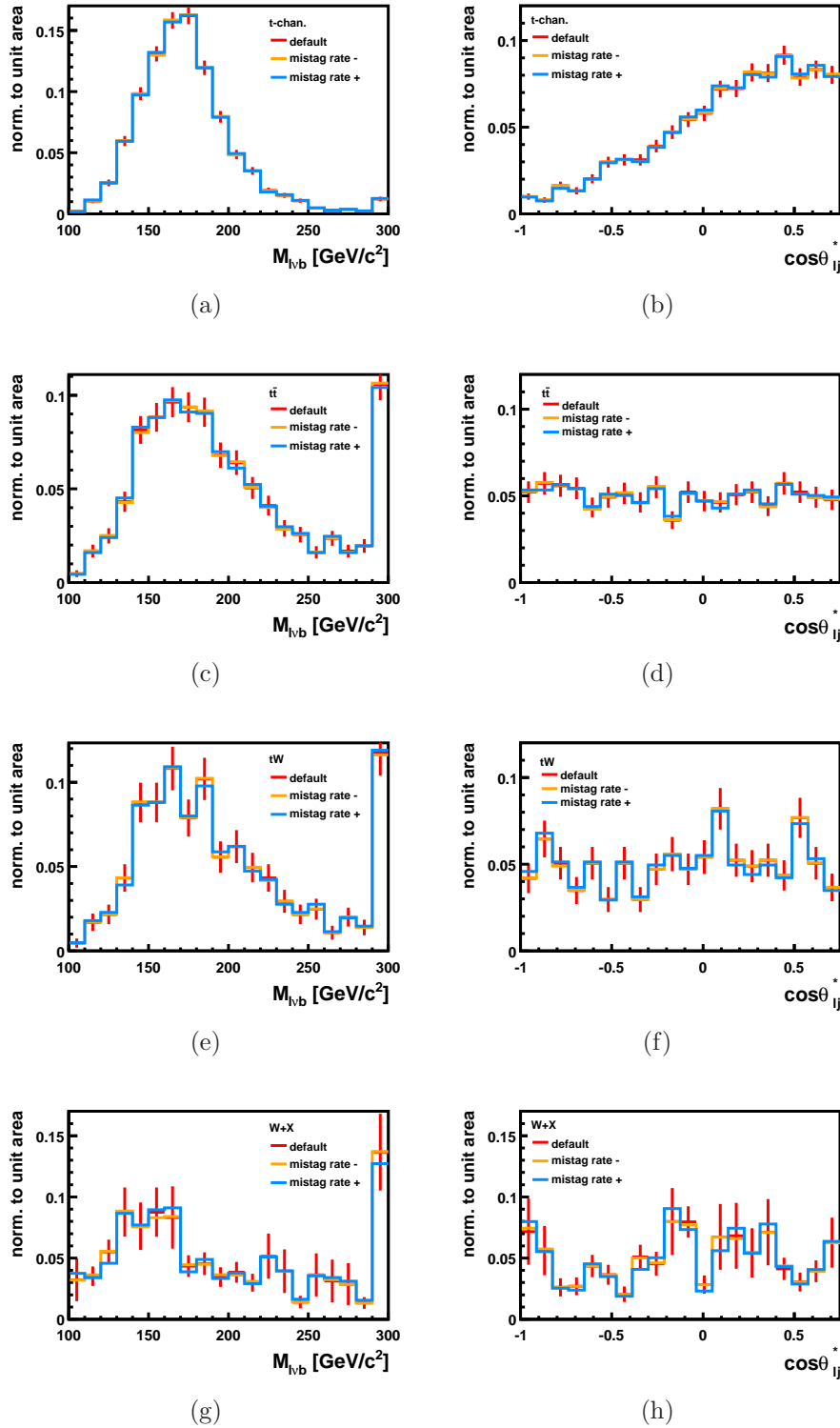
Figure 6.15: Shape comparisons for the invariant top-quark mass $M_{l\nu b}$ (left column) and the restricted $\cos\theta^*_{lj}$ (right column), where the applied discriminator working points are modified with respect to the expected uncertainty on the corresponding **mistag rate**; for signal ((a), (b)), $t\bar{t}$ ((c), (d)), tW ((e), (f)), and W+X ((g), (h)).

A summary of the impact of the theoretical uncertainties and of the systematic uncertainties of instrumental origin like JES, E_T^{miss}, and b tagging on the event yields is provided in table 6.4 for the signal and the main background processes. While the theoretical uncertainties as well as the variation of E_T^{miss} and the b-tagging parameters have only a moderate influence, the variation of the JES leads to significant deviations in the rate of $t\bar{t}$ events of up to about 25%. However, the rate deviation has an opposite sign for different processes, depending on their typical jet topology. This reduced the overall rate uncertainty due to the JES variation to 15.5% when all background processes are considered at once according to their expected contribution.

Process	PDF	JES	E_T^{miss}	ϵ_{btag}	ϵ_{mistag}	ISR/FSR	ME
signal	+5.8% −4.5%	−0.2% −1.6%	+4.7% −6.4%	−6.8% +7.2%	+0.1% −0.4%	−	−
tW	+3.4% −3.9%	−13.9% +11.9%	+4.2% −5.9%	−5.1% +6.5%	+0.5% −0.3%	−	−
$t\bar{t}$	+2.9% −3.2%	−23.4% +24.8%	+3.8% −5.3%	−0.9% −0.1%	+0.1% −0.3%	−6.3% +14.5%	+10.0% −
W+X	−	+14.8% −9.9%	+10.1% −8.4%	+0.3% −1.1%	−12.3% +8.8%	−	−
Total background		−11.0% +15.5%	+7.4% −7.6%	−1.1% +0.3%	−3.4% +1.9%	−	−

Table 6.4: Relative rate uncertainties corresponding to the difference between the number of selected events in the modified sample and the number of events after the selection of the standard sample N_0, normalized to N_0. The uncertainties related to the PDF parametrization, the jet energy scale (JES), the missing transverse energy (E_T^{miss}), the b-tagging efficiency (ϵ_{btag}), the mistag rate (ϵ_{mistag}), the radiation probability (ISR/FSR), and the matrix-element modeling of the hard process (ME) are listed for those process categories they have been considered for. The total background uncertainty corresponds to the weighted average uncertainty according to the respective background contributions.

6.2.2 Effects on Signal Extraction

In order to estimate the effect of systematic uncertainties on the signal extraction method, parameters for their strength are introduced in the definition of each pseudo-experiment. In this approach, the likelihood function remains unchanged with respect to equation 6.1, while the presence of systematic effects is accounted for in the preparation of the pseudo-data distributions, yielding a so-called prior-predictive ensemble. Systematic rate uncertainties (SRU) are taken into account by modifying the mean value of the Poisson for the expected number of events $\hat{\nu}_j$ as:

$$\hat{\nu}'_j = \hat{\nu}_j \cdot \prod_{i=1}^{S} (1 + |\delta_i| \cdot (\epsilon_{ji+} H(\delta_i) + \epsilon_{ji-} H(-\delta_i))). \tag{6.9}$$

Herein, S is the number of SRUs and i is the index of the SRU. The relative rate uncertainty for a process j is represented by ϵ_{ij}, with the strength δ_i being assigned to it, and controlled via the Heavyside step function denoted by $H(x)$. The strength δ_i is drawn from a Gaussian distribution centered at zero with a unit standard deviation. The number of events of a certain process, which is used in the pseudo-experiment, is then diced from the Poisson distribution with modified mean value $\hat{\nu}'_j$.

Concerning the implementation of systematic shape uncertainties (SSU), the content of each bin k of the normalized histogram of the discriminating observable is modified yielding systematically shifted bin content fractions α'_{jk}:

$$\alpha'_{jk} = \alpha_{jk} \cdot \sum_{l=1}^{S'} (1 + |\delta_l| \cdot (\kappa^+_{jlk} H(\delta_l) + \kappa^-_{jlk} H(-\delta_l))). \tag{6.10}$$

Here, S' is the number of SSUs, l is the index of the SSU, and δ_l indicates the strength of the considered uncertainty l. If an uncertainty causes both shape and rate effects, the strength δ_l takes the same value as δ_i, thus the two parameters are 100% correlated. In case that only the shape is affected by the systematic effect, the δ_l is drawn from a Gaussian distribution centered at zero with a standard deviation equal to one. The relative shape uncertainties for a process j are represented by $\kappa^\pm_{jlk}$, which are derived from normalized, systematically shifted histograms providing α^+_{jlk} and α^-_{jlk} for the different directions of a systematic effect. The relative shape uncertainties are then calculated as:

$$\kappa^\pm_{jlk} = \frac{\alpha^\pm_{jlk} - \alpha_{jk}}{\alpha_{jk}} \tag{6.11}$$

and fulfill $\sum_{k=1}^{B} \alpha_{jk} \cdot \kappa^\pm_{jlk} = 0$ for all j.

Using these prior-predictive ensembles, the further statistical treatment is identical to the methods described in section 6.1.1. The expected sensitivity is estimated by conducting two different ensemble tests for the hypotheses H_0 and H_1. In the following, the fit to the two discriminating observables $M_{l\nu b}$ and $\cos\theta^*_{lj}$ is only

(a)   (b)
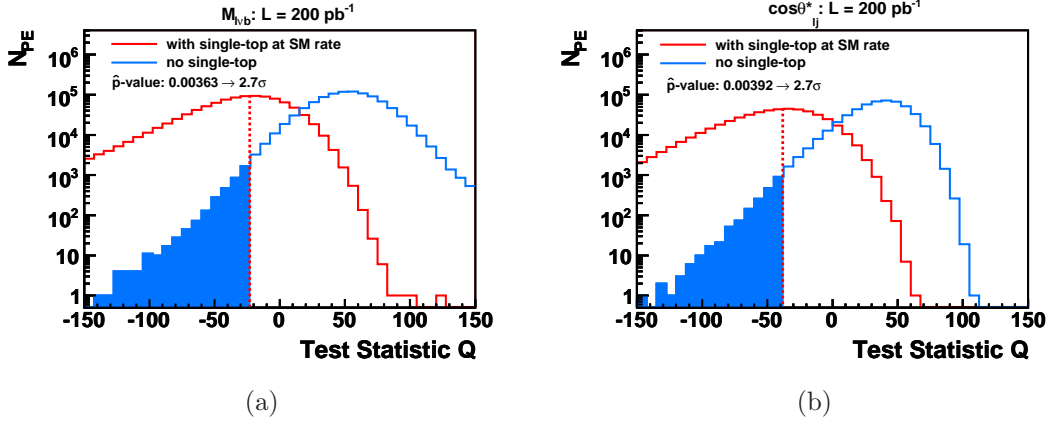
Figure 6.16: Q-value distributions for $M_{l\nu b}$ fitted in the S_1 scenario (a) and for $\cos\theta^*_{lj}$ fitted in the S_{flat} scenario (b), as expected for $L = 200\,\text{pb}^{-1}$, based on a signal rate as predicted by the SM. The resulting $\hat{p}$ values, corresponding to the areas indicated in blue, are $3.63\cdot10^{-3}$ for $M_{l\nu b}$ and $3.92\cdot10^{-3}$ for $\cos\theta^*_{lj}$. These values can be translated into a number of standard Gaussian deviations, yielding about 2.7σ for both $M_{l\nu b}$ and $\cos\theta^*_{lj}$.

performed in the standard scenarios S_1 and S_{flat}, respectively.

In order to study the impact of a single systematic uncertainty on the sensitivity of the method, ensemble tests are conducted where only one systematic effect is considered at a time. The results for the discriminating observable $M_{l\nu b}$ are summarized in table 6.5. The sensitivity of the fit to the invariant top-quark mass without considering any systematic uncertainty was estimated as 3.8σ. The largest impact is observed when JES and $E_{\text{T}}^{\text{miss}}$ uncertainties are taken into account, each reducing the sensitivity to 3.5σ. However, if all systematic uncertainties are regarded simultaneously, the expected sensitivity is significantly reduced to 2.7σ. The corresponding Q-value distribution is shown in figure 6.16 (a).

As presented in the previous section, a fit to the polarization variable $\cos\theta^*_{lj}$ yields a statistically limited sensitivity of 2.8σ. The impact of the different considered systematic uncertainties on this value is summarized in table 6.6. It turns out that the chosen method is very stable in the presence of sources for systematic uncertainties, yielding a sensitivity of 2.7σ when all systematic effects are included. This is certainly due to the fact that the degrees of freedom are significantly reduced by the approximation of the different background processes by a single flat distribution. Thus, only the shape of the signal template is considered as to be affected by systematic shape uncertainties. In addition, the shape of the polarization variable was shown to be in general very indifferent to systematical modifications as presented in section 6.2.1. The Q-value distribution obtained from the ensemble test where all considered systematic effects are included is shown in figure 6.16 (b).

In order to test the assumption of a flat overall background model for the likelihood fit to $\cos\theta^*_{lj}$, different robustness tests were conducted. The impact of an unflat behavior of the real background processes is studied by replacing subsequently the

$M_{l\nu b}$	
Source of Uncertainty	Expected Sensitivity S_{exp}
Statistical and BG Rate Uncertainties	3.8σ
$t\bar{t}$ modeling (ISR/FSR and ME)	3.6σ
PDF	3.6σ
JES	3.5σ
$E_{\mathrm{T}}^{\mathrm{miss}}$ scale	3.5σ
ϵ_{btag}	3.6σ
$\epsilon_{\mathrm{mistag}}$	3.6σ
All Uncertainties	2.7σ

Table 6.5: Impact of the systematic uncertainties on the expected sensitivities from the fit to the invariant top-quark mass $M_{l\nu b}$. On top of the first line, showing the result if only the background (BG) uncertainties are considered, the different systematic uncertainties are included separately: the modeling of the $t\bar{t}$ process with respect to the radiation probability (ISR/FSR) and the matrix element calculation (ME), the PDF parametrization, the jet energy scale (JES), the missing transverse energy ($E_{\mathrm{T}}^{\mathrm{miss}}$), the b-tagging efficiency (ϵ_{btag}), and the mistag rate ($\epsilon_{\mathrm{mistag}}$). The last line contains the result if all uncertainties are considered simultaneously.

flat background shape by one of the background process category shapes, $t\bar{t} + tW$, W+X, and QCD. As can be seen in the lower section of table 6.6, these shape variations have only a minor impact on the sensitivity of the fit, with QCD yielding the only notable deviation. This approach can certainly be considered as conservative, as the total background is modeled by the deviating QCD shape. However, QCD events are expected to amount only about a tenth of the total background rate. Thus, the non-flatness is expected to be by far less pronounced as in this test. In a further robustness test the overall background rate is fluctuated by a fraction of $\pm 50\%$. It was checked that the signal extraction remains unbiased in this scenario, while the statistical uncertainty increases to 40.8% for the upward variation and is reduced to 27.8% for the downward fluctuation. For the expected sensitivity, the values are determined as 2.2σ and 3.2σ, respectively.

In addition to the study of the effect on the expected sensitivity, the impact of the different systematic effects on the measured signal parameter β_1 is investigated in a complementary study. In this approach a fixed strength of 1σ for each source of uncertainty is assumed. Equations 6.9 and 6.10 can then be simplified to:

$$\hat{\nu}'^{\pm}_{ji} = \hat{\nu}^{\pm}_{ji} \cdot \left(1 + \epsilon^{\pm}_{ji}\right), \tag{6.12}$$

$$\alpha'^{\pm}_{jlk} = \alpha^{\pm}_{jlk} \cdot \left(1 + \kappa^{\pm}_{jlk}\right), \tag{6.13}$$

where deviations in the negative and positive direction are treated in separate ensemble tests. Since most uncertainties affect the rate and the shape of a process at the same time, these systematic effects are treated as correlated in one common

$\cos\theta_{lj}^*$	
Source of Uncertainty	Expected Sensitivity S_{exp}
Statistical and BG Rate Uncertainties	2.8σ
PDF	2.7σ
JES	2.7σ
$E_{\mathrm{T}}^{\mathrm{miss}}$ scale	2.7σ
ϵ_{btag}	2.7σ
$\epsilon_{\mathrm{mistag}}$	2.7σ
All Uncertainties	2.7σ
Robustness Test	
background shape =	
$t\bar{t}+tW$ shape	2.7σ
$W/Z+X$ shape	2.7σ
QCD shape	2.6σ
$+50\%$ background	2.2σ
-50% background	3.2σ

Table 6.6: The upper part shows the impact of the systematic uncertainties on the expected sensitivity of the fit to $\cos\theta_{lj}^*$ in the standard scenario S_{flat}. On top of the first line, showing the result if only the background (BG) uncertainties are considered, the different systematic uncertainties are included separately. The last line of the upper part contains the result if all uncertainties are considered simultaneously. In the lower part of the table, the results of the different robustness tests are listed.

ensemble test. If, however, the effect of a systematic uncertainty is only reflected in the rate or the shape of a process, the source is treated in a separate ensemble test.

The resulting β_1 distributions are no longer centered at one, but the mean is shifted due to the presence of a fixed bias. This shift is then interpreted as the uncertainty of the extracted signal parameter β_1. For each source of systematic effect, a separate ensemble test is conducted. The results are summarized in the upper section of table 6.7 for both discriminating observables, $M_{l\nu b}$ and $\cos\theta_{lj}^*$. While the uncertainties of the fit to $\cos\theta_{lj}^*$ turn out to be moderate, the quality of the fit to the invariant top-quark mass is significantly degraded by the JES uncertainty. Investigating this observation one finds that the alteration of the $M_{l\nu b}$ shape for a reduced jet energy is the main reason for the large resulting uncertainty. Testing the different background categories separately yields that the uncertainty is driven by the modified template for the $t\bar{t}$ processes.

The total systematic uncertainty is derived from a quadratic sum of the symmetrized maximal absolute values of each source listed in table 6.7.

The measured signal parameter β_1 can be translated into a cross-section estimation via

$$\sigma^{\text{est.}}_{\text{t-chan.}} = \beta_1 \cdot \sigma^{\text{SM}}_{\text{t-chan.}} \,, \tag{6.14}$$

where $\sigma^{\text{SM}}_{\text{t-chan.}}$ is the theoretical cross section used to compute the number of expected signal events. The studies performed in the present thesis have shown that the cross-section of the t-channel single top-quark production is expected to be determined with the following uncertainties when assuming a measured signal parameter $\beta_1 = 1$:

$$\boldsymbol{M_{l\nu b}}: \quad \left.\frac{\Delta\sigma^{\text{est.}}_{\text{t-chan.}}}{\sigma^{\text{est.}}_{\text{t-chan.}}}\right|_{\sigma^{\text{est.}}_{\text{t-chan.}}=\sigma^{\text{SM}}_{\text{t-chan.}}} = \pm 26\% \,(\text{stat.}) \pm 48\% \,(\text{syst.}) \pm 10\% \,(\text{lum.})$$

if the invariant top-quark mass is exploited as discriminating observable, while a likelihood fit to the polarization variable $\cos\theta^*_{lj}$ yields

$$\boldsymbol{\cos\theta^*_{lj}}: \quad \left.\frac{\Delta\sigma^{\text{est.}}_{\text{t-chan.}}}{\sigma^{\text{est.}}_{\text{t-chan.}}}\right|_{\sigma^{\text{est.}}_{\text{t-chan.}}=\sigma^{\text{SM}}_{\text{t-chan.}}} = \pm 35\% \,(\text{stat.}) \pm 15\% \,(\text{syst.}) \pm 10\% \,(\text{lum.})$$

For both methods an integrated luminosity of $200\,\text{pb}^{-1}$ collected at $\sqrt{s} = 10\,\text{TeV}$ has been assumed. In addition to the evaluated statistical and systematic uncertainties, an uncertainty on the integrated luminosity of the analyzed data sample of 10% is assigned, corresponding to an estimation obtained from a combination of several measurements [134]. It turned out that the invariant mass, although having a priori a larger discriminating power than the polarization observable, is seriously affected by systematic effects concerning the kinematics of the visible jets in the event. The expected significance obtained from the likelihood fit has shown to be 2.7σ for both discriminating observables, $M_{l\nu b}$ and $\cos\theta^*_{lj}$, while the latter one behaves by far more robust in the presence of systematic uncertainties.

Source of uncertainty	$\cos\theta^*_{lj}$	$M_{l\nu b}$
PDF	+5.5% −4.7%	+4.9% −5.0%
JES	−1.3% −5.5%	−40.9% +21.5%
$E_{\mathrm{T}}^{\mathrm{miss}}$	+6.2% −9.9%	+8.9% −14.5%
ϵ_{btag}	−6.5% +7.3%	−7.4% +6.9%
$\epsilon_{\mathrm{mistag}}$	∼0% −0.4%	−0.3% −0.4%
$t\bar{t}$ modeling (ISR/FSR and ME)	–	−16.9% −6.4%
Total systematic uncertainty	14.6%	47.5%
		(24.0% w/o JES)

Table 6.7: Impact of the systematic uncertainties on the signal parameter β_1 obtained from the fit to $\cos\theta^*_{lj}$ (center column) and $M_{l\nu b}$ (right column). The strength of the systematic effects is fixed to the 1σ deviation, thus the systematically modified pseudo-data distributions are obtained by respecting equations 6.12 and 6.13. The impact of the uncertainties related to the PDF parametrization, the jet energy scale (JES), the missing transverse energy ($E_{\mathrm{T}}^{\mathrm{miss}}$), the b-tagging efficiency (ϵ_{btag}), and the mistag rate ($\epsilon_{\mathrm{mistag}}$) are listed. For $M_{l\nu b}$, also the uncertainties due to the radiation probability (ISR/FSR), and the matrix-element modeling of the hard process (ME) are considered, which is not the case for the assumed flat background model in the fit to $\cos\theta^*_{lj}$.

Summary and Outlook

Since its discovery at the Tevatron in 1995 [5, 6], the production mechanisms of the top quark and its properties have been intensively studied and predictions of the Standard Model (SM) have successfully been tested. The largest part of this knowledge has been extracted from the analysis of top-quark pair production via the strong interaction, constituting the dominant production mechanism at the Tevatron as well as at the LHC. A complementary production mechanism is predicted in the electroweak sector, where the top-quarks are produced singly in charged current interactions. Recently, the Tevatron experiments have announced the discovery of singly produced top quarks [11, 12]. Although having achieved a statistically significant signal observation, the experimental environment at the Tevatron is not able to provide conditions required for precise tests of this electroweak top-quark production mode. This statistical limitation is expected to be overcome at the LHC. As a proton-proton collider operating at a center-of-mass energy of up to 14 TeV, top quarks are produced with considerably higher rates than at the Tevatron. While the analysis of top-quark pairs produced via the strong interaction has shown to be feasible with a data amount corresponding to an integrated luminosity of a few pb^{-1} at $\sqrt{s} = 10$ TeV [15], the observation of singly produced top quarks will require some more data as the cross section is by a factor of about 3.5 smaller than for top-quark pair production and the background processes are much harder to control.

In the present thesis the prospects of a single top-quark rediscovery with the CMS experiment have been investigated, assuming an early analysis scenario. The studies have been focused on the t-channel production mode, where a b quark from an initial gluon splitting is scattered at a light quark by the exchange of a W boson. Thus, the final state is characterized by a spectator jet produced in the forward region, which is initiated by the scattered light quark, a jet stemming from the so-called spectator b-quark from the initial gluon splitting, and the decay products of the top-quark, where the top quark decays according to $t \rightarrow bW$. In the analysis presented in this thesis only the muonic decay mode of the W boson is considered, leading to an experimental signature that features another b-quark jet, missing transverse energy due to the non-detectable neutrino, and one isolated muon being far away from a jet. The advantage of this channel is the presence of the isolated muon, which can be exploited to suppress very effectively QCD multijet events.

Previous studies on this field, carried out for the official report on the CMS physics performance [135], assumed an analyzed data amount of $L = 10$ fb^{-1} collected at $\sqrt{s} = 14$ TeV. However, in preparation of the LHC start-up in 2008, the

operation plan had foreseen a first physics data taking period at a center-of-mass energy of 10 TeV. The data amount to be collected by the experiments in this first period was estimated as $L = 200 \, \text{pb}^{-1}$. As a central result of this thesis I have shown that it is realistic to provide a first evidence of single-top quark production in the dominating t-channel considering an analysis scenario which corresponds to the above given conditions.

In preparation of the analysis, I studied in detail the modeling of the t-channel signal by Monte-Carlo (MC) simulations. A dedicated matching procedure based on the kinematics of the spectator b-quark is applied to the MadGraph simulations of the t-channel single top-quark production in order to account for crucial NLO contributions. The technical realization of this matching has been optimized in a way that the two processes are combined prior to the time-consuming detector simulation step. This approach avoids the processing of half of the events being eventually rejected by the matching. In order to validate the results of the matching, I have performed a comparison of the matched signal sample to a similar matrix-element approach based on CompHep as well as to MC@NLO, a MC model combining NLO matrix-element calculations with parton shower simulations. All the three methods have shown a reasonable agreement. Recently, first NLO calculations of fully differential distributions for the t-channel process assuming a finite b-quark mass, have been published [24]. A first comparison of these distributions to the outcome of the MadGraph MC simulation has been performed in close collaboration with the authors of the NLO calculations. In this study, I have observed significant differences between the NLO description of the spectator b-quark and its modeling in the matched MadGraph simulation. These findings suggest to adjust the matching procedure in the future, in order to account for the NLO corrections to the spectator b-quark.

En route to a re-discovery of electroweakly produced top quarks at CMS, a straightforward analysis strategy has been chosen such that the dependence on a comprehensive data understanding is minimized. With a predicted signal cross-section of about 124 pb, only one event out of about 750 million is expected to be a t-channel single top-quark event. Thus, a dedicated event selection has been developed in order to enhance the fraction of signal events in the analyzed event sample. The two most dominant background contributions come from QCD multijet events and from the production of W bosons in association with jets, $W + \text{jets}$, with predicted cross-sections being, respectively, about six and three orders of magnitude larger than the signal cross-section. As already mentioned, the requirement of one isolated muon in the final state allows to reduce the amount of QCD events to a rate significantly smaller than the signal rate. As I have shown, the remaining QCD events which contain an isolated muon object, can efficiently be suppressed by a cut on the transverse W-boson mass, since the muons occurring in QCD multijet processes typically do not stem from the decay of a W boson. Concerning the $W + \text{jets}$ background, the usage of b-tagging allows to control its contribution. Requiring the event to have one jet which is likely to stem from a b-quark, the rate of this background process can successfully be reduced by three orders of magnitude. After applying the complete chain of dedicated selection cuts, the selected sample of signal-event

candidates exhibits a signal-to-background ratio of about 0.45, while being dominated by background events stemming from top-quark pair production. Since this signal-to-background ratio is still small and the uncertainty on the rate of certain background processes are expected to be considerably large, a counting experiment would not be able to establish the observed signal events in a statistically significant way.

Thus, the necessary separation power of the signal from background for the extraction of the signal fraction is achieved by exploiting a discriminating observable in a binned likelihood fit. In this thesis, the potential of two different variables has been investigated, the invariant top-quark mass $M_{l\nu b}$, and an observable related to the polarization of the top-quark, $\cos\theta^*_{lj}$, where θ^*_{lj} is the angle between the direction of the muon and the direction of the spectator jet, originating from the recoiling light quark, as measured in the rest frame of the top-quark. This observable exploits a spin basis where the top quarks are expected to be almost fully polarized, yielding a strong angular correlation between the muon and the spectator jet and thus a maximal discriminating power. Since both variables require the information of the top-quark kinematics, the reconstruction of its four-vector from the measured decay products is necessary. The method chosen here combines a well validated neutrino reconstruction with a simple but very accurate jet assignment strategy, providing a correct ascription of the b-quark jet stemming from the top-quark decay in more than 90 % of the cases.

Comparing the results obtained from a fit to the two considered observables, it has been found that the statistically limited separation power of the invariant top-quark mass is a priori significantly better than the separation obtained from a fit to the polarization observable $\cos\theta^*_{lj}$. In order to establish the presence of the signal in the starting period, hypothesis tests have been performed to estimate the expected sensitivity of the applied likelihood fit procedure. The obtained values for $M_{l\nu b}$ and $\cos\theta^*_{lj}$ are 3.8σ and 2.8σ, respectively. However, after consideration of theoretical and instrumental sources of systematical uncertainties, the result obtained from a fit to $M_{l\nu b}$ is significantly degraded. The dominant source here is the uncertainty of the jet energy scale, which not only affects the rate of the processes but also has a large impact on the shape of the $M_{l\nu b}$ observable. In contrast to that, I have shown that the performance of the fit to the polarization observable is largely unaffected. Measurements of the t-channel single top-quark cross section are expected to be feasible within the following uncertainties:

$$\boldsymbol{M_{l\nu b}}: \quad \left.\frac{\Delta\sigma^{\text{est.}}_{\text{t-chan.}}}{\sigma^{\text{est.}}_{\text{t-chan.}}}\right|_{\sigma^{\text{est.}}_{\text{t-chan.}}=\sigma^{\text{SM}}_{\text{t-chan.}}} = \pm26\%\,(\text{stat.}) \pm 48\%\,(\text{syst.}) \pm 10\%\,(\text{lum.})$$

$$\boldsymbol{\cos\theta^*_{lj}}: \quad \left.\frac{\Delta\sigma^{\text{est.}}_{\text{t-chan.}}}{\sigma^{\text{est.}}_{\text{t-chan.}}}\right|_{\sigma^{\text{est.}}_{\text{t-chan.}}=\sigma^{\text{SM}}_{\text{t-chan.}}} = \pm35\%\,(\text{stat.}) \pm 15\%\,(\text{syst.}) \pm 10\%\,(\text{lum.})$$

assuming a measured signal cross-section of about 133 pb, as predicted by the SM. The impact of the systematic uncertainties on the expected sensitivity is quite different for the two considered observables. While the expected sensitivity obtained

from a fit to $M_{l\nu b}$ is significantly reduced to 2.7σ, the sensitivity of the fit to the polarization variable $\cos\theta^*_{lj}$ remains very stable and yields a value of 2.7σ.
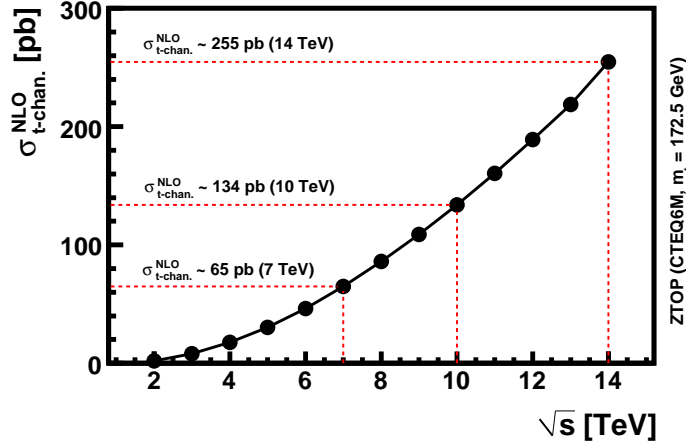
Figure 6.17: NLO cross-section of electroweakly produced top- and antitop-quarks in the t-channel as a function of the center-of-mass energy of the proton-proton collisions, calculated with ZTOP [21].

The operation plans published right after the LHC incident in September 2008 had still been adhering to the originally foreseen center-of-mass energy of 10 TeV. Technical issues having been investigated over the last year, however, advised to modify this scenario. Thus, it has been decided recently to reduce the center-of-mass energy for the first physics-data taking phase further to 7 TeV. The data amount expected to be delivered by the LHC in this first physics run is about $1\,\text{fb}^{-1}$, which is foreseen to take about one year with the machine operating in collision mode. Concerning the single top-quark production in the t-channel, the lower center-of-mass energy implies a reduction of the production cross-section of about a factor of two with respect to the scenario considered for the studies presented in this thesis. Figure 6.17 shows the NLO cross-section of the t-channel single top-quark production calculated with ZTOP [21] as a function of $\sqrt{s}$. The rate of the main background processes, top-quark pair production and the production of W bosons, will be lowered by a factor of about 2.3 [100] and 1.5 [19], respectively, when reducing the collision energy to 7 TeV. Thus, the general analysis preconditions concerning the signal-to-background ratio remain in the same order of magnitude as found in the context of this thesis. However, the impact of a significantly reduced signal cross-section suggests the application of more sophisticated analysis strategies compared to the method presented here. Combining several discriminating properties of signal events by means of a multivariate method allows to exploit more effectively the information provided by an event candidate and is thus able to extract significant results in much smaller datasets. Increasing the number of properties of a candidate event used in the analysis requires much more effort to verify the modeling of these observables and to minimize systematic biases. Based on the promising results

presented in this thesis, however, an extension of the analysis towards multivariate applications can certainly be considered as a realistic strategy for an observation of singly produced top quarks at the LHC within the first physics data taking period until the end of 2011.

List of Figures

List of Tables

Bibliography

[1] E. Rutherford, "The scattering of α and β particles by matter and the structure of the atom", Phil. Mag. 21, 669–688 (1911).

[2] M. Gell-Mann, "A Schematic Model of Baryons and Mesons", Phys. Lett. 8, 214–215 (1964).

[3] G. Zweig, "An SU$_3$ model for strong interaction symmetry and its breaking - Part II", CERN-TH-412 (1964).

[4] K. Kodama et al., DONUT , "Observation of tau-neutrino interactions", Phys. Lett. B504, 218–224 (2001).

[5] F. Abe et al., CDF Collaboration , "Observation of Top Quark Production in $p\bar{p}$ Collisions", Phys. Rev. Lett. 74, 2626–2631 (1995).

[6] S. Abachi et al., DØ Collaboration , "Observation of the Top Quark", Phys. Rev. Lett. 74, 2632–2637 (1995).

[7] J. R. Incandela, A. Quadt, W. Wagner, and D. Wicke, "Status and Prospects of Top-Quark Physics", Prog. Part. Nucl. Phys. 63, 239–292 (2009).

[8] CDF Collaboration , "Combination of CDF top quark pair production cross section measurements with up to $4.6\,\mathrm{fb}^{-1}$", CDF Conference Note 9913 (2009).

[9] M. Kobayashi and T. Maskawa, "CP Violation in the Renormalizable Theory of Weak Interaction", Prog. Theor. Phys. 49, 652–657 (1973).

[10] N. Cabibbo, "Unitary Symmetry and Leptonic Decays", Phys. Rev. Lett. 10, 531–532 (1963).

[11] T. Aaltonen, CDF Collaboration , "Observation of Electroweak Single Top Quark Production", Phys. Rev. Lett. 103, 092002 (2009).

[12] V. M. Abazov, DØ Collaboration , "Observation of Single Top-Quark Production", Phys. Rev. Lett. 103, 092001 (2009).

[13] P. W. Higgs, "Broken Symmetries and the Masses of Gauge Bosons", Phys. Rev. Lett. 13, 508–509 (1964).

[14] J. M. Campbell, J. W. Huston, and W. J. Stirling, "Hard Interactions of Quarks and Gluons: A Primer for LHC Physics", Rept. Prog. Phys. 70, 89 (2007).

[15] CMS Collaboration , "Plans for an early measurement of the $t\bar{t}$ cross section in the muon+jets channel at 10 TeV", CMS PAS TOP-09-003 (2009).

[16] J. M. Campbell, R. Frederix, F. Maltoni, and F. Tramontano, "NLO predictions for t-channel production of single top and fourth generation quarks at hadron colliders", JHEP 10, 042 (2009).

[17] J. Campbell, R. K. Ellis, and F. Tramontano, "Single top production and decay at next-to-leading order", Phys. Rev. D 70, 094012 (2004).

[18] J. Campbell and F. Tramontano, "Next-to-leading order corrections to Wt production and decay", Nucl. Phys. B 726, 109 (2005).

[19] F. Maltoni and T. Stelzer, "MadEvent: Automatic event generation with MadGraph", JHEP 02, 027 (2003).

[20] T. Sjostrand et al., "High-energy physics event generation with PYTHIA 6.1", Comput. Phys. Commun. 135, 238–259 (2001).

[21] Z. Sullivan, "Understanding single-top-quark production and jets at hadron colliders", Phys. Rev. D70, 114012 (2004).

[22] E. Boos, V. E. Bunichev, L. V. Dudko, V. I. Savrin, and A. V. Sherstnev, "Method for simulating electroweak top-quark production events in the NLO approximation: SingleTop event generator", Phys. Atom. Nucl. 69, 1317–1329 (2006).

[23] S. Frixione and B. R. Webber, "Matching NLO QCD computations and parton shower simulations", JHEP 06, 029 (2002).

[24] J. M. Campbell, R. Frederix, F. Maltoni, and F. Tramontano, "Next-to-Leading-Order Predictions for t-Channel Single-Top Production at Hadron Colliders", Phys. Rev. Lett. 102, 182003 (2009).

[25] T. Chwalek, "Measurement of the W-Boson Helicity-Fractions in Top-Quark Decays with the CDF II Experiment and Prospects for an Early $t\bar{t}$ Cross-Section Measurement with the CMS Experiment", PhD Thesis, Karlsruhe Institute of Technology, IEKP-KA/2010-5 (2010).

[26] G. Mahlon and S. Parke, "Single Top Quark Production at the LHC: Understanding Spin", Phys. Lett. B 476, 323 (2000).

[27] Tevatron Electroweak Working Group , "Combination of CDF and DØ Results on the Mass of the Top Quark", `arXiv:0903.2503` (2009).

[28] C. Amsler et al., Particle Data Group , "Review of Particle Physics", Phys. Lett. B667, 1 (2008).

[29] E. Pessa, "The concept of particle in Quantum Field theory", `arXiv:physics.gen-ph/0907.0178` (2009).

[30] A. Einstein, "Grundlage der Allgemeinen Relativitätstheorie", Annalen Phys. 49, 769–822 (1916).

[31] S. Khalil and E. Torrente-Lujan, "Neutrino Mass and Oscillation as Probes of Physics Beyond the Standard Model", J. Egyptian Math. Soc. 9, 91–141 (2001).

[32] F. De Bernardis, P. Serra, A. Cooray, and A. Melchiorri, "An improved limit on the neutrino mass with CMB and redshift-dependent halo bias-mass relations from SDSS, DEEP2, and Lyman-Break Galaxies", Phys. Rev. D 78, 083535 (2008).

[33] E. K. et al., "Five-Year Wilkinson Microwave Anisotropy Probe (WMAP) Observations: Cosmological Interpretation", The Astrophysical Journal 180, 330 (2009).

[34] H. Fritzsch, M. Gell-Mann, and H. Leutwyler, "Advantages of the Color Octet Gluon Picture", Phys. Lett. B47, 365–368 (1973).

[35] M. Y. Han and Y. Nambu, "Three-Triplet Model with Double SU(3) Symmetry", Phys. Rev. 139, B1006–B1010 (1965).

[36] D. J. Gross and F. Wilczek, "Asymptotically Free Gauge Theories. I", Phys. Rev. D 8, 3633–3652 (1973).

[37] R. P. Feynman, "Mathematical Formulation of the Quantum Theory of Electromagnetic Interaction", Phys. Rev. 80, 440–457 (1950).

[38] S. L. Glashow, "Partial Symmetries of Weak Interactions", Nucl. Phys. 22, 579–588 (1961).

[39] A. Salam and J. C. Ward, "Electromagnetic and Weak Interactions", Phys. Lett. 13, 168–171 (1964).

[40] S. Weinberg, "A Model of Leptons", Phys. Rev. Lett. 19, 1264–1266 (1967).

[41] J. Goldstone, A. Salam, and S. Weinberg, "Broken Symmetries", Phys. Rev. 127, 965–970 (1962).

[42] The LEP Working Group for Higgs Boson Searches , "Search for the Standard Model Higgs boson at LEP", Phys. Lett. B 565, 61 – 75 (2003).

[43] The LEP Electroweak Working Group , "LEP/TEV EW WG Plots for Summer 2009", (2009).

[44] Tevatron New Phenomena and Higgs Working Group , "Combined CDF and DØ Upper Limits on Standard Model Higgs- Boson Production with 2.1 - 5.4 fb^{-1} of Data", `arXiv:0911.3930` (2009).

[45] D. J. Griffiths, "Introduction to Elementary Particle Physics", Nucl. Phys. 22, 579–588 (1961).

[46] D. Stump et al., "Inclusive jet production, parton distributions, and the search for new physics", JHEP 10, 046 (2003).

[47] J. C. Collins, D. E. Soper, and G. Sterman, "Inclusive jet production, parton distributions, and the search for new physics", Nucl. Phys. B 263, 37–60 (1986).

[48] M. Cacciari, S. Frixione, M. L. Mangano, P. Nason, and G. Ridolfi, "Updated predictions for the total production cross sections of top and of heavier quark pairs at the Tevatron and at the LHC", JHEP 0809, 127 (2008).

[49] B. W. Harris, E. Laenen, L. Phaf, Z. Sullivan, and S. Weinzierl, "Fully differential single-top-quark cross section in next-to-leading order QCD", Phys. Rev. D 66, 054024 (2002).

[50] J. Alwall et al., "Is V(tb) = 1?", Eur. Phys. J. C49, 791–801 (2007).

[51] N. Kidonakis, "Higher-order soft gluon corrections in single top quark production at the LHC", Phys. Rev. D75, 071501 (2007).

[52] A. D. Martin, W. J. Stirling, and R. S. Thorne, "MRST partons generated in a fixed-flavour scheme", Phys. Lett. B636, 259–264 (2006).

[53] C. D. White, S. Frixione, E. Laenen, and F. Maltoni, "Isolating Wt production at the LHC", `arXiv:hep-ph/0908.0631` (2009).

[54] S. Frixione, E. Laenen, P. Motylinski, B. Webber, and C. D. White, "Single-top hadroproduction in association with a W boson", JHEP 7, 029 (2008).

[55] W. K. Tung et al., "Heavy quark mass effects in deep inelastic scattering and global QCD analysis", JHEP 02, 053 (2007).

[56] P. M. Nadolsky et al., "Implications of CTEQ global analysis for collider observables", Phys. Rev. D78, 013004 (2008).

[57] Z. Sullivan, "Fully differential W' production and decay at next-to-leading order in QCD", Phys. Rev. D 66, 075011 (2002).

[58] T. Tait and C. P. Yuan, "Single Top Production as a Window to Physics Beyond the Standard Model", Phys. Rev. D 63, 014018 (2001).

[59] D. Espriu and J. Manzano, "Measuring effective electroweak couplings in single top quark production at the CERN LHC", Phys. Rev. D 65, 073005 (2002).

[60] T. Han, M. Hosch, K. Whisnant, B.-L. Young, and X. Zhang, "Single top quark production via FCNC couplings at hadron colliders", Phys. Rev. D 58, 073008 (1998).

[61] M. S. Carena et al., Higgs Working Group , "Report of the Tevatron Higgs working group", `arXiv:hep-ph/0010338` (2000).

[62] S. Abel et al., SUGRA Working Group , "Report of the SUGRA Working Group for run II of the Tevatron", `arXiv:hep-ph/0003154` (2000).

[63] CDF Collaboration , "Search for Heavy Top $t' \rightarrow Wq$ In Lepton Plus Jet Events", Public CDF Note 9446 (2008).

[64] "CERN Document Server - Multimedia and Outreach", CERN-AC-9906026, http://cdsweb.cern.ch/record/40525, (1999).

[65] K. Aamodt et al., ALICE , "The ALICE experiment at the CERN LHC", JINST 0803, S08002 (2008).

[66] A. A. Alves et al., LHCb , "The LHCb Detector at the LHC", JINST 3, S08005 (2008).

[67] O. Adriani et al., LHCf , "The LHCf detector at the CERN Large Hadron Collider", JINST 3, S08006 (2008).

[68] G. Anelli et al., TOTEM , "The TOTEM experiment at the CERN Large Hadron Collider", JINST 3, S08007 (2008).

[69] G. Aad et al., ATLAS , "The ATLAS Experiment at the CERN Large Hadron Collider", JINST 3, S08003 (2008).

[70] "CERN FAQ - LHC the guide", http://cdsweb.cern.ch/record/1165534/files/, (2009).

[71] C. E. Hill, "Ion and electron sources", Talk at the CAS - CERN Accelerator School : Cyclotrons, Linacs and Their Applications, La Hulpe, Belgium, 28 Apr - 5 May (1994).

[72] K. Schindl, "The PS booster as pre-injector for LHC", Part. Accel. 58, 63–78 (1997).

[73] R. Cappi, "The PS in the LHC injector chain", Part. Accel. 58, 79–89 (1997).

[74] T. Linnecar, "Preparing the SPS for LHC", Part. Accel. 58, 91–101 (1997).

[75] L. Evans and P. Bryant, "LHC Machine", JINST 3, S08001 (2008).

[76] D. Acosta, M. Della Negra, L. Fo, A. Herv, and A. Petrilli, "CMS physics: Technical Design Report". Technical Design Report CMS. CERN, Geneva, (2006).

[77] CMS Collaboration , "The CMS CRAFT Exercise", Internal CMS Note CFT-09-008 (unpublished) (2009).

[78] R. Adolphi et al., CMS Collaboration , "The CMS experiment at the CERN LHC", JINST 0803, S08004 (2008).

[79] V. Karimki, "The CMS tracker system project: Technical Design Report". Technical Design Report CMS. CERN, Geneva, (1997).

[80] CMS Collaboration , "Alignment of the CMS Silicon Tracker during Commissioning with Cosmic Rays", arXiv:0910.2505 (2009).

[81] CMS Collaboration , "The CMS electromagnetic calorimeter project: Technical Design Report". Technical Design Report CMS. CERN, Geneva, (1997).

[82] CMS Collaboration , "Performance and Operation of the CMS Electromagnetic Calorimeter", arXiv:0910.3423 (2009).

[83] CMS Collaboration , "Use of $Z \rightarrow e^+e^-$ events for ECAL calibration", Internal CMS NOTE-2006/039 (unpublished) (2006).

[84] CMS Collaboration , "The CMS hadron calorimeter project: Technical Design Report". Technical Design Report CMS. CERN, Geneva, (1997).

[85] C. Collaboration, "Performance of the CMS Hadron Calorimeter with Cosmic Ray Muons and LHC Beam Data", arXiv:0911.4991 (2009).

[86] CMS Collaboration , "The CMS muon project: Technical Design Report". Technical Design Report CMS. CERN, Geneva, (1997).

[87] S. Cittolin, A. Rcz, and P. Sphicas, "CMS trigger and data-acquisition project: Technical Design Report". Technical Design Report CMS. CERN, Geneva, (2002).

[88] J. Shiers, "The Worldwide LHC Computing Grid (worldwide LCG)", Computer Physics Communications 177, 219 – 223 (2007), no. 1-2,.

[89] G. L. Bayatyan, M. Della Negra, Fo, A. Herv, and A. Petrilli, "CMS computing: Technical Design Report". Technical Design Report CMS. CERN, Geneva, (2005).

[90] G. Altarelli and G. Parisi, "Asymptotic Freedom in Parton Language", Nucl. Phys. B126, 298 (1977).

[91] V. N. Gribov and L. N. Lipatov, "Deep inelastic e-p-scattering in perturbation theory", Sov. J. Nucl. Phys. 15, 438–450 (1972).

[92] Y. L. Dokshitzer, "Calculation of the Structure Functions for Deep Inelastic Scattering and e^+e^- Annihilation by Perturbation Theory in Quantum Chromodynamics", Sov. Phys. JETP 46, 641–653 (1977).

[93] G. Corcella et al., "HERWIG 6.5: an event generator for Hadron Emission Reactions With Interfering Gluons (including supersymmetric processes)", JHEP 01, 010 (2001).

[94] S. Frixione, Z. Kunszt, and A. Signer, "Three jet cross-sections to next-to-leading order", Nucl. Phys. B467, 399–442 (1996).

[95] J. Alwall et al., "A standard format for Les Houches event files", Comput. Phys. Commun. 176, 300–304 (2007).

[96] S. Catani, F. Krauss, R. Kuhn, and B. R. Webber, "QCD Matrix Elements + Parton Showers", JHEP 11, 063 (2001).

[97] S. Hoche et al., "Matching parton showers and matrix elements", `arXiv:hep-ph/0602031` (2006).

[98] P. Sturm, "Studies for the Measurement of Single-Top-Quark-Events with the CMS Experiment", CMS Thesis CMS TS-2008/011 (2008).

[99] E. Boos et al., CompHEP Collaboration , "CompHEP 4.4: Automatic computations from Lagrangians to events", Nucl. Instrum. Meth. A534, 250–259 (2004).

[100] J. M. Campbell, R. K. Ellis, and F. Tramontano, "Single top production and decay at next-to-leading order", Phys. Rev. D70, 094012 (2004).

[101] M. Krämer, F. I. Olness, and D. E. Soper, "Treatment of heavy quarks in deeply inelastic scattering", Phys. Rev. D 62, 096007 (Oct, 2000).

[102] J. C. Collins, "Hard-scattering factorization with heavy quarks: A general treatment", Phys. Rev. D 58, 094002 (Sep, 1998).

[103] S. Agostinelli et al., GEANT4 , "GEANT4: A simulation toolkit", Nucl. Instrum. Meth. A506, 250–303 (2003).

[104] CMS Collaboration , "Fast Simulation of the CMS detector", CMS Conference Report CR-2009/074 (2007).

[105] R. Fruhwirth, "Application of Kalman filtering to track and vertex fitting", Nucl. Instrum. Meth. A262, 444–450 (1987).

[106] CMS Collaboration , "Algorithms for b Jet Identification in CMS", CMS PAS BTV-09-001 (2009).

[107] R. Fruhwirth, W. Waltenberger, K. Prokofiev, T. Speer, and P. Vanlaer, "New developments in vertex reconstruction for CMS", Nucl. Instrum. Meth. A502, 699–701 (2003).

[108] CMS Collaboration , "Muon Reconstruction in the CMS Detector", CMS Analysis Note AN-2008/097 (unpublished) (2008).

[109] CMS Collaboration , "Performance of CMS Muon Reconstruction in Cosmic-Ray Events", `arXiv:0911.4994` (2009).

[110] CMS Collaboration , "The CMS Muon System", CMS Conference Report CR-2006/006 (2006).

[111] CMS Collaboration , "Muon Identification in CMS", CMS Analysis Note AN-2008/098 (unpublished) (2008).

[112] R. Fruhwirth and T. Speer, "A Gaussian-sum filter for vertex reconstruction", Nucl. Instrum. Meth. A534, 217–221 (2004).

[113] CMS Collaboration , "A cut based method for electron identification in CMS", CMS Analysis Note AN-2008/082 (unpublished) (2008).

[114] CMS Collaboration , "Performance of the SISCone Jet Clustering Algorithm", CMS Analysis Note AN-2008/002 (unpublished) (2008).

[115] CMS Collaboration , "Performance of Jet Algorithms in CMS", CMS PAS JME-07-003 (2007).

[116] G. P. Salam and G. Soyez, "A practical Seedless Infrared-Safe Cone jet algorithm", JHEP 05, 086 (2007).

[117] S. Catani, Y. L. Dokshitzer, M. H. Seymour, and B. R. Webber, "Longitudinally invariant K_T clustering algorithms for hadron hadron collisions", Nucl. Phys. B406, 187–224 (1993).

[118] M. Cacciari, G. P. Salam, and G. Soyez, "The anti-k_T jet clustering algorithm", JHEP 04, 063 (2008).

[119] M. Wobisch and T. Wengler, "Hadronization corrections to jet cross sections in deep- inelastic scattering", `arXiv:hep-ph/9907280` (1998).

[120] CMS Collaboration , "Plans for Jet Energy Corrections at CMS", CMS PAS JME-07-002 (2009).

[121] CMS Collaboration , "$E_\mathrm{T}^\mathrm{miss}$ performance in CMS", CMS PAS JME-07-001 (2007).

[122] CMS Collaboration , "Impact of Tracker Misalignment on the CMS b-Tagging Performance", CMS PAS BTV-07-003 (2008).

[123] CMS Collaboration , "FlavorHistory: A Heavy Flavor Overlap Tool", CMS Analysis Note AN-2009/147 (unpublished) (2009).

[124] J. E. Gaiser, "Charmonium Spectroscopy from radiative decays of J/Ψ and Ψ'", Appendix F, PhD Thesis, SLAC-R-225 (1982).

[125] CMS Collaboration , "Prospects for the measurement of the single top t-channel cross section in the muon channel, with the first $200\,\mathrm{pb}^{-1}$ of CMS data at $10\,\mathrm{TeV}$", CMS Analysis Note AN-2009/069 (unpublished) (2009).

[126] CMS Collaboration , "Jet reconstruction in the CMS Forward Hadron (HF) calorimeter in proton-proton collisions at $\sqrt{s} = 14\,\mathrm{TeV}$", CMS PAS FWD-08-001 (2008).

[127] F. James and M. Roos, "Minuit: A System for Function Minimization and Analysis of the Parameter Errors and Correlations", Comput. Phys. Commun. 10, 343–367 (1975).

[128] J. Neyman and E. S. Pearson, "On the Problem of the Most Efficient Tests of Statistical Hypotheses", Phil. Trans. R. Soc. Lond. A 231, 289–337 (1933).

[129] J. Pumplin et al., "New generation of parton distributions with uncertainties from global QCD analysis", JHEP 07, 012 (2002).

[130] T. Plehn, D. Rainwater, and P. Z. Skands, "Squark and gluino production with jets", Phys. Lett. B645, 217–221 (2007).

[131] S. Jadach, Z. Was, R. Decker, and J. H. Kuhn, "The tau decay library TAUOLA: Version 2.4", Comput. Phys. Commun. 76, 361–380 (1993).

[132] CMS Collaboration , "Performance Measurement of b-tagging Algorithms Using Data containing Muons within Jets", CMS PAS BTV-07-001 (2008).

[133] CMS Collaboration , "Evaluation of udsg Mistags for b-tagging using Negative Tags", CMS PAS BTV-07-002 (2008).

[134] Z. J. Ajaltouni et al., "Proceedings of the workshop: HERA and the LHC workshop series on the implications of HERA for LHC physics", `arXiv:0903.3861` (2009).

[135] G. L. Bayatian et al., CMS Collaboration , "CMS technical design report, volume II: Physics performance", J. Phys. G34, 995–1579 (2007).

Danksagung

Viele Personen, sowohl im beruflichen als auch im privaten Umfeld, haben mich im Laufe der letzten Jahre in unterschiedlichen Phasen auf ganz eigene Weise unterstützt und somit wesentlich zum Gelingen dieser Arbeit beigetragen.

Am Anfang stand natürlich das Vertrauen von Herrn Professor Dr. Thomas Müller, der mich in seine Arbeitsgruppe aufnahm und mir als seine Doktorandin die Möglichkeit gab, als Teil seiner Arbeitsgruppe zu lernen und zu wirken. Meine Abordnung ans CERN für zehn Monate hat nicht nur mich persönlich um viele Erfahrungen bereichert, sondern auch die Entwicklung der Arbeit und die Etablierung der Analyse innerhalb von CMS stark vorangetrieben. Für diese Möglichkeit möchte ich Herrn Müller an dieser Stelle besonders danken.

Ein besonderer Dank geht an Herrn Professor Dr. Wolfgang Wagner, der nicht nur das Korreferat meiner Arbeit übernommen hat, sondern mich auch von Anfang an umfassend betreut hat. Gemeinsam arbeiteten wir vor allem zu Beginn gegen manch Widerstand innerhalb der CMS-Kollaboration an unserem Ziel, seine langjährige CDF-Erfahrung auf dem Gebiet der Single-Top-Analyse in die CMS-Kollaboration zu transferieren. Auch nach seinem Wechsel an die Universität Wuppertal hat Wolfgang mich stets unterstützt und war bei Fragen immer erreichbar. Ich konnte bis zum Schluss sehr viel von ihm lernen, wofür ich ihm ausgesprochen dankbar bin.

Moreover, I would like to express my deep gratitude towards my external colleague Dr. Andrea Giammanco, who gradually took over the role of a mentor after Wolfgang had left Karlsruhe. Working hand in hand most of the time during my stay at CERN I was able to enjoy the inspiring advice and support of this particularly creative scientist. His supervision and networking have been indispensable for the success of the analysis within the CMS collaboration.

Zurück in Karlsruhe fand ich stets Unterstützung von Dr. Jeannine Wagner-Kuhr. Egal, ob es um die Analyse, das Verhandeln von Positionen und Strategien oder auch das Schreiben von Papern ging, sie war immer für mich da und hat mir den Rücken gestärkt, wofür ich mich bei ihr auch hier bedanken möchte.

Was wäre der einzelne Wissenschaftler ohne seine Arbeitsgruppe? Zusammen diskutiert man Probleme, sucht Lösungen und hilft sich gegenseitig. Gemeinsam freut man sich dann auch über erreichte Ziele und Fortschritte. Ein dickes Danke an die Top-Gruppe für die tolle Zusammenarbeit und Unterstützung! Ein zusätzliches Dan-